Recycling as a mechanism for extracellular matrix remodeling at the synapse

Dissertation

for the award of the degree
Doctor rerum naturalium
(Dr. rer. nat.)
by the Georg-August-Universität Göttingen

within the doctoral program *IMPRS for Neuroscience*
of the Georg-August University School of Science (GAUSS)

submitted by
Tal M. Dankovich

born in
Givatayim, Israel

Göttingen 2021

Members of the Thesis Advisory Committee

Prof. Dr. Silvio O. Rizzoli
(First referee)

Dept. of Neuro- and Sensory Physiology, University Medical Center, Göttingen

Prof. Dr. Dr. Oliver Schlüter
(Second referee)

Dept. of Psychiatry and Psychotherapy, University Medical Center, Göttingen

Prof. Dr. André Fischer

German Center for Neurodegenerative Diseases (DZNE), Göttingen

Members of the examination board

Prof. Dr. Tiago Outeiro

Dept. of Experimental Neurodegeneration, University Medical Center, Göttingen

Dr. Sarah Adio

Dept. of of Molecular Structural Biology, Institute for Microbiology and Genetics, Göttingen

Prof. Dr. Carolin Wichmann

Institute for Auditory Neuroscience & InnerEarLab, University Medical Center, Göttingen

Date of oral examination: September 21st, 2021

Declaration

I hereby declare that I have written the thesis independently, and with no other sources and aids than quoted.

Tal Dankovich

Göttingen, July 20th, 2021

"In general, no problems have been exhausted;
instead, men have been exhausted by the problems."

Santiago Ramón y Cajal, "Advice for a young investigator".

Table of Contents

Acknowledgements

First and foremost, to my supervisor Silvio Rizzoli – I would like to thank you for being a 'Doktorvater' in the true sense of the word. You were a mentor to me before all else. Thank you for your time, your patience and your humor, and for helping me gain perspective on a not-so-rare Saturday morning when I was doubtful about my data. I always left your office having learnt something new, be it biology, zoology or the workings of academia. Lastly, I can wholeheartedly say that there is not a single skill I learnt throughout my PhD that didn't benefit from your guidance.

I am grateful to Oliver Schlüter and André Fischer for agreeing to be a part of my thesis committee, and for the instructive scientific input during our meetings. I am indebted to Alexander Dityatev for the invaluable expertise and advice, and to my student army, Gabriel Petersen, Philipp Giro, Hannah Hadi, Jose Doeren and Simon Klöppner, for their hard work and enthusiasm, and without whom this thesis would have had several less figures.

I would like to thank all of my colleagues in the Rizzoli lab for the incomparable atmosphere over the last five years. To Christina Schäffer-Zeising, Nicole Hartelt and Christina Patzelt - thank you for preparing all of the neuronal cultures and slices for this project, and for answering all of my questions, no matter how small or stupid. To Eugenio Fornasiero - thank you for the unlimited patience and advice, and for always opening the door on the weekends that I locked myself out of the lab. To my original officemates Martin Helm and Sinem Sertel – thank you for being equally insane, and for ensuring that even a five-minute break from work was a lively one (to say the least). Martin, thank you for your supervision during my Master thesis, for being the second half of the nPreSC, and for our past and present discussions.

I am grateful to the IMPRS Neuroscience team, Michael Hörner, Sandra Drube, Jonas Barth and Franziska Kühne, for making it seem as if the non-scientific parts of a PhD are non-existent. And mostly, thank you for selecting me to be a part of the Neuro family. To my program-mates – thank you for making my first two years in Göttingen so memorable. I anticipate learning all about your achievements in the future.

To Ronja, Linda, Ali, Myrto and Mayukh – thank you for being my Göttingen family. Ronja, thank you for your gentle tyranny, which earned me several days of freedom after submitting both of my theses. Linda, thank you for being the necessary Gryffindor of our group. Myrto, your couch deserves to be first author on my manuscripts. Thank you so much for making me a part of your ohana. Lastly to Mayukh, thank you for solving my problems as fast as I can explain them, for being an endless source of motivation, and for your contagious enthusiasm and ambition. Our adventures made these years fly by, and I look forward to many more adventures in the future.

Last but not least, I would like to thank my parents, who wanted me to become an electrical engineer. *But always continue to give me their support nonetheless.*

Summary

In the adult brain, the extracellular matrix (ECM) forms lattices that sheath neurons and synapses. The exceptional longevity of ECM molecules lends these lattices a unique durability, and as such, they are deemed to stabilize neural circuits and restrict their plasticity. At the same time, the adult ECM retains the ability to be occasionally remodeled, in order to allow neural circuits to be altered throughout adulthood. According to the dominant paradigm in the current literature, this remodeling occurs through the transient release of proteolytic enzymes to cleave the ECM near synapses, followed by the secretion of newly-synthesized molecules that embed into the ECM, thereby resulting in ECM changes that fit this structure to the needs of synaptic plasticity. A problem arises when considering that structural changes to synapses *in vivo* are surprisingly frequent (on a timescale of minutes to hours). Supporting such frequent remodeling through *de novo* synthesis of ECM molecules would be costly for the cell in metabolic terms. Importantly, such a view is not in line with the measured lifetimes of these molecules, of weeks to months. How, then, can the cell sustain a continual remodeling of the ECM at synapses? In this thesis, I propose the existence of an additional mechanism, whereby the ECM can be continually remodeled through a recycling of its components. This mechanism lends the ECM the flexibility that is necessary for frequent synaptic changes. I expect that such a mechanism would operate constitutively, but would also be intimately linked to synaptic activity.

In **Chapter 1**, I summarize the existing knowledge on the configuration and function of the ECM in the adult brain, and discuss the potential interactions of ECM molecules with the pre- and postsynaptic machinery. After a brief discussion of the dominant paradigm for ECM remodeling through proteolytic cleavage, I present the body of literature to support the hypothesis of ECM recycling at synapses. Accordingly, I conclude that ECM molecules can be secreted in an activity-dependent manner from both the pre- and postsynaptic compartments. By contrast, I hypothesize that the locus of ECM entry into the recycling route is restricted to the postsynaptic side, where there is a considerably greater presence of local trafficking machinery. I remark, however, that it has not yet been established whether (and how) the presence of this local machinery is related to synaptic activity.

In **Chapter 2**, I present a collaborative project that endeavored to bridge the knowledge gap described in Chapter 1, and establish a link between the amounts of postsynaptic trafficking machinery and local synaptic activity. This was accomplished through the use of super-resolution microscopy and automated quantitative image analysis to successfully correlate the local distribution and abundance of several postsynaptic trafficking elements to local synaptic activity.

In **Chapter 3**, I present the primary investigation of this thesis, which directly tests the hypothesis of ECM recycling at synapses, using the glycoprotein TNR as an archetype. Here, we used an array of imaging assays, including super-resolution fluorescence imaging and nanoscale secondary ion mass spectrometry, to test the hypothesis that TNR molecules undergo continual recycling. We demonstrated the existence of a pool of mobile TNR molecules that are enriched at synapses, and cycle in and out of the perisynaptic ECM via a surprisingly long route (lasting approximately three days). Further investigation revealed that these molecules are trafficked as far as the Golgi apparatus in the neuronal soma, where they presumably undergo a re-glycosylation, and are then trafficked to synapses once again. Finally, we established a link between synaptic activity and the extent of TNR recycling.

Lastly, in **Chapter 4**, I discuss the primary conclusions of this thesis, as well as existing caveats and outstanding unanswered questions. I present possible experiments that could address these in the future, and discuss new areas of research that warrant further investigation.

1: Introduction

1.1. The brain extracellular matrix

1.1.1. Overview

Like any other tissue in the body, a large portion of the brain consists of space filled with extracellular matrix (ECM), but uniquely, it is mostly devoid of fibrous matrix proteins like collagen that are abundant in other tissues. These proteins appear transiently in the embryonic brain to guide migrating neurons, but once development has ended, they are mostly found surrounding the blood vessels that contribute to the blood-brain barrier (Baeten and Akassoglou, 2011; Ruoslahti, 1996; Syková and Nicholson, 2008). Rather, the immediate space surrounding the neurons becomes dominated by a more stabilizing presence of matrix, arising from a family of sulfated proteoglycans called lecticans and two molecules that they bind, hyaluronic acid and tenascin. Together, these molecules form a mesh-like coat that enwraps neurons very finely but leaves gaps where synaptic contacts can exist (Dityatev et al., 2010; Ruoslahti, 1996). On some neurons, the ECM coat is particularly dense around the soma, proximal dendrites, and axon initial segment. These dense structures, termed perineuronal nets (PNNs), were already observed by Camillo Golgi in 1893 through the use of his eponymous silver staining (Figure 1). He described these as "a delicate coating… mainly reticular in structure …covering not only the cell body but also stretching along the protoplasmic extensions" (Golgi, 1898). Several decades later, the function of the PNNs slowly began to be elucidated [1]. It was discovered that PNNs are present in virtually all parts of the mammalian central nervous system, particularly (but not exclusively) around inhibitory neurons that express the calcium buffer parvalbumin (Härtig et al., 1992; Yamada and Jinno, 2013). The formation of PNNs is one of the final acts of neural development, coinciding with the closure of the critical period for plasticity [2] (around 2-5 weeks postnatally in rodents and around 2-8 years postnatally in humans) (Fawcett et al., 2019). As a result, it is widely believed that the PNNs stabilize key neurons in circuits that encode sensory information and potent memories such as fear, and restrict further changes to these circuits. Indeed, if PNNs are broken down enzymatically, juvenile forms of plasticity can be restored, like the ability of neurons in the visual cortex to reduce their response to an eye that is deprived of light and increase their response to the non-deprived eye (known as ocular dominance plasticity) (Pizzorusso, 2002). Astonishingly, even drug addiction and early fear memories can be erased (Banerjee et al., 2017; Gogolla et al., 2009; Xue et al., 2014).

Being so conspicuous, PNNs were a major focus of studies that investigated the neuronal ECM. With advances in immunostaining techniques and imaging resolution, it became apparent that the neuronal ECM is ubiquitous in the brain (albeit in a looser and more molecularly heterogeneous configuration), and that it can also be found in close proximity to synapses. It was soon recognized that this loose ECM plays an equally important role at synapses, performing a delicate balancing act of restricting and permitting synaptic

---

[1] It would be several decades before the function of these structures would be explored, due to Ramón y Cajal's vehement claim that these observations were nothing more than fixation artifacts (Ramón y Cajal, 1909; Vitellaro-Zuccarello et al., 1998).

[2] During development, the circuitry in different brain regions is highly sensitive to experience for a limited window of time. Once this window closes, these circuits become fixed, and plasticity declines to adult (mostly latent) levels.

plasticity, not only by acting as a physical barrier, but also by directly interacting with synaptic machinery (Dityatev and Schachner, 2003). This gradual understanding ultimately led to concept of the "tetrapartite synapse", which upgraded the existing model (consisting of the pre- and postsynaptic compartments, and the nearby glial processes) to also include the surrounding ECM (Dityatev et al., 2006). Since then, the concept of the tetrapartite synapse has been substantiated by a wealth of evidence for the modulation of synaptic components (such as the actin cytoskeleton and local ion channels) by the perisynaptic ECM, as well as evidence that its removal is deleterious to both synaptic transmission plasticity. These studies, along with more speculative evidence of molecular interactions, will be reviewed in greater detail in Chapter 1.2.
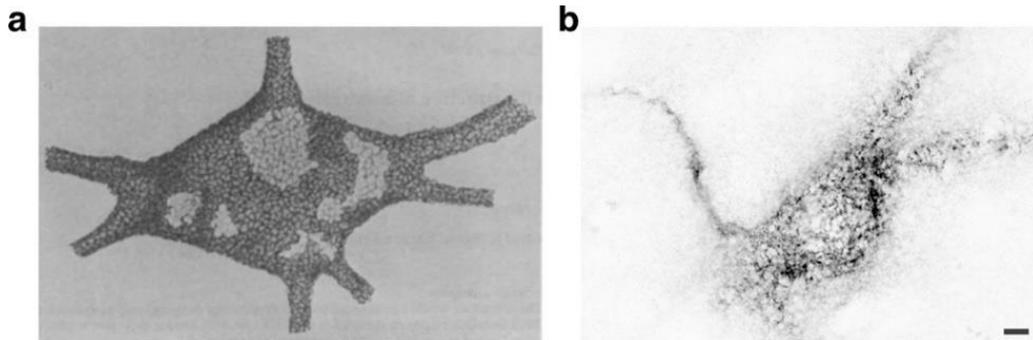
Figure 1 Perineuronal nets. **a**, A sketch by Camillo Golgi, showing the reticular covering on a neuron from the rat spinal cord (Golgi, 1898). **b**, A PNN-wrapped neuron in an organotypic hippocampal slice, imaged with confocal microscopy. Scale bar = 5 μm.

1.1.2. Major molecular components

As I stated in the overview, the neural ECM is mainly composed of a family of sulfated proteoglycans named lecticans, and their binding partners, hyaluronic acid and tenascin. Despite their association with neurons, many of these molecules are also produced and secreted by glial cells, and some might be exclusively produced by glia. One important quality that is highly relevant for this thesis is that all of these molecules are exceptionally long-lived as compared with intracellular proteins (*e.g.,* months versus days in rodents *in vivo*) (Dörrbaum et al., 2018; Fornasiero et al., 2018; Heo et al., 2018; Toyama et al., 2014). Structurally, the ECM molecules form a lattice, where complexes of lectican-decorated hyaluronan molecules are extensively cross-linked by tenascins. These lattices are tethered to the neuronal surface through the hyaluronan molecules, which stay attached to their membrane-associated synthase (Figure 2) (Dityatev et al., 2010; Sorg et al., 2016). This general configuration holds true for all forms of neuronal ECM, and the variability (between loose ECM formations and PNNs, different brain regions and cell types) stems from differences in the types and amounts of the various proteoglycans (Zimmermann and Dours-Zimmermann, 2008).
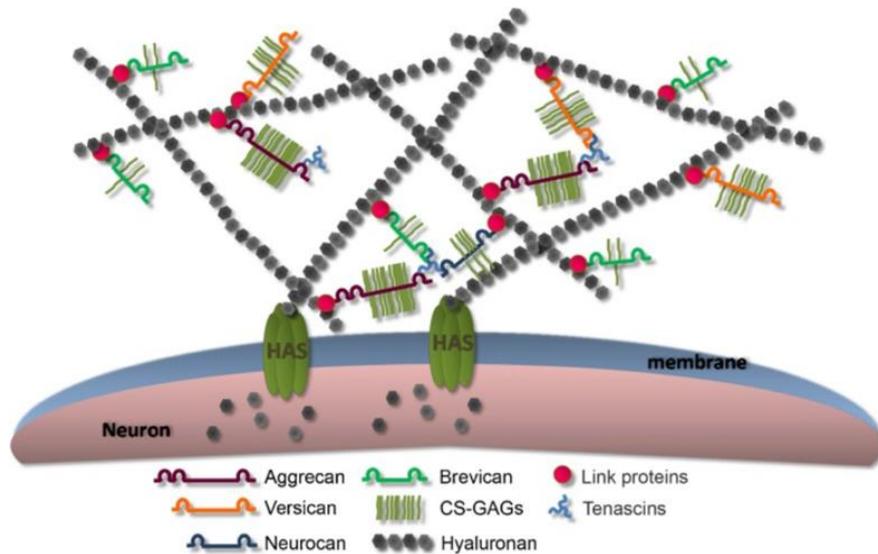
Figure 2 Lattice organization of the brain ECM. A model showing the organization of hyaluronan (linked to its membrane-bound synthase), lecticans, and tenascin R. The interactions between hyaluronan and lecticans are strengthened by hyaluronan and proteoglycans link proteins (Haplns). Reproduced with permission from (Djerbal et al., 2017) (http://creativecommons.org/licenses/by/4.0/).

In the following section, I will briefly describe the major components of the ECM. These descriptions are primarily derived from studies of these molecules in rodents, but these show a close homology to humans. I will give special attention to the glycoprotein tenascin-R (TNR) since the experiments I present in Chapter 3 focus specifically on this molecule. That being said, the hypotheses that drove these experiments pertain to other components of the neuronal ECM as well, though we have gathered far less evidence for these molecules at this stage.

1.1.2.1.   Lecticans, hyaluronan, and link proteins

Lecticans, a sub-family of chondroitin sulfate proteoglycans (CSPGs), are the most abundant proteoglycans in the brain ECM (Djerbal et al., 2017). CSPGs comprise one or more unbranched glycosaminoglycan chains covalently bound to a protein core. As the name suggests, sulfation is one of the main modifications to these chains, and the diversity of sulfation patterns confers different biological functions to the molecules (Herndon and Lander, 1990). Nevertheless, the functions are (mostly) restrictive: to neuronal migration, neurite outgrowth, and to plasticity (Laabs et al., 2005). The major lecticans are aggrecan (>500 kDa), versican (~400 kDa), neurocan (~240 kDa), and brevican (~145 kDa) [3] (Deepa et al., 2006). All of these share a globular hyaluronan-binding domain at their amino-terminal, and a globular domain at their carboxyl-terminal that binds glycoproteins such as tenascins (Aspberg et al., 1997). The central region containing the glycosaminoglycan attachment sites is variable, with as few as three potential sites (brevican) and as many as 120 (aggrecan) (Yamaguchi, 2000). The cellular source of these molecules has been difficult to determine since they may be synthesized by more than one cell type. This is further complicated by the

---

[3] The molecular weights correspond to the full-length core proteins, derived from the bands detected in Western Blots of brain homogenates.

fact that their expression can be transient (*e.g.,* expressed at certain stages of development or in response to injury). To put it briefly, it appears that *in vivo,* both neurons and astrocytes have the capability of producing all lecticans. However, the evidence suggests that neurocan is derived exclusively from neurons in the healthy brain (Dzyubenko et al., 2016).

Unlike the lecticans, hyaluronan (also known as hyaluronic acid; HA) is a pure glycosaminoglycan that is not covalently bound to a protein core. It is unbranched and can be extremely long (ranging from 2 μm up to 25 μm, and from 10^6 to 10^7 kDa). It is ubiquitously expressed in the ECM and, in fact, is expressed all tissues in vertebrates, and even in some types of bacteria. As I mentioned, HA is produced by synthases which are positioned on the inner face of the membrane (in contrast to all other glycans, whose production requires the endoplasmic reticulum (ER) and the Golgi apparatus. It exudes into the pericellular space while remaining attached to the enzyme (Fraser et al., 1997; Toole, 2004). Both neurons and astrocytes can produce HA. However, the formation of PNNs is dependent on neuronal HA (Miyata et al., 2005). In contrast to the lecticans, hyaluronan is believed to be a promoter of cell migration during development. It has a remarkable ability to become hydrated, which forces barriers away from the cell that extrudes it, creating a cell-free space for migration (Toole, 2004). It is, therefore, unsurprising that the amount of HA is significantly reduced in the adult brain (Jenkins and Bachelard, 1988; Margolis et al., 1975).

The interaction between HA and lecticans is strengthened by a family of four ancillary glycoproteins collectively termed hyaluronan and proteoglycan link proteins (Haplns). The structure of the link proteins strongly resembles the HA-binding domain of the lecticans, allowing them to interact with both molecules simultaneously to form ternary complexes. As a remarkable example of molecular evolution, the genes of the four Haplns are physically adjacent to the genes of the four lecticans (Spicer et al., 2003). Two of the Haplns (Hapln1 and Hapln4) are found exclusively in PNNs and are essential for their formation (Oohashi et al., 2015). It still remains to be determined, however, if and to what extent they are present in looser ECM formations.

1.1.2.2.   Tenascins

Tenascins are a large family of multimeric glycoproteins that are unique to vertebrates. To date, four members have been identified in mammals, namely, tenascin-C, -R, -W/N, and -X. The members share common structural motifs, all arranged in the same sequence. The amino-terminal of the proteins is rich in cysteines, which mediates interactions between the monomers, allowing them to assemble into dimers, trimers, or hexamers. This is followed by a varying number of epidermal growth factor (EGF)-like repeats, and then a series of fibronectin type III-like domains. The latter mediates the interactions of tenascins with lecticans, among other binding partners (Hsia and Schwarzbauer, 2005; Jones and Jones, 2000; Midwood et al., 2016). I will not elaborate on TNW/N or TNX since their expression in the central nervous system is either controversial or does not reach significant levels (Matsumoto et al., 1994; Neidhardt et al., 2003; Scherberich et al., 2004). TNC was the first member to be discovered, and remains the most extensively studied [4]. In the central nervous system, TNC is strongly expressed by glial cells as well as a limited number

---

[4] The family name "tenascin" reflects the tissue in which the founding member tenascin-C was found to be most abundant – the Latin verb *tenere* meaning "to hold" (tendons), and *nasci* meaning "to be born" (embryos).

of neurons during development. In the adult brain, its expression is significantly reduced and only persists in select regions (Bartsch, 1996; Ferhat et al., 1996; Oliet et al., 1997; Stamenkovic et al., 2017). However, it is transiently upregulated following injury and, interestingly, also during synaptic plasticity (Nakic et al., 1998; Okada and Suzuki, 2021). Functionally, TNC appears to be a stress protein that modulates cell adhesion, proliferation, and migration (Midwood et al., 2016).

Unlike TNC, the expression of TNR (also known as J1-160/180 or *Janusin*) begins late in development, and is restricted to the central nervous system (Kruse et al., 1985). It exists in two isoforms, with a weight of 160 kDa and 180 kDa, generated by alternative splicing, though both the biochemical and functional differences between these remain to be determined (Carnemolla et al., 1996; Fuss et al., 1993). Electron microscopy of rotary shadowed molecules [5] revealed that these could build dimers (160) or trimers (180) (Pesheva et al., 1989). TNR is first detected around birth, expressed by oligodendrocyte precursors and type-2 astrocytes [6], and is highly abundant during myelination. When myelination has ceased, it is downregulated to adult levels and localizes to the outer parts of the myelin sheaths and the nodes of Ranvier (Bartsch et al., 1993; Wintergerst et al., 1993). In the adult brain (starting from about 2-3 weeks after birth), TNR is also consistently expressed by a subpopulation of neurons in the hippocampus, cortex, cerebellum, and olfactory bulb, and contributes to the formation of their PNNs (Fuss et al., 1993; Wintergerst et al., 1993, 2001). The interaction of TNR with lecticans has been demonstrated *in vitro* to occur through fibronectin type III domains 3 through 5. In particular, the affinity for brevican was found to be over 10-fold higher than for any of the other lecticans. In addition, TNR co-precipitates with brevican from the adult brain, and the two colocalize immunohistochemically, strengthening the claim that these molecules interact *in vivo* (Aspberg et al., 1997; Hagihara et al., 1999; Lundell et al., 2004). Functionally, TNR has seemingly contradicting effects *in vitro* [7]. It can both promote and inhibit neurite outgrowth depending on the type of cell it is presented to, and on how it is presented (arranged as a boundary or uniformly). Depending on the developmental stage and the cell type, it can also be either adhesive to the cells or anti-adhesive (Becker et al., 2000; Faissner, 1997; Morganti et al., 1990; Pesheva et al., 1993). One function is coherent with its apparent involvement in myelination: it supports the adhesion of oligodendrocyte progenitors and promotes their maturation (Pesheva et al., 1997). This is further strengthened by the finding that TNR can interact with the β2-subunit of voltage-gated sodium channels, which are known to be present at the nodes of Ranvier (Srinivasan et al., 1988; Xiao et al., 1999). An additional function of TNR is the inhibition of axon outgrowth through its interaction with the adhesion molecule F3/F11/Contactin, which is expressed on axonal growth cones during development (Bartsch et al., 1993; Pesheva et al., 1993; Xiao et al., 1996). It is likely that the interaction of contactins present in the growth cone membrane with extracellular TNR steers it away from off-target regions during development. Considering these seemingly important functions, it is surprising to learn that TNR-knockout mice are both viable and fertile and that brain regions expressing TNR appear to develop normally. They do, however, have slower axonal

---

[5] In rotary shadowing electron microscopy, a heavy metal is evaporated onto the sample at an oblique angle. The surfaces that are facing away from the source are shielded from the metal deposits, creating a "shadow".

[6] Oligodendrocytes and type-2 astrocytes develop from the same bi-potential precursor cells (ffrench-Constant and Raff, 1986).

[7] The name *Janusin* was chosen due to the duality of its functions (depending on the cell type and the developmental age). It is derived from Janus, who was the Roman god of dualities (usually depicted as having two faces).

conduction velocities, further reinforcing the assumption that TNR is a modulator of voltage-gated sodium channels at the nodes of Ranvier (Weber et al., 1999). Another prominent phenotype of these mice is an abnormal morphology of the PNNs (Brückner et al., 2000; Haunsoø et al., 2000; Morawski et al., 2014). Over time, more subtle phenotypes were discovered, and it was understood that TNR deficiency leads to broad changes in the electrophysiological properties of neurons. This is due to its important role as a modulator of synaptic function, as I will describe in greater detail in Chapter 1.2.

1.1.2.3.   Integrins: extracellular matrix receptors

Many transmembrane proteins are known to act as receptors for ECM molecules. Through these receptors, mechanical or biochemical changes to the ECM can initiate intracellular signaling cascades that affect the cell's differentiation, migration, survival and proliferation (Kim et al., 2011). The best-studied ECM receptors are integrins, which are relevant here due to the presumed interaction of TNR with integrin receptors containing the β1 subunit (from hereon referred to as β1-integrins) (Liao et al., 2008). Integrins are heterodimers consisting of α and β subunits, which bind non-covalently to form 24 known combinations (Takada et al., 2007). Among the ECM ligands for integrins are those that contain a specific motif consisting of Arg-Gly-Asp (known as the RGD motif). This was first discovered in fibronectin but was later found in additional ECM proteins, including laminin and tenascin (Aumailley et al., 1990; Bourdon and Ruoslahti, 1989). The intracellular tail of the receptors binds to various signaling molecules, and importantly, the β subunit interacts with actin-associated proteins such as talin and kindlin, which effectively links the ECM to the cell's cytoskeleton (Kerrisk et al., 2014). This allows integrins to mediate the attachment of cells to the ECM and promote or inhibit their migration. Expectedly, integrins expressed in the brain play an essential role in neuronal migration during development and mediate neurite outgrowth (Gupton and Gertler, 2010; McCarty et al., 2005; Rehberg et al., 2014). Integrins are also abundantly expressed in the adult brain (both in neurons and glial cells), and are particularly enriched at synapses. Here they have been shown to play an important role both in pre- and postsynaptic functions (Park and Goda, 2016; Shi and Ethell, 2006).

1.2.   The "tetrapartite synapse"

The concept of the *tri*-partite synapse was introduced over two decades ago when it was understood that glial cells in close proximity to synapses are integral to their function, and that the existing model (which included only the pre and postsynaptic elements of two communicating neurons) is incomplete (Araque et al., 1999). Several years later, the tripartite model was upgraded to also include the extracellular molecules that are secreted by the cells into the perisynaptic space, giving rise to the concept of the *tetra*-partite synapse (Dityatev et al., 2006). A focus of research that led to this understanding is the vertebrate neuromuscular junction, where the presynaptic bouton of the motoneuron is enwrapped by Schwann cells, and the synaptic cleft between the bouton and the postsynaptic membrane of the muscle is filled with a basal lamina [8]

---

[8] The basal lamina is a thin network of extracellular matrix forming a sheet under epithelial cells (to separate them from the underlying connective tissue), and enwraps muscle and fat tissues. Major components of the basal lamina are laminin and collagen. In the brain, basal laminae are present on the epithelial cells that line the ventricles and the endothelial cells of the vessels that form the blood-brain-barrier (Benarroch, 2015; Timpl, 1996).

(Faissner et al., 2010). Despite many similarities between the neuromuscular junction and central nervous system synapses, the latter have no basal lamina, and their synaptic cleft is significantly smaller (~20 nm versus ~50 nm). Due to the minute size of the synaptic cleft, it was once presumed that the formation, differentiation, and maintenance of new synapses occurs through a direct interaction between pre- and postsynaptic transmembrane adhesion proteins (Giagtzoglou et al., 2009). However, studies now show that the ECM in the synaptic cleft and in the perisynaptic region is equally important for these functions. As I explained in the overview, the ECM can be permissive or restrictive, largely depending on the developmental age of the brain. This is also the case at synapses: during development, the ECM contributes to the formation of new synapses, and in the mature brain, it contributes to their stabilization, while still allowing for occasional synaptic plasticity. Here, I will focus on the role of the perisynaptic ECM in the maintenance of mature synapses and in synaptic plasticity. In addition, I will limit my discussion to the secreted extracellular molecules of the perisynaptic ECM and their receptors, though it should be mentioned that trans-synaptic interactions between transmembrane pre- and postsynaptic adhesion molecules, such as neurexins and neuroligins, are also crucial for the stabilization of synapses (Dalva et al., 2007). As a note, I will refer to the molecules of the hyaluronan-based ECM collectively as the 'perisynaptic ECM', though as the studies I present suggest, it is likely that they also exude into the synaptic cleft, where they potentially interact with synaptic proteins.

1.2.1. Interaction of the extracellular matrix with postsynaptic machinery

Stabilization and maintenance of synapses: Expectedly, the perisynaptic ECM acts as a physical barrier that prevents transmembrane molecules from diffusing away from the synaptic area. When a synapse is first formed, neurotransmitter receptors accumulate at the postsynaptic membrane by interacting with local scaffolding proteins (this process is well-documented in excitatory glutamatergic synapses, where glutamate receptors become anchored by scaffolds at the postsynaptic density (PSD) [9]; Li and Sheng, 2003) [10]. Nevertheless, these receptors retain a degree of lateral mobility in the membrane, despite their association with scaffolding proteins (Triller and Choquet, 2008). In cultured hippocampal neurons, the mobility of AMPA receptors significantly decreases after 2-3 weeks *in vitro*, around the same time that the neuronal ECM begins to form (Borgdorff and Choquet, 2002; John et al., 2006). This heightened mobility can be restored by enzymatically cleaving hyaluronan to disrupt the ECM. This holds true not only for AMPA receptors but also for an artificially-introduced transmembrane protein, which indicates that the perisynaptic ECM stands as an unspecific physical block to all transmembrane proteins at the synapse (Frischknecht et al., 2009). On a larger scale, it appears that the ECM stabilizes the entire synaptic structure.

---

[9] Seen by electron microscopy, the PSD is an electron-dense region in the membrane of excitatory postsynapses. The PSD contains neurotransmitter receptors and associated signaling molecules, as well as scaffolding proteins that hold these in place (Sheng and Kim, 2011).

[10] A caveat to the hypothesis that glutamate receptors are anchored at the PSD by scaffolding proteins such as the post-synaptic density protein PSD95 (*e.g.*, Schnell et al., 2002) should be noted: mice deficient in PSD95 have enhanced long-term potentiation, a process which is dependent on glutamate receptor signaling (see subsection '*Long-term potentiation*' below) (Migaud et al., 1998). Therefore, an alternative view is that PSD95 serves as a scaffold for a variety of post-synaptic signaling proteins (including glutamate receptors), rather than a bona fide anchor for these receptors (Xu et al., 2008).

In most excitatory synapses in the brain, the postsynaptic compartments are in the form of conspicuous membrane protrusions called dendritic 'spines' (Gray, 1959). Enzymatic cleavage of CSPGs in the adult visual cortex *in vivo* and in organotypic hippocampal slices *in vitro* leads to an increase in dendritic spine motility and in spine head outgrowth (Orlando et al., 2012; de Vivo et al., 2013). Beyond relieving the physical barrier imposed by the ECM, this treatment might also breach direct interactions between transmembrane proteins in the spine and the ECM. In support of this claim, it was found that the hyaluronan receptor CD44 contributes to the maintenance of spine morphology by modulating the activity of actin cytoskeleton regulators (Roszkowska et al., 2016). This was similarly shown for β1 integrins, which are known to interact with both CSPGs and TNR (Liao et al., 2008; Sloan Warren et al., 2012; Tan et al., 2011). This latter finding may offer an explanation as to why mice deficient in TNR have a reduced spine density in the olfactory bulb (David et al., 2013).

Long-term potentiation [11]: In many types of synapses, activity-dependent changes are instigated when the intracellular concentration of calcium at the postsynapse exceeds a critical threshold. This is typically achieved through the opening of postsynaptic calcium-permeable NMDA receptors, whose activation may result in long-term potentiation (LTP) of synapses (Herring and Nicoll, 2016). The results from several studies point to an essential role for β1-integrins in producing LTP: their activation increases the amplitude and duration of NMDA-mediated currents, and promotes polymerization and subsequent stabilization of the actin cytoskeleton (which enlarges the spine head) (Bernard-Trifilo et al., 2005; Kramar et al., 2006; Rex et al., 2009). These observations are further supported by the finding that a neuron-specific knockout of β1-integrins in the hippocampus results in impaired LTP (Chan et al., 2006; Huang et al., 2006).

Another ECM molecule known to modulate LTP is reelin, a secreted glycoprotein that is well-studied as a regulator of neuronal migration during brain development (D'Arcangelo, 2014; Tissir and Goffinet, 2003). In the adult, it is now fairly well-established that reelin is an important modulator of synaptic plasticity. It was shown that reduced levels of reelin lead to impairments in LTP (Qiu et al., 2006), while reelin supplementation enhances LTP (Beffert et al., 2005; Pujadas et al., 2010; Rogers et al., 2011). This is likely to occur through its ability to enhance the activation of NMDA receptors (Weeber et al., 2002).

Besides NMDA receptors, postsynaptic L-type voltage-gated calcium channels (LVGCC) can also contribute to the influx of calcium ions, and in this way, promote some forms of LTP (Herring and Nicoll, 2016). Interestingly, TNC was found to be necessary for LVGCC-dependent LTP in the hippocampus (as mentioned in the previous section, despite its prominent expression during development, this molecule was shown to be upregulated during synaptic plasticity events in the adult), although it remains to be determined whether it interacts with the channels directly (Evers et al., 2002). Similarly, hyaluronan was shown to

---

[11] Long-term potentiation (LTP) is an activity-driven long-lasting strengthening of synaptic responses, and thus a presumed mechanism for memory storage. It is divided into an early phase, during which calcium influx into the spine leads to an insertion of AMPA receptors in the synaptic membrane and an enlargement of the spine head, and a late phase, in which gene transcription and protein synthesis in the postsynaptic cell allow for the maintenance of the memory (Herring and Nicoll, 2016).

modulate LGVCCs in the hippocampus, though proof of a direct interaction is also still lacking (Kochlamazashvili et al., 2010).

Metaplasticity: Synapses also have the capacity to adjust their predisposition to undergo plastic changes (Abraham and Bear, 1996). Typically, this is achieved by modifying the basal excitatory activity of the neuron, which then increases or decreases the threshold stimulation required for LTP induction. TNR is highly relevant in this regard since it has been extensively shown to regulate GABA-mediated inhibition, which determines the level of basal excitatory transmission (Nikonenko et al., 2003; Saghatelyan et al., 2001, 2003). Mice deficient in TNR have increased basal excitatory transmission and, as expected, an increased threshold for LTP induction (Bukalo et al., 2007; Saghatelyan et al., 2001). One possible explanation is a loss of the direct interaction of specific oligosaccharide structures on the TNR molecules called human natural killer 1 (HNK1) with $GABA_B$ receptors, which inhibits their activity (Kruse et al., 1985; Saghatelyan et al., 2001, 2003). Interestingly, this reduction in perisomatic GABAergic signaling is specific to the CA1 region of the hippocampus, and inhibition is actually increased in the dentate gyrus. This is in line with observations that behaviorally, mice deficient in TNR have faster reversal learning and increased reactivity to novelty, which are both correlated to activity in the dentate gyrus (Morellini et al., 2010).

1.2.2.   Interaction of the extracellular matrix with presynaptic machinery

Since studies of ECM interactions at presynapses in the central nervous system are relatively scarce, this section will be considerably more speculative in nature. I mentioned before that hyaluronan was shown to restrict the lateral diffusion of postsynaptic AMPA receptors. However, the observation that the mobility of an artificially introduced transmembrane protein is also reduced suggests that it may generally restrict receptor mobility, including at the presynapse (Frischknecht et al., 2009). Evidence of a direct influence of hyaluronan comes from the observation that a knockdown of the hyaluronan receptor CD44 (shown to be present at hippocampal presynapses) reduced the number of presynapses (identified by a labeling of the active zone [12] marker bassoon) (Roszkowska et al., 2016). Nevertheless, evidence that hyaluronan may interact directly with presynaptic receptors does not preclude the possibility that it also stabilizes the synapse by acting as a bona fide physical barrier.

Additional evidence for the interaction of the ECM with presynaptic machinery comes from cochlear inner hair cell synapses, where the tight clustering of presynaptic calcium channels in front of PSD is necessary for fast synaptic transmission (Fell et al., 2016). It was discovered that mice deficient in brevican experience a mild hearing loss due to the misalignment of these channels (Sonntag et al., 2018). A possible explanation is that the calcium channels are clustered through an interaction of the $\alpha_2\delta2$ subunit with brevican, since a similar phenotype was observed for mice deficient in this subunit (Fell et al., 2016). The absence of brevican was also shown to affect synaptic transmission in a central auditory synapse, the calyx of Held. Though the mechanism was not described, the change in the dynamics of synaptic transmission was also congruent with a change in the distribution of presynaptic calcium channels (Blosa et al., 2015).

---

[12] The active zone is a specialized region in the presynaptic plasma membrane where synaptic vesicle exocytosis takes place (Südhof, 2012).

Additional ECM molecules known to modulate presynaptic function are laminins. These are large, secreted glycoproteins (~400 to ~900 kDa) that form heterotrimers consisting of α, β and γ subunits. Laminins are a major component of the basal lamina which, as I mentioned, is lacking in central nervous system synapses. Nevertheless, subtypes of laminins are found in the brain, and recent evidence suggests that they play an essential role in the organization of presynaptic machinery (Nirwane and Yao, 2019). In mice deficient in laminin β2, the anchoring of active zone proteins at presynaptic membranes in the retina is disrupted, resulting in a spatial disorganization of the presynapse (Hunter et al., 2019). This may be due to a direct interaction between laminin β2 chains and presynaptic calcium channels since these are known to interact at the neuromuscular junction synapse (Nishimune et al., 2004). Laminin α5 chains also play an important role at the neuromuscular junction synapse by interacting with synaptic vesicle protein 2 (SV2), which is required for the activity-dependent release of synaptic vesicles (Chang and Sudhof, 2009; Son et al., 2000). Recently, laminin α5 was also shown to be present at central nervous system synapses, raising the possibility that this mechanism might also occur in the brain (Omar et al., 2017). It is also worth mentioning that laminins could exert some effects through their interaction with integrins, which are widely known to be receptors for these molecules (Nirwane and Yao, 2019).

As for the postsynapse, it appears that integrins also have important functions at the presynapse, and here also, β1 integrins stand out as a focus of research. Though less abundant than at the postsynaptic side, β1 integrins were shown to be present at hippocampal presynapses (Mortillo et al., 2012). Mice in which β1 integrins were knocked out in hippocampal neurons, have modified synaptic responses indicative of a smaller reserve pool of synaptic vesicles [13] or a defect in their mobilization (Huang et al., 2006). In addition, at the neuromuscular junction, α3-containing integrins are known to be complexed with presynaptic calcium channels, though it remains to be determined whether this is also the case in the central nervous system (Carlson et al., 2010).

Presynaptic vesicle release also appears to be modulated by reelin (previously introduced for its role in postsynaptic LTP). The application of exogenous reelin to mature hippocampal neurons was shown to significantly enhance spontaneous vesicle release. This was suggested to occur through the interaction of reelin with its canonical receptors VLDLR and ApoER2 at the presynapse, which results in an increase of presynaptic calcium levels. Interestingly, reelin treatment was also shown to specifically mobilize reserve pool vesicles that are enriched in the vesicular protein VAMP7, suggesting that the reelin receptors might additionally function as modulators of these vesicles (Bal et al., 2013).

TNR is also likely to be involved in presynaptic function, since mice deficient in TNR show a disorganization in perisomatic synapses in the CA1 pyramidal layer of the hippocampus. Among other findings, it was observed that synaptic vesicles have a reduced tendency to cluster (a property which is known to be necessary for functional transmission; Fletcher et al., 1994), and that fewer vesicles are found

---

[13] The reserve pool contains synaptic vesicles that are only released during an intense electrical stimulation and are believed to be only rarely released under physiological conditions. The pool is thought to act as a buffer for synaptic vesicles proteins, to prevent them from escaping into the axon (Denker et al., 2011).

in proximity to the active zone (indicating a smaller readily-releasable pool [14]). The study did not examine excitatory dendritic synapses in detail, and it is possible that TNR could exert similar effects at these synapses (Nikonenko et al., 2003).
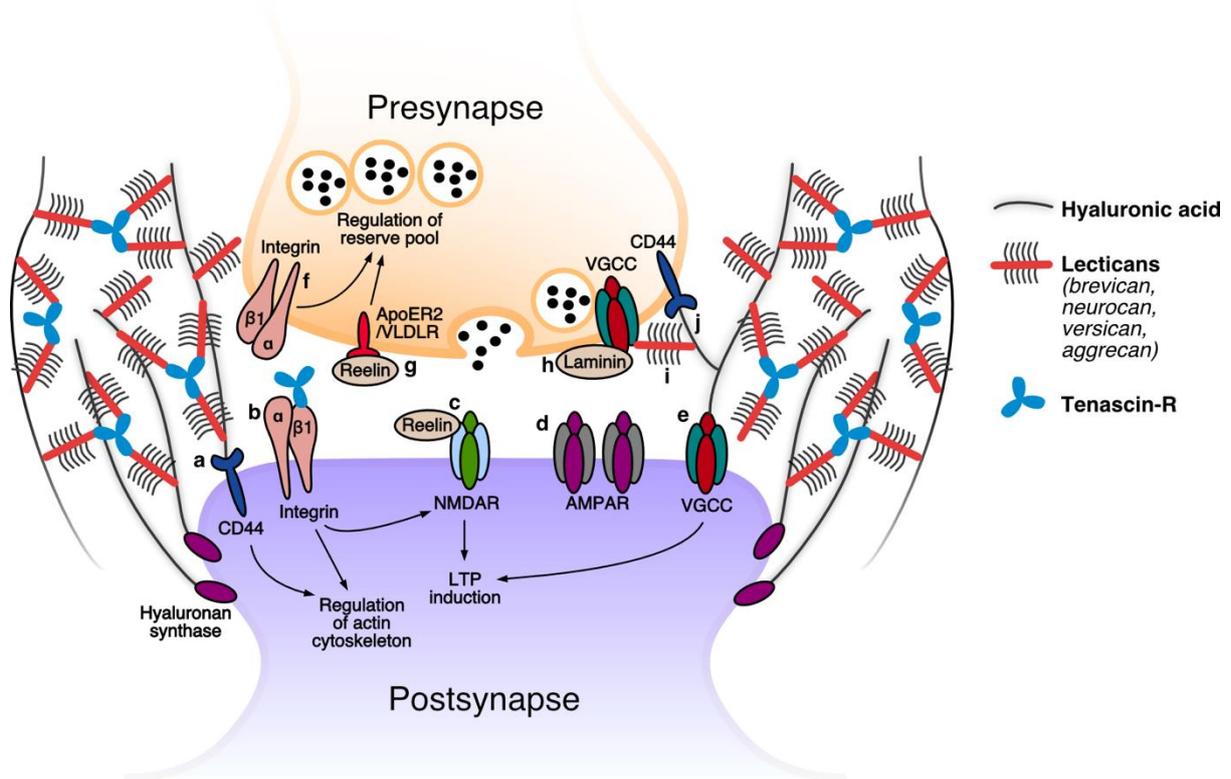
Figure 3 Presumed interactions and functions of ECM at the tetrapartite synapse. Postsynapse: **a**, The hyaluronan receptor CD44 was shown to support spine stabilization by modulating actin cytoskeleton regulating proteins (Roszkowska et al., 2016). **b**, β1 integrins stabilize spines and promote LTP by modulating NMDARs and the actin cytoskeleton. They have been shown to interact with TNR *in vitro* (Bernard-Trifilo et al., 2005; Liao et al., 2008; Sloan Warren et al., 2012; Tan et al., 2011). **c**, Reelin promotes LTP by enhancing the activity of NMDARs (Weeber et al., 2002). **d**, The lateral diffusion of AMPARs is restricted by the perisynaptic ECM (Frischknecht et al., 2009). **e**, VGCCs, which are known to promote certain forms of LTP, are modulated by hyaluronan (Kochlamazashvili et al., 2010). Presynapse: **f**, β1 integrins may be necessary for maintaining the synaptic vesicle reserve pool (Huang et al., 2006). **g**, Reelin interacts with VLDLR and ApoER2 to modulate the release of reserve pool vesicles (Bal et al., 2013). **h**, β2 laminins are necessary for anchoring active zone proteins at the presynaptic membrane. This could hypothetically occur through an interaction with VGCCs. (Hunter et al., 2019; Nishimune et al., 2004). **i**, Brevican is necessary for aligning VGCCs in front of the PSD (Sonntag et al., 2018). **j**, The hyaluronan receptor CD44 is present at presynapses, and is necessary for their stabilization (Roszkowska et al., 2016).
*Note: The major findings are merged here in a single scheme, though the studies were performed in different models, and it is therefore likely that these interactions differ across brain regions and different types of synapses.

---

[14] The readily-releasable pool contains synaptic vesicles which are docked at the active zone of the presynaptic membrane and primed for release, and are therefore released immediately upon stimulation. (Rosenmund and Stevens, 1996)

1.3. ECM remodeling at the synapse

Many of the studies reviewed in the previous section indicate that the principal role of the perisynaptic ECM is to maintain the status quo of the synapse. However, synapses continue to be plastic throughout adulthood, and it therefore stands to reason that they should be capable of transiently remodeling their surrounding ECM. Much like the intracellular changes that a synapse undergoes during plasticity, the changes to the ECM should likewise be driven by its activity level. The current paradigm, whereby ECM remodeling occurs through proteolytic cleavage of its molecules, fulfills this criterion. Nevertheless, it is possible that additional mechanisms exist that do not involve the destruction of ECM molecules. In this section, I will describe the best-studied mechanisms of ECM proteolytic cleavage at the synapse in response to changes in synaptic activity levels. Then, I will call attention to a dilemma that arises when considering this to be the sole mechanism for ECM remodeling at synapses, thus laying the groundwork for this thesis.

1.3.1. Proteolytic cleavage of synaptic ECM: the dominant paradigm

Structural synaptic plasticity has primarily been studied in dendritic spines, where the mechanism is broadly described as follows: (1) the increase in synaptic activity leads to the local activation of ECM-cleaving enzymes, (2) cleavage of the ECM at the synapse allows the activity-dependent elongation and enlargement of the spine, and may also unmask latent sequences in the ECM molecules that bind receptors at the synapse and promote plasticity-related changes, (3) the activity of the enzymes is inhibited, and newly-synthesized ECM molecules are secreted, which allows the plasticity-induced changes to persist. In the following section, I will review the major enzymes involved in ECM proteolysis and potential mechanisms for their activity-dependent activation.

Matrix metalloproteinases (MMPs) are a large family of zinc-binding endopeptidases (*i.e.,* break peptide bonds within the molecule) consisting of over 20 members (Löffek et al., 2011). MMPs can be secreted or membrane-associated, and target a variety of molecules, including ECM proteins, signaling molecules, and membrane-associated receptors (Visse and Nagase, 2003). In the central nervous system, both neurons and glia synthesize MMPs whose functions have, in the past, primarily been associated with roles in brain development. Nevertheless, it has now become clear that MMPs play an equally important role in the adult synapse (Huntley, 2012). By far the best-studied member in the brain is MMP9, which is known to be abundant at excitatory hippocampal synapses (its protein as well as its mRNA) (Bozdagi et al., 2007; Dziembowska et al., 2012; Konopacki et al., 2007). An increase in neuronal activity leads to the transport of MMP9 mRNA to synapses, where it undergoes local translation (Dziembowska et al., 2012; Zagulska-Szymczak et al., 2001). Furthermore, it was shown that the expression level of MMP9 increases during LTP in the CA1 region of the hippocampus, and that a decrease in its amount (either through genetic knockout or pharmacological inhibition) precludes LTP maintenance (Nagy et al., 2006; Wang et al., 2008). Mechanistically, it appears that MMP9 activity leads to an increase in the motility of dendritic spines and to an enlargement of the spine head (processes which are both known to accompany LTP). Evidence suggests that these are realized through two effects of the enzyme: the cleavage of perisynaptic ECM molecules such as aggrecan to make room for spine growth (Mercuri et al., 2000), and the activation of β1-integrin receptors on the spines which initiate a downstream signaling cascade, resulting in a remodeling of the actin cytoskeleton (Michaluk et al., 2011; Wang et al., 2008). For the latter mechanism, it is still not known how

MMP9 activity leads to the activation of β1-integrins, but one possibility is that its activity leads to the exposure of previously hidden regions in ECM molecules that can function as ligands for the receptors (*e.g.,* Giannelli, 1997). A possible target of MMP9 cleavage is ICAM5, whose soluble form increases following LTP induction, and promotes spine elongation (Conant et al., 2011; Tian et al., 2007). Another target may be the hyaluronan receptor CD44, whose cleavage following the stimulation of serotonin receptors was also shown to result in spine elongation (Bijata et al., 2017). Besides LTP in the hippocampus, roles for MMP9 in plasticity have also been described in other brain regions, including the prefrontal cortex (Okulski et al., 2007) and the amygdala (Stefaniuk et al., 2017). Lastly, it is worth mentioning that two additional MMPs, MMP3 and MMP7, also appear to play a role in synaptic plasticity by driving changes in dendritic spine structure that are dependent on NMDAR activation (Aerts et al., 2015; Bilousova et al., 2006; Brzdąk et al., 2017; Wójtowicz and Mozrzymas, 2014).

Another important family of ECM-cleaving proteases is "a disintegrin and metalloproteinase with TSP motifs" (ADAMTS), which comprises 19 members (Apte, 2004). ADAMTSs are expressed throughout the brain, where they are produced by astrocytes, and to a lesser extent, by neurons and microglia (Lemarchant et al., 2013). ADAMTSs have the ability to cleave both lecticans (Stanton et al., 2011) and reelin (Hisanaga et al., 2012), making them likely contributors to synaptic plasticity. Two family members with evident roles in the adult brain are ADAMTS1 and ADAMTS4 which, in contrast to other ADAMTSs, are also are abundant post-development (Gottschall and Howell, 2015). Both were shown to be upregulated following kainic acid-induced seizures in rats, resulting in a cleavage of brevican and a reduction in synapse density in the dentate gyrus (Yuan et al., 2002). In addition, the overexpression of ADAMTS4 *in vitro* leads to an elongation of neurites (Hamel et al., 2008). Nevertheless, further studies which block specific ADAMTS activity with inhibitors or siRNA are needed to verify the causality between the activity of these enzymes and synaptic remodeling.

Despite being less extensively studied, the protease neurotrypsin is also briefly worth mentioning. Neurotrypsin is predominantly secreted by neurons in the hippocampus, cortex, and amygdala (Gschwend et al., 1997). Currently, the only known substrate of neurotrypsin is agrin, a protein that is best known for its role in the development of the neuromuscular junction synapse (Gautam et al., 1996; Glass et al., 1996). Agrin has also been shown to promote spine formation in the central nervous system, including at mature neurons (Annies et al., 2006; McCroskery et al., 2006). At hippocampal synapses, neurotrypsin cleaves agrin locally in response to NMDAR activation (Frischknecht et al., 2008; Stephan et al., 2008), which presumably liberates cleavage fragments of agrin that induce the formation of new spines. This notion is supported by the finding that mice deficient in neurotrypsin do not form dendritic filopodia (spine precursors) in response to LTP-inducing stimuli, and that this can be rescued by the addition of soluble cleavage fragments of agrin, produced by neurotrypsin treatment (Matsumoto-Miyai et al., 2009).

Besides activity-dependent activation, an essential quality of ECM-cleaving proteases is they operate transiently (*i.e.,* be inhibited in a timely manner) in order for plasticity-induced changes to cease. Among other proteins, this is achieved by a family of four tissue inhibitors of metalloproteinases (TIMPs) that act in concert with MMPs and ADAMTSs (Arpino et al., 2015; Murphy, 2011). As of yet, few studies elucidate the role of TIMPs in plasticity. However, one highly relevant example is the inhibition of MMP9 by TIMP1, which is as necessary for LTP as the initial activation of the protease (Magnowska et al., 2016). Similar to

MMP9, the expression of TIMP1 can be activity-dependent (Okulski et al., 2007), and it is therefore possible that its activity is slower than that of MMP9, allowing its delayed inhibition.

As a final point, it is likely that newly-synthesized ECM molecules are secreted following proteolytic cleavage to stabilize the structural changes to the synapse. Indeed, several studies have shown that an increase in activity leads to a transient upregulation in the expression of ECM (Heck et al., 2004; Niekisch et al., 2019; Rao-Ruiz et al., 2019). It remains to be determined whether this expression takes place locally at active synapses, or if (and how) these molecules are trafficked to their synaptic destinations.

1.3.2. A flaw in the proteolysis paradigm

ECM remodeling through its proteolysis meets the necessary criteria for mediating synaptic plasticity: it can be initiated as a result of changes in synaptic activity levels, and it is transient. A problem arises, however, when considering that structural changes to synapses are remarkably frequent. Super-resolution imaging of dendritic spines and the PSD *in vitro* and *in vivo* have shown that their morphology can fluctuate on a timescale of minutes to hours (Berning et al., 2012; Fischer et al., 1998; Testa et al., 2012; Wegner et al., 2018; Willig et al., 2014) (Figure 4).
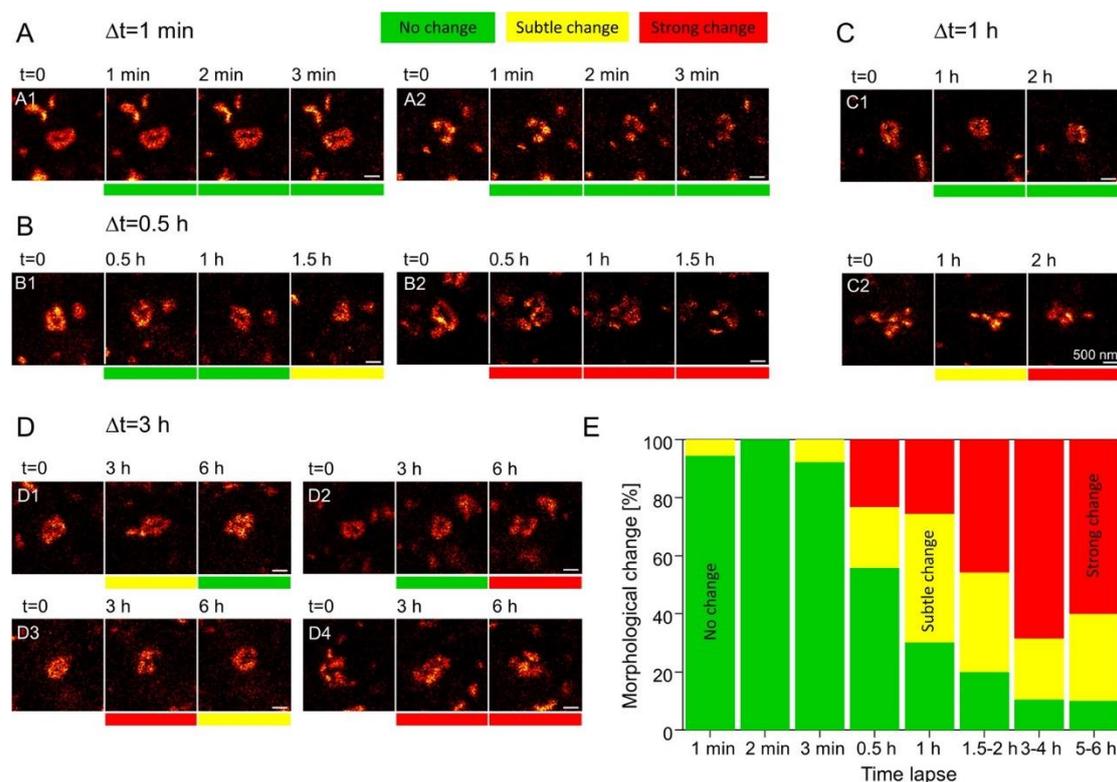
Figure 4 Fast dynamics of dendritic spines. The morphology of the PSD was tracked in knock-in mice whose endogenous postsynaptic density protein 95 (PSD95) is fused to a fluorescent protein. Live super-resolution Stimulated Emission Depletion (STED) imaging was performed in the visual cortex through a cranial window to follow individual PSD assemblies for up to 6 hours. **a,** When imaging at a time interval of 1 minute, few morphological changes are observed. **b-c,** 0.5 to 2 hours from the start of imaging, some assemblies remain stable (B1, C1), while others undergo significant changes (B2, C2). **d,** When imaging for up to 6 hours, some assemblies may change and then revert to their original morphology (D1), remain stable for several hours but change morphology towards the end of the imaging period (D2), or change morphology multiple times (D3, D4). Scale bars = 500 nm. **e,** A histogram showing the frequency of strong, subtle or no morphological changes to PSD95 assemblies. N = 18 (1, 2 minutes),

If we are to assume that a local remodeling of the ECM is necessary for realizing these fluctuations, achieving this through proteolytic cleavage of ECM followed, presumably, by the secretion of newly-synthesized replacements, would entail a very fast turnover of these molecules. This would be highly metabolically costly for the cell, but more importantly, this is not in line with the existing measurements of the lifetimes of these molecules. As I mentioned previously (Chapter 1.1.2), the components of the ECM are some of the most long-lived molecules in the brain (and, for that matter, in the entire body; Truscott et al., 2016). The half-life of our protagonist TNR was measured at ~7 days *in vitro* (hippocampal cultures; Dörrbaum et al., 2018) and ~40 days *in vivo* (cortex and cerebellum; Fornasiero et al., 2018). With the exception of brevican, whose half-life was measured at ~5 days *in vitro* and ~ 17 days *in vivo*, all of the ECM proteins mentioned previously were even longer-lived than TNR. It is therefore extremely unlikely these molecules are destroyed and synthesized *de novo* with every morphological change to the spine. So, while the proteolysis paradigm may be adequate to describe events of infrequent ECM remodeling, it is insufficient for describing continual changes to the ECM.

At the basis of this thesis is the hypothesis that an additional mechanism should exist that allows a continual remodeling of the ECM without the need for its proteolysis and *de novo* synthesis. Rather than being cleaved, an attractive possibility is that ECM molecules can be internalized into the cell without being targeted for degradation. Later on, these same molecules can be exocytosed to re-integrate back into the ECM. In the following section, I will discuss the plausibility of this proposed mechanism, whereby the ECM is 'reshuffled' through the continual recycling of its molecules.

1.4.   The plausibility of ECM recycling as a remodeling mechanism

In order for ECM recycling to be a feasible mechanism for ongoing synaptic changes, synapses should contain the machinery to both internalize and secrete ECM locally. This mechanism should also be correlated to synaptic activity, which is a strong influencer of the degree of morphological fluctuations (Hazan and Ziv, 2020). In the following section, I will review existing studies that support these premises.

1.4.1.   Can synapses internalize ECM molecules?

Besides acting as a scaffold for the synapse, many ECM molecules can initiate intracellular signaling cascades by interacting (either as a whole molecule or as a cleaved fragment) with synaptic transmembrane receptors. The question then arises whether these receptors can mediate the internalization of their ligands. Outside the brain, ECM molecules have been shown to readily undergo receptor-mediated endocytosis [15]. Though it is farfetched to claim that ECM molecules will necessarily undergo endocytosis with any receptor

---

[15] Most research has focused on the internalization of ECM molecules for the purpose of degradation as a process to maintain ECM homeostasis. Specifically, many studies assessed the dysregulation of this process in diseases such as cardiomyopathy, osteoarthritis, fibrosis and cancer (Rainero, 2016).

with which they interact, I will give several examples from the literature where this was shown to be the case (see Table 1 below).

ECM molecule / receptor	Evidence for internalization	Are receptors present at central nervous system synapses?	Other known ECM ligands
Laminin / dystroglycan	Fluorescently labeled laminin was endocytosed in mammary epithelial cells over the course of ~8 hours. The internalization was strongly reduced in a cell line deficient in dystroglycan (Leonoudakis et al., 2014)	Dystroglycan is present at mature inhibitory synapses in the forebrain and cerebellum, preferentially at the postsynaptic side (Briatore et al., 2020; Lévi et al., 2002; Zaccaria et al., 2001).	Agrin (the substrate of the protease neurotrypsin; see Chapter 1.3.1) (Gesemann et al., 1998).
Laminin / α3β1 integrin	Laminin peptides were endocytosed into acidified vesicles by α3β1 integrin in human breast cancer cells (Coopman et al., 1996) (to my knowledge, it has not been explored whether this also occurs in healthy cells).	Integrins are enriched at pre- and postsynapses (see Chapter 1.2), including both the α3 and β1 subunits (e.g., Huang et al., 2006; Kramár et al., 2002). α3β1 specifically was shown to be present at cerebellar (mostly GABAergic) postsynapses (Kawaguchi and Hirano, 2006).	Reelin (Dulabon et al., 2000). TNR and TNC were shown to bind β1-containing integrins (Liao et al., 2008; Probstmeier and Pesheva, 1999).
Hyaluronan / CD44	Fluorescently labeled HA was internalized together with CD44 into acidified vesicles in chondrocytes (cartilage cells) and keratinocytes (epidermal skin cells) (Aguiar et al., 1999; Knudson et al., 2002; Tammi et al., 2001).	Present at hippocampal synapses (Roszkowska et al., 2016) and mossy fiber synapses (Apóstolo et al., 2020).	Versican (Kawashima et al., 2002). Aggrecan (Fujimoto et al., 2001) (in fact, aggrecan was shown to co-internalize with hyaluronan into intracellular compartments; Embry and Knudson, 2003) [16]
Fibronectin / α5β1 integrin	Exogenous fibronectin (either fluorescently labeled or detected by antibodies) was internalized together with α5β1 integrins in fibroblasts and myofibroblasts (Lobert et al., 2010; Shi and Sottile, 2008).	Both β1 and α5 integrins are enriched at synapses (see above and Izumi et al., 2017; Marchetti et al., 2010; Webb et al., 2007).	TNR and TNC (see above).

Table 1 Exemplary studies showing receptor-mediated internalization of ECM molecules.

The studies described above almost entirely focused on the internalization of ECM for the purpose of its degradation, and the majority did not continue to explore whether a portion of these molecules eventually recycled back to the plasma membrane. Nevertheless, this demonstrates that, in many cases, ECM molecules are internalized by their receptors. It is also noteworthy that many of the ECM receptors are known to undergo constitutive recycling (a prominent example being integrins; Bridgewater et al., 2012). It remains to be determined whether this could also be a mechanism for the recycling of their ECM ligands.

---

[16] In theory, lecticans could also undergo CD44-mediated internalization by remaining attached to hyaluronan (to which they have a strong affinity; see Chapter 1.1.2.1).

1.4.2. Do synapses contain the machinery required for ECM release?

As a matter of course, the presynapse is well-equipped for exocytosis. Synaptic vesicles and their associated proteins are generated in the ER and then traffic through the Golgi apparatus and possibly endosomes before interacting with motor proteins on the axonal microtubules. These lead them via anterograde transport to eventually be picked off at individual presynapses. At the synapse, the vesicles undergo further maturation steps and are ultimately pumped with neurotransmitter. The vesicles fuse with the plasma membrane to release their neurotransmitter content through the interaction of soluble NSF-attachment protein receptor (SNARE) proteins on the vesicles and on the plasma membrane. This fusion is triggered by calcium levels by virtue of the vesicular protein synaptotagmin, which functions as a calcium sensor. It can be triggered by an action potential that induces calcium influx (synchronous release) or can be spontaneous. Following the fusion of the vesicles with the plasma membrane and the release of their contents, they may undergo endocytosis and recycle to be reused locally (Rizzoli, 2014). All of these qualities make synaptic vesicles an attractive mechanism for the local release of ECM molecules. These may be packaged inside the vesicles during their formation in the soma and be released alongside neurotransmitter or independent of neurotransmitter release. Perhaps fused vesicles also retrieve ECM molecules from the extracellular space as they endocytose to undergo recycling. Although these scenarios are plausible, I would believe that this is unlikely to be the case, since synaptic vesicles, being ~40 nm in diameter (Qu et al., 2009), appear too small to house large ECM molecules (TNR trimers, for example, were shown to have dimensions of ~100 nm *in vitro;* Pesheva et al., 1989). It is quite surprising then, that proteomic mappings of synaptic vesicles also report a wide variety of ECM components. However, in all probability, these findings reflect a contamination of the samples from other synaptic compartments, as is inevitably the case in these types of studies. This is bolstered by the fact that a component of myelin can be found among the 70 most abundant proteins in these samples (Taoufiq et al., 2020).

Larger vesicles that exocytose at the presynapse are dense-core vesicles (~100 nm in diameter; Merighi, 2018) [17], which are known to carry neuropeptides such as dopamine as well as various substances that modulate neuronal activity (De Camilli and Jahn, 1990). Unlike synaptic vesicles, which recycle locally and can be reloaded with neurotransmitter, dense-core vesicles are released in a single-shot manner, and must be formed *de novo* in the Golgi apparatus (Bharat et al., 2017; Kim et al., 2006; Wong et al., 2012). Though much less is known about the specific events that lead to the exocytosis of dense-core vesicles (as compared with synaptic vesicles), their fusion is also dependent on calcium influx and the action of SNAREs. Interestingly, despite being associated with fairly low molecular weight cargos, dense-core vesicles have also been shown to carry larger molecules such as bassoon and piccolo (~530 and 420 kDa, respectively), which are part of the synaptic vesicle release machinery (Zhai et al., 2001). However, to the best of my knowledge, there are no proteomics data from neuronal dense-core vesicles that will allow us to assess if they also contain ECM molecules. Some clues can be obtained from dense-core vesicles derived from adrenal chromaffin cells, which are a well-known model for neuronal vesicle release. Proteomic mapping of these vesicles has revealed that they carry a variety of ECM molecules, eluding to the possibility that this might

---

[17] The name "dense-core vesicle" stems from the observation that their cargo is electron-dense when observed with electron microscopy in most preparations.

also be the case in neurons (Wegrzyn et al., 2010). However, as was already mentioned above, one cannot rule out the possibility that the presence of this molecules merely reflects a contamination of the samples.

Another possible means of ECM release is via exosomes (up to ~150 nm) (Tkach and Théry, 2016), which are derived from invaginations of endosomal membranes that seal to generate intraluminal vesicles (Colombo et al., 2014). It was only recently discovered that exosomes are an important form of inter-neuronal communication, and are able to transport cargo such as RNA, neurotransmitter receptors, and synaptic vesicle proteins (Budnik et al., 2016; Fauré et al., 2006; Pastuzyn et al., 2018; Vilcaes et al., 2021). Notably, it was also shown that exosome release could be modulated by calcium and by synaptic activity (Lachenal et al., 2011), making it reasonable to assume that exosomes can be released locally at synapses. A recent proteomics analysis of exosomes derived from hippocampal neuron cultures (the same one that demonstrated the presence of synaptic vesicle proteins) identified a large number of ECM molecules (Vilcaes et al., 2021). However, the abundance of these molecules in the exosome was not quantified, making it difficult to determine if these results are accurate or whether they represent impurities in the samples. It is interesting to note that outside the brain, exosomes are well-known to be carriers of ECM molecules (www.vesiclepedia.org, www.exocarta.org), and it has been suggested that exosome-mediated trafficking may coexist with the canonical secretion pathways.

At the postsynapse, local exocytosis is also well-established, the most obvious example being the exocytosis of AMPA receptors during LTP. This is believed to be achieved, in part, by the fusion of local AMPAR-containing intracellular organelles (recycling endosomes) at or near the postsynaptic membrane through the activity of SNARE proteins. In a study by Jurado and colleagues, it was proposed that this fusion is rapidly induced by an increase in synaptic activity, namely, the influx of calcium through open NMDARs (Jurado, 2014). Besides their induced fusion during LTP, recycling endosomes also constitutively fuse at the synapse to replenish local AMPARs (since these are also regularly internalized) (Parkinson and Hanley, 2018). Using the activity-dependent and constitutive fusion of AMPARs as a paradigm, it is also possible to imagine that ECM-containing endosomes are located in the vicinity of synapses and support their rapid activity-dependent and independent delivery to the membrane.

Apart from the existence of endosomes at the postsynapse, it has also become apparent that dendrites have an extensive local secretory capacity. This includes extensions of the ER, satellite ER-to-Golgi intermediate compartments (ERGIC) and Golgi 'outposts' (Tang, 2008). What is more, we recently demonstrated that trafficking proteins are also present within spines. In a collaborative study I took part in, led by M. Helm, we mapped over 100 proteins in dendritic spines using a combination of super resolution microscopy, quantitative biochemistry and electron microscopy. We found that both the ER marker calreticulin and the trans-Golgi network marker TGN38 could be found in spine heads and in extrasynaptic regions (calreticulin in particular was found to be among the more abundant proteins in the spine) (Helm et al., 2021). This on-site satellite secretory system is believed to support the local synthesis and modification of proteins *in situ*, which is believed to occur at synapses (Holt et al., 2019). However, such a system would naturally also allow for the fast and specific delivery of recycled ECM molecules to the synapse to be locally secreted. On a different note, it is also possible to imagine that the presence of local trafficking machinery would allow any endocytosed molecules to be rapidly entered into the recycling route. This suggests that besides local

secretion, the postsynapse is also competent to endocytose ECM molecules and traffic these towards recycling (as I explore in greater detail in the following section).

1.4.3. Do synapses contain the machinery required for recycling-targeted ECM endocytosis?

As I discussed previously (Chapter 1.4.1), it is plausible that ECM molecules are endocytosed through their interaction with receptors at the synapse. Typically, this occurs through clathrin-mediated endocytosis (hence, historically referred to as "receptor-mediated endocytosis"), whereby a clathrin coat assembles around the cargo as the membrane on which it rests invaginates. Ultimately, the invaginating membrane undergoes fission, mediated by the GTPase dynamin, to become a clathrin-coated vesicle. Alternatively, receptors can be internalized via clathrin-independent routes mediated, for example, by invaginations in the plasma membrane called caveolae or the scaffolding protein flotillin (Kumari et al., 2010). All of these forms of endocytosis are known to take place at synapses. At the presynapse, clathrin-mediated endocytosis is thought to be the major pathway for the local retrieval of synaptic vesicle membranes, although caveolae were also shown to be involved in this process (Jung and Haucke, 2007; Koh et al., 2021). At the postsynapse, AMPARs undergo both activity-induced and constitutive endocytosis via clathrin-dependent and independent pathways (Bodrikov et al., 2017; Ehlers, 2000; Glebov et al., 2015; Man et al., 2000). Any one of these mechanisms could accommodate the endocytosis of ECM molecules locally at the synapse.

Following their endocytosis, molecules are trafficked to early endosomes where their cellular destination is determined: they may be delivered to the lysosome (via a late endosome) (Gruenberg and Stenmark, 2004), recycled back to the plasma membrane (via a recycling endosome), or undergo further retrograde trafficking to the trans-Golgi network (TGN) and, in some cases, the ER (Johannes and Popoff, 2008). Both endosomes and ER are known to be present in presynapses. However, the existing evidence suggests that the presynaptic ER functions to support local calcium signaling (Collin et al., 2005; McGraw et al., 1980). Furthermore, presynaptic endosomes are known to exist, but these are mostly believed to support the sorting and recycling of synaptic vesicle proteins (Jähne et al., 2015; Rizzoli, 2014). With this in mind, the presynapse does not seem to have extensive capabilities for the local recycling of non-synaptic-vesicle proteins, nor for the retrograde trafficking of molecules.

In contrast, the postsynapse and its vicinity in the dendrite are equipped with endosomes, ER, and Golgi outposts. Importantly, it was found that these Golgi outposts are endowed with TGN-associated proteins (Chua and Tang, 2008; Pierce et al., 2001). Since the TGN functions in both exocytic and endocytic pathways, this further supports the premise that this machinery is involved not only in local synthesis but also in local recycling. Nevertheless, for this to be a feasible mechanism for local secretion or recycling-targeted endocytosis of ECM molecules, it should presumably be linked to local synaptic activity. Unlike the activity-dependent trafficking of AMPAR to and from local endosomes, the activity-dependent dynamics of other components of the satellite secretory machinery have not yet been explored. Understanding this link is pertinent to our hypothesis of local ECM remodeling at synapses, and so, the first part of this thesis was dedicated to this investigation. To answer this, we used super-resolution imaging to quantify the abundance and the distribution of trafficking elements in and around dendritic spines, and determine if these correlate to synaptic activity. Predictably, we found that local synaptic activity strongly influences the distribution of these elements, presumably leading to their recruitment to synaptic regions

(Chapter 2). This finding lead us to believe that the postsynapse is an ideal locus for activity-dependent local recycling, and strengthens the plausibility of synaptic ECM recycling as a remodeling mechanism.

1.4.4.   Unexpectedly, a longer-loop mechanism is necessary

The second part of this thesis was dedicated to directly assessing whether ECM recycling takes place at synapses. To do so, we focused on TNR, which is present at mature synapses (*e.g.,* Apóstolo et al., 2020) and is necessary for synaptic plasticity (see Chapter 1.2.1). To assess whether TNR recycles at synapses, we used a simple experimental design to label actively recycling molecules in live cells. In the first step, we exposed live cultured neurons to an excess of unlabeled antibodies against TNR in order to tag all of the TNR molecules present at the surface of the neurons (the 'surface-blocking' step). Since antibodies are unable to penetrate the plasma membrane, the intracellular TNRs remained untagged. After a period of time, we exposed the neurons to the same antibodies linked to fluorescent molecules (the labeling step). These labeled antibodies are unable to bind the TNR molecules that were exposed at the neuronal surface during the previous step, since their epitopes are still blocked by unlabeled antibodies. Thus, the only molecules that will become fluorescently labeled are those that were previously inside the cell, and only recently emerged at the surface. Inevitably, some of these 'newly-emerged' molecules will be freshly synthesized molecules that are surfacing for the first time. In the case of ECM molecules, however, if the time period between the blocking and labeling steps is sufficiently short (*e.g.*, several hours), the amount of *de novo* synthesis should be minimal, since the turnover of these molecules is exceptionally slow.

As we speculated, this assay revealed a large amount of TNR molecules that continually recycle in neurons. Using super-resolution fluorescence microscopy, we also confirmed that these recycling TNR molecules are released at synapses, and that their appearance is correlated to local synaptic activity. However, when continuing to follow the recycling TNRs, we also met an unexpected observation: while most known recycling pathways last minutes to hours (*e.g.,* Bretscher, 1989; Bridgewater et al., 2012; Koenig and Edwardson, 1997), the cycle for TNR lasted approximately 3 days. Inside the cell, we observed that TNR molecules reached both satellite and somatic Golgi apparatus before cycling back to the membrane. We therefore hypothesized that the molecules trafficked to the soma to undergo re-glycosylation, a process which is known to occur outside the brain (*e.g.*, in liver cells; Wratil et al., 2016), but nevertheless remains poorly studied. These latter findings led to the realization that the mechanism of synaptic ECM recycling is more elaborate than we originally presumed, and worth investigating in greater depth.

2: Original publication: synaptic activity and strength are reflected by changes in the postsynaptic secretory pathway

Authors

Gürth, CM.*, **Dankovich, T.M.***, Rizzoli, S.O., D'Este, E.. Synaptic activity and strength are reflected by changes in the post-synaptic secretory pathway. *Sci Rep* 10, 20576 (2020). https://doi.org/10.1038/s41598-020-77260-2

*Shared first authorship

Personal contribution: I assisted with the immunostaining experiments and was responsible for the design of the data analysis workflow, under the supervision of S.O.R. (see Supplementary Figure 4 for a scheme of the workflow). In addition, I wrote and implemented the code for these analyses to produce the visualizations and plots shown in Figures 2-5 and Supplementary Figures 2-10. Lastly, I contributed to the design of the figures and the writing of the manuscript.

scientific reports

OPEN

Synaptic activity and strength are reflected by changes in the post-synaptic secretory pathway

Clara-Marie Gürth[1,2,5], Tal M. Dankovich[3,5], Silvio O. Rizzoli[3] & Elisa D'Este[4✉]

Neurons are highly asymmetric cells that span long distances and need to react promptly to local demands. Consequently, neuronal secretory pathway elements are distributed throughout neurites, specifically in post-synaptic compartments, to enable local protein synthesis and delivery. Whether and how changes in local synaptic activity correlate to post-synaptic secretory elements is still unclear. To assess this, we used STED nanoscopy and automated quantitative image analysis of post-synaptic markers of the endoplasmic reticulum, ER-Golgi intermediate compartment, trans-Golgi network, and spine apparatus. We found that the distribution of these proteins was dependent on pre-synaptic activity, measured as the amount of recycling vesicles. Moreover, their abundance correlated to both pre- and post-synaptic markers of synaptic strength. Overall, the results suggest that in small, low-activity synapses the secretory pathway components are tightly clustered in the synaptic area, presumably to enable rapid local responses, while bigger synapses utilise secretory machinery components from larger, more diffuse areas.

The secretory pathway elements support cellular functions by ensuring local delivery and post-translational modifications of secreted and transmembrane proteins. These proteins are translated directly into the endoplasmic reticulum (ER) lumen, and transported to the Golgi apparatus via the ER-Golgi intermediate compartment (ERGIC)[1,2]. Then, cargoes exit the Golgi apparatus via the trans-Golgi network (TGN), where the proteins are sorted and transported to their respective sites of action[3]. Due to their highly asymmetrical shape, size and subcellular specialisation, neurons need to organise protein synthesis along their entire volume (for reviews[4-8]). Protein processing through a secretory pathway organised exclusively in the soma would not allow a prompt supply of newly synthesised proteins to distal regions, and would not meet the specific needs of each subcellular compartment[9]. To compensate for this limitation, the protein synthesis machinery (mRNAs and ribosomes) has been reported in both pre- and post-synaptic areas[10], and other secretory pathway elements are also widespread or asymmetrically distributed, to ensure an adequate protein supply at specific subcellular locations[11].

The neuronal ER forms a branched network, stretching from the soma to dendrites and axonal pre-synaptic terminals, albeit it is far more abundant in dendrites than in axons[11,12]. Although it spans over long distances, the ER still remains one single membrane organelle, with a continuous lumen[13]. The ER has been found within dendritic spines, where it shows high turnover, contributes to long-term potentiation (LTP), and a specialised, smooth ER variant forms the spine apparatus (SA)[14,15]. The SA has been documented in a subset of spines and is involved in calcium storage, synaptic strength, and robust potentiation[16-20]. The SA is bound to the actin cytoskeleton of the spine by the marker and essential component synaptopodin[21-23]. This protein is required for calcium regulation and actin remodelling[18-20,24]. However, synaptopodin has also been shown to be a potential marker of SA-unrelated dynamics[15,25].

Similar to the ER, the neuronal ERGIC is also found in the cell body and dendritic shafts, but is rarely present in spines[11,26-28]. Within the spine, ERGIC is often located in close proximity to recycling endosomes, which are similar in shape. Thus, discriminating between them unambiguously by electron microscopy is difficult[26,27].

[1]Department of NanoBiophotonics, Max Planck Institute for Biophysical Chemistry, Am Fassberg 11, 37077 Göttingen, Germany. [2]Department of Optical Nanoscopy, Max Planck Institute for Medical Research, Jahnstr. 29, 69120 Heidelberg, Germany. [3]Institute for Neuro- and Sensory Physiology, University Medical Center Göttingen, Humboldtallee 23, 37073 Göttingen, Germany. [4]Optical Microscopy Facility, Max Planck Institute for Medical Research, Jahnstr. 29, 69120 Heidelberg, Germany. [5]These authors contributed equally: Clara-Marie Gürth and Tal M. Dankovich. ✉email: elisa.deste@mr.mpg.de

nature research

1

Trafficking of ERGIC vesicles along dendrites is restricted by increased neuronal activity, indicating that this post-ER compartment can be subjected to synaptic activity-dependent regulation[29].

Unlike the other organelles of the secretory pathway, the neuronal Golgi apparatus localises mainly around the nucleus and along the first portion of the apical or longer dendrite[30,31]. However, smaller Golgi outposts can be found in a subset of dendrites and small Golgi satellite structures have been observed throughout the entire dendritic tree, often in close association to the ERGIC[31,32]. In addition, a marker of the trans-Golgi network, TGN38, has been observed along the whole dendritic tree, including small dendrites and spines[2,33–35]. TGN38, whose synthesis can be modulated by neuronal activity, is present in vesicles that cycle between the plasma membrane and intracellular membranes, probably facilitating rapid changes in the protein composition of post-synaptic membranes[33,36].

Synapses are plastic and functionally diverse compartments where information is passed from the pre- to the post-synaptic cell. The amplitude of the post-synaptic response, commonly referred to as the synaptic strength, can be modulated by changes at both the pre- and post-synaptic levels (for reviews see[37–42]). At the post-synapse, larger post-synaptic densities (PSD) reflect a higher number of functional receptors, and hence a stronger and more potentiated synapse[43,44]. At the pre-synaptic level, synaptic strength can be modulated, among others, by the availability of vesicles and release machinery proteins[45]. In glutamatergic neurons, pre-synaptic strength can be approximated by labelling the vesicular glutamate transporter vGLUT1[46], which reveals the entire vesicle pool. At the same time, synaptic activity can be approximated for the pre-synaptic compartment by measuring the size of the recycling pool of vesicles, using a live labelling of the vesicular protein synaptotagmin-1 (SYT1), which specifically reveals these vesicles[47–49]. The recycling vesicles compose about 20 to 50% of all vesicles[49]. Their number is variable, and depends not only on the size of the total pool of vesicles, but also on many other parameters, as the metabolic age of the vesicles[49]. Therefore, although the last two measurements are related, they are not identical, with the vGLUT1 amounts providing only a measurement of the vesicle numbers, while the live SYT1 labelling also provides an indication of local activity.

The brief overview provided in this introduction indicates that the neuronal distribution of the secretory organelles is well studied, and that several lines of evidence connect them to synaptic dynamics. However, it is still unclear whether and how the characteristics of the synapses impact the abundance and localisation of the secretory pathway elements. Here, we used STED nanoscopy and quantitative image analysis to investigate the relationship between several secretory elements and synaptic activity. By using calreticulin, ERGIC53, TGN38 and synaptopodin as markers for the ER, ERGIC, TGN and SA, respectively, we found a positive correlation between indicators of synaptic strength and the abundance of these markers in close proximity of the synaptic area. Furthermore, a read-out of pre-synaptic activity correlated strongly with the distribution of secretory pathway elements. Therefore, these results indicate that both the quantity and position of the secretory elements is dependent on synaptic strength and activity, presumably in order to enable an optimal synaptic response.

Results

Secretory pathway elements are present in proximity to post-synaptic sites.　To determine whether the features of a synapse influence the local distribution and abundance of the elements of the secretory pathway, or their proximity to the synapse, we designed a high throughput experiment that enabled simultaneous super-resolution imaging of multiple proteins and parameters in cultured hippocampal neurons. The parameters selected to define synapses were the fluorescence signal intensities of the following: homer, a post-synaptic structural marker[44]; vGLUT1, a marker of the entire pre-synaptic vesicle population of excitatory nerve terminals in these cultures[46]; and live labelling of SYT1 for identifying only the actively recycling synaptic vesicles in pre-synaptic boutons[48]. While the first two markers provide indications on the strength of the synapse, the latter is a proxy for synaptic activity (Fig. 1a,b). Next, we chose calreticulin, ERGIC53, TGN38 and synaptopodin as markers for the ER, ERGIC, TGN and SA, respectively. Lastly, dendritic spines were identified by phalloidin labelling of actin. Four-colour images were acquired on proximal dendrites (within ~ 80 μm from the soma) of primary hippocampal neurons (17–20 days in vitro), co-labelled with a component of the secretory pathway, homer, either vGLUT1 or SYT1, and phalloidin. All channels, with the exception of phalloidin, were acquired in STED mode, to allow an accurate localisation of the structures within the confined post-synaptic space. Using this approach, we could identify all components of the secretory pathway in proximity to the post-synaptic site in the dendritic compartment, and observed that none was present at substantial levels in the pre-synaptic boutons (Fig. 1c,d, Supplementary Fig. 1). The brightness of their signals was significantly higher than the background due to non-specific binding of the secondary antibody (Supplementary Fig. 2). While the synaptopodin signal was clearly concentrated in the spine head, calreticulin, ERGIC53 and TGN38 appeared as sparse, but distinct, spots in both the dendritic shaft and spines. On average, the number of spots per spine head was three or four, with synaptopodin being the most abundant, while calreticulin and TGN38 were the least abundant (Supplementary Fig. 3).

Post-synaptic structure correlates with the abundance of secretory pathway elements.　Having identified several components of the secretory pathway in proximity to post-synaptic sites, we set out to investigate whether the post-synaptic strength influences the distribution of the dendritic secretory machinery. To this aim, we used an approach already applied for similar tasks[50] and described in Supplementary Fig. 4. Briefly, a 3×3 μm area centred on the synaptic sites, regardless of its position with respect to the post-synaptic compartment, was cropped, and the homer signal intensity within this crop was evaluated. The area dimension was chosen to include the whole post-synaptic site (considering an average spine length of ~ 1.5 μm) and to minimise the contribution from neighbouring synapses or structures. Crops were then sorted into five bins of equal size, based on homer signal intensity, and an average image of the protein of interest (POI) was generated

29
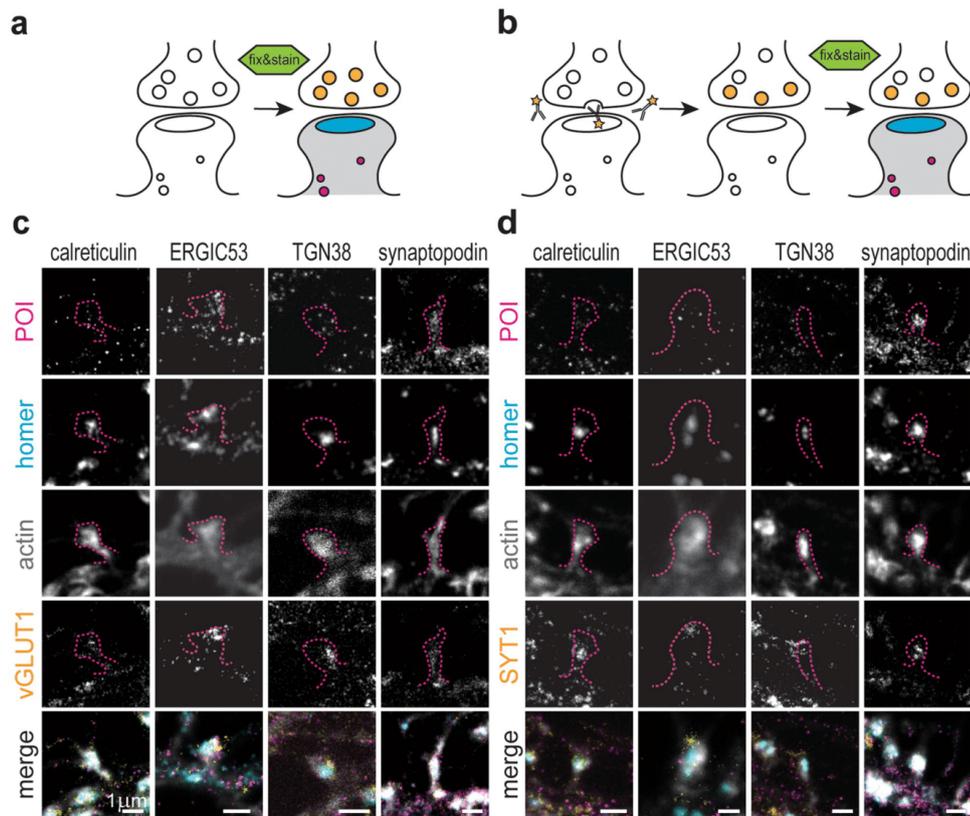
Figure 1. Experimental design and presence of secretory elements at post-synaptic sites. (**a**) Cells were either directly fixed and stained when visualising vGLUT1 or (**b**) incubated with an Atto647N-tagged anti-SYT1 antibody directed towards the extracellular domain of SYT1 prior to fixation. When a vesicle fuses with the pre-synaptic site, the SYT1 epitope becomes accessible to the antibody, which is incorporated by endocytosis within the recycling synaptic vesicle. Thereby, this label provides an estimate of activity at the respective synaptic boutons. (**c,d**) Representative STED images of individual synaptic sites in mature hippocampal neuron cultures. Samples were stained for several proteins of interest (POI: calreticulin, ERGIC53, TGN38, synaptopodin), with pre- and post-synaptic sites markers (vGLUT1 or SYT1, and homer, respectively), and phalloidin (actin, confocal). Secretory elements were found in the proximity of post-synaptic sites. Dashed lines represent the spine outline as labelled by phalloidin. Scale bars: 1 μm.

for each bin. The average images represent the protein distribution around the synaptic sites, sorted by their respective homer intensity: a strong signal at the centre indicates a higher relative protein level in proximity of the synaptic site, while a more diffuse signal indicates that the protein is probably present in compartments more distant to the synaptic site, such as the dendritic shaft (Fig. 2a). Interestingly, while only a minor increase in the spread was noticed for calreticulin, ERGIC53 and synaptopodin at increasing homer intensities, TGN38 appeared vastly affected by low and intermediate post-synaptic strengths. To quantify this redistribution, a radial analysis was performed on the average images, and the ratio between the signal in the periphery and at the centre was calculated (Fig. 2b, Supplementary Fig. 5a). Low ratio values indicate a higher concentration of the POI at the synaptic site, while values close to 1 indicate a spread-out distribution. Such analyses revealed that calreticulin, ERGIC53, and synaptopodin exhibit a slight linear increase in their distribution in the area surrounding the synaptic site (the radial intensity profile ratio increased by 0.18, 0.15 and 0.13, respectively). On the other hand, TGN38 spread appeared to be modulated already by small increases in the post-synaptic strength (0.3 increase of radial intensity profile ratio between bin 1 and bin 3), but this modulation rapidly reached a plateau. From these results it could be concluded that the strength of the post-synapse has a minor influence on the distribution of the elements of the secretory pathway in the synaptic site.
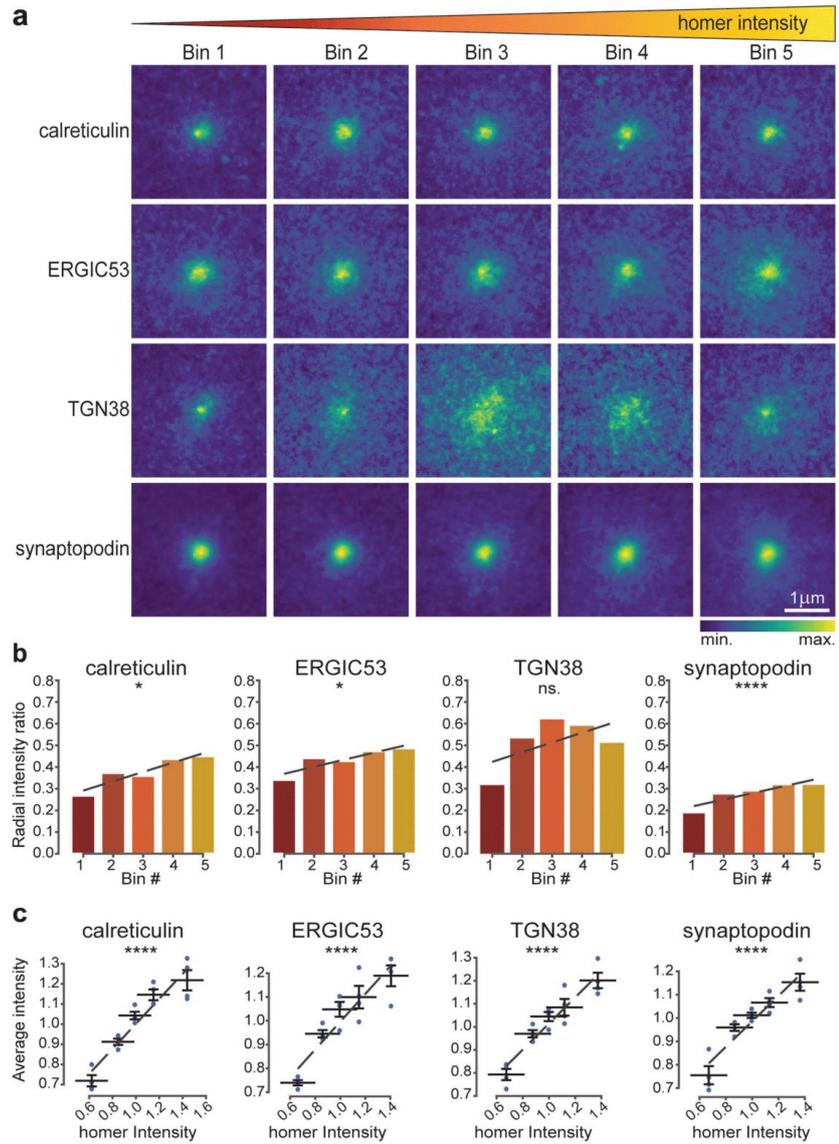
Figure 2. Correlation between post-synaptic strength and secretory pathway elements. (**a**) Average images for the different POIs based on five homer intensity bins displayed in 3×3 μm crops around the synaptic site. Bin 1 has the lowest homer intensity and bin 5 the highest. (**b**) Ratio between signal intensity at the periphery and at the centre of the average images, calculated by radial analysis. (**c**) Correlation of homer intensities and the average intensities of the POIs. Dashed lines are linear fits. All data were collected from four independent experiments. * $= p < 0.05$, ** $= p < 0.01$, *** $= p < 0.001$, **** $= p < 0.0001$, and ns. $=$ non-significant. Whiskers represent S.E.M. Number of synapses per bin and Spearman's rho are listed in Supplementary Table 1.

31

To further investigate whether the observed effects on protein distribution are also connected to an increase in the protein abundance, the intensity of each POI within a bin was plotted against the intensity of the homer signal (Fig. 2c). A strong correlation was observed for all elements, suggesting that the abundance of these proteins is increased in the proximity of bigger post-synaptic sites. Altogether, these data indicate that homer intensity, as a proxy of the post-synaptic strength, differentially correlates with the distribution and abundance of elements of the secretory pathway.

The abundance of post-synaptic secretory pathway elements also correlates with pre-synaptic strength. After having investigated the relationship between secretory pathway elements and post-synaptic site size, we wondered whether the same influence could be observed for the pre-synaptic site traits. The question is highly relevant, since in our experimental setup there is no significant correlation between pre- and post-synaptic site strength (Supplementary Fig. 6). Therefore, we performed the same analysis as conducted above, but we analysed the vGLUT1 intensity instead of that of homer, thereby estimating the size of the synaptic vesicle pool in the pre-synapse. Labelling of vGLUT1 was achieved using a primary nanobody, which provided a well-defined number of fluorophores per labelled structure[51]. The resulting averaged images for the different secretory elements showed a mixed pattern of responses (Fig. 3a,b, Supplementary Fig. 5b). Calreticulin and synaptopodin exhibit a linear redistribution at increasing vGLUT1 intensities, visible from both the average images and the radial analysis (the radial intensity profile ratios increased by 0.36 and 0.25, respectively). This increase was less pronounced, and was also non-linear, in the case of ERGIC53 (0.15 increase in radial intensity profile ratio), and was abolished for TGN38 (0.05 decrease in radial intensity profile ratio), whose distribution fluctuated between the different bins. Therefore, the influence of vGLUT1 abundance, as representation of pre-synaptic strength, on the distribution of post-synaptic elements of the secretory pathways appears heterogeneous.

When analysing the intensities of the POIs with respect to vGLUT1 intensity, all elements exhibited a clear linear correlation, which was particularly strong for calreticulin, TGN38, and synaptopodin (Fig. 3c). These data indicate that larger quantities of secretory pathway proteins are recruited into the post-synapses opposing strong pre-synapses. With the exception of TGN38, the higher quantity of POIs seems also to be reflected by their more dispersed distribution in the dendritic regions neighbouring the post-synaptic site.

The distribution of post-synaptic secretory pathway elements is highly dependent on pre-synaptic activity. After having assessed the relationship between post- and pre-synaptic strength and secretory pathway components, we proceeded to address the existence of a functional correlation to synaptic activity. To this aim, we replaced vGLUT1 labelling by live-SYT1 staining in our experimental setup (Fig. 1b,d), which provided an estimate of synaptic activity based on the level of actively recycled vesicles. To our surprise, all POIs, including TGN38, showed a linear redistribution at increasing SYT1 intensities, as demonstrated by both average images and radial analysis (Fig. 4a,b, Supplementary Fig. 5c). For all POIs, the differences between the radial intensity profile ratios of bins 5 and 1 was higher than those observed for homer and vGLUT1 (Figs. 2b, 3b). This difference was least prominent for synaptopodin (0.3 increase in radial intensity ratio), and most prominent for calreticulin (0.45 increase in radial intensity ratio). Therefore, one can conclude that the localisation of all of the analysed post-synaptic elements of the secretory pathway is intimately linked to the amount of recycling vesicles and hence to pre-synaptic activity.

When correlating the POIs levels to SYT1 intensities, we found only a small correlation with calreticulin abundance in the region neighbouring the synaptic sites (Fig. 4c). On the contrary, the amounts of ERGIC53, TGN38, and synaptopodin were strongly correlated with SYT1 intensity. Taken together, these data indicate that the secretory organelles at the synapse are increasingly dispersed with increasing amounts of recycling vesicles, though the effect of activity on their abundance varies depending on the organelle.

Post-synaptic strength strongly modulates the secretory machinery in mushroom spines. The analyses conducted so far assessed how synaptic strength and activity relate to the abundance of secretory pathway elements in the synapse and the extent of their dispersion, without considering the actual size of the spines containing them. Furthermore, it did not discriminate between different spine morphologies. To account for this, a manual classification and segmentation of spines was performed based on the actin (phalloidin) staining. In this way, spines that had a clear mushroom or stubby morphology were selected from the 3×3 μm crops, and their axes were aligned. The corresponding average images confirmed the results obtained with the automatic analysis in the previous figures, and demonstrated that the signal of the POIs derives predominantly from the dendritic, rather than the axonal compartment (Fig. 5a and Supplementary Fig. 7). The POIs were enriched in proximity to the synaptic site, with TGN38 having the most dispersed distribution, and synaptopodin the most confined distribution in both spine types. Furthermore, the average intensity for most of the POIs was comparable between both mushroom and stubby spines, and only synaptopodin showed a slight enrichment in mushroom spines, as expected from the literature (Supplementary Fig. 8)[17,20].

The analysis of the manually segmented images indicated that the levels of all POIs strongly correlated with homer levels, regardless of the spine type. Moreover, in mushroom spines most POIs correlated with vGLUT1 intensity (Fig. 5b,c and Supplementary Fig. 9). This positive correlation is most likely due to the fact that the number of POI spots in the spine head grows with the size of the post-synaptic site. However, the size of the spots decreased with increasing post-synaptic density size (Supplementary Fig. 10), suggesting the presence of more but smaller organelles. These results confirmed the previously observed correlations between the abundance of secretory pathway elements and markers of pre- and post-synaptic strength, as was assessed with the automatic analysis presented above (Figs. 2, 3).

32
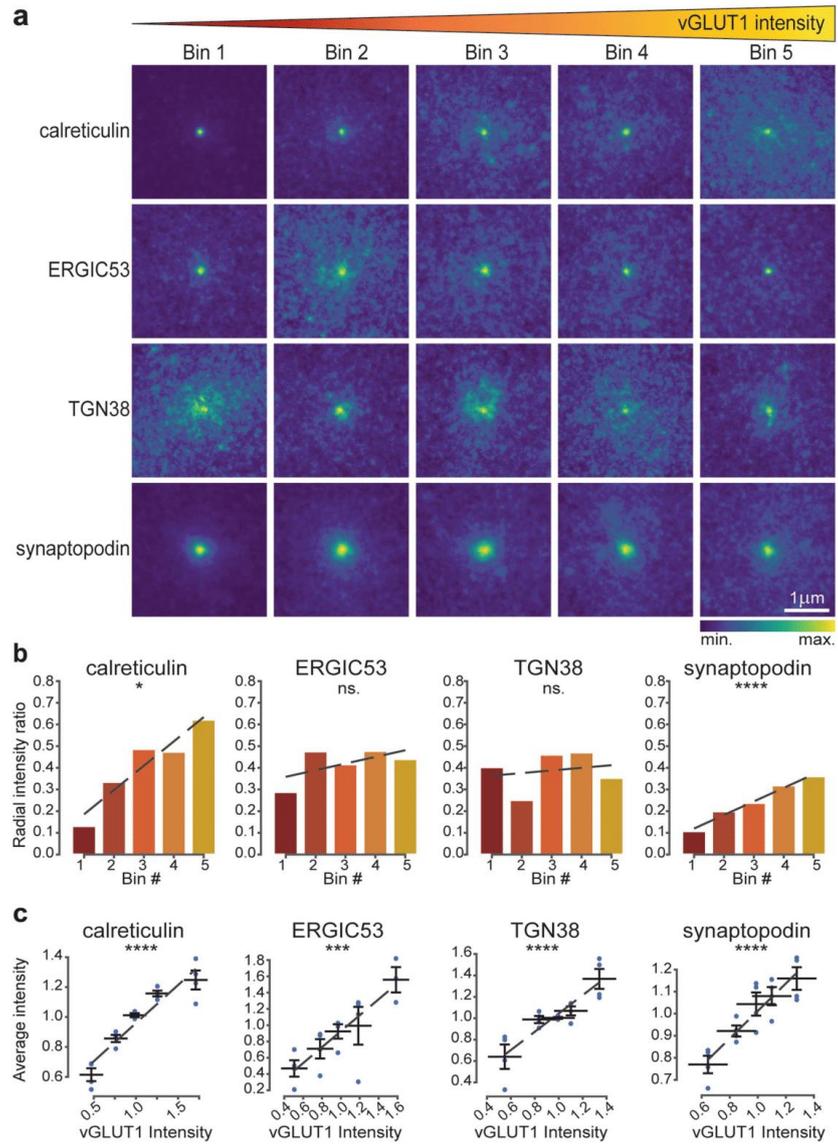
Figure 3. Correlation between pre-synaptic strength and secretory pathway elements. (**a**) Average images for the different POIs based on five vGLUT1 intensity bins displayed in 3 × 3 μm crops around the synaptic site. Bin 1 has the lowest vGLUT1 intensity and bin 5 the highest. (**b**) Ratio between signal intensity at the periphery and at the centre of the average images calculated based on radial analysis. (**c**) Correlation of vGLUT1 intensities and the average intensities of the POIs. Dashed lines are linear fits. All data were collected from four independent experiments. $* = p < 0.05$, $** = p < 0.01$, $*** = p < 0.001$, $**** = p < 0.0001$, and ns. = non-significant. Whiskers represent S.E.M. Numbers of synapses per bin and Spearman's rho are listed in Supplementary Table 1.

33
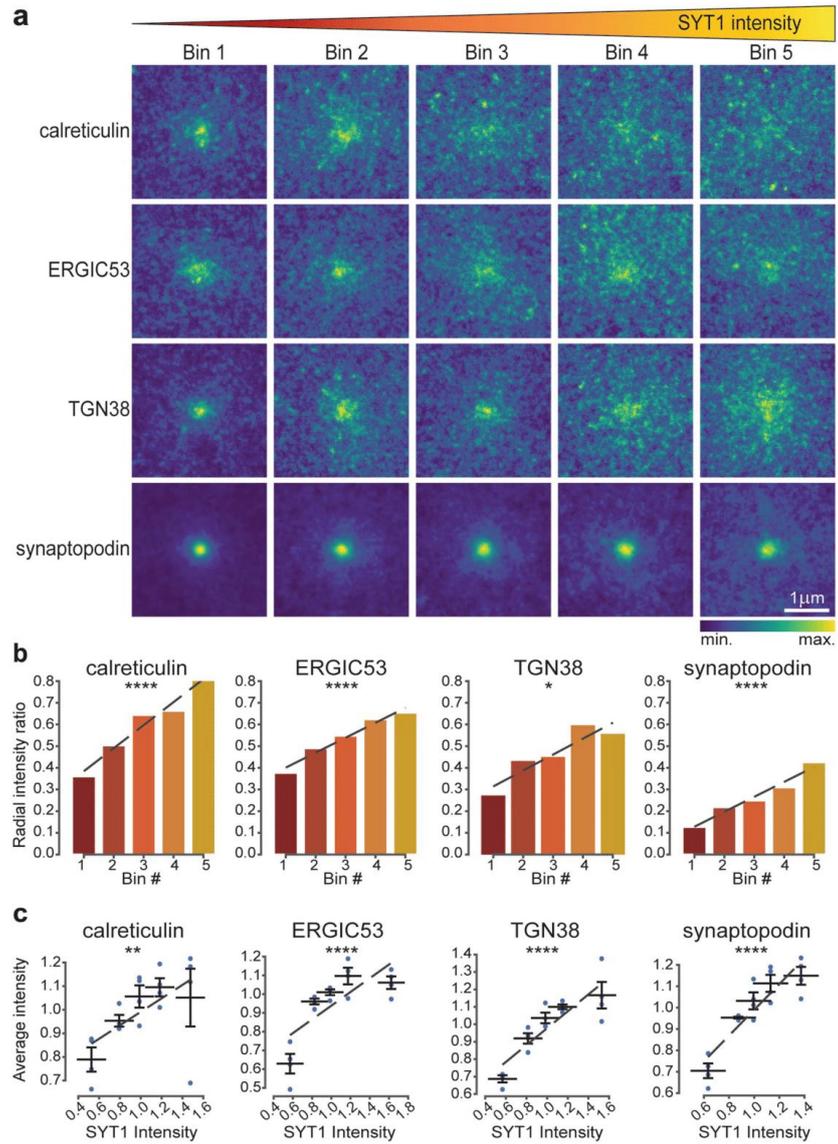
Figure 4. Correlation between pre-synaptic activity and secretory pathway elements. (**a**) Average images for the different POIs based on five SYT1 intensity bins displayed in 3×3 µm crops around the synaptic site. Bin 1 has the lowest SYT1 intensity and bin 5 the highest. (**b**) Ratio between signal intensity at the periphery and at the centre of the average images calculated based on radial analysis. (**c**) Correlation of SYT1 intensities and the average intensities of the POIs. Dashed lines are linear fits. All data were collected from four independent experiments. $* = p < 0.05$, $** = p < 0.01$, $*** = p < 0.001$, $**** = p < 0.0001$, and ns. = non-significant. Whiskers represent S.E.M. Numbers of synapses per bin and Spearman's rho are listed in Supplementary Table 1.

34
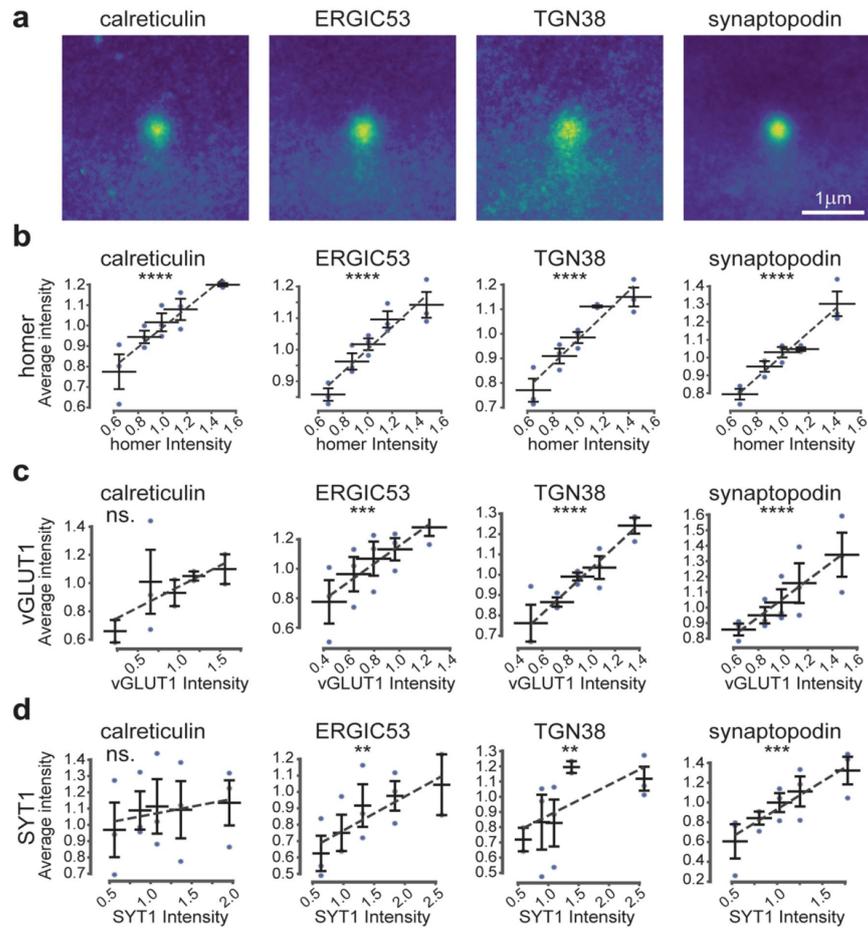
Figure 5. Correlations of secretory elements in mushroom spines. (**a**) Average 3×3 μm images of POIs in mushroom spines as defined by manual segmentation. Images were vertically aligned with the spine head at the centre and the dendritic shaft at the bottom. All data were collected from three independent experiments. (**b**–**d**) Average intensity correlations after manual spine segmentation and classification as mushroom type spines. Correlation of the average intensities of calreticulin, ERGIC53, TGN38, and synaptopodin with average intensities of homer (**b**), vGLUT1 (**c**), and SYT1 (**d**). Where $* = p < 0.05$, $** = p < 0.01$, $*** = p < 0.001$, $**** = p < 0.0001$, and ns. = non-significant. Whiskers represent S.E.M. Number of synapses per bin and Spearman's rho are listed in Supplementary Table 1.

When analysing the synaptic activity in the manually segmented images, however, a correlation was observed exclusively in mushroom spines, and only for ERGIC53, TGN38, and synaptopodin (Fig. 5d). The previously observed correlation for calreticulin was lost in both spine types. Therefore, these results suggest that the structure of the pre- and post-synaptic site has a high impact in regulating the amount of secretory pathway elements present in the neighbouring post-synaptic regions, and that pre-synaptic activity has differential effects, depending on the post-synaptic morphology.

Discussion

Neurons have a highly elaborated network of secretory elements that allows for locally-independent production and processing of proteins[5,8,10,52,53]. However, the extent to which synaptic activity, size and morphology steer local protein synthesis machinery is not fully understood[11,54]. Here we systematically analysed the abundance and distribution of several secretory elements at synaptic sites by means of STED optical nanoscopy, in dependence

35

of proxies of synaptic strength and activity. With quantitative image analysis, we investigated the correlations between the abundance and distribution of calreticulin (endoplasmic reticulum marker), ERGIC53 (ER-Golgi intermediate compartment marker), TGN38 (trans-Golgi network marker), and synaptopodin (spine apparatus marker), and the pre-synaptic markers vGLUT1 or SYT1, as well as the post-synaptic marker homer.

The use of optical nanoscopy has the advantage of providing molecular specificity and allowing the unambiguous discrimination of organelles, which can be difficult in electron microscopy[27]. Furthermore, a higher throughput required for extensive analyses, and the visualisation of the entire three-dimensional synaptic site are both more easily achievable with optical microscopy. However, in case of overlapping structure, signal coming from superimposed compartments or synaptic sites could be misinterpreted, since the axial resolution in two-dimensional STED is limited to 500–700 nm. Moreover, the results are influenced by the specificity of the markers for the structures of interest and by the precision of the related antibodies, which were validated by western blot and STED imaging in cell lines (Supplementary Fig. 11). In the context of this study, this is relevant for synaptopodin, since it is not uniquely a spine apparatus marker, and it can be found in spines prior to the formation of the spine apparatus, as well as in the axon initial segment[15,55]. Lastly, the presence of non-specific binding of the primary antibody cannot be completely ruled out and could only be verified on cultures derived from knock-out animals.

Our data analysis was largely automated, thus limiting biases in the image quantification and evaluation. With this approach, thousands of synaptic sites could be analysed to gain information on the behaviour of the "average" synaptic site. However, rare events are not represented, as they would require the manual inspection of each individual site in order to be identified. One bias of our analysis is that larger post-synaptic sites, particularly when considering the manually selected mushroom or stubby spines, will intrinsically lead to a higher occupancy of the image space and thus to higher protein levels (assuming that the proteins are homogeneously distributed in the spine head). However, none of the proteins we analysed exhibits a volume labelling-like staining, limiting this drawback. The manual identification of post-synaptic sites might also intrinsically predispose to the selection of bigger synaptic sites, whose behaviour may not be representative of all synapses. This influence might explain, to some extent, the differences observed between automated and manually selected synapse. Lastly, it should be mentioned that in our experimental setup no correlation between the levels of vGLUT1 and homer was observed (Supplementary Fig. 6). Therefore, the responses of the POIs to pre- and post- synaptic strength can be considered independently from each other.
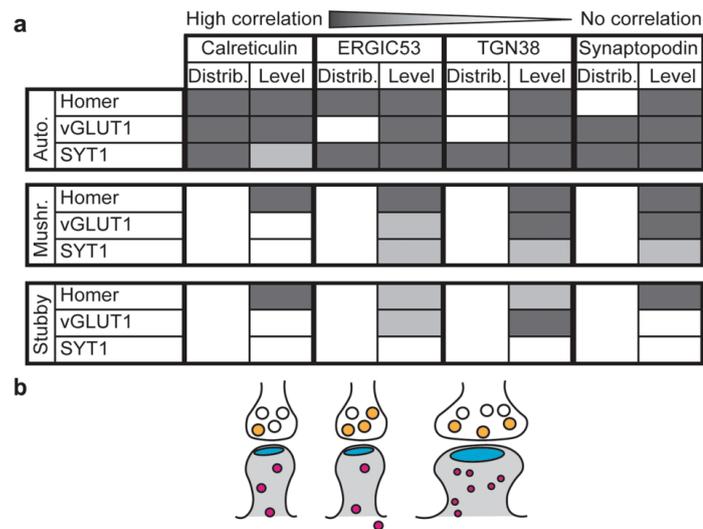
STED imaging showed a higher concentration of some of the chosen markers in the soma or along the apical dendrite. Nevertheless, in our experimental setup all POIs could be identified unambiguously in the dendritic shafts and at post-synaptic compartments. According to previous studies, the ERGIC was proposed to be rarely present in dendritic spines[26]. However, it should be noted that in electron microscopy the ERGIC resembles endosomes, which are often found in spines, and therefore this similarity might lead to misinterpretation of the images[27]. Furthermore, fine ERGIC53 puncta could be easily overseen or mislocalised when using diffraction-limited light microscopy. Regarding TGN38, a detailed description of its presence at synaptic sites has so far been reported only in overexpression experiments, and was not investigated in detail at endogenous levels[2,33,35].

Overall, we found strong correlations of the expression levels of the components of the secretory pathway to synaptic strength and activity, and in particular to the post-synaptic size (Fig. 6a). However, several details should be discussed for each of the individual markers. Calreticulin distribution was dependent on post-synaptic size, and even stronger effects were observed for pre-synaptic strength and activity. The amounts of the protein were dependent on the strength of the synapse, but correlated less with synaptic activity. The correlation with pre-synaptic markers was heavily abolished when analysing mushroom and stubby spines specifically. These effects are in line with a model in which synaptic activity recruits the local ER resources to the synaptic site, thereby explaining the correlation between activity and calreticulin distribution. Later on, persistent activity results in the recruitment of the ER from more distant areas, thereby leading to an increase in ER abundance and explaining the correlation between calreticulin levels and synaptic strength. This model is in agreement with the evidence that the ER has a high turnover and that it primes new spines for future plasticity, contributing to LTP[14,15,56].

ERGIC53 levels directly correlated with the levels of all three synaptic markers, also in mushroom spines, and its distribution was mainly affected by pre-synaptic activity. These results suggest that ERGIC-mediated protein trafficking is required for the maintenance of synaptic strength (and presumably for plasticity), and that it responds readily to synaptic activity, in agreement with previous investigations[29].

The TGN38 behaviour was to some extent similar to that of ERGIC53. The TGN38 distribution in connection to post-synaptic strength appears highly sensitive to changes for low homer intensities, and becomes saturated for high values. The pre-synaptic strength appears to have no effect on the TGN38 localisation. Pre-synaptic activity correlated strongly with both TGN38 distribution and levels, but this correlation was strongly reduced when manually segmenting spines. This difference might be ascribed to the analysis itself: (1) mushroom and stubby spines that can be identified unambiguously may already be relatively mature, and therefore maintenance mechanisms will predominate over plasticity; (2) both spine types generally have the synaptic contact in the head region, and hence to some distance from the dendritic shaft, whose contribution in the analysis is therefore reduced. Therefore, a potential recruitment of TGN38 in the shaft region would be quantified in the automatic analysis, but would not be measured in the analysis of the individual spine types. We therefore propose that TGN38 is mobilised in the proximity of the post-synapse, in relation to activity, but not necessarily in the spine head. Some of the TGN38 molecules may have been synthesised in response to activity[36], albeit this is only speculative, since the age of the compartments was not analysed in our experiments.

In principle, one would expect a strong similarity between the ERGIC and TGN compartments. However, neurons also have unconventional secretion pathways that bypass the TGN[57], thereby explaining why these compartments do not behave in an identical fashion.

a

		Calreticulin		ERGIC53		TGN38		Synaptopodin	
		Distrib.	Level	Distrib.	Level	Distrib.	Level	Distrib.	Level
Auto.	Homer								
	vGLUT1								
	SYT1								
Mushr.	Homer								
	vGLUT1								
	SYT1								

High correlation ▬▬▬▶ No correlation

b

Figure 6. Summary of effects and proposed model. (**a**) Summary of the correlation between the elements of the secretory pathway (in terms of distribution and levels), and post-synaptic strength (homer), pre-synaptic strength (vGLUT1), or pre-synaptic activity (SYT1) for the different analysis performed (automatic analysis of all synapses, or manual analyses of mushroom spines and stubby spines). The different shades of grey correspond to high correlation/influence (darker grey), or less (light grey) to no (white) correlation/influence. (**b**) Model for the effect of synaptic strength and activity on the elements of the secretory pathway. Increased activity initially mobilizes the locally available resources, whose availability increases to support spine enlargement and maintenance.

Synaptopodin showed a strong correlation to all synaptic markers and in both automatically and manually selected mushroom spines. On the other hand, synaptopodin distribution seemed to be less influenced by post-synaptic strength but more by pre-synaptic modulations. Because of its functions, synaptopodin is specifically accumulated in the spine head and neck in mushroom spines[17,18,20]. Therefore, it is not surprising that all tested synaptic characteristic proxies showed a good correlation with synaptopodin abundance, and that even at increasing post-synaptic strength, synaptopodin stayed in close synaptic proximity. However, it is important to consider that the presence of synaptopodin in the spines is not necessarily related to the presence of the SA, and therefore the results might be partially connected to the ability of synaptopodin to bind the actin cytoskeleton[17–20].

Altogether, our data suggest that the pre-synaptic activity has the highest influence on the distribution of secretory pathway elements in the proximity of post-synaptic sites, while the post-synaptic architecture has the highest influence on their abundance. Therefore, we propose a model in which increased synaptic activity initially mobilises the locally available resources to the synaptic area. Sustained activity then leads to increases in synapse strength, and promotes the recruitment of more secretory organelles that are important for the maintenance of the large synapses (Fig. 6b). However, it should be noted that the observed effects are not homogenous for all the components of the secretory pathway, further proving the presence of unconventional pathways in neurons[57].

A basic conclusion of our study is that both pre- and post-synaptic features correlate in multiple ways to the post-synaptic secretory pathway. Further work will be required to understand the exact synaptic mechanisms modulating protein secretion in the context of synaptic plasticity and activity. Finally, the behaviour of other organelles, such as the Golgi outposts and the recycling endosomes, should also be considered in the future.

Methods

Sample preparation. Cultures of dissociated rat hippocampal primary neurons were prepared from postnatal P0–P2 Wistar rats of either sex and as described in[58]. Procedures were performed in accordance with the Animal Welfare Act of the Federal Republic of Germany (Tierschutzgesetz der Bundesrepublik Deutschland, TierSchG) and the Animal Welfare Laboratory Animal Regulations (Tierschutzversuchsverordnung). According to the TierSchG and the Tierschutzversuchsverordnung no ethical approval from the ethics committee is required for the procedure of sacrificing rodents for subsequent extraction of tissues, as performed in this study. The procedure for sacrificing P0–P2 rats performed in this study was supervised by animal welfare officers of the Max Planck Institute for Medical Research (MPImF) and conducted and documented according to the guidelines of the TierSchG (permit number assigned by the MPImF: MPI/T-35/18).

37

For the labelling of the actively recycled vesicle pool, mature cultures (17–20 days in vitro) were incubated for 1 h with a Atto647N-labelled mouse antibody against the luminal domain of synaptotagmin 1 (Synaptic Systems, cat. 105 311AT1, 1:500 in culture medium). Afterwards cultures were washed three times in warm ACSF (126 mM NaCl, 2.5 mM KCl, 2.5 mM$CaCl_2$, 1.3 mM $MgCl_2$, with 30 mM Glucose, 27 mM Hepes). Labelled and unlabelled samples were fixed for 30 min in 4% PFA in PBS, pH 7.4, and quenched for 5 min in quenching buffer (PBS, 100 mM glycine, 100 mM ammonium chloride). Cells were permeabilised for 5 min in 0.1% Triton X-100 and blocked with 1% BSA for 1 h. Samples were incubated with primary antibody dilutions in PBS for 1 h at room temperature. Primary antibodies used were: homer1 (Synaptic Systems, cat. 160 004, 1:500 dilution), calreticulin (Cell Signaling, cat. 12238S, 1:100 dilution), ERGIC-53/p58 (Sigma E1031, 1:200 dilution), TGN38 (Sigma, cat. T9826, 1:100 dilution), synaptopodin (Synaptic Systems, cat. 163,002, 1:200 dilution). Samples were washed and incubated with secondary antibody dilutions (Alexa Fluor 488 anti-guinea pig, Thermo Fisher, cat. A-11073 and Alexa Fluor 594 anti-rabbit, Thermo Fisher, cat. A-21207), Phalloidin (Alexa Fluor 405 Thermo Fisher, cat. A30104; all at 1:100 dilution) and single domain antibody against vGLUT1 (Synaptic Systems, cat. N1602-Ab635P-S, 1:200 dilution), for 1 h at room temperature. After washing, samples were embedded in Mowiol supplemented with DABCO.

Imaging.   Samples were imaged on an Abberior expert line (Abberior Instruments GmbH, Germany) with pulsed STED lines at 775 nm and 595 nm, excitation lasers at 355 nm, 405 nm, 485 nm, 580 nm, and 640 nm, and spectral detection. Detection windows were set to 650–725 nm, 600–630 nm, 505–540 nm, and 420–475 nm to detect Atto647N, Alexa Fluor 594, Alexa Fluor 488 and Alexa Fluor 405, respectively. Images were acquired with a 100x/1.4 NA magnification oil immersion lens. Pixel size was set to 30 nm, pinhole to 100 μm (1 AU). Laser powers, line accumulations and dwell times were kept consistent throughout the entire study. Alexa Fluor 594 and Atto647N were imaged semi-simultaneously during a first acquisition with STED at 775 nm, while Alexa Fluor 488 was imaged afterwards using STED at 595 nm. Confocal acquisition of the Alexa Fluor 488 channel was performed in all the image sequences to monitor lateral drift. Axial drift was minimized by the Z-focus drift compensation unit.

Image processing.   Images were visualised and processed with Imspector (Abberior Instruments GmbH, Göttingen Germany) and ImageJ 1.52p (imagej.nih.gov/ij/). In the figures, images are shown as smoothed data with a low pass Gaussian filter and 5% background subtraction. Brightness was adjusted uniformly throughout the images. For analysis of the radial intensity in average images, the ImageJ plugin radial profile plot was used. The ratio was calculated by dividing the average intensity of peripheral 35–45 radial pixels by the average intensity of the centre 10 pixels.

Data analysis.   Analyses were performed in Matlab (MathWorks, Natick, MA, USA) and Python (Python Software Foundation) (Supplementary Fig. 4). For the automatic spine analysis, the homer, vGLUT1 or SYT1 channels were manually thresholded and used to locate the coordinates of the synapses within the image. Square regions of 3×3 μm, centered on the homer, vGLUT1 or SYT1 puncta were excised in order to obtain the average images shown in Figs. 2, 3, 4. The radial intensity values were then measured in the average images, and a ratio was calculated between a 10 pixel-wide ring in the periphery and in the center of the image. The individual image segments were binned in five ordinal groups based on the mean fluorescence intensity of the pre- or post-synapse markers, to include a similar number of synapses. For each experiment, the mean fluorescence was calculated in each bin, and was normalized to the median intensity of the experiment.

For the manual segmentation of spines (Fig. 5 and Supplementary Fig. 7), spines were selected based on the homer signal, which indicates the post-synaptic site, and on the actin signal, which provides the overall organization of the spine and of the dendritic shaft. A smaller selection area, of 3×3 μm, centred on the homer puncta, was then processed further. The identity of the synapse was assigned (mushroom or stubby), and then the main landmarks of the spine were marked manually. These included the top, bottom, right and left borders of the head of the spine, the top and bottom points of the neck (in mushroom spines), as well as the position of the junction between the shaft and the spine neck. The spines were then aligned, relying on these landmarks, and they were overlaid, resulting in the images shown in Fig. 5 and Supplementary Fig. 7. The fluorescence intensity for the POIs and the synaptic markers was calculated as above. For the calculation of protein spot size, the images were automatically segmented into spots using a wavelet transformation with a Spot Detection plugin for icy[59,60]. The scale 2 and an 80% threshold were used. All images were thresholded to remove background signal; regions above an empirically defined threshold were treated to contain real signals for further analysis. Outliers exceeding the range of mean ± 3 standard deviations were excluded from the analyses.

References

1. Aebi, M., Bernasconi, R., Clerc, S. & Molinari, M. N-glycan structures: recognition and processing in the ER. *Trends Biochem. Sci.* **35**, 74–82. https://doi.org/10.1016/j.tibs.2009.10.001 (2010).
2. Gardiol, A., Racca, C. & Triller, A. Dendritic and postsynaptic protein synthetic machinery. *J. Neurosci.* **19**, 168–179. https://doi.org/10.1523/JNEUROSCI.19-01-00168.1999 (1999).
3. Griffiths, G. & Simons, K. The trans Golgi network: sorting at the exit site of the Golgi complex. *Science* **234**, 438–443. https://doi.org/10.1126/science.2945253 (1986).

38

4. Glock, C., Heumüller, M. & Schuman, E. M. mRNA transport & local translation in neurons. *Curr. Opin. Neurobiol.* **45**, 169–177. https://doi.org/10.1016/j.conb.2017.05.005 (2017).
5. Rangaraju, V., Tom Dieck, S. & Schuman, E. Local translation in neuronal compartments: how local is local?. *EMBO* **18**, 693–711. https://doi.org/10.15252/embr.201744045 (2017).
6. Terenzio, M., Schiavo, G. & Fainzilber, M. Compartmentalized signaling in neurons: from cell biology to neuroscience. *Neuron* **96**, 667–679. https://doi.org/10.1016/j.neuron.2017.10.015 (2017).
7. Biever, A. *et al.* Monosomes actively translate synaptic mRNAs in neuronal processes. *Science* https://doi.org/10.1126/science.aay4991 (2020).
8. Holt, C. E., Martin, K. C. & Schuman, E. M. Local translation in neurons: visualization and function. *Nat. Struct. Mol. Biol.* **26**, 557–566. https://doi.org/10.1038/s41594-019-0263-5 (2019).
9. Williams, A. H., O'Donnell, C., Sejnowski, T. J. & O'Leary, T. Dendritic trafficking faces physiologically critical speed-precision tradeoffs. *eLife* https://doi.org/10.7554/eLife.20556 (2016).
10. Hafner, A.-S., Donlin-Asp, P. G., Leitch, B., Herzog, E. & Schuman, E. M. Local protein synthesis is a ubiquitous feature of neuronal pre- and postsynaptic compartments. *Science* https://doi.org/10.1126/science.aau3644 (2019).
11. Kennedy, M. J. & Hanus, C. Architecture and dynamics of the neuronal secretory network. *Ann. Rev. Cell Dev. Biol.* **35**, 543–566. https://doi.org/10.1146/annurev-cellbio-100818-125418 (2019).
12. Ramírez, O. A. & Couve, A. The endoplasmic reticulum and protein trafficking in dendrites and axons. *Trends Cell Biol.* **21**, 219–227. https://doi.org/10.1016/j.tcb.2010.12.003 (2011).
13. Spacek, J. & Harris, K. M. Three-dimensional organization of smooth endoplasmic reticulum in hippocampal CA1 dendrites and dendritic spines of the immature and mature rat. *J. Neurosci.* **17**, 190–203. https://doi.org/10.1523/JNEUROSCI.17-01-00190.1997 (1997).
14. Toresson, H. & Grant, S. G. N. Dynamic distribution of endoplasmic reticulum in hippocampal neuron dendritic spines. *Eur. J. Neurosci.* **22**, 1793–1798. https://doi.org/10.1111/j.1460-9568.2005.04342.x (2005).
15. Chirillo, M. A., Waters, M. S., Lindsey, L. F., Bourne, J. N. & Harris, K. M. Local resources of polyribosomes and SER promote synapse enlargement and spine clustering after long-term potentiation in adult rat hippocampus. *Sci. Rep.* **9**, 3861. https://doi.org/10.1038/s41598-019-40520-x (2019).
16. Vlachos, A. *et al.* Synaptopodin regulates plasticity of dendritic spines in hippocampal neurons. *J. Neurosci.* **29**, 1017–1033. https://doi.org/10.1523/JNEUROSCI.5528-08.2009 (2009).
17. Jedlicka, P. & Deller, T. Understanding the role of synaptopodin and the spine apparatus in Hebbian synaptic plasticity—new perspectives and the need for computational modeling. *Neurobiol. Learn. Memory* **138**, 21–30. https://doi.org/10.1016/j.nlm.2016.07.023 (2017).
18. Deller, T. *et al.* A role for synaptopodin and the spine apparatus in hippocampal synaptic plasticity. *Ann. Anat.* **189**, 5–16. https://doi.org/10.1016/j.aanat.2006.06.013 (2007).
19. Segal, M., Vlachos, A. & Korkotian, E. The spine apparatus, synaptopodin, and dendritic spine plasticity. *Neuroscientist* **16**, 125–131. https://doi.org/10.1177/1073858409355829 (2010).
20. Vlachos, A. Synaptopodin and the spine apparatus organelle-regulators of different forms of synaptic plasticity?. *Ann. Anat.* **194**, 317–320. https://doi.org/10.1016/j.aanat.2011.10.014 (2012).
21. Mundel, P. *et al.* Synaptopodin: an actin-associated protein in telencephalic dendrites and renal podocytes. *J. Cell Biol.* **139**, 193–204. https://doi.org/10.1083/jcb.139.1.193 (1997).
22. Deller, T., Merten, T., Roth, S. U., Mundel, P. & Frotscher, M. Actin-associated protein synaptopodin in the rat hippocampal formation: localization in the spine neck and close association with the spine apparatus of principal neurons. *J. Comp. Neurol.* **418**, 164–181. https://doi.org/10.1002/(sici)1096-9861(20000306)418:2%3c164::aid-cne4%3e3.0.co;2-0 (2000).
23. Deller, T. *et al.* Synaptopodin-deficient mice lack a spine apparatus and show deficits in synaptic plasticity. *Proc. Natl. Acad. Sci. USA* **100**, 10494–10499. https://doi.org/10.1073/pnas.1832384100 (2003).
24. Deller, T., Mundel, P. & Frotscher, M. Potential role of synaptopodin in spine motility by coupling actin to the spine apparatus. *Hippocampus* **10**, 569–581. https://doi.org/10.1002/1098-1063(2000)10:5%3c569::AID-HIPO7%3e3.0.CO;2-M (2000).
25. Bas Orth, C. *et al.* Lamina-specific distribution of Synaptopodin, an actin-associated molecule essential for the spine apparatus, in identified principal cell dendrites of the mouse hippocampus. *J. Comp. Neurol.* **487**, 227–239. https://doi.org/10.1002/cne.20539 (2005).
26. Bowen, A. B., Bourke, A. M., Hiester, B. G., Hanus, C. & Kennedy, M. J. Golgi-independent secretory trafficking through recycling endosomes in neuronal dendrites and spines. *elife* **6**, e27362 (2017).
27. Wu, Y. *et al.* Contacts between the endoplasmic reticulum and other membranes in neurons. *Proc. Natl. Acad. Sci. USA* **114**, E4859–E4867. https://doi.org/10.1073/pnas.1701078114 (2017).
28. Saraste, J. & Marie, M. Intermediate compartment (IC): from pre-Golgi vacuoles to a semi-autonomous membrane system. *Histochem. Cell Biol.* **150**, 407–430. https://doi.org/10.1007/s00418-018-1717-2 (2018).
29. Hanus, C. *et al.* Synaptic control of secretory trafficking in dendrites. *Cell Rep.* **7**, 1771–1778. https://doi.org/10.1016/j.celrep.2014.05.028 (2014).
30. Lowenstein, P. R. *et al.* Polarized distribution of the trans-Golgi network marker TGN38 during the in vitro development of neocortical neurons: effects of nocodazole and brefeldin A. *Eur. J. Neurosci.* **6**, 1453–1465. https://doi.org/10.1111/j.1460-9568.1994.tb01007.x (1994).
31. Horton, A. C. *et al.* Polarized secretory trafficking directs cargo for asymmetric dendrite growth and morphogenesis. *Neuron* **48**, 757–771. https://doi.org/10.1016/j.neuron.2005.11.005 (2005).
32. Mikhaylova, M., Bera, S., Kobler, O., Frischknecht, R. & Kreutz, M. R. A Dendritic Golgi Satellite between ERGIC and Retromer. *Cell Rep.* **14**, 189–199. https://doi.org/10.1016/j.celrep.2015.12.024 (2016).
33. McNamara, J. O., Grigston, J. C., VanDongen, H. M. A. & VanDongen, A. M. J. Rapid dendritic transport of TGN38, a putative cargo receptor. *Brain Res. Mol. Brain Res.* **127**, 68–78. https://doi.org/10.1016/j.molbrainres.2004.05.013 (2004).
34. Chen, A. *et al.* Regional and subcellular distribution of the receptor-targeting protein PIST in the rat central nervous system. *J. Comp. Neurol.* **520**, 889–913. https://doi.org/10.1002/cne.22774 (2012).
35. Cox, D. J. & Racca, C. Differential dendritic targeting of AMPA receptor subunit mRNAs in adult rat hippocampal principal neurons and interneurons. *J. Comp. Neurol.* **521**, 1954–2007. https://doi.org/10.1002/cne.23292 (2013).
36. Grigston, J. C., VanDongen, H. M. A., McNamara, J. O. & VanDongen, A. M. J. Translation of an integral membrane protein in distal dendrites of hippocampal neurons. *Eur. J. Neurosci.* **21**, 1457–1468. https://doi.org/10.1111/j.1460-9568.2005.03999.x (2005).
37. Murthy, V. N. Synaptic plasticity: step-wise strengthening. *Curr. Biol.* **8**, R650–R653. https://doi.org/10.1016/S0960-9822(07)00414-9 (1998).
38. Atwood, H. L. & Karunanithi, S. Diversification of synaptic strength: presynaptic elements. *Nat. Rev. Neurosci.* **3**, 497–516. https://doi.org/10.1038/nrn876 (2002).
39. Branco, T. & Staras, K. The probability of neurotransmitter release: variability and feedback control at single synapses. *Nat. Rev. Neurosci.* **10**, 373–383. https://doi.org/10.1038/nrn2634 (2009).
40. Tønnesen, J. & Nägerl, U. V. Dendritic spines as tunable regulators of synaptic signals. *Front. Psychiatry* **7**, 101. https://doi.org/10.3389/fpsyt.2016.00101 (2016).
41. Choquet, D. & Triller, A. The dynamic synapse. *Neuron* **80**, 691–703. https://doi.org/10.1016/j.neuron.2013.10.013 (2013).

39

42. Humeau, Y. & Choquet, D. The next generation of approaches to investigate the link between synaptic plasticity and learning. *Nat. Neurosci.* **22**, 1536–1543 (2019).
43. Meyer, D., Bonhoeffer, T. & Scheuss, V. Balance and stability of synaptic structures during synaptic plasticity. *Neuron* **82**, 430–443. https://doi.org/10.1016/j.neuron.2014.02.031 (2014).
44. Clifton, N. E., Trent, S., Thomas, K. L. & Hall, J. Regulation and function of activity-dependent homer in synaptic plasticity. *Mol. Neuropsychiatry* **5**, 147–161. https://doi.org/10.1159/000500267 (2019).
45. de Jong, A. P. H., Schmitz, S. K., Toonen, R. F. G. & Verhage, M. Dendritic position is a major determinant of presynaptic strength. *J. Cell Biol.* **197**, 327–337. https://doi.org/10.1083/jcb.201112135 (2012).
46. Grønborg, M. *et al.* Quantitative comparison of glutamatergic and GABAergic synaptic vesicles unveils selectivity for few proteins including MAL2, a novel synaptic vesicle protein. *J. Neurosci.* **30**, 2–12. https://doi.org/10.1523/JNEUROSCI.4074-09.2010 (2010).
47. Willig, K. I., Rizzoli, S. O., Westphal, V., Jahn, R. & Hell, S. W. STED microscopy reveals that synaptotagmin remains clustered after synaptic vesicle exocytosis. *Nature* **440**, 935–939. https://doi.org/10.1038/nature04592 (2006).
48. Westphal, V. *et al.* Video-rate far-field optical nanoscopy dissects synaptic vesicle movement. *Science* **320**, 246–249. https://doi.org/10.1126/science.1154228 (2008).
49. Truckenbrodt, S. *et al.* Newly produced synaptic vesicle proteins are preferentially used in synaptic transmission. *EMBO J.* https://doi.org/10.15252/embj.201798044 (2018).
50. Wilhelm, B. G. *et al.* Composition of isolated synaptic boutons reveals the amounts of vesicle trafficking proteins. *Science* **344**, 1023–1028. https://doi.org/10.1126/science.1252884 (2014).
51. Sograte-Idrissi, S. *et al.* Circumvention of common labelling artefacts using secondary nanobodies. *Nanoscale* https://doi.org/10.1039/d0nr00227e (2020).
52. Nakahata, Y. & Yasuda, R. Plasticity of spine structure: local signaling, translation and cytoskeletal reorganization. *Front. Synaptic Neurosci.* **10**, 29. https://doi.org/10.3389/fnsyn.2018.00029 (2018).
53. Biever, A., Donlin-Asp, P. G. & Schuman, E. M. Local translation in neuronal processes. *Curr. Opin. Neurobiol.* **57**, 141–148. https://doi.org/10.1016/j.conb.2019.02.008 (2019).
54. Bailey, C. H., Kandel, E. R. & Harris, K. M. Structural components of synaptic plasticity and memory consolidation. *Cold Spring Harb. Perspect. Biol.* **7**, a021758. https://doi.org/10.1101/cshperspect.a021758 (2015).
55. Schlüter, A. *et al.* Structural plasticity of synaptopodin in the axon initial segment during visual cortex development. *Cereb. Cortex* **27**, 4662–4675. https://doi.org/10.1093/cercor/bhx208 (2017).
56. Kulik, Y. D., Watson, D. J., Cao, G., Kuwajima, M. & Harris, K. M. Structural plasticity of dendritic secretory compartments during LTP-induced synaptogenesis. *eLife* **8**, e46356 (2019).
57. Hanus, C. *et al.* Unconventional secretory processing diversifies neuronal ion channel properties. *eLife* https://doi.org/10.7554/eLife.20609 (2016).
58. D'Este, E., Kamin, D., Göttfert, F., El-Hady, A. & Hell, S. W. STED nanoscopy reveals the ubiquity of subcortical cytoskeleton periodicity in living neurons. *Cell Rep.* **10**, 1246–1251. https://doi.org/10.1016/j.celrep.2015.02.007 (2015).
59. de Chaumont, F. *et al.* Icy: an open bioimage informatics platform for extended reproducible research. *Nat. Methods* **9**, 690–696. https://doi.org/10.1038/nmeth.2075 (2012).
60. Olivo-Marin, J.-C. Extraction of spots in biological images using multiscale products. *Pattern Recognit.* **35**, 1989–1996. https://doi.org/10.1016/S0031-3203(01)00127-3 (2002).

Acknowledgements

Author contributions

C.M.G and T.M.D. acquired and analysed data. S.O.R. and E.D. designed research. C.M.G., T.M.D., S.O.R. and E.D. wrote the manuscript.

Funding

Competing interests

S.O.R. is funder shareholder of NanoTag Biotechnologies. S.O.R. received compensation as consultant of NanoTag Biotechnologies. All the other authors declare no competing interests.

Additional information

Supplementary information is available for this paper at https://doi.org/10.1038/s41598-020-77260-2.

Correspondence and requests for materials should be addressed to E.D.

Reprints and permissions information is available at www.nature.com/reprints.

Publisher's note Springer Nature remains neutral with regard to jurisdictional claims in published maps and institutional affiliations.

40

Supplemental Information:

Synaptic activity and strength are reflected by changes in the post-synaptic secretory pathway

Clara-Marie Gürth [1, 2, #], Tal M. Dankovich [3, #], Silvio O. Rizzoli [3], Elisa D'Este [4, *]

[1] Department of NanoBiophotonics, Max Planck Institute for Biophysical Chemistry, Am Fassberg 11, 37077 Göttingen, Germany

[2] Department of Optical Nanoscopy, Max Planck Institute for Medical Research, Jahnstr. 29, 69120 Heidelberg, Germany

[3] Institute for Neuro- and Sensory Physiology, University Medical Center Göttingen, Humboldtallee 23, 37073 Göttingen, Germany

[4] Optical Microscopy Facility, Max Planck Institute for Medical Research, Jahnstr. 29, 69120 Heidelberg, Germany

[#] Contributed equally to this work

[*] Corresponding author: elisa.deste@mr.mpg.de

1

**Supplementary Table 1**: List of statistical values and number of synapses per individual experiments.

Type of analysis	Synaptic marker	POI	Synapses /bin	Total synapses	Rho	P (spearmen)
Automatic analysis of all synapses	homer	calreticulin	643	3215	0.956	0.00000000
		ERGIC53	680	3400	0.889	0.00000016
		TGN38	379-380	1899	0.925	0.00000000
		synaptopodin	542-543	2712	0.968	0.00000000
		vGLUT1	1138	5690	0.435	0.05505578
		SYT1	1156-1157	5781	0.754	0.00012247
	vGLUT1	calreticulin	487-488	2439	0.956	0.00000000
		ERGIC53	265-266	1326	0.765	0.00013235
		TGN38	117-118	588	0.876	0.00000039
		synaptopodin	159-160	796	0.833	0.00000492
	SYT1	calreticulin	249	1245	0.656	0.00168277
		ERGIC53	176-177	883	0.784	0.00004172
		TGN38	152-153	763	0.895	0.00000009
		synaptopodin	213-214	1068	0.882	0.00000025
Analysis of mushroom spines	homer	calreticulin	186	930	0.820	0.0000034
		ERGIC53	208	1040	0.901	0.0000001
		TGN38	122	610	0.860	0.0000006
		synaptopodin	140	700	0.840	0.0000016
	vGLUT1	calreticulin	99	495	0.351	0.0546565
		ERGIC53	100	500	0.583	0.0009192
		TGN38	75	375	0.781	0.0000124
		synaptopodin	79	395	0.705	0.0000665
	SYT1	calreticulin	87	435	0.026	0.5600091
		ERGIC53	107	535	0.448	0.0087806
		TGN38	47	235	0.482	0.0083918
		synaptopodin	61	305	0.687	0.0001321
	head size	calreticulin size	182-183	914	0.550	0.001554104
		ERGIC53 size	209-210	1047	0.761	0.00002167
		TGN38 size	131-132	657	0.001	0.90780719
		synaptopodin size	139-140	696	0.820	0.00000339
		calreticulin number	182-183	914	0.705	0.000008845
		ERGIC53 number	209-210	1047	0.901	0.00000006
		TGN38 number	131-132	657	0.653	0.0002669
		synaptopodin number	139-140	696	0.964	0.0000000
Analysis of stubby spines	homer	calreticulin	61	305	0.820	0.0000034
		ERGIC53	81	405	0.651	0.0002730
		TGN38	51	255	0.502	0.0030688
		synaptopodin	53	265	0.860	0.0000006
	vGLUT1	calreticulin	24	120	0.193	0.1757708
		ERGIC53	46	230	0.687	0.0001321
		TGN38	36	180	0.820	0.0000034
		synaptopodin	31	155	0.260	0.0620052
	SYT1	calreticulin	37	185	0.129	0.1874141
		ERGIC53	34	170	0.316	0.0363651
		TGN38	15	75	0.396	0.0378569
		synaptopodin	22	110	0.193	0.1325609

Supplementary Table 1 continued: List of statistical values and number of synapses per individual experiments.

| Type of analysis	Synaptic marker	POI	Synapses /bin	Total synapses	Rho	P (spearmen)
Automatic analysis of all synapses - Radial redistribution	homer	calreticulin	643	3215	0.899	0.03738607
		ERGIC53	680	3400	0.899	0.03738607
		TGN38	379-380	1899	0.300	0.62383766
		synaptopodin	542-543	2712	0.999	0.00000000
	vGLUT1	calreticulin	487-488	2439	0.899	0.03738607
		ERGIC53	265-266	1326	0.499	0.39100221
		TGN38	117-118	588	0.199	0.74706007
		synaptopodin	159-160	796	0.999	0.00000000
	SYT1	calreticulin	249	1245	0.999	0.00000000
		ERGIC53	176-177	883	0.999	0.00000000
		TGN38	152-153	763	0.899	0.03738607
		synaptopodin	213-214	1068	0.999	0.00000000
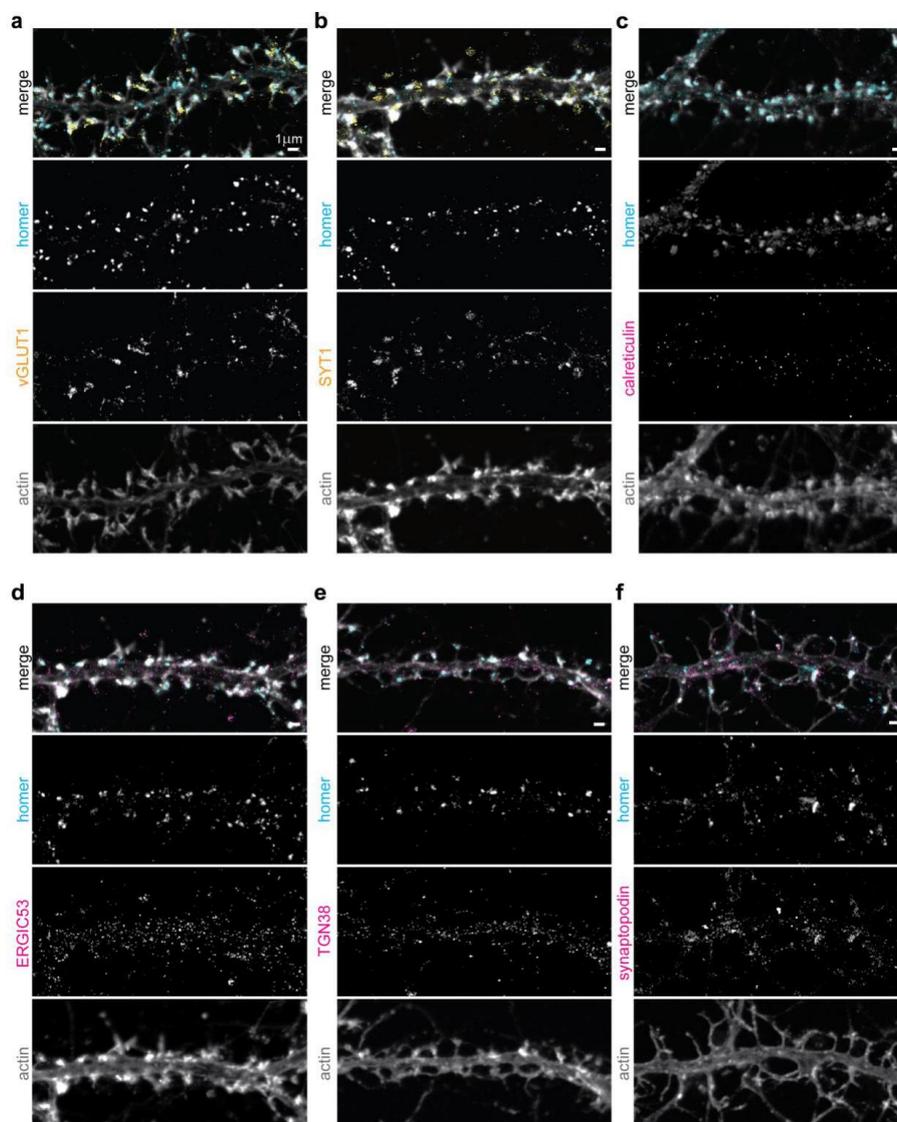
Supplementary Figure 1: Representative images of vGLUT1 and SYT1 compared to homer, and of the POIs stainings. Representative STED images of dendrites in mature hippocampal neuronal cultures. Samples were all stained with homer, phalloidin (actin, confocal), with pre- and post-synaptic sites markers vGLUT1 **(a)** or SYT1 **(b)**, and for the proteins of interest: calreticulin **(c)**, ERGIC53 (same dendrite as shown in b) **(d)**, TGN38 **(e)**, and synaptopodin **(f)**. Scale bars: 1 μm.
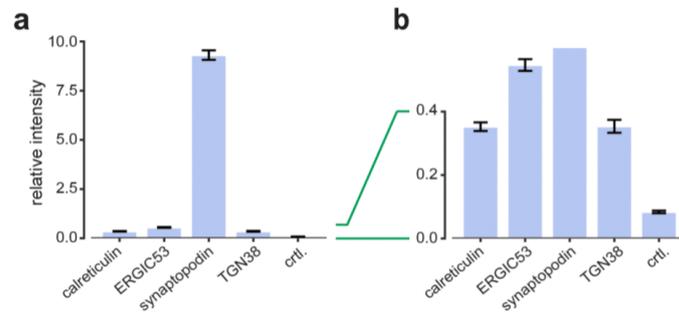
Supplementary Figure 2: Comparison of average intensities of the individual POIs.
Average staining intensity of the different POIs and control samples in which the primary antibody was omitted. Comparison of all stainings (**a**) and close up on the lower intensities (**b**). All data was collected from 3 independent experiments. Whiskers represent S.E.M.

5
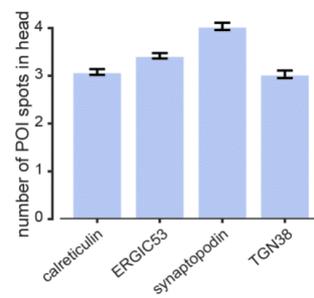
Supplementary Figure 3: Average spot number of secretory elements in mushroom spines. Average numbers of spots of calreticulin, ERGIC53, TGN38, and synaptopodin inside the spine head after manual segmentation. All data was collected from 3 independent experiments. Whiskers represent S.E.M.

6

46
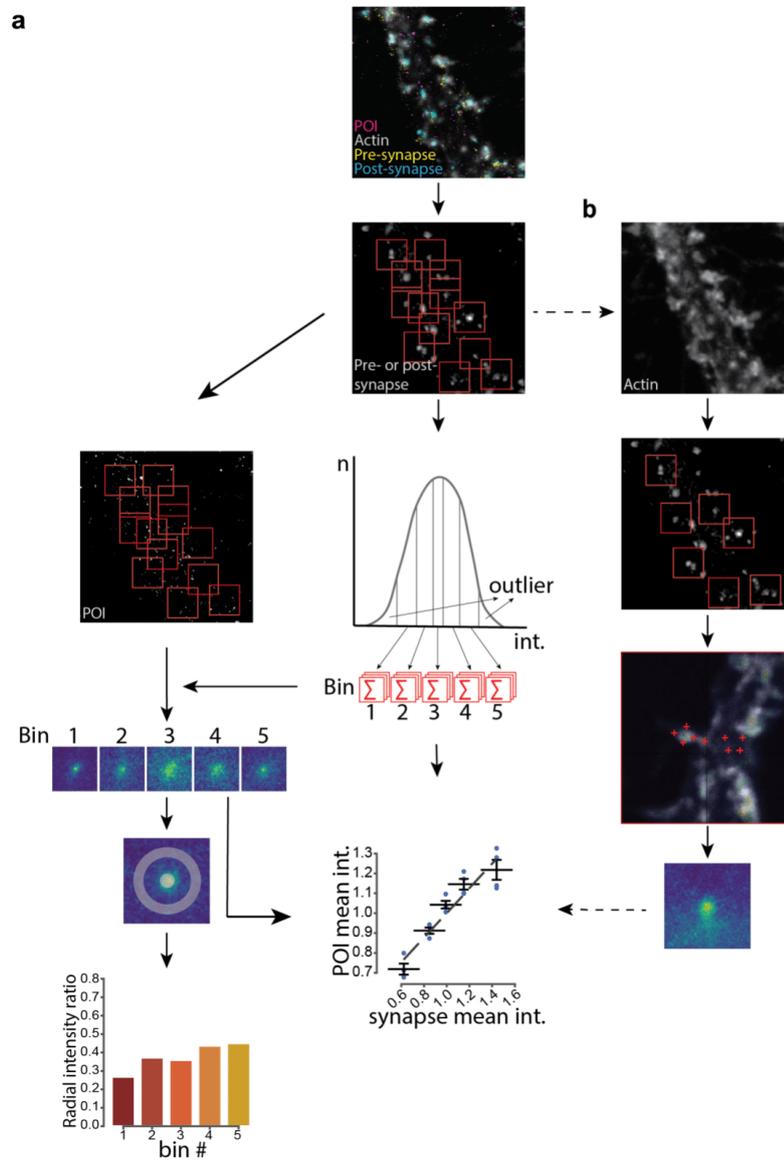
Supplementary Figure 4: Image analysis workflow. 4-colour images were acquired of the protein of interest (magenta), actin (white) and pre- and post-synaptic markers (yellow and cyan respectively). (a) Automatic analysis: the pre-/post-synaptic markers were used to identify synaptic puncta in the images. 3 x 3 μm square regions were extracted for each synapse and pooled into five bins based on increasing fluorescence intensity of the synaptic

markers. The POI images were averaged for each bin and correlated to the average intensity of the synaptic markers. Alternatively, a ratio was calculated between the outer rim and the central area of each average image to determine the tendency of the POI to localize to the synapse proximity. (b) Manual analysis: the post-synaptic marker was used to locate dendritic spines and extract 3 x 3 µm square regions as in (a). The actin channel of the images was then used to manually determine the borders of the spines in order to align them to a similar orientation before subsequent analysis.

8
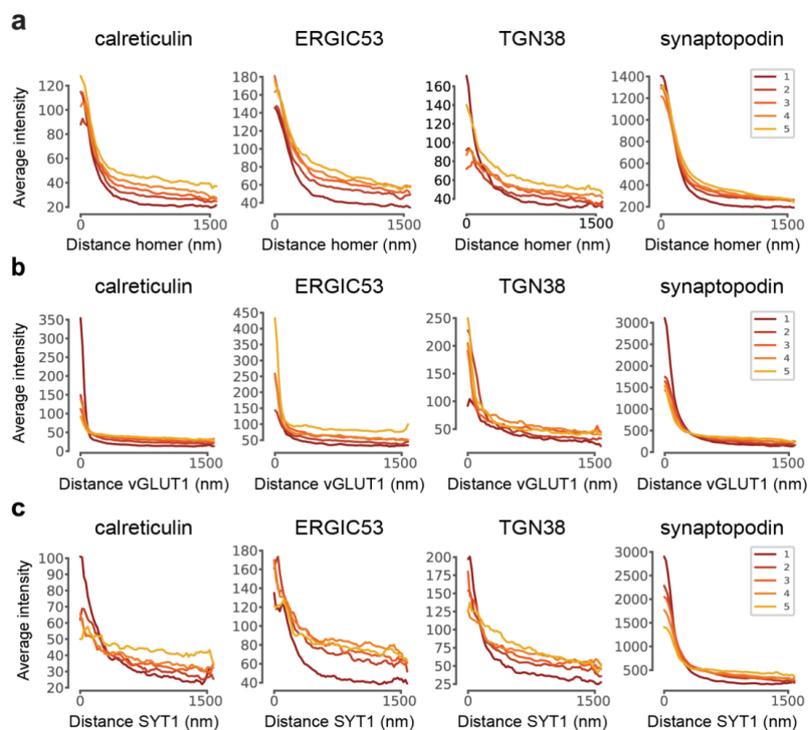
Supplementary Figure 5: Radial profile plots of the average intensity images. Radial profiles for bins of each POI: homer (**a**), vGLUT1 (**b**), and SYT1 (**c**). Bins 1-5 (dark red-yellow) were used for calculating the ratios depicted in Fig. 2b, 3b, and 4b, respectively.

9

49
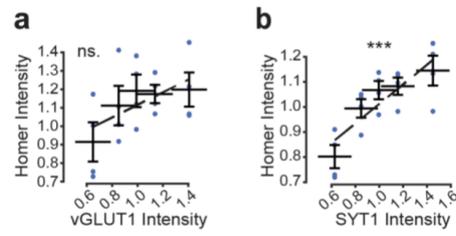
Supplementary Figure 6: Intensity correlations of pre-and post-synaptic markers.
Correlation of homer intensities and the average intensities of vGLUT1 (**a**) and SYT1 (**b**).
Dashed lines are the linear fits. All data was collected from four independent experiments.
Where *=p<0.05, **=p<0.01, ***=p<0.001, ****=p<0.0001, and ns.=non-significant. Whiskers
represent S.E.M. Numbers of synapses per each bin and Spearman's rho are listed in
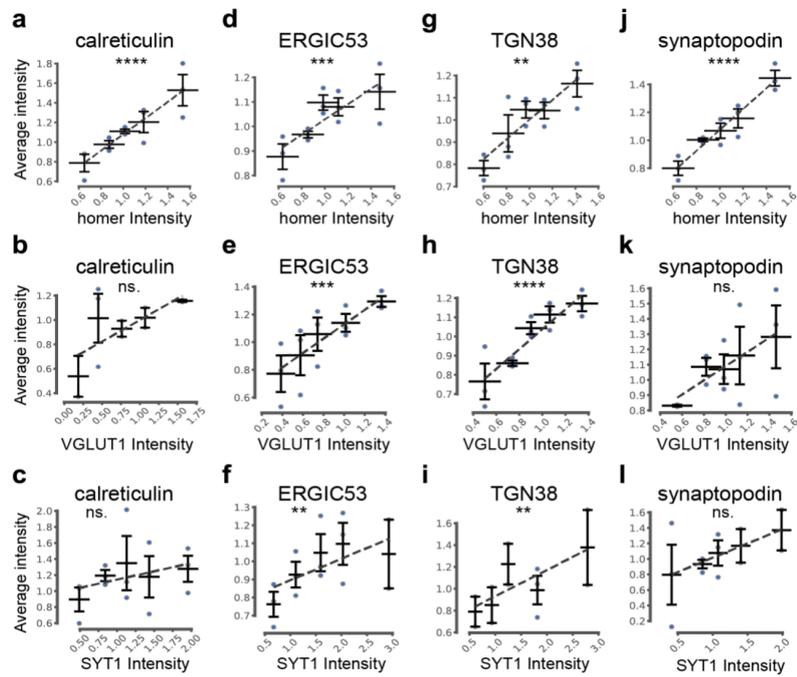Supplementary Table 1.
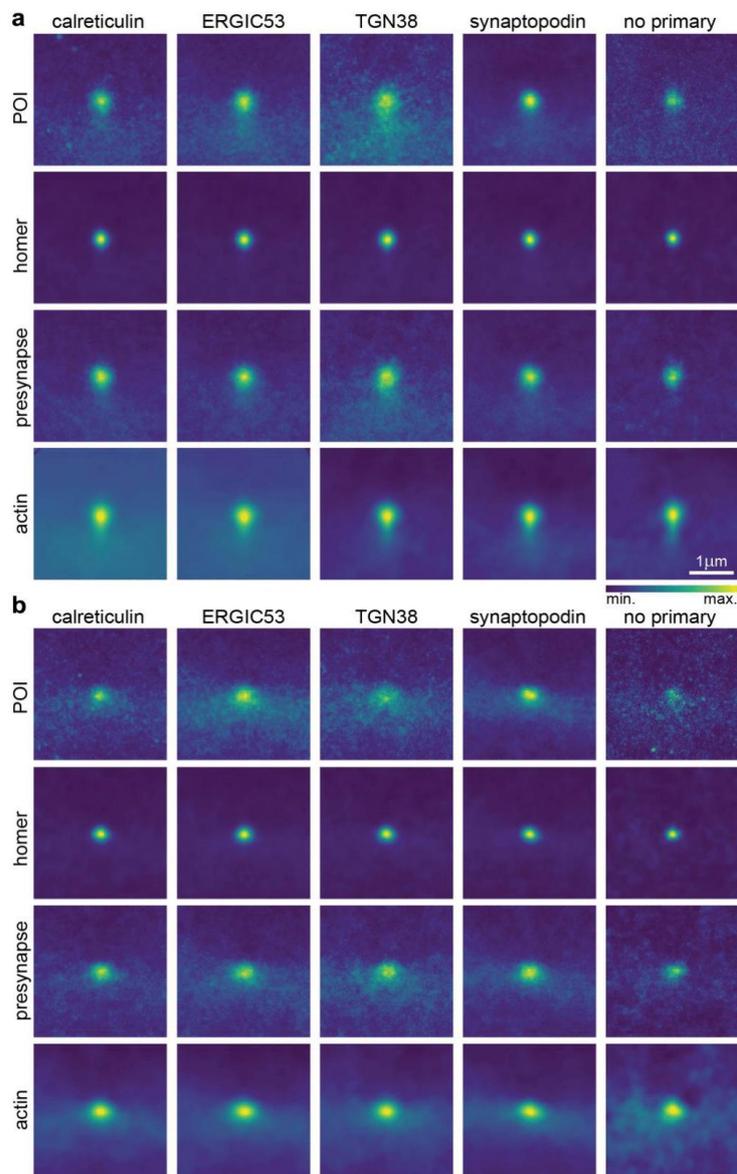
Supplementary Figure 7: Average images of spines after manual segmentation.
Average images of mushroom **(a)** and stubby **(b)** spines of the POIs, homer, average pre-synaptic markers vGLUT1 and SYT1, and phalloidin. Intensities have been adjusted for each image. Average images of the POIs shown in panel (a) are the same average images depicted in Fig. 5a.
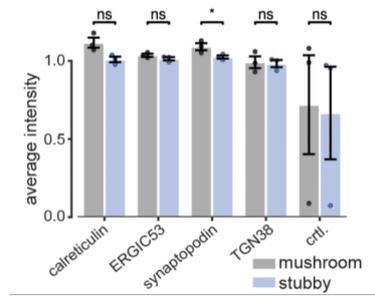
Supplementary Figure 8: Comparison of average intensities of mushroom and stubby spines. Average staining intesities of POI normalised to experimental means. Whiskers represent S.E.M.

Supplementary Figure 9: Correlations of secretory elements at stubby spines. (a-l)
Average intensity correlations after manual spine segmentation and classification of stubby
type spines. Average intensities of calreticulin (a-c), ERGIC53 (d-f), TGN38 (g-i), and
synaptopodin (j-l) correlated with average intensities of homer (a,d,g,j), vGLUT1 (d,e,h,k),
and SYT1 (c,f,i,l). Dashed lines are linear fits. All data were collected from three independent
experiments. Where *=p<0.05, **=p<0.01, ***=p<0.001, ****=p<0.0001, and ns.=non-
significant. Whiskers represent S.E.M. Numbers of synapses per each bin and Spearman's
rho are listed in Supplementary Table 1.

13

53
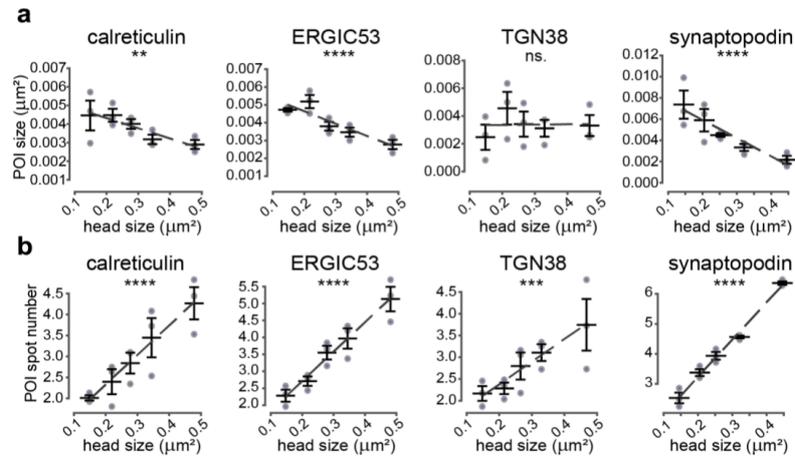
Supplementary Figure 10: Correlations of POI spot size and numbers and synaptic size in mushroom spines. (a) Correlation between average protein spot size of calreticulin, ERGIC53, TGN38, and synaptopodin inside the spine head and head size, as defined by manual segmentation. **(b)** Correlation between average spot numbers of calreticulin, ERGIC53, TGN38, and synaptopodin inside the spine head correlated to the head size as defined by manual segmentation. Dashed lines are linear fits. Where *=$p<0.05$, **=$p<0.01$, ***=$p<0.001$, and ****=$p<0.0001$. Whiskers represent S.E.M. Numbers of synapses per each bin and Spearman's rho are listed in Supplementary Table 1.

a

calreticulin   ERGIC53   TGN38   synaptopodin

b

	calreticulin	ERGIC53	TGN38	synaptopodin
merge				
POI				
Actin				
DAPI				

10μm

c

calreticulin   ERGIC53   TGN38   synaptopodin

15
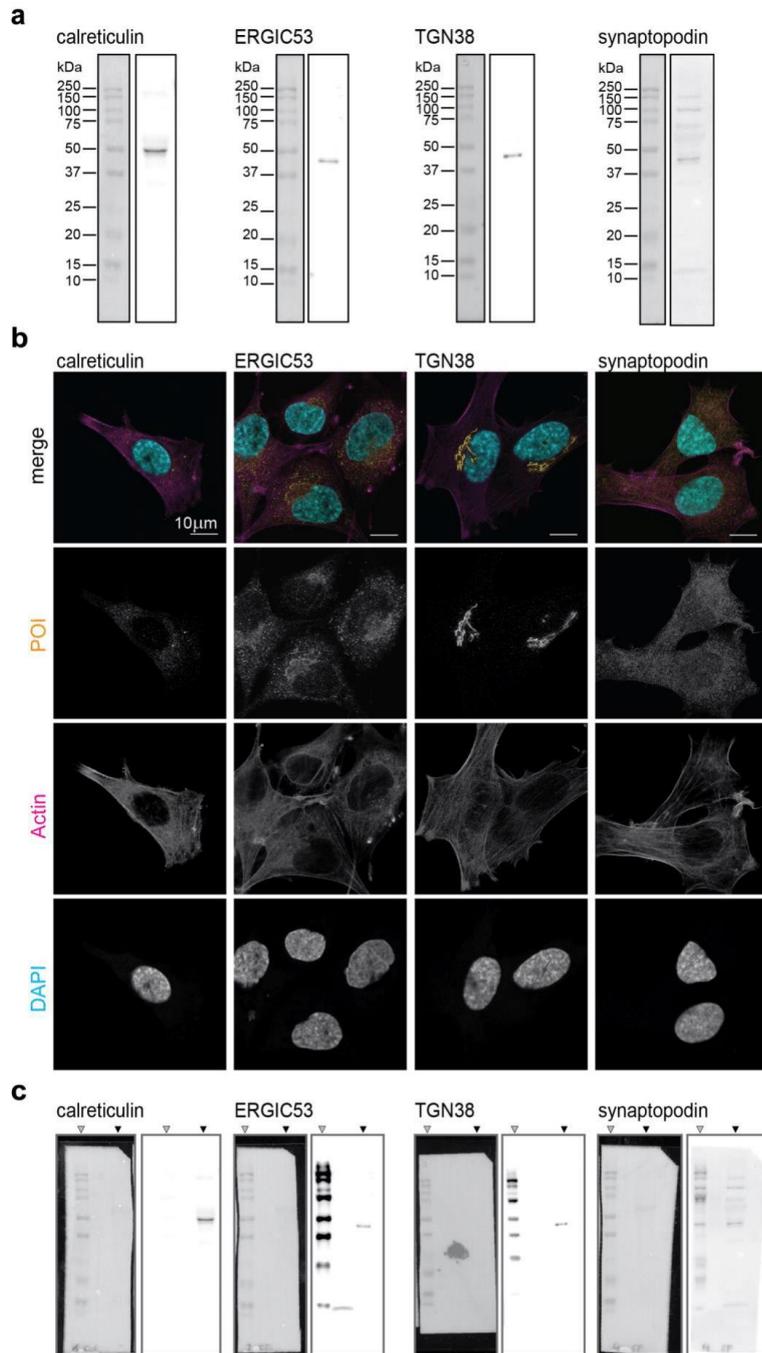
Supplementary Figure 11: Antibody validation. (a) Western blot validation of used POI antibodies in whole cell lysate of PC12 cells (calreticulin, ERGIC53 and synaptopodin) or rat cultured primary cortical neurons (TGN38). Displayed are colourimetric images of the protein ladder (left) and the respective antibody chemilumenescence signal (right) of each individual full-length membrane. Proteins have been blotted and analysed on separate membranes. Brightness and contrast have not been modified and are displayed as raw data. Full colourimetric and chemiluminescence images of the membranes are shown in panel (c).
(b) Representative STED images of immunofluorescence in PC12 cells labelled with DAPI (confocal), phalloidin (actin), and the proteins of interest: calreticulin, ERGIC53, TGN38, and synaptopodin. Scale bars: 10 µm. **(c)** Full size membrane images used for panel (a). Left: colourimetric; right: chemilumenescence. Grey arrows indicate the position of the protein ladder; black arrows indicate the lane of the respective cell lysate, as shown in (a). The protein ladder shows aspecific chemilumenescence signal in the case of ERGIC53, TGN38 and synaptopodin. Brightness and contrast have not been modified.

Supplementary Methods

Sample preparation and imaging of PC12 cells

PC12 adh cells (AddexBio, cat. C0032002) were cultured on glass coverslips and processed as described in the main text. Actin was labelled with phalloidin-Star635P (Abberior, cat. 2-0205-002-5; 1:100 dilution) and nucleus with DAPI (Biomol, cat. AG-CR1-3668-M005, 1:5000 dilution). Imaging was performed as previously described.

Western Blot

Whole cell lysate from PC12 adh cells or cultured cortical primary neurons (18 days *in vitro*, prepared as hippocampal cultures), in Laemmli buffer (Bio-Rad, cat. 161-0747) were loaded in a 12% SDS gel (Bio-Rad, cat. 4561045) and subjected to electrophoresis at 50 V for 5 min, followed by 10 V for 80 min. Separated proteins were then transferred onto a PVDF membrane (Bio-Rad, cat. 162-0260) at 120 V for 50 min. The blotted membranes were blocked in Tris-buffered saline, 0.1% Tween (TBST), 3% BSA and incubated overnight with previously described primary antibodies (calreticulin 1:500, ERGIC53 1:1000, TGN38 1:500, synaptopodin 1:1000) in TBST, 1% BSA. Then the membranes were washed five times in TBST and incubated with secondary antibody dilution (Thermo Fisher, cat. 31466, 1:10000) in TBST 1% BSA for 1 hour at room temperature. Afterwards membranes were washed five times in TBST, incubated for 1 min with ECL western blotting substrate (Thermo Fisher, cat. 32109) and signal was detected in a Chemidoc System (Bio-Rad Laboratories GmbH, Germany).

3: Original publication: extracellular matrix remodeling through endocytosis and resurfacing of Tenascin-R

Authors

Tal M. Dankovich[1,2*], Rahul Kaushik[3,4], Linda H.M. Olsthoorn[2,5], Gabriel Cassinelli Petersen[1], Philipp Emanuel Giro[1], Verena Kluever[1], Paola Agüi-Gonzalez[1], Katharina Grewe[1], Guobin Bao[1,6], Sabine Beuermann[7], Hannah Abdul Hadi[1], Jose Doeren[1], Simon Klöppner[1], Benjamin H. Cooper[7], Alexander Dityatev[3,4,8], Silvio O. Rizzoli[1,9*]

Affiliations

[1]University Medical Center Göttingen, Institute for Neuro- and Sensory Physiology, Göttingen, Germany.
[2]International Max Planck Research School for Neuroscience, Göttingen, Germany.
[3]Molecular Neuroplasticity, German Center for Neurodegenerative Diseases (DZNE), Magdeburg, Germany.
[4]Center for Behavioral Brain Sciences (CBBS), Magdeburg, Germany.
[5]Max Planck Institute for Biophysical Chemistry, Göttingen, Germany.
[6]University Medical Center Göttingen, Institute of Pharmacology and Toxicology, Göttingen, Germany.
[7]Max Planck Institute for Experimental Medicine, Göttingen, Germany.
[8]Medical Faculty, Otto –von Guericke University, Magdeburg, Germany.
[9]Biostructural Imaging of Neurodegeneration (BIN) Center, Göttingen, Germany.
***Correspondence**: Tal M. Dankovich: tal.dankovich@med.uni-goettingen.de, Silvio O. Rizzoli: srizzol@gwdg.de

Personal contribution: I performed the majority of the experiments in this study. The exceptions are the experiments shown in Figures 2b,c, 8 and Extended Data Figures 1a and 20.

Below is my contribution for collaborative experiments:

- Fig. 10c,d (correlative optical fluorescence microscopy and nanoSIMS): immunostaining of brain slices and fluorescence imaging.
- Extended Data Fig. 1b (shRNA-mediated knockdown of TNR in neuronal cultures): immunostaining and imaging of neuronal cultures.
- Extended Data Fig. 1c,d (electrophysiology of TNR treated cultures): treatment of cultures and assistance with measurements.
- Extended Data Fig. 15h (immunoprecipitation of TNR from synaptosomes): the experiment was performed jointly.

In addition, I performed most of the data analysis, under the supervision of S.O.R. I prepared the manuscript draft, and revised it in collaboration with S.O.R. (and with contributions from A.D.).

ARTICLE

Check for updates

Extracellular matrix remodeling through endocytosis and resurfacing of Tenascin-R

Tal M. Dankovich [1,2✉], Rahul Kaushik[3,4], Linda H. M. Olsthoorn[2,5], Gabriel Cassinelli Petersen [1], Philipp Emanuel Giro[1], Verena Kluever [1], Paola Agüi-Gonzalez [1], Katharina Grewe[1], Guobin Bao[1,6], Sabine Beuermann[7], Hannah Abdul Hadi[1], Jose Doeren [1], Simon Klöppner[1], Benjamin H. Cooper [7], Alexander Dityatev [3,4,8] & Silvio O. Rizzoli [1,9✉]

The brain extracellular matrix (ECM) consists of extremely long-lived proteins that assemble around neurons and synapses, to stabilize them. The ECM is thought to change only rarely, in relation to neuronal plasticity, through ECM proteolysis and renewed protein synthesis. We report here an alternative ECM remodeling mechanism, based on the recycling of ECM molecules. Using multiple ECM labeling and imaging assays, from super-resolution optical imaging to nanoscale secondary ion mass spectrometry, both in culture and in brain slices, we find that a key ECM protein, Tenascin-R, is frequently endocytosed, and later resurfaces, preferentially near synapses. The TNR molecules complete this cycle within ~3 days, in an activity-dependent fashion. Interfering with the recycling process perturbs severely neuronal function, strongly reducing synaptic vesicle exo- and endocytosis. We conclude that the neuronal ECM can be remodeled frequently through mechanisms that involve endocytosis and recycling of ECM proteins.

[1] University Medical Center Göttingen, Institute for Neuro- and Sensory Physiology, Excellence Cluster Multiscale Bioimaging, Göttingen, Germany. [2] International Max Planck Research School for Neuroscience, Göttingen, Germany. [3] Molecular Neuroplasticity, German Center for Neurodegenerative Diseases (DZNE), Magdeburg, Germany. [4] Center for Behavioral Brain Sciences (CBBS), Magdeburg, Germany. [5] Max Planck Institute for Biophysical Chemistry, Göttingen, Germany. [6] University Medical Center Göttingen, Institute of Pharmacology and Toxicology, Göttingen, Germany. [7] Max Planck Institute for Experimental Medicine, Göttingen, Germany. [8] Medical Faculty, Otto von Guericke University, Magdeburg, Germany. [9] Biostructural Imaging of Neurodegeneration (BIN) Center, Göttingen, Germany. ✉email: tal.dankovich@med.uni-goettingen.de; srizzol@gwdg.de

he extracellular matrix (ECM) molecules of the brain form
lattices that enwrap neurons and fill perisynaptic spaces[1].

These structures appear to be particularly durable, owing
to the exceptional longevity of the ECM molecules[2,3], and they
are deemed to stabilize neurons and synapses[4,5]. Nevertheless, the
ECM must remain alterable to allow for the structural changes
that occur in response to activity and plasticity. Such changes
have long been thought to be infrequent in the adult brain, but
this notion has been recently challenged by a series of super-
resolution imaging studies. Synapses were found to change shape
and location continually, on a time scale of minutes, both in acute
brain slices[6] and in the adult brain[7,8]. These findings therefore
suggest that the ECM may be remodeled relatively frequently.

This notion is difficult to accommodate with the best-known
mechanisms for ECM remodeling, which involve ECM cleavage
by proteolytic enzymes such as matrix metalloproteinases, fol-
lowed by the secretion and incorporation of newly-synthesized
ECM molecules[9,10]. An alternative solution to ECM remodeling
seems therefore necessary, through mechanisms that reuse
existing molecules, rather than relying on de novo synthesis. To
search for such a mechanism, we focused on Tenascin-R (TNR), a
matrix glycoprotein that is predominantly expressed in the cen-
tral nervous system[11]. TNR is highly enriched in perineuronal
nets (PNNs), a condensed ECM lattice surrounding a subset of
inhibitory interneurons, and is essential for PNN formation. TNR
is also expressed in the more diffuse perisynaptic ECM associated
in the neuropil with both inhibitory and excitatory synapses on a
broad range of neuronal cell types[12].

We targeted TNR by several advanced imaging assays, and we
found that a subset of the TNR molecules, found especially in the
vicinity of synapses, cycled between the ECM and neuronal
organelles. We termed these TNR molecules the "recycling pool,"
in analogy to the recycling pool of synaptic vesicles[13,14], which
also cycle between the cell surface (exocytosed) and internal
(endocytosed) states. The recycling TNR molecules were secreted
mainly at synapses, in a process that was dependent not only on
the overall network activity levels, but also on the activity levels of
the particular synapses. These molecules were then endocytosed
by the neurons and were recycled back to the perisynaptic ECM,
over ~3 days. Most molecules appeared to undergo several cycles
without being degraded. Finally, perturbing the recycling TNR
pool disrupted synaptic function, which suggests that these
molecules are intimately linked to synaptic activity. We conclude
that neurons maintain a pool of TNR that continually recycles in
and out of perisynaptic ECM, allowing for frequent ECM
remodeling without the need to synthesize new molecules, and
thereby explaining how synaptic fluctuations could be dealt with
without compromising the exceptionally long lifetime of ECM
molecules.

Results
**A classical biotinylation assay suggests that TNR molecules are
recycled**. To test whether ECM molecules can indeed be reused,
we first used a classical biotinylation-based assay that has been
instrumental in determining the reuse (recycling) of neuronal
surface proteins, and especially of neurotransmitter receptors[15].
We employed the same system used previously for determining
the recycling of neurotransmitter receptors, rat cultured hippo-
campal neurons.

TNR is well detectable in these cultures, as observed by
immunostaining, and is also found in PNNs (Supplementary Fig. 1a).
Moreover, it is present at both excitatory and inhibitory synapses, as
indicated in the Introduction (Supplementary Fig. 1b). Therefore, a
biotinylation assay should be able to detect the dynamics of TNR in
culture.

We treated the neurons with a cleavable, membrane-
impermeable biotin derivative, to tag all proteins at the cell
surface. We allowed the neurons to internalize molecules for 6 h,
and we then stripped biotin from the cell surface, thus leaving this
label only on the endocytosed proteins (Fig. 1a). To measure the
potential recycling of the internalized molecules, we incubated the
neurons a further 18 h, to allow for protein resurfacing, and then
performed a second round of biotin stripping (Fig. 1a). We
collected the biotin-tagged proteins on streptavidin beads, and we
then tested the recycling of TNR and other proteins by
immunolabeling the beads and imaging them in confocal
microscopy (Fig. 1b). This is a particularly sensitive technique,
enabling the detection of proteins in minute sample volumes[16].
We found that TNR is indeed endocytosed during the initial 6 h
of incubation, and that a significant proportion of the molecules
resurfaces during the subsequent 18 h. This behavior was similar
to that of a positive control, the synaptic vesicle protein
synaptotagmin 1, Syt1, which participates in the well-known
recycling of synaptic vesicles (Fig. 1c). In addition, we tested a
membrane protein that is endocytosed, but is not expected to
recycle (the lysosomal protein LAMP1), and a membrane-
resident protein, which is very rarely endocytosed (myelin basic
protein, MBP). Both behaved in the expected fashion (Fig. 1d, e),
suggesting that this assay reports accurately the protein behavior.

In principle, the recycling TNR molecules could have as a
source neurons or glia cells. To verify this, we first characterized
our cell cultures (Supplementary Fig. 2), noting that astrocytes
make up ~60% of all cells, with neurons making up ~38%, and
the MBP-containing oligodendrocytes ~2%. PNN-containing
neurons made up 11% of all neurons, in agreement to the
literature[17]. In spite of their large number, astrocytes internalized
very little TNR (around 5%, Supplementary Fig. 3), implying that
most of the TNR recycling observed in the biotinylation assay
must be in neurons. The original source of TNR (the original
location of TNR synthesis), however, cannot be determined by
these experiments, and could potentially also be found in
astrocytes, at least to some level, since astrocyte cultures can
produce the molecule[18].

Finally, the loss of biotinylated TNR cannot be ascribed to its
degradation, since this molecule is extremely stable (see
Supplementary Fig. 4, including a characterization of TNR
degradation via imaging and Western blotting), and since we
blocked lysosomal degradation during these experiments.

**An imaging assay suggests that TNR molecules emerge pre-
ferentially near synapses**. To verify these findings by an imaging
assay, we turned to a knock-out validated TNR antibody[19]
(Supplementary Fig. 5a, b). Application of the antibody to neu-
ronal cultures did not appear to cause any changes in their
behavior, as was verified by electrophysiological measurements
(Supplementary Fig. 5c, d). We applied fluorophore-conjugated
TNR antibodies to the cultures, and imaged them at 37 °C, for
several hours. We observed the accumulation of TNR antibodies
in the neuronal somas, indicative of endocytosis (Supplementary
Fig. 6). However, many other cellular regions remained virtually
unchanged, which suggests that not all TNR molecules are
dynamic.

To focus on the dynamic TNR molecules, we relied on an assay
used extensively for synaptic vesicle proteins, a 'blocking-labeling'
assay (see[20] and references therein). The surface TNR epitopes were
blocked using unconjugated antibodies. Fluorophore-conjugated
TNR antibodies were then applied at different intervals, to label
newly-emerged epitopes (Fig. 2a). This assay enabled us to detect a
slow but steady appearance of such epitopes (Fig. 2b, c). A super-
resolution investigation using STED microscopy revealed that these

60
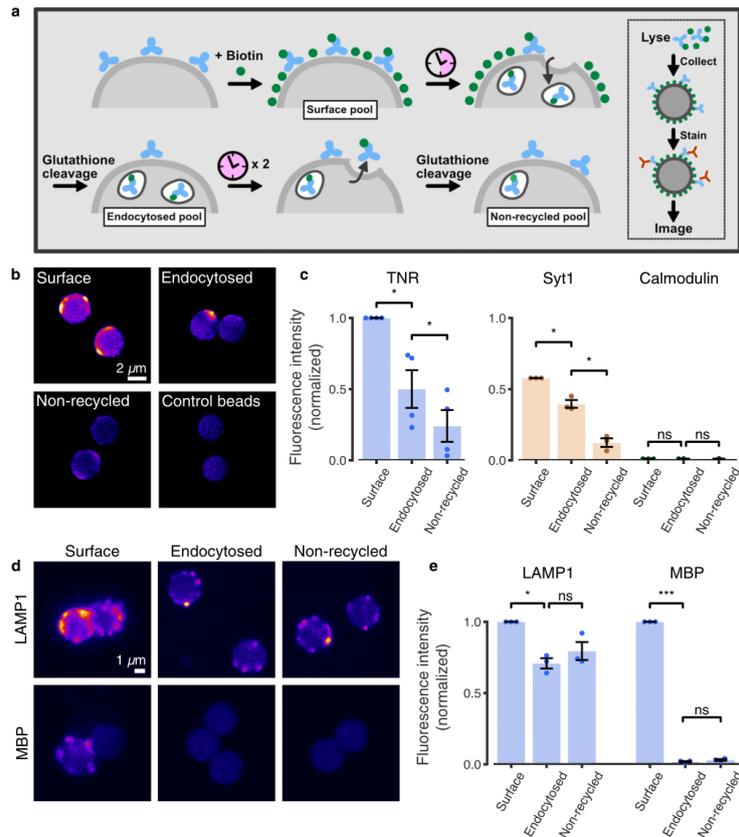
Fig. 1 TNR molecules endocytose and subsequently resurface in neurons. a Neurons were treated with sulfo-NHS-S-S-biotin to label cell-surface proteins. Following a 6-h incubation, allowing for internalization, remaining cell-surface proteins were stripped of their labels with glutathione. After a further 18 h of incubation, allowing for recycling, the neurons were again treated with glutathione. Lysates representing surface, endocytosed or non-recycled pools, were collected on streptavidin-coupled beads, immunostained for TNR, immobilized on glass slides and imaged with confocal microscopy. **b** Example beads collecting TNR pools, or controls incubated without primary antibodies. Scale bar = 2 μm. **c** A quantification of TNR fluorescence intensity normalized to the 'surface' mean in the corresponding experiment, indicates that a large fraction of TNR molecules endocytose within 6 h, and many subsequently resurface within 24 h. As positive/negative controls, the synaptic vesicle protein Syt1, well-known to recycle, and the intracellular protein calmodulin were tested. The plots are scaled by the ratio between the 'surface' mean for these proteins and that of TNR. $N = 4$ (TNR) and 3 (Syt1/calmodulin) independent experiments with >100 (TNR) and >50 (Syt/calmodulin) beads. **d, e** As additional controls, the lysosomal marker LAMP1, known to endocytose but scarcely recycle, and myelin basic protein (MBP), which should not endocytose, were also tested. Scale bar = 1 μm. **e** Quantification of LAMP1/MBP fluorescence intensity, normalized to the 'surface' mean of the corresponding experiment. $N = 3$ independent experiments with > 50 beads. Statistical significance was evaluated using repeated-measures one-way ANOVA, (**c** TNR: $F_{1.153,3.458} = 28.29$, **$p = 0.009$; Syt1: $F_{1.007,2.014} = 62.98$, *$p = 0.015$; calmodulin: $F_{1,2} = 0.016$, $p = 0.912$; **e** LAMP1: $F_{1.293,2.585} = 19.6$, *$p = 0.028$; MBP: $F_{1.52,3.041} = 28337$, ***$p < 0.001$), followed by the Holm-Sidak multiple comparisons test comparing 'surface'/'endocytosed' and 'endocytosed'/'non-recycled' (**c** TNR: *$p = 0.032$, *$p = 0.021$; Syt1: *$p = 0.044$, *$p = 0.044$; calmodulin: $p = 0.933$, $p = 0.993$; **e** LAMP1: *$p = 0.045$, $p = 0.162$; MBP: ***$p < 0.001$, $p = 0.068$). Data represent the mean ± SEM, dots indicate individual experiments. Source data are provided in Source Data file.

TNR molecules were enriched near synapses (Fig. 2d), where they also emerged more rapidly than for the cell as a whole (compare Fig. 2c, e). Importantly, their appearance was potentiated by enhancing neuronal activity using the GABA$_A$ blocker bicuculline, and was inhibited by reducing neuronal activity using the glutamate receptor blockers CNQX/AP5 (Fig. 2f).

We analyzed the distribution of the TNR signals along dendrites or axons (labeled using the lipophilic tracer DiO),

moving from synapses (identified by immunostaining the synaptic vesicle marker VGlut1) along the neurites. A substantial enrichment can be found at synapses for newly-emerged epitopes, which is much higher than that observed for all TNR epitopes (Fig. 2g). This indicates that newly-emerged TNR epitopes are preferentially found in the vicinity of synapses.

To test whether this preference is accidental, or whether it depends on the local synaptic characteristics, we compared the
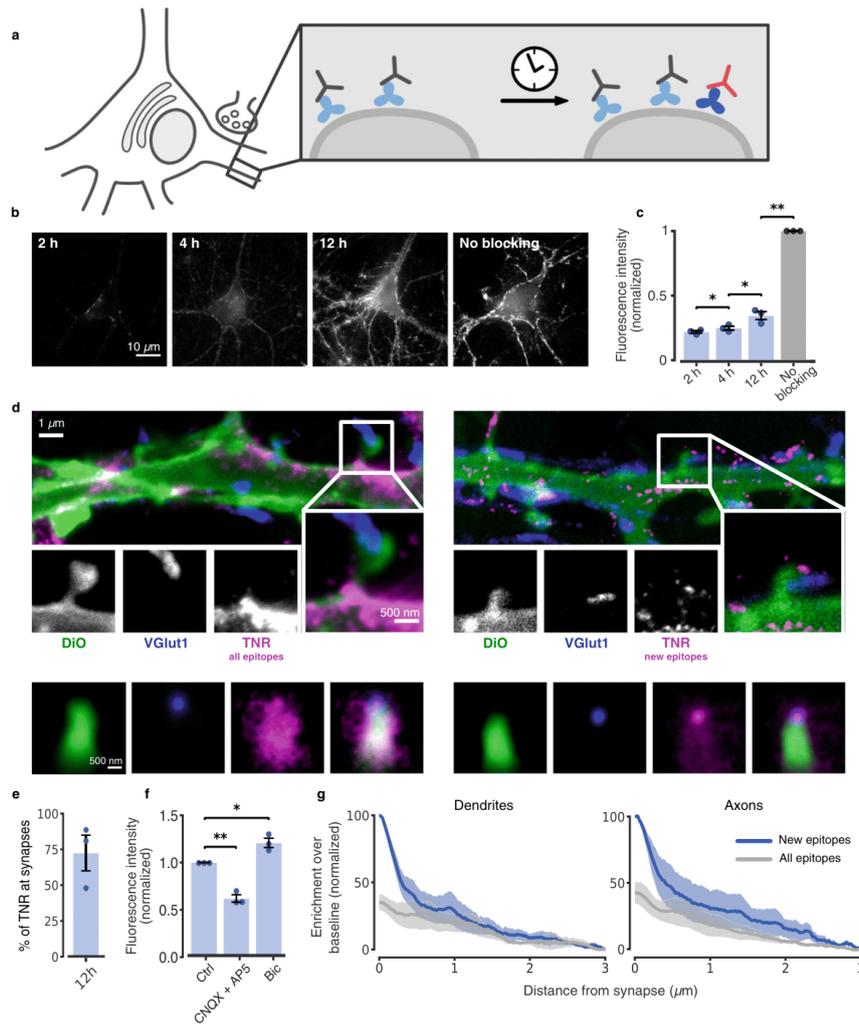
TNR labeling to synaptic strength. To estimate this on the presynaptic side, we labeled the active vesicle pools using an antibody directed to the intra-vesicular domain of synaptotagmin 1 (Syt1), which has been employed for this type of assay for more than two decades[20–23]. This antibody enters actively-recycling vesicles during exo- and endocytosis, and marks them fluorescently, thereby providing a measure of the amount of vesicle activity at the particular synapse. We found a remarkably strong correlation between the amount of TNR epitopes present at a particular synapse and its estimated activity (its estimated synaptic strength; Fig. 3a). To perform a similar measurement for the postsynaptic side, we took the spine head size as a proxy for synaptic strength[24]. Again, the amounts of newly-emerged epitopes were found in higher amounts at synapses with larger spines (Fig. 3b). This suggests that the emergence of these TNR molecules on the surface correlates to synaptic weight.

To further confirm this issue, we turned to an analysis of the TNR levels in the neurites (axonal or dendritic) of individual DiO-labeled neurons. The literature suggests that the total TNR levels in individual neurons should correlate among all neurites, with specific neurons exhibiting high or low TNR levels[11,25]. We indeed found this to be the case (Supplementary Fig. 7a). However, this should *not* be the case for newly-emerged TNR epitopes, if their emergence is dependent on the local synapse strength. This hypothesis was confirmed by our measurements (Supplementary Fig. 7b), as the dendrites and axonal branches of individual neurons had widely variable fluorescence levels for the newly-emerged epitopes.

Overall, these experiments suggest that this assay is able to detect TNR molecules appearing on the surface, from an intracellular TNR population. However, new TNR epitopes could also emerge through the un-binding of unconjugated antibodies

62

Fig. 2 Dynamic TNR molecules emerge at synapses, in an activity-dependent fashion. a To monitor dynamic TNR molecules, surface epitopes were blocked by incubating with non-fluorescent TNR antibodies (gray). After some time, fluorophore-conjugated antibodies were applied (red) to reveal newly-emerged epitopes (dark blue). **b** Newly-emerged epitopes 2/4/12 h post-blocking in cultures treated with bicuculline (the dark blue). Scale bar = 10 µm. **c** Fluorescence intensity, normalized to non-blocked neurons. $N = 3$ independent experiments, ≥10 neurons per datapoint. Repeated-measures one-way ANOVA: $F_{1.089,2.179} = 790.8$, ***$p < 0.001$, followed by Fisher's LSD: '2 h'/'4 h':*$p = 0.041$; '4 h'/'12 h':*$p = 0.032$; '12 h'/'no blocking': **$p = 0.002$. **d** All TNR epitopes (left) or newly-emerged epitopes 12 h post-blocking (right) were revealed (magenta, STED imaging). Membranes of a subset of neurons were labeled using sparse DiO labeling (green, confocal imaging). Presynapses were identified by VGlut1 (blue, STED imaging). Scale bars: 1 µm (full images), 500 nm (insets). Bottom: hundreds of synapses were averaged by centering synapse images on the VGlut1 puncta and orienting the dendritic DiO signals vertically. "All" TNR epitopes cover the entire bouton-dendrite area (left), while newly-emerged epitopes are enriched in the bouton region (right). **e** Quantification of TNR exchange at synapses (as in **c**, measuring exclusively TNR at VGlut1-labeled synapses). $N = 3$ independent experiments with >100 synapses. **f** Comparison of newly-emerged TNR epitopes 12 h post-blocking in cultures treated with bicuculline (40 µM), or CNQX (10 µM) and AP5 (50 µM). Intensity is normalized to the corresponding control (DMSO). $N = 3$ experiments, ≥10 neurons per datapoint. One-way ANOVA on rank: $F_{2,6} = 42$, ***$p < 0.001$, followed by Dunn's multiple comparisons test: 'ctrl'/'CNQX + AP5': **$p = 0.003$; 'ctrl'/'bic': *$p = 0.042$. Data represent the mean ± SEM, dots indicate individual experiments. **g**, Analysis of 2-color-STED images (as shown in **d**). Synaptic enrichment is substantially higher for newly-emerged epitopes. $N = 3$ independent experiments with >100 synapses. Repeated-measures one-way ANOVA on log-transformed data: $F_{1.977,3.954} = 24.13$, **$p = 0.006$, followed by Fisher's LSD: 'new'/'all' epitopes: *$p = 0.024$ (dendrites); *$p = 0.036$ (axons). Data represent the mean (line) ± SEM (shaded region). Source data are provided in Source Data file.
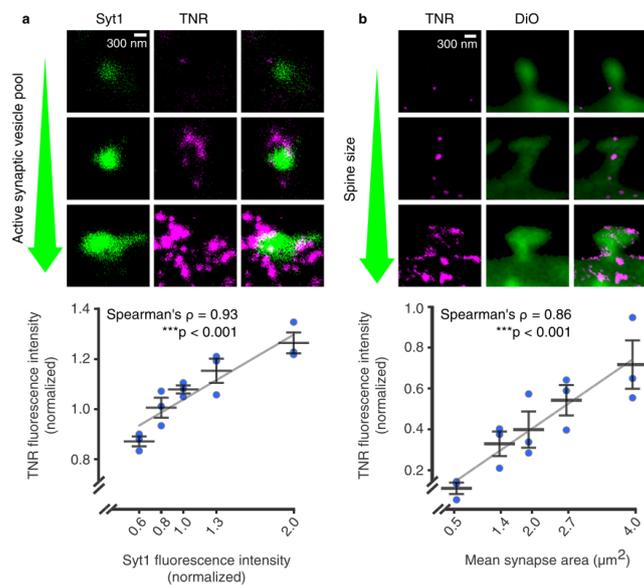
Fig. 3 The emergence of TNR epitopes is dependent on synaptic weight. a The TNR epitopes in the ECM were blocked as in the previous experiments, and 12 h later the cultures were incubated with fluorophore-conjugated TNR antibodies (magenta) and with fluorophore-conjugated antibodies for the intra-vesicular domain of Syt1 (green), which reveal the synaptic vesicle pool that undergoes exo- and endocytosis (the active pool). The size of this pool is a measure of the activity of the respective boutons. The panels show example synapses with different active vesicle pools, imaged in STED (TNR) and confocal (Syt1). Scale bar = 300 nm. The graph shows the mean fluorescence intensities normalized to the median intensity of the respective experiment. The Syt1 intensities are binned to include an equal number of synapse images. An analysis of the correlation of the TNR signal at Syt1-labeled synapses indicates that the TNR signals correlate strongly with the size of the active vesicle pool in the respective boutons. $N = 3$ independent experiments, with >1100 synapses per datapoint, Spearman's ρ = 0.927, ***$p = 6.489 × 10^{-7}$ (two-sided). **b** Newly-emerged TNR epitopes (magenta) were labeled after 12 h as in panel a, and the neuronal plasma membrane was visualized with DiO (green). The panels show example spines with different sizes, imaged in STED (TNR) and confocal (DiO). Scale bar = 300 nm. The graph shows the mean fluorescence intensity of TNR and the mean synapse area, normalized to the median values in the respective experiment. The synapse area values are binned to include an equal number of synapse images. An analysis of the correlation of the TNR signal at DiO-labeled spines indicates that the TNR signals correlate strongly with the size of the dendritic spine for newly-emerged TNR epitopes. $N = 3$ independent experiments, with >280 synapses per datapoint, Spearman's ρ = 0.862, ***$p = 3.601 × 10^{-5}$ (two-sided). All data represent the mean ± SEM, with dots indicating individual experiments. Source data are provided in Source Data file.

from their epitopes, which would allow the fluorophore-conjugated ones to take their place. In control experiments, we found no evidence for such un-binding, either from the surface of fixed cells at 37 °C (Supplementary Fig. 8) or in live cells at 4 °C (Supplementary Fig. 9). A second possible source for such epitopes would be a pre-existing population of molecules that were present on the cell surface, but were previously unavailable to antibody binding, due to effects such as steric hindrance. Such molecules would be revealed by antibodies when the steric hindrance is eliminated by treatments that change the neuronal surface profoundly. To test this, we subjected the neurons to treatments that modify the membrane proteins (aldehyde treatment), or that remove glycan chains (chondroitinase ABC). We found that such treatments cause no changes in TNR epitope availability (Supplementary Fig. 10a). A third potential source of new TNR epitopes is the proteolytic cleavage of pre-existing surface TNR molecules or their binding partners, which would reduce steric hindrance and make TNR epitopes available for antibody binding. We found no evidence for this, since the TNR epitopes appeared in the same fashion after blocking the activity of matrix metalloproteinases that might cleave existing ECM (Supplementary Fig. 10b).

We therefore conclude that most neurons contain a dynamic pool of TNR molecules, which appear on the surface preferentially near synapses. PNN-containing neurons also exhibit similar TNR dynamics, having higher levels of both total TNR and newly-emerged TNR (albeit somewhat lower ratios of new TNR to total TNR; Supplementary Fig. 11). Moreover, as expected from the limited involvement of astrocytes in TNR endocytosis (Supplementary Fig. 3), we observed ample emergence of new TNR epitopes also in hippocampal neurons that were grown at a large distance above an astrocyte feeder layer (Banker cultures[26]; Supplementary Fig. 12).

The newly-emerged TNR epitopes recycle over 3 days in culture. We imaged these epitopes in living cells, and found that after surfacing they are endocytosed on a time scale of hours (Fig. 4a). To visualize the location of the internalized molecules in neurites, we allowed endocytosis to proceed for several hours, and then eliminated all surface molecules by a proteinase K treatment (Fig. 4b). We found internalized TNR to be present not only in the cell body (where it is prominent, Fig. 4a), but also in both axons and dendrites (Fig. 4b). To then verify whether these molecules resurface, we designed an assay in which we tested the amounts of antibody-labeled TNR present on the surface at different timepoints (Fig. 4c). Immediately after antibody labeling of TNR, the antibodies are found mostly on the surface, as expected, and neurites are fully visible. A day or two later, the antibodies are no longer on the surface, as they have been endocytosed, and, since many of the organelles have already reached the cell body (Fig. 4a), neurites are virtually invisible. Remarkably, this situation changes at 3 days after labeling, and a high proportion of the antibodies are again on the surface, especially in neurites (Fig. 4c). These antibodies are later again endocytosed, and will return to the surface over 3 days (Fig. 4c).

To verify the recycling assay, we also targeted Syt1, as a molecule that is known to recycle, and the EGF receptor, as a molecule that is endocytosed, but does not recycle readily. Both molecules were on the surface at "time 0", and were endocytosed after 15 min. A proportion of the Syt1 molecules returned to the surface after another 45 min, while no EGF receptors returned (Supplementary Fig. 13).

This assay therefore suggests that TNR molecules endocytose and are then repeatedly recycled. Importantly, this conclusion is independent of any problems with, for example, antibodies leaving their epitopes. Random un-binding of blocking antibodies

would allow fluorophore-conjugated TNR antibodies to take their place, therefore resulting in immobile, non-dynamic spots on the surface. The un-binding of fluorophore-conjugated TNR antibodies would simply make the respective TNR molecules invisible. Therefore, none of these scenarios would report either endocytosis or recycling of TNR, implying that our interpretation is independent of such problems (which anyway appear to be negligible, Supplementary Figs. 8–10).

However, a more significant problem is that antibodies may cross-link the TNR molecules, and may thereby change their behavior. To control for this, we repeated our key experiments using monovalent Fab fragments. They could be successfully used for our 'blocking-labeling' assay (Supplementary Fig. 14a–d), and showed the recycling of TNR in the same fashion as the antibodies (Supplementary Fig. 14e). The use of Fab fragments also enabled a more elaborate labeling experiment, based on the detection of Fab fragments with unconjugated or fluorophore-conjugated anti-mouse nanobodies (Fig. 5a). This strategy only reveals TNR epitopes that have completed an entire cycle of endocytosis and resurfacing, and again showed ample signals at ~3 days after the initiation of the experiment (Fig. 5b).

To verify this important conclusion by an experiment not involving the live application of affinity tags, like antibodies or Fab fragments, we turned to the use of purified, recombinant TNR containing a His-tag. Exogenous TNR applied to the culture medium has been previously demonstrated to integrate into the ECM and promote assembly of aggrecan in PNNs[27]. Recombinant TNR was identified, at any desired timepoint, by immunostaining for the His-tag. The recombinant TNR incorporated well into the cultures, as expected, and was more prominently seen on PNN-exhibiting cells, again as expected (Fig. 5c). We then analyzed its location over time. Immediately after application it was found mostly on the cell surface, and it was mostly internalized after 1 day in culture. The recombinant TNR returned to the cell surface after 3 days, in the same fashion as we observed for the experiments involving antibodies or Fab fragments (Fig. 5d, e).

We therefore conclude that a dynamic population of TNR molecules surfaces regularly, preferentially near synapses, and is then endocytosed and recycled over the course of a few days.

Endocytosed TNR molecules reach the Golgi apparatus. To first validate the endocytosis of TNR molecules, we marked the newly-emerged TNR molecules using fluorescently-conjugated antibodies, we allowed them to endocytose, and we then applied LysoTracker to the neurons, which labels virtually all acidic organelles of the neurons, including synaptic vesicles[28]. In the live cells, we observed that ~70% of the TNR spots colocalized with the organelle marker, which provides ample evidence that these molecules had been endocytosed (Fig. 6a).

To identify the compartments to which the TNR molecules were internalized, we immunostained the cells for an assortment of intracellular targets, and searched for a colocalization with internalized TNR (Fig. 6b–g). We observed that only a small quantity of TNR molecules was found in Rab5-positive early endosomes and Rab7- or Rab11-positive late or recycling endosomes (Fig. 6g). This, however, does not demonstrate that these organelles do not participate in TNR dynamics, since their slow recycling kinetics (days) implies that only a handful of molecules will be found, at any given time, in compartments involved in rapid molecule sorting, as these endosomes. More importantly, we found that a significant number of molecules colocalized with the Golgi apparatus, including dendritic Golgi outposts (Fig. 6e, h), and with the endoplasmic reticulum (ER). A

64
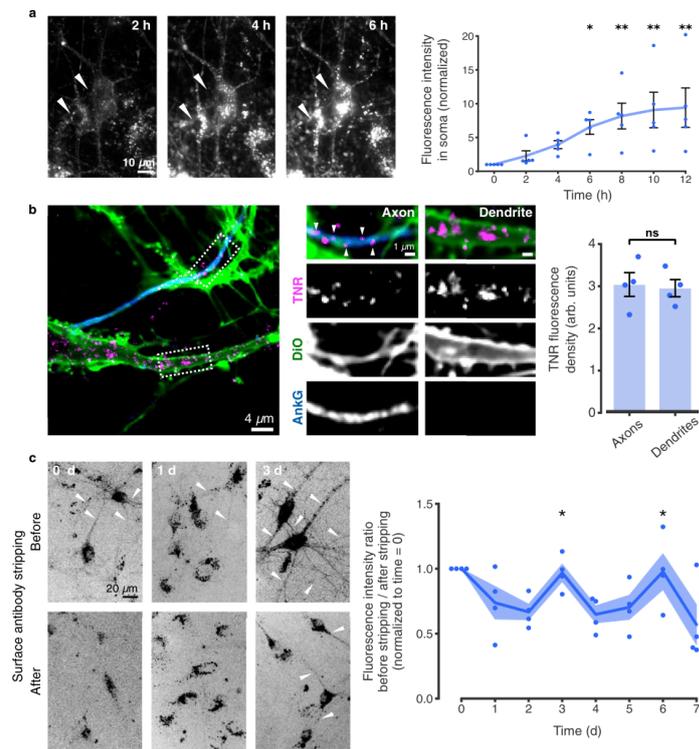
Fig. 4 Dynamic TNR molecules are endocytosed in neurons over hours, and recycle with a periodicity of ~3 days. a Newly-emerged TNR epitopes were labeled 4 h post-blocking, and monitored by live epifluorescence imaging. Arrowheads indicate neuronal somas. Scale bar = 10 μm. Quantification of the intensity in somas (normalized to t_0 timepoint) indicates significant internalization. N = 5 independent experiments, 1-4 neurons per datapoint. Friedman test ($\chi^2_6 = 25.46$, ***$p < 0.001$), followed by two-sided Dunn's multiple comparisons test ('6 h': *$p = 0.033$; '8 h': **$p = 0.005$; '10 h': **$p = 0.005$; '12 h': **$p = 0.002$). Data represent mean ± SEM, dots indicate individual experiments. **b** Internalized TNR in axons vs. dendrites. Epitopes were allowed to internalize for 12 h, followed by surface stripping with proteinase K. The remaining signal was imaged with confocal microscopy in neurites visualized using DiO (green), with axons identified by immunostaining AnkyrinG (blue). Scale bar = 4 μm (1 μm zoom). Quantification of the signal density reveals no differences between dendrites and axons. N = 4 experiments, ≥10 neurons per datapoint. Two-sided paired *t*-test (t = 0.741, p = 0.513). Data represent mean ± SEM, dots indicate individual experiments. **c** Newly-emerged TNR epitopes were labeled 6 h post-blocking. The fraction present on the surface of neurites was measured at different intervals by imaging neurons in epifluorescence before and after stripping with proteinase K. Quantification of the fluorescence ratio before/after stripping (normalized to the '0d' timepoint) reveals peaks of TNR resurfacing at 3 and 6 days post-labeling (~3 day periodicity). Amounts stripped at '3d' and '6d' are significantly higher than at '1d' and '2d', or '5d' and '7d'. N = 4 independent experiments, 5 before/after images per datapoint. Kruskal-Wallis followed by Fisher's LSD (Days 2, 3, 4: $H_2 = 8.29$, *$p = 0.016$, '3d'/'2d': *$p = 0.046$; '3d'/'4d': **$p = 0.005$; Days 4, 5, 6: $H_2 = 6.74$, *$p = 0.036$, '6d'/'5d': *$p = 0.022$, '6d'/'7d': *$p = 0.028$). Scale bar = 20 μm. Data represent the mean (lines) ± SEM (shaded regions); dots indicate individual experiments. Source data are provided in Source Data file.

proportion of the TNR molecules could also be found in lysosomes, pointing to some degree of degradation. These observations also explain why a measurable proportion of TNR spots are not found in acidified organelles, since the ER tubules have a neutral pH.

To further verify that TNR molecules rely on intracellular trafficking for their recycling pathway, we blocked dynamin, which is thought to be involved in most endocytosis reactions, and we also perturbed cellular trafficking with monensin or brefeldin. Dynamin inhibition with Dyngo reduced substantially TNR endocytosis (Supplementary Fig. 15a). Monensin and brefeldin also reduced the appearance of newly-emerged TNR epitopes (Supplementary Fig. 15b). Inhibition of dynamin could

also be demonstrated to prevent the recycling of TNR (Supplementary Fig. 15c). Moreover, the involvement of dynamin in TNR dynamics could be verified by a dynamin knock-down (Supplementary Fig. 15d–g). Finally, dynamin could be co-immunoprecipitated from synaptosomal material together with TNR (Supplementary Fig. 15h), suggesting that the two molecules interact either directly or indirectly, thereby implying again that TNR spends a substantial proportion of its lifetime in intracellular compartments that rely on dynamin function.

Integrins are involved in TNR recycling. In addition to operating as a scaffold, the ECM actively regulates neuronal function
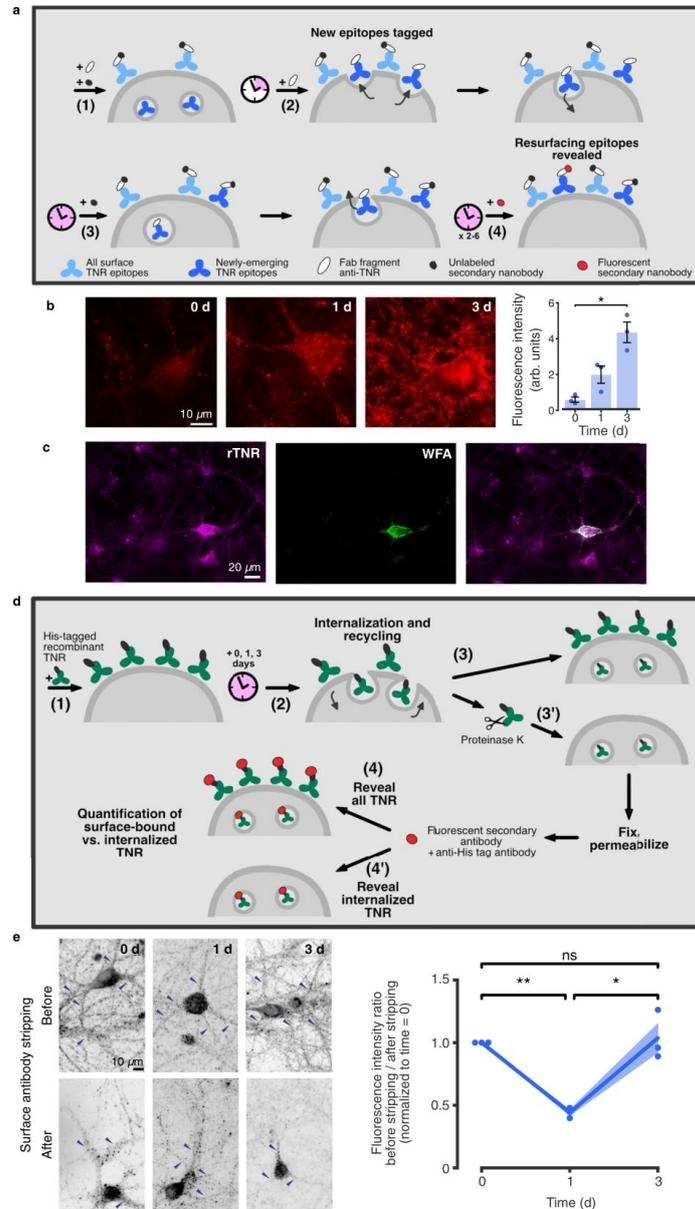
by interacting with ECM receptors on the plasma membrane, such as the integrins, which link the ECM to the cell cytoskeleton[29]. A class of integrin receptors containing the β1 subunit has been shown to functionally interact with TNR[30] and to be particularly enriched at hippocampal synapses, where they mediate outcomes on dendritic spine motility and LTP development[31]. Since the endocytosis and recycling of integrins

are well-established phenomena[32], we wondered whether the trafficking of the recycling TNR pool might be related to β1-integrins.

We examined the colocalization of TNR with β1-integrin at two stages of its recycling pathway, by labeling surface-bound β1-integrins together with the newly-emerged TNR epitopes (Fig. 7a, b). We found that the recycling TNR molecules often colocalized

66

Fig. 5 The 3 day-long recycling observed by labeling with Fab fragments or His-tagged TNR. a Assay to label molecules completing a full endocytosis/resurfacing cycle. (1) Surface TNR epitopes are blocked with TNR Fab fragments and non-fluorescent secondary nanobodies. (2) 4 h later, newly-emerged epitopes are tagged with new Fab fragments, without secondary nanobodies. (3) Following a 12-h incubation, allowing for internalization, newly-emerged epitopes remaining at the surface are blocked with non-fluorescent nanobodies. (4) Immediately afterwards, or 1–3 days later, the newly-emerged and then internalized epitopes that resurfaced are revealed with fluorophore-conjugated secondary nanobodies. **b** Neurons were imaged in epifluorescence microscopy. Substantial fluorescence is visile at both the 1- and 3-day time points. $N = 3$ independent experiments, $\geq$15 neurons per datapoint. Kruskal-Wallis ($H_2 = 7.2$, $^*p = 0.0273$), followed by two-sided Dunn's multiple comparisons test: '0 d'/'3 d': $^*p = 0.0199$. Scale bar = 10 μm. Data represent mean ± SEM, dots indicate individual experiments. **c–e** Recycling of recombinant His-tagged TNR (rTNR). **c** rTNR distributes similarly to endogenous TNR, after pulsing neurons with rTNR for 1 h and staining with WFA to label PNNs (epifluorescence). Scale bar = 20 μm. $N = 3$ independent experiments. **d** rTNR recycling assay: (1) Neurons were pulsed with rTNR for 1 h, and then incubated for 0–3 days, allowing for internalization and recycling (2). Neurons were fixed immediately (3), or first incubated with proteinase K to remove surface-bound rTNR (3'). Neurons were permeabilized and immunostained with anti-His tag antibodies to reveal all rTNR (4), or internalized rTNR (4'). **e** At time = 0, rTNR staining was strongly reduced by stripping. At 1d, similar staining was observed in stripped/non-stripped cultures. At 3d, staining was again reduced after stripping. Scale bar = 10 μm. $N = 3$ independent experiments, 5 before/after images per datapoint. Repeated-measures one-way ANOVA ($F_{1.044, 2.088} = 28,6$, $^*p = 0.03$), followed by Fisher's LSD ('0 d'/'1 d': $^{**}p = 0.002$; '1 d'/'3 d': $^*p = 0.027$; '0 d'/'3 d': $p = 0.775$). Data represent mean (lines) ± SEM (shaded regions), dots indicate individual experiments. Source data are provided in Source Data file.

with surface-bound β1-integrins immediately after their emergence, as well as with internalized β1-integrins 12 h later (Fig. 7a, b). This implies that TNR recycling relies on organelles involved in β1-integrin dynamics. To verify this hypothesis in a more direct fashion, we used an antibody that blocks β1-integrin[33]. This reduced profoundly the TNR internalization (Fig. 7c), suggesting that this molecule indeed serves as a receptor involved in the recycling of TNR-containing ECM.

The purpose of TNR recycling may be to renew the glycosylation of these molecules. While recycling processes through different endosomal systems are well understood, and have long been discussed in synapses[13,34], TNR recycling through the Golgi/ER appears rather unusual. Such a pathway would be needed, however, if the surface-exposed TNR molecules suffer modifications to their sugar moieties, and therefore require re-glycosylation, and/or a specific glycosylation pattern is needed to recycle perisynaptic TNR. This type of Golgi/ER recycling and re-glycosylation pathway has been less investigated than many other trafficking reactions, but has been demonstrated for several cell surface glycoproteins, especially in liver cells[35]. To test whether TNR follows such a pathway, we labeled newly O-glycosylated proteins by feeding the neurons with azide-modified galactosamine (GalNAz) and glucosamine (GlcNAz), which were then revealed by tagging with a fluorophore, using a click chemistry reaction[36]. We found that the recycling TNR pool colocalized to a significant extent with GalNAz, and less with GlcNAz (Fig. 8). This in agreement with previous studies that showed that GalNAc (but not GlcNAc) is a dominant component of O-linked glycosylations on TNR[37–39]. As a control, we performed the same experiment by feeding the neurons with the methionine analog azidohomoalanine (AHA), which incorporates into de novo synthesized proteins and is then similarly tagged using click chemistry[40], and we found little colocalization between TNR and AHA (Fig. 8), in agreement with the expectation that this is a very long-lived protein[3].

The resolution of the imaging approach we used (two-color STED microscopy) is insufficient to demonstrate whether the recycling TNR molecules are themselves newly glycosylated, or whether their presence in the ER/Golgi compartments simply places them near newly-glycosylated proteins, resulting in the colocalization we measured optically. However, if the latter were true, the TNR molecules would also colocalize with newly-secreted proteins (labeled by AHA), which are abundant in the ER/Golgi compartments. As this was not the case, the overall interpretation of these experiments is that the recycling pool of TNRs consists of molecules that are not metabolically young, and

that their trafficking to the ER/Golgi might function as means of re-glycosylation.

Perturbing newly-emerged TNR epitopes blocks synaptic function and modifies synaptic structure. To test whether the dynamic pool of TNR is relevant for synaptic transmission, we performed a crude experiment in which these molecules were bound by large aggregates of antibodies[41], and we then analyzed synaptic vesicle exo-/endocytosis. In brief, we tagged the newly-emerged TNR epitopes with biotin-coupled antibodies (Fig. 9a). These were then immediately bound by large aggregates formed by goat anti-biotin antibodies and donkey anti-goat antibodies (Fig. 9b, c). In principle, such aggregates should block TNR endocytosis, and should perturb severely the bound molecules (Fig. 9a). We then stimulated the synapses in the presence of Syt1 antibodies (as used in Fig. 3), to determine the overall degrees of exo-/endocytosis. Adding the antibody aggregates for just 30 min eliminated presynaptic vesicle release in response to stimulation (Fig. 9d, e). This was only true for the newly-emerged TNR epitopes, as the antibody aggregates had no effect when they were bound specifically to the surface-resident, non-recycling TNR epitopes (Fig. 9e).

The elimination of stimulation-induced vesicle release that we observed was not due to perturbing Ca^{2+} influx in synapses, since the stimulus-induced rise in intracellular Ca^{2+} was not affected by the treatment (Supplementary Fig. 16), which leaves the mechanism linking synaptic vesicle dynamics to TNR open. Hypotheses involving the interactions between TNR, integrins and the presynaptic active zone could be verified in the future[42,43], including the possibility of multipartite interactions between synaptic vesicle proteins, integrins, laminins and TNR[44,45]. An additional perturbation of neuronal activity became evident when we examined the spontaneous Ca^{2+} activity in the absence of stimulation. The addition of antibody aggregates raised substantially the spontaneous firing rates (Supplementary Fig. 16), despite the inhibition of vesicular trafficking. As TNR has previously been shown to interact with voltage-gated Na^+ channels (Na_vs)[46], this effect may be due to the TNR perturbation affecting Na_v activity, which may, in turn, increase the excitability of the neurons.

To also analyze the effects of these aggregates on structural changes in synapses, we applied them for 12 h, and we then analyzed spine morphology both in dissociated cultures and in organotypic slices (Fig. 9f, g). A significant reduction of spine head sizes was observed both in culture and in slices. As spine head size is an important reporter for synaptic strength[24], this implies that TNR dynamics are closely linked
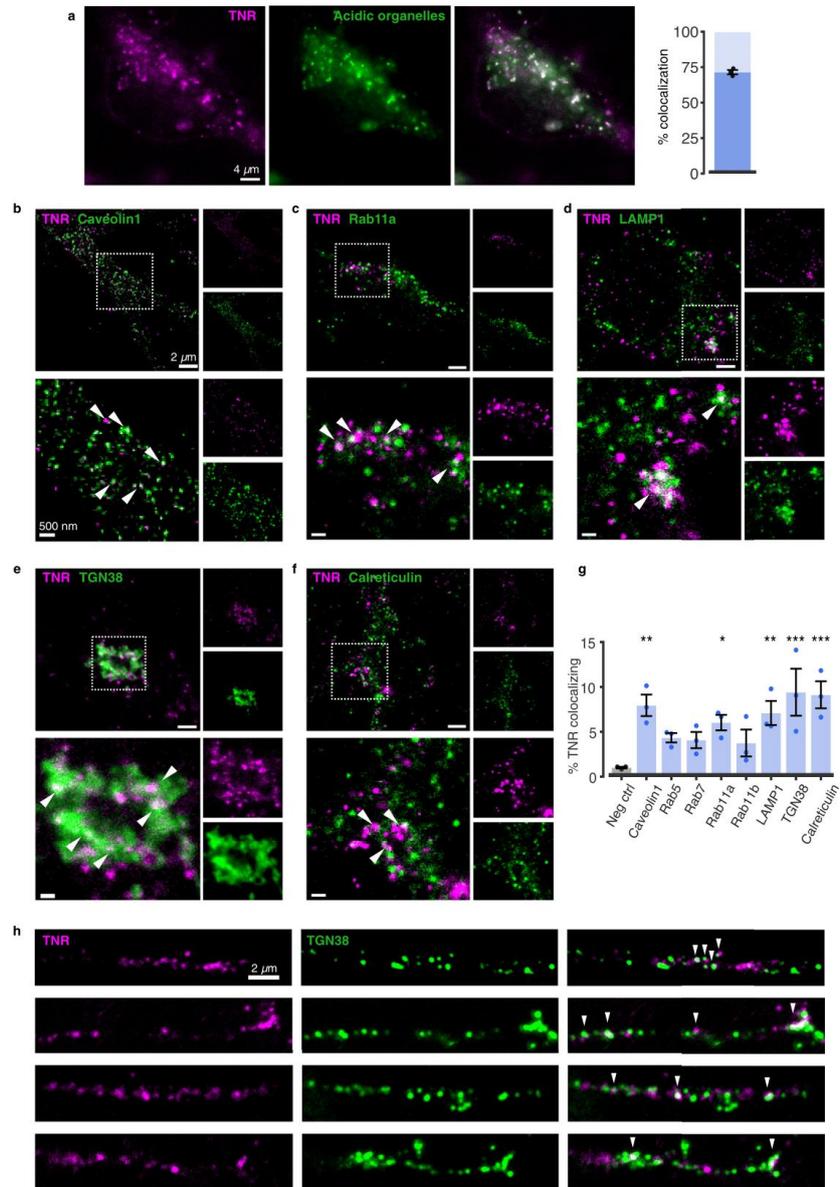
to synaptic plasticity. Importantly, the antibody aggregates had no effect when they were bound to the surface-resident, non-recycling TNR epitopes, as also observed above for the presynaptic dynamics.

At the moment it is difficult to pursue the mechanisms behind this type of manipulation further, without a major effort in developing new tools for interference with TNR recycling. Newly-emerged TNR integrates into the ECM at synapses, along with older TNR molecules (Supplementary Fig. 17), and its localization does not suggest a special positioning within synapses, which could be used to derive interpretations on its function relating to synapse activity and plasticity.

Fig. 6 An overview of organelles involved in the trafficking of newly-emerged TNR epitopes. a Newly-emerged TNR epitopes were labeled 12 h post-blocking, concurrently with the application of LysoTracker™ Green, to label acidic organelles. After a 6-h incubation, allowing for internalization, surface TNR was stripped with proteinase K. Neurons were imaged live (epifluorescence). Scale bar = 4 μm. >70% of internalized TNR is present in acidic organelles. N = 3 independent experiments, ≥4 neurons per datapoint. Data represent mean ± SEM, dot indicate individual experiments. **b–g** To identify the compartments containing internalized TNR, newly-emerged TNR epitopes were labeled 12 h post-blocking and allowed to internalize for 6 h, after which remaining surface-bound TNR was stripped with proteinase K. The neurons were fixed and immunostained with organelle markers. Shown are 2-color-STED images of TNR (magenta) and organelle markers (green): caveolin1, Rab11a (recycling endosomes), LAMP1 (lysosomes), TGN38 (trans-Golgi network) and calreticulin (ER). The right side of each panel shows zoomed views of the dashed boxes. Arrowheads indicate colocalizing signals. Scale bar = 2 μm (full images), 500 nm (zoomed images). **g** Quantification of % TNR spots colocalizing with organelle markers, compared to a negative control (using non-specific primary antibodies). TNR colocalizes significantly with ER, TGN, LAMP1, Rab11a and caveolin. N = 3 independent experiments, ≥10 neurons per datapoint. One-way ANOVA ($F_{8,18} = 4.284$, **$p = 0.005$), followed by Fisher's LSD to compare all markers with 'neg ctrl' (Caveolin1: **$p = 0.002$; Rab5: $p = 0.099$; Rab7: $p = 0.126$; Rab11a: *$p = 0.017$; Rab11b: $p = 0.169$; LAMP1: **$p = 0.005$; TGN38: ***$p < 0.001$; Calreticulin: ***$p < 0.001$). Data represent mean ± SEM, dots indicate individual experiments. **h** A fraction of newly-emerged TNR localizes to dendritic Golgi outposts following endocytosis. Newly-emerged TNR epitopes (magenta) were labeled 4 h post-blocking, and allowed to internalize over 12 h. The neurons were fixed and immunostained with TGN38 to identify dendritic Golgi outposts[78,79]. Representative images, taken with confocal microscopy, are shown. Arrowheads indicate colocalizing signals. Scale bar = 2 μm. N = 4 independent experiments. Source data are provided in Source Data file.

TNR dynamics are also observed in organotypic and in acute hippocampal slices. Having already observed that TNR manipulations affect synapse structure in cultured organotypic slices (Fig. 9g), we turned to testing the 'blocking-labeling' assay in this model. We observed a similar behavior to the dissociated cultures (Supplementary Fig. 18a). The slices showed higher levels of newly-emerged epitopes after activation by the addition of bicuculline, and lower levels after silencing via CNQX and AP5 (Supplementary Fig. 18b), as observed in Fig. 2 for the dissociated cultures. Moreover, the application of recombinant, His-tagged TNR resulted in ample endocytosis, which was stimulated by bicuculline (Supplementary Fig. 18c).

To come closer to the in vivo situation, we first verified whether substantial TNR amounts could be found within the cell bodies of neurons in the hippocampi of adult mice. This could be indeed observed, using conventional immunostaining techniques (Fig. 10a). Moreover, intracellular TNR was subject to changes according to the functional state of the neurons. To increase the activity rate of the neurons, they were stimulated by in vivo kainic acid administration, in what constitutes a well-studied mouse model of epilepsy[47]. This enhanced the levels of intracellular somatic TNR, while leaving TNR unaffected in other locations (Fig. 10a). Finally, the accumulation of intracellular somatic TNR was not simply an effect of neuronal damage, since a mouse model in which neuronal damage is prominent (5xFAD mice as a model of familial Alzheimer disease), showed no effects on intracellular TNR accumulation (Fig. 10b).

Second, we turned to the question of whether the intracellular TNR molecules are newly synthesized, or are older molecules that the cells have endocytosed from the ECM. To analyze this, we used a technique we introduced in the past, correlated optical and isotopic nanoscopy (COIN[48]). Wild-type mice were pulsed with the essential amino acid lysine containing 6 stable ^{13}C isotopes, for 14 or 21 days, and hippocampal slices were then immunostained, as above. After imaging the slices, we analyzed them using nanoscale secondary ion mass spectrometry (nanoSIMS). In nanoSIMS a primary Cs$^+$ beam irradiates the sample and causes the sputtering of secondary particles from the sample surface. These particles are partly ionized and are then identified by mass spectrometry. This reveals the ^{13}C isotopes, and enables us to test whether the TNR-containing spots consisted of newly-synthesized proteins (i.e. rich in ^{13}C isotopes), or whether they contained older proteins (lacking ^{13}C isotopes; Fig. 10c, d). We found intracellular TNR objects were substantially older than the rest of the cell (Fig. 10e). This implies that they are not newly synthesized, and therefore need to be molecules that the cell has endocytosed from the ECM, in line with our model.

Third, we also sought to verify that acute slices from adult mice can internalize TNR, and that increased neuronal activity enhances TNR internalization. To test this, we applied the His-tagged version of TNR to the slices, and followed its internalization by fluorescence imaging (Supplementary Fig. 19). His-tagged TNR was indeed taken up by the cells, and its uptake was enhanced by stimulation of neuronal activity with bicuculline (Supplementary Fig. 19).

We conclude that our model of TNR recycling is plausible both in brain slices and in vivo.

Other ECM molecules also show similar dynamics to TNR. To test whether our observations extend to other ECM molecules, we used the 'blocking-labeling' assay to assess neurocan, chondroitin-sulfate (CS)-bearing proteoglycans (predominantly aggrecan) labeled by *Wisteria floribunda* agglutin (WFA), and hyaluronic acid (HA)[10]. In a similar fashion to TNR, we observed that the amount of newly-emerged epitopes was far larger than would be predicted from their exceptionally long half-lives[2,3], and that the epitope emergence increased after culture activation using bicuculline (Supplementary Fig. 20a–c).

To verify the turnover dynamics of the ECM by a completely different approach, we used a fluorescence recovery after photo-bleaching (FRAP)-based assay to observe the hyaluronan-binding protein HAPLN1, which is substantially easier to express and monitor than all other molecules tested here (Supplementary Fig. 20d–f, Supplementary Movie 1). HAPLN1 dynamics were far higher than expected according to its lifetime[2,3] and were also significantly faster in synaptic regions, supporting our previous observations for TNR. Moreover, organelle transport of HAPLN1 appeared to take place, as observed in long-term imaging of HALPN1-expressing cultures (Supplementary Movie 1).

While these last experiments do not constitute a direct proof of endocytosis or recycling for these ECM molecules, they complement the more direct assays used for TNR, and suggest that the potential for remodeling by recycling should be analyzed for these molecules as well.

Discussion

ECM remodeling in the adult brain is thought to occur in sparse, isolated events that take a high metabolic toll on the cells. Based on the current dogma, existing ECM structures are cleaved by secreted matrix proteases to enable synaptic remodeling, and are then re-stabilized by the addition of freshly-synthesized proteins[9,10]. Indeed, numerous studies have demonstrated that synaptic plasticity events (*e.g.* learning) can induce the release of ECM-cleaving enzymes, and
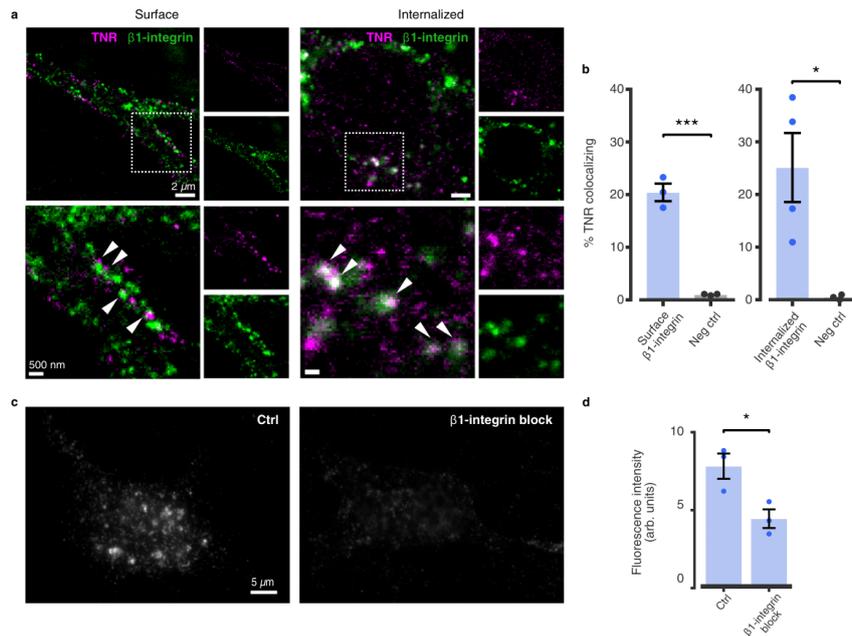
Fig. 7 TNR recycling is mediated by integrins. a, b Assessment of colocalization between recycling TNR molecules and β1-integrin. **a** Left: newly-emerged TNR epitopes were labeled 12 h post-blocking concurrently with a labeling of surface-bound β1-integrins, by applying fluorophore-conjugated antibodies directed against the extracellular domain of the receptors. The neurons were fixed and imaged with 2-color-STED. Right: newly-emerged TNR epitopes were labeled 4 h post-blocking, concurrently with β1-integrin. Neurons were incubated a further 12 h to allow for internalization, and remaining surface-bound molecules were stripped with proteinase K. The neurons were fixed and imaged with confocal microscopy. Images on the right of each panel show zoomed views of the dashed boxed. Scale bars = 2 μm (full images), 500 nm (zoomed images). **b** Quantification of % colocalizing TNR signal (for **a**) shows newly-emerged TNR epitopes colocalize with both cell surface-bound and internalized β1-integrins. The values are significantly higher than negatives controls, relying on non-specific primary antibodies. Controls were imaged in STED/confocal for comparison to images in the left/right panels, respectively. $N = 3$ ('surface β1-integrin' experiments and negative controls), and 4 ('internalized β1-integrin') independent experiments, ≥10 neurons per datapoint. Two-sided Student's t-test ('surface integrin' vs. 'neg ctrl': t = 11.61, ***$p = 0.0003$; 'internalized integrin' vs. 'neg ctrl': $t = 3.177$, *$p = 0.025$. Data represent mean ± SEM, dots indicate individual experiments. **c** To assess whether β1-integrin receptors are required for TNR endocytosis, newly-emerged TNR epitopes were labeled 12 h post-blocking, after which the neurons were immediately incubated with function-blocking anti-β1-integrin antibodies[33] for 6 h. Neurons were then incubated with proteinase K, to remove remaining surface-bound TNR, and imaged with epifluorescence microscopy. A reduction in fluorescence signal is evident in integrin-blocked cultures. Scale bar = 5 μm. **d** Quantification of the fluorescence intensity confirms that the amount of internalized TNR is significantly reduced following the blocking of β1-integrin receptors. $N = 3$ independent experiments, ≥15 neurons per datapoint. Two-sided Student's t-test ($t = 3.343$, *$p = 0.029$). Data represent mean ± SEM, dots indicate individual experiments. Source data are provided in Source Data file.

result in a transient upregulation of ECM protein synthesis[49–51]. While this notion of ECM remodeling can account for infrequent events such as synaptic plasticity, it is at odds with the observation that synaptic morphology changes continually, even at rest. For example, long-term imaging of synapses in slices of rat hippocampi revealed that dendritic spines continue to be generated and eliminated, and undergo significant volume changes, even when synaptic plasticity is suppressed[52]. Such severe changes to synapses are likely to necessitate the reorganization of peri-synaptic ECM[6–8,53–55]. We would therefore expect that ECM remodeling does not solely occur during infrequent plasticity events[56], but is rather a constitutive process in the brain. In this case, the components of the peri-synaptic ECM would need to turn over frequently, at a significantly higher rate than would be expected from their extremely long lifetimes[2,3]. The discrepancy between the high frequency of remodeling events and the slow rate of ECM protein synthesis can be reconciled by the

existence of a mobile, recycling pool of ECM molecules that can be continually incorporated and re-internalized at synapses, without the need for novel protein secretion, as we found here.

Overall, our results demonstrate that the neural ECM is significantly more plastic than previously assumed. As this mechanism may not be limited to TNR, our observations open a new field of investigation that should prove important in understanding not only ECM regulation in the brain, but also brain plasticity and stability in general. Finally, as ECM changes are known to accompany a plethora of brain diseases, these findings should also prove relevant for clinical research in the future.

Methods

70
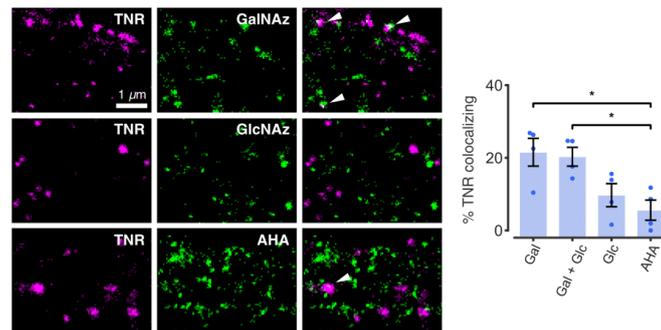
Fig. 8 TNR recycling possibly relates to TNR re-glycosylation. Newly O-glycosylated proteins were labeled by feeding neurons with azide-modified galactosamine (GalNAz) and/or glucosamine (GlcNAz), which were then revealed by click chemistry. Alternatively, newly-synthesized proteins were labeled by feeding neurons with azidohomoalanine (AHA), which was also tagged using click chemistry. Newly-emerged TNR epitopes were labeled 6 h post-blocking and visualized at the surface. The neurons were imaged with 2-color-STED. Scale bar = 1 μm. Quantification of the colocalization of the signals confirmed that internalized TNR epitopes colocalize significantly with GalNAz or GalNAz+GlcNAz, at levels substantially higher than the minimal AHA colocalization, which is not significantly different from negative controls (relying on non-specific primary antibodies). N = 4 independent experiments, ≥10 neurons per datapoint. Kruskal-Wallis test (H_3 = 9.022, *p = 0.029), followed by two-sided Fisher's LSD (*p = 0.014 and *p = 0.021 for 'GalNAz' and 'GalNAz+GlcNAz' respectively). Data represent mean ± SEM, dots indicate individual experiments. Source data are provided in Source Data file.

Animals. All animals were handled according to the specifications of the University of Göttingen or DZNE Magdeburg and of the local authorities, the State of Lower Saxony (Landesamt für Verbraucherschutz, LAVES, Braunschweig, Germany) and State of Saxony-Anhalt (Landeswervaltungsamt, Halle, Germany). All animal experiments and tissue collection were performed in accordance with the European Communities Council Directive (2010/63/EU) and approved by the local authority, the Lower Saxony State Office for Consumer Protection and Food Safety (Niedersächsisches Landesamt für Verbraucherschutz und Lebensmittelsicherheit) or by the Ethical Committee on Animal Health and Care and the local authority of the State of Saxony-Anhalt, Germany (license numbers: 42502-2-1316 DZNE and 42502-2-1322 DZNE).

Preparation of rat dissociated hippocampal cultures. Dissociated primary hippocampal cultures were prepared from newborn rats (*Rattus norvegicus*) as previously described[26,57]. Briefly, hippocampi of newborn Wistar rat pups were dissected in HBSS (140 mM NaCl, 5 mM KCl, 6 mM glucose, 4 mM NaHCO₃, 0.3 mM Na₂HPO₄ and 0.4 mM KH₂PO₄) and incubated for one hour in enzyme solution (DMEM containing 0.5 mg/mL cysteine, 100 mM CaCl₂, 50 mM EDTA and 2.5 U/mL papain, bubbled with carbogen for 10 min). Dissected hippocampi were then incubated for 15 min in a deactivating solution (DMEM containing 0.2 mg/mL bovine serum albumin, 0.2 mg/mL trypsin inhibitor and 5% fetal calf serum). The cells were triturated and seeded on circular glass coverslips (18 mm diameter) at a density of ~ 80,000 cells per coverslip. Before seeding, the coverslips were treated with nitric acid, sterilized, and coated overnight with 1 mg/mL poly-L-lysine. The neurons were allowed to adhere to the coverslips for 1–4 h at 37 °C in plating medium (DMEM containing 3.3 mM glucose, 2 mM glutamine, and 10% horse serum), after which they were switched to Neurobasal-A medium (Life Technologies, Carlsbad, CA, USA) containing 2% B27 (Gibco, Thermo Fisher Scientific, USA) supplement, 1% GlutaMax (Gibco, Thermo Fisher Scientific, USA) and 0.2% penicillin/streptomycin mixture (Biozym Scientific, Germany). The cultures were maintained in a cell incubator at 37 °C, and 5% CO₂ for 14–16 days before use, and the culture medium was replaced at most once per week, if the pH indicator suggested a loss of medium quality. Percentages represent volume/volume.

Preparation of organotypic hippocampal slice cultures. Organotypic hippocampal slice cultures were prepared as previously described[58], with the modifications described in[59]. In brief, hippocampi of postnatal day 3 (P3) C57BL/6 J mice (*Mus musculus*) were isolated, and 300-μm thick transverse slices were cut and placed on support membranes (Millicell-CM Inserts, PICMORG50; Millipore). The surface of the slices was covered with culture medium consisting of 50% MEM with Earle's salts (#M4655; Merck, Germany), 25 mM HEPES, 6.5 mg/ml glucose, 25% horse serum, 25% Hanks solution buffered with 5 mM Tris and 4 mM NaHCO₃, pH 7.3. The slices were maintained in a cell incubator at 37 °C and 5% CO₂ for 14 days before use, and the culture medium was replaced every other day. Percentages represent volume/volume.

Cell-surface biotinylation assay
Biotinylation and glutathione treatment. The assay was adapted from[15]. Briefly, neurons were incubated with 100 μM Leupeptin (#L2884; Merck, Germany-Aldrich,
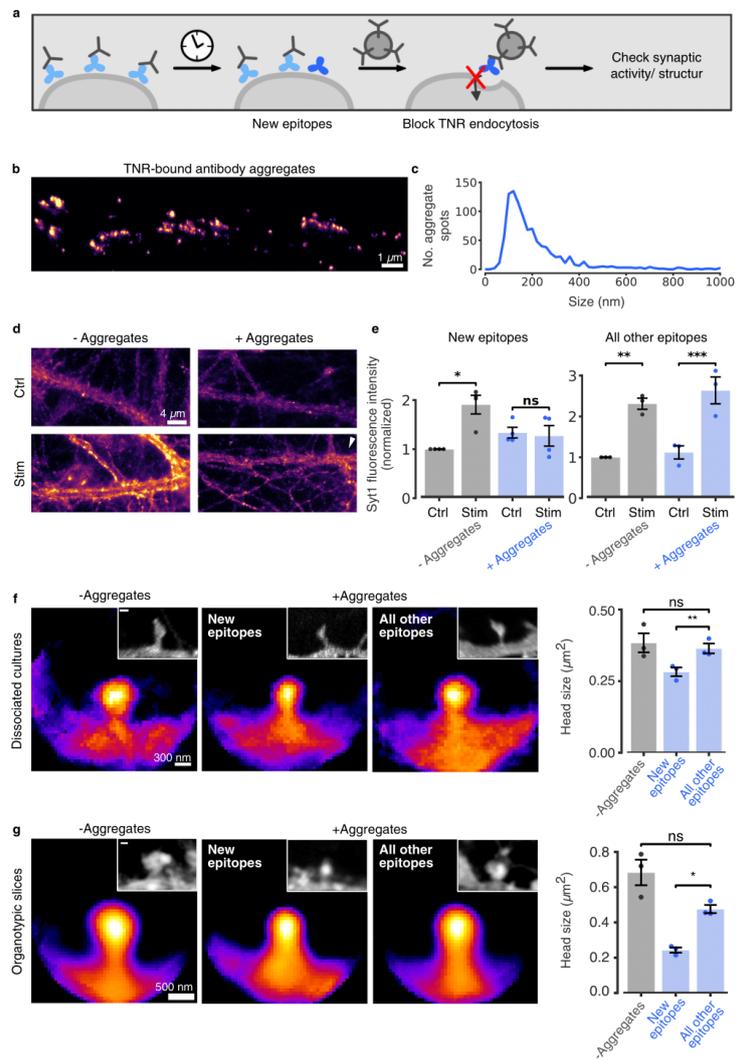
Germany) for 1 h at 37 °C, to inhibit lysosomal protein degradation. Leupeptin was also present in the cell media throughout the remainder of the experiment. The neurons were incubated with 1.5 mg/mL EZ-Link™ Sulfo-NHS-S-S-Biotin (#21331; Thermo Fisher Scientific, USA) in PBS for 30 min at 37 °C. The neurons were subsequently washed in PBS containing 10 mM glycine to quench the unreacted biotin. The neurons were either immediately scraped into lysis buffer, to detect the entire surface pool (50 mM Tris-HCl, 150 mM NaCl, 2 mM EDTA, 0.5% IGEPAL, 0.5% sodium deoxycholate, 0125 mM PMSF protease inhibitor, and 1x protease inhibitor cocktail: #87786; Thermo Fisher Scientific, US), or were returned to their original culture media and incubated at 37 °C, to allow for endocytosis of cell-surface proteins. After a further 6 h, the neurons were incubated with glutathione cleavage buffer containing 50 mM glutathione (#G6013; Merck, Germany), 75 mM NaCl, 10 mM EDTA, 75 mM NaOH and 1% BSA in H₂O, for 20 min at 4 °C. Subsequently, the neurons were either returned to their original cell media supplemented with 10 mM glutathione, or quenched in iodoacetamide buffer containing 50 mM iodoacetamide (#A1666; Applichem GmbH, Germany) and 1% BSA in PBS, for 30 min at 4 °C, and were immediately scraped into lysis buffer, to reveal the endocytosed pool of molecules. The remaining neurons were incubated a further 18 h at 37 °C, to allow for the resurfacing of endocytosed proteins, and were then subjected to a second glutathione cleavage reaction to cleave, the newly-surfacing biotinylated proteins. The neurons were then quenched in iodoacetamide buffer and scraped in lysis buffer, thereby revealing the non-recycling pool.

Precipitation of biotinylated proteins and immunostaining. Biotinylated cell-surface proteins were pulled down with streptavidin-coupled magnetic beads (#11205D; Thermo Fisher Scientific, US). The beads were isolated, were washed, and were then blocked with PBS containing 2.5%, bovine serum albumin (BSA) (A1391-0250; Applichem, Germany) and 0.1% Tween20 (9005-64-5; Merck, Germany) for 1 h. They were then immunostained with 1:500 monoclonal mouse anti-TNR (#217 011; Synaptic Systems, Göttingen, Germany), 1:100 monoclonal mouse anti-Syt1 (#105 311; Synaptic Systems, Göttingen, Germany), 1:100 monoclonal mouse anti-calmodulin (#MA3-917; Thermo Fisher Scientific, US), 10 μg/mL monoclonal mouse anti-LAMP1 (#MA1-164; Thermofisher Scientific, USA) or 1:1000 monoclonal mouse anti-myelin basic protein (#NBP1-05203, Novus Biologicals, Germany), together with 1:100 STAR635P-conjugated anti-mouse secondary nanobodies (NanoTag, Göttingen, Germany), overnight at 4 °C in. The beads were subsequently washed and mounted on glass slides in Mowiol for imaging.

Imaging. Confocal imaging was performed on a Leica TCS SP5 microscope (Leica, Wetzlar, Germany) equipped with an HCX Plan Apochromat 63×1.4 NA oil objective. The 561 nm or 633 nm lines of a Helium-Neon laser were utilized for excitation, using acousto-optic tunable filters to select appropriate emission wavelengths. The images were acquired with photomultiplier tubes. For each channel the pinhole was set to 1 Airy unit.

Blocking-labeling assay and live treatments
TNR blocking-labeling with antibodies. To block surface epitopes of TNR, neurons were incubated with knock-out-validated antibodies[19] (#217 011; clone 619;

71

a

New epitopes   Block TNR endocytosis   Check synaptic activity/ structur

b
TNR-bound antibody aggregates

1 μm

c

No. aggregate spots

Size (nm)

d

-Aggregates   +Aggregates

Ctrl

Stim

4 μm

e

New epitopes   All other epitopes

Syt1 fluorescence intensity (normalized)

*   ns   **   ***

Ctrl Stim Ctrl Stim   Ctrl Stim Ctrl Stim
-Aggregates +Aggregates   -Aggregates +Aggregates

f

Dissociated cultures

-Aggregates   +Aggregates

New epitopes   All other epitopes

300 nm

Head size (μm²)

ns
**

-Aggregates   New epitopes   All other epitopes

g

Organotypic slices

-Aggregates   +Aggregates

New epitopes   All other epitopes

500 nm

Head size (μm²)

ns
*

-Aggregates   New epitopes   All other epitopes

Synaptic Systems, Göttingen, Germany) diluted 1:100 in their own cell media, for 2 h. The neurons were subsequently washed in Tyrode's solution (124 mM NaCl, 30 mM glucose, 25 mM HEPES, 5 mM KCl, 2 mM $CaCl_2$, 1 mM $MgCl_2$, pH 7.4) and returned to their original conditioned media. For labeling of newly-emerged TNR epitopes, neurons were incubated with antibodies conjugated to the fluorescent dye Atto647N, Atto550 or STAR580 (custom-made; clone 619; Synaptic Systems, Göttingen, Germany) diluted 1:500 in their own cell media, for 1 h. The labeling was performed after either 0, 2, 4, 6 or 12 h post-blocking. After labeling, the neurons were fixed either immediately, or after a further incubation of 6 or 12 h, in their original culture media allowing for epitope internalization. In some experiments, the surface-bound antibodies were stripped at the end of the blocking-labeling assay. These details are denoted in the figure legends. For the 2-color STED experiment comparing old and newly-emerged TNR epitopes (Supplementary Fig. 17), the blocking step was performed with STAR580-conjugated TNR antibodies. As a control for unspecific uptake or binding of antibodies, neurons were incubated with 1:500 Atto647N-conjugated goat anti-mouse IgG (#610-156-121 S; Rockland, USA).

Experiments with TNR Fab fragments. The blocking-labeling assay using Fab fragments (Fig. 5a, b and Supplementary Figs. 14 and 18b), surface TNR epitopes were blocked with 10 μg/mL (cultured neurons) or 50 μg/mL (organotypic slices) unlabeled Fab fragments directed against TNR (custom-made from the same TNR antibody used in the rest of the work; Synaptic Systems, Göttingen, Germany), applied together with 1 mg/mL unlabeled FluoTag-X2 anti-mouse secondary nanobody (custom-made; NanoTag, Göttingen, Germany), diluted in their own cell media for 2 h, and newly-emerged TNR epitopes were labeled with 2 μg/mL Fab fragments directed against TNR, applied together with 1:500 FluoTag-X2 STAR635P or STAR580-conjugated anti-mouse secondary nanobodies (#N1202-Ab635P, #N1202-Ab580; NanoTag, Göttingen, Germany).

For the experiment described in Supplementary Fig. 14c, d, newly-emerged epitopes were labeled 12 h post-blocking. The neurons were mounted for live imaging 4 h after labeling, and the Fab fragments bound to surface TNR molecules were stripped by incubation with proteinase K (see 'Surface antibody stripping with proteinase K'). For the experiment described in Supplementary Fig. 14e, newly-emerged TNR epitopes were labeled 4 h post-blocking. The neurons were mounted

Fig. 9 Perturbing the recycling TNR pool modulates synaptic function. a Assay to perturb TNR recycling: newly-emerged TNR epitopes were labeled 12 h post-blocking with biotinylated antibodies, and bound to large aggregates of antibodies. As control, all other epitopes (non-recycling) were labeled. **b** STED images of aggregates. Scale bar = 1 μm. **c** Histogram of aggregate size (FWHM). $N = 4$ independent experiments, 995 aggregates. **d** Neurons were incubated with aggregates for 30 min. Synaptic activity was assessed by uptake of Syt1 antibodies (as in Fig. 3). Without stimulation, Syt1 antibodies detect the surface vesicle population (40–50% of actively-recycling vesicles[20]). Stimulation results in signal increase (exo-/endocytosis of new vesicles) in controls, but not in aggregate-treated cultures (epifluorescence). Scale bar = 4 μm. **e** Quantification of Syt1 fluorescence intensity confirms this observation and indicates that tagging all other epitopes has no effects. $N = 4$ ('new epitopes')/3 ('all other') independent experiments, ≥ 15 neurons per datapoint. Repeated-measures ANOVA on rank ('new epitopes': $F_{1,6} = 12.54$, *$p = 0.012$; 'all other epitopes': $F_{1,4} = 1.5$, $p = 0.288$) for the interaction Stim/ctrl x +/− Aggregates), followed by Sidak's multiple comparisons test ('new epitopes': *$p = 0.02$, $p = 0.419$; 'all other epitopes': **$p = 0.002$, ***$p < 0.001$ for 'stim' vs. 'ctrl' for untreated and treated neurons, respectively). **f, g** Effect of recycling perturbation on synapse structure. Dissociated cultures (**f**) and organotypic hippocampal slices (**g**) were treated with aggregates for 12 h. Plasma membranes were visualized with DiO (**f**) or by infection with AAV9-Syn-eGFP (**g**), in averaged spines or individual examples (insets). Scale bar = 300 nm (**f**), 500 nm (**g**). $N = 3$ independent experiments, >80 (**f**), >60 (**g**) synapses per condition. One-way ANOVA (**f**: $F_{2, 6} = 5.269$, *$p = 0.05$) or repeated-measures one-way ANOVA (**g**: $F_{1.041, 2.083} = 20.76$, *$p = 0.042$), followed by Fisher's LSD (**f**:** $p = 0.005$, $p = 0.418$; **g**: *$p = 0.025$, $p = 0.16$), to compare 'all other epitopes'/'new epitopes' and 'all other epitopes'/'Tyrode', respectively. Data represent mean ± SEM, dots indicate individual experiments (**d–g**). Source data are provided in Source Data file.

for live imaging 1, 2 or 3 days after labeling and the Fab fragments bound to surface TNR molecules were stripped by incubation with proteinase K. For the experiment described in Fig. 5a, b, newly-emerged TNR epitopes were tagged with unlabeled Fab fragments directed against TNR 4 h later post-blocking. The tagged epitopes that remained exposed on the surface 12 h later were blocked by an additional incubation with 1 mg/mL unlabeled FluoTag-X2 anti-mouse secondary nanobodies for 2 h. Subsequently, the remaining Fab-tagged epitopes that had internalized were revealed at the surface with 1:500 STAR635P-conjugated anti-mouse secondary nanobodies immediately after the second blocking step, or following an additional incubation of 1–3 days. To visualize the active synaptic vesicle pool, neurons were incubated with 1:500 polyclonal rabbit antibodies directed against the lumenal domain of Syt1 conjugated to the fluorescent dye Oyster488 (#105 103C2; Synaptic Systems, Göttingen, Germany) during the TNR labeling step.

Additional ECM molecules and integrins. For the experiments with alternative ECM components, surface epitopes were blocked with 1:100 Wisteria floribunda agglutinin WFA (#L8258; Merck, Germany), 1:50 Hyaluronan binding protein HABP (#H0161; Merck, Germany) or 1:100 mouse anti-Neurocan (#N0913; clone 650.24; Merck, Germany) together with 1 mg/mL unlabeled FluoTag-X2 secondary anti-mouse nanobodies (custom-made; NanoTag, Göttingen, Germany). Labeling was performed with 1:500 biotinylated WFA or HABP followed by 1:500 streptavidin-Atto647N (#AD 647-61; ATTO-TEC GmbH, Germany), or 1:500 anti-Neurocan and 1:500 FluoTag-X2 anti-mouse secondary nanobodies conjugated to STAR635P (#N1202-Ab635P; NanoTag, Göttingen, Germany). For experiments with β1-integrin (Fig. 7), its labeling was performed concurrently with TNR labeling (4 or 12 h after the initial TNR surface epitope blocking, as denoted in the figure legend), with 1:250 FITC hamster anti-CD29 (#561796; clone Ha2/5; BD Biosciences, CA, USA) from a 0.5 mg/mL stock solution. The neurons were fixed immediately or after a further incubation of 12 h, followed by surface antibody stripping with proteinase K (see 'Surface antibody stripping with proteinase K'). For the blocking of β1-integrins, the neurons were treated with 1:25 hamster anti-CD29 (#555003; clone Ha2/5; BD Biosciences, CA, USA) immediately after labeling the newly-emerged TNR epitopes, and remained for an additional 6 h.

Live labeling of acidic organelles. To label acidic organelles, LysoTracker™ Green DND-26 (#L7526, Thermofisher Scientific, USA) was added throughout the labeling of the newly-emerged TNR epitopes, at a concentration of 75 nm.

Drug treatments. Unless otherwise specifed, the drug applications in these experiments began after the TNR blocking step and lasted until fixation. To enhance culture activity, the neurons/slices were treated with 40 μM bicuculline (#485-49-4; Merck, Germany) or 0.1% volume/volume DMSO (#67-68-5; Merck, Germany) as a control. To reduce culture activity by inhibiting AMPA and NMDA receptors, neurons were treated with 10 μM CNQX (#0190; Tocris Bioscience, Germany) and 50 μM AP5 (#0106; Tocris Bioscience, Germany). To block the activity of matrix metalloproteinases, neurons were treated with 10 μM GM6001 (#CC1010, Merck, Germany). To digest glycosaminoglycans, neurons were treated with 0.5 units/mL Chondroitinase ABC from *Proteus vulgaris* (#C3667, Merck, Germany) for 30 min following the blocking step. To perturb dynamin-dependent endocytosis, neurons were treated with 30 μM Dyngo® 4a (#ab120689; Abcam, United Kingdom) for 2 h following the labeling step (for the experiment shown in Supplementary Fig. 15a) or throughout the experiment (for the experiment shown in Supplementary Fig. 15c). To perturb Golgi trafficking, neurons were treated with 5 μg/mL brefeldin (#B7651; Merck, Germany) or 1 μM monensin (#M5273; Merck, Germany) for 4 h, added from the onset of blocking.
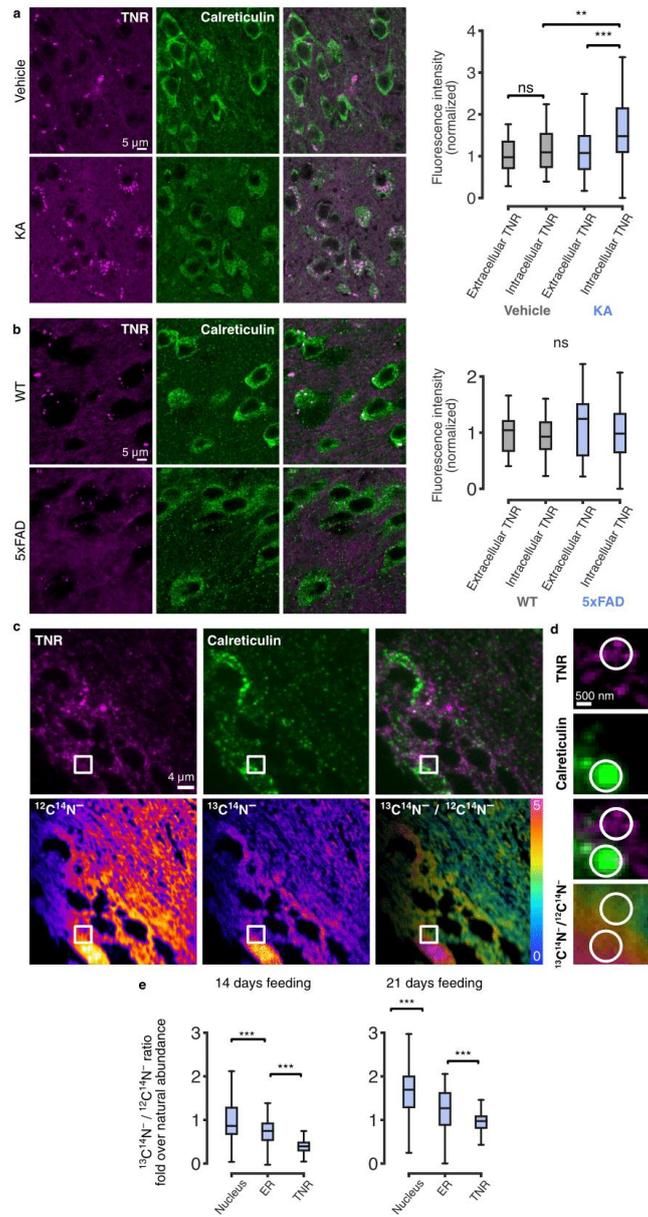
Live labeling of synaptotagmin 1 and EGF receptors. For the surface antibody stripping experiments of with Syt1 and EGF, neurons were incubated with 1:100

monoclonal mouse antibodies directed against the lumenal domain of Syt1 conjugated to Atto647N (custom made, Synaptic Systems, Göttingen, Germany), or 1:100 epidermal growth factor (EGF), complexed to Alexa Fluor® 647 (#E35351; Thermo Fisher Scientific, USA). The incubations were performed for 5 min at 4 °C. The neurons were imaged before and after stripping with proteinase K (see 'Surface antibody stripping with proteinase K') immediately after labeling, following a short incubation of 15 min, or after a longer incubation of 60 min (for Syt1) or 4 h (for EGF).

Antibodies were diluted from 1 mg/ml stocks, unless specified otherwise. Live-cell incubations were performed at 37 °C, and live washing steps were performed in pre-warmed Tyrode.

Surface antibody stripping with proteinase K. For surface antibody stripping, neurons were incubated with 8 units/ml Proteinase K from *Tritirachium album* (#P2308, Merck, Germany) in Tyrode for 5 min at room temperature. The neurons were then washed and mounted for live imaging or immediately fixed and post-immunostained, as described in the figure legends.

Fixation and post-fixation immunostaining. Neurons/slices were fixed in 4% PFA in PBS (137 mM NaCl, 10 mM Na_2HPO_4, 2 mM KH_2PO_4, 2.7 mM KCl, pH 7.4) for 20 min on ice followed by 20 min at room temperature. The fixation reaction was quenched with 100 mM NH_4Cl in PBS for 30 min. For subsequent immunostainings, neurons were permeabilized and blocked with PBS containing 2.5%, bovine serum albumin (BSA) (#A1391-0250; Applichem, Germany) and 0.1% Tween20 (#9005-64-5; Merck, Germany) or Triton X (#9005-64-5, Merck, Germany) for 1 h. In addition to the labels mentioned under the corresponding experiments, the following labels were used for post-fixation immunostainings. Primary antibodies and labels: to identify excitatory glutamatergic synapses and visualize the synaptic vesicle pool: FluoTag-X2 anti-VGlut1 nanobodies directly conjugated to STAR580 (#N1602; NanoTag, Göttingen, Germany); to identify inhibitory synapses: 1:200 rabbit polyclonal anti-VGAT (#131 103; Synaptic Systems, Göttingen, Germany); to identify perineuronal nets: 1:500 biotinylated *Wisteria floribunda* agglutinin WFA (#L8258; Merck, Germany); to identify the neuronal axons (for the experiment described in Fig. 4b): 1:100 mouse monoclonal directed against Ankyrin G (#75-146; NeuroMab, USA); to identify organelles: 1:100 rabbit polyclonal anti-LAMP1 (#ab24170; Abcam, United Kingdom), 1:200 rabbit monoclonal anti-Rab5 (#C8B1; Cell Signaling, Germany), 1:100 rabbit monoclonal anti-Rab7 (#9367; Cell Signaling, Germany), 1:100 rabbit polyclonal anti-TGN38 (#T9826, Merck, Germany), 1:100 rabbit polyclonal anti-calreticulin (#12238 S; Cell Signaling, Germany), 1:100 rabbit polyclonal anti-Caveolin1 (#ab2910; Abcam, United Kingdom), rabbit polyclonal anti-Rab11a (#2413; Cell Signaling, Germany) and 1:100 rabbit polyclonal anti-Rab11b (#ab3612; Abcam, United Kingdom); to identify neurons: 1:100 mouse monoclonal or guinea pig polyclonal anti-NeuN (#266 011 and #266 004; Synaptic Systems, Göttingen, Germany); to identify astrocytes: 1:1000 rabbit polyclonal anti-GFAP (#173 002; Synaptic Systems, Göttingen, Germany); to identify oligodendrocytes: rabbit monoclonal anti-myelin basic protein (#78896; Cell Signaling, Germany), to identify microglia: 1:500 guinea pig polyclonal anti-Iba1 (#234 004; Synaptic Systems, Göttingen, Germany). Secondary antibodies and labels were used,: 1:200 Cy3-conjugated goat anti-mouse IgG (#115-035-146; Dianova, Germany); 1:500 Atto647N-conjugated goat anti-mouse IgG (#610-156-121 S; Rockland, USA); 1:500 STAR580-conjugated FluoTag-X2 anti-mouse secondary nanobodies (#N1202-Ab580; NanoTag, Göttingen, Germany); 1:500 STAR580-conjugated goat anti-mouse IgG (#ST580-1001; Abberior GmbH, Göttingen, Germany); 1:200 Cy3-conjugated goat anti-rabbit IgG (#111-165-144; Dianova, Germany); 1:200 Cy5-conjugated goat anti-rabbit IgG (#111-175-144; Dianova, Germany); 1:200 STAR580-conjugated goat anti-rabbit IgG (#ST580-1002; Abberior GmbH, Göttingen, Germany); 1:200 Cy3-conjugated goat a anti-guineapig IgG (#706-165-148; Dianova, Germany); 1:200 STAR635P-conjugated streptavidin (#ST635P-0120;

15

73

37 °C, washed once and left overnight. Neurons were subsequently washed twice and embedded in Mowiol (Calbiochem, Billerica, MA, USA). To label nuclei, neurons were incubated with Hoechst 33342 (#62249, Thermofisher Scientific, USA) for 10 min before mounting.

4 day-long live imaging of TNR-labeled neuronal cultures. Neurons were plated on 24 well glass-bottomed cell culture plates (#P24-1.5H-N, Cellvis, USA) at a

Fig. 10 TNR dynamics are observed in brain slices from adult mice, and are altered in an epilepsy model. a, b Intracellular TNR in disease models. Hippocampal slices from kainic acid (KA)-induced epilepsy model mice and 5xFAD familial Alzheimer's disease model mice were immunostained for TNR and the ER marker calreticulin, to enable identification of intracellular (somatic) TNR. All other TNR was presumed extracellular. **a** Imaged regions (confocal) from mice pre-treated with vehicle or KA. The proportion of intracellular TNR is increased in KA-treated mice. $N = 3$ mice per treatment, 60 (vehicle) and 67 (KA) regions analyzed. Kruskal-Wallis ($H_3 = 27.93$, ***$p < 0.001$), followed by two-sided Dunn's multiple comparisons test ('vehicle; extracellular TNR'/'vehicle; intracellular TNR': '$p = 0.932$; 'KA; extracellular TNR'/'KA; intracellular TNR': ***$p < 0.001$; 'vehicle; intracellular TNR'/'KA; intracellular TNR': **$p = 0.004$). **b** Similar analysis for 5xFAD mice. No significant differences are observed. $N = 3$ mice per treatment, 68 (WT) and 29 (5xFAD) regions analyzed. Kruskal-Wallis ($H_3 = 3.233$, $p = 0.357$). Scale bar = 5 μm. **c–e** Isotopic imaging in adult mice suggests intracellular TNR is not newly synthesized. TNR turnover in vivo was measured with correlative fluorescence and isotopic imaging (COIN[20,48,72,80,81]) in brain slices of mice pulsed with isotopically stable $^{13}C_6$-lysine for 14 or 21 days (previously characterized in[2]). **c** Top: section stained for TNR and calreticulin (epifluorescence). Bottom: nanoSIMS images of $^{12}C^{14}N^-$ (left) and $^{13}C^{14}N^-$ (middle) secondary ions. The $^{13}C^{14}N^-/^{12}C^{14}N^-$ ratio image (right) indicates the enrichment of ^{13}C. Scale bar = 4 μm. **d** Zoom of square regions in **c**. Scale bar = 500 nm. **e** Quantification of $^{13}C^{14}N^-/^{12}C^{14}N$ ratio as fold over the natural abundance level. TNR-enriched areas exhibit the lowest ^{13}C enrichment in these cells (lowest newly synthesized protein levels). $N = 6$ sections from 3 mice per condition. Kruskal-Wallis ($H_2 = 167.2$, ***$p < 0.001$), followed by two-sided Dunn's multiple comparisons test (***$p < 0.001$ for all comparisons). For all panels: boxes show median (mid-line) and quartiles, whiskers show minimum/maximum values. Outliers were omitted according to inter-quartile range (IQR) proximity (exceeding 1.5*IQR). Source data provided in Source Data file.

density of ~50,000 cells per well as described (see 'Preparation of rat dissociated hippocampal cultures'). At DIV14, all or newly-emerged TNR molecules were labeled with Atto550-conjugated TNR antibodies, as described above (see 'Blocking-labeling assay and live treatments'), and in the figure legend. The neurons were transferred to an automated live-cell incubator/imaging system (BioSpa™ 8 Automated Incubator coupled with a Cytation™ 5 Cell Imaging Multi-Mode Reader, BioTek, USA). The plates were incubated in the BioSpa at 37 °C and 5% CO₂ for 4 days. Every 4 h, the plates were automatically transferred to the Cytation 5, also set to 37 °C and 5% CO₂, and imaged using a 20x Plan Fluorite, 0.45 NA (#1320517, BioTek PN) objective in the RFP imaging channel, in addition to a phase-contrast channel overlay. For each well, 16 fields of view were acquired (a total 6.3 × 4.7 mm imaging area per well).

TNR/brevican KO mouse brain slices. TNR/brevican KO mice were first deeply anesthetized by ketamine (90 mg/kg of body weight) and xylazine (18 mg/kg of body weight) in a 0.9% NaCl solution and perfused transcardially with 4% paraformaldehyde (PFA) in 0.1 M PBS (PH 7.2) for 10 min. The dissected brains were incubated in 4% PFA containing PBS at 4 °C for 2 h. Fifty-micrometer thin sagittal sections were cut using a microslicer (HM650V, MICROM). The sections were first washed with PBS and then permeabilized with 0.1% Triton X-100 (#T9284, Merck, Germany-Aldrich) in PBS for 10 min at room temperature. Next, the sections were incubated for 1 h (at room temperature with gentle shaking) in a blocking solution containing 10% normal goat serum (16210064, Life Technologies), 0.4% Triton X and 0.1% glycine in PBS. Then, the sections were incubated for 24 h (at room temperature with gentle shaking) with a mixture of 1:500 *Wisteria floribunda* agglutinin (WFA) (#B-1355; Vector Laboratories, California, USA) and 1:200 monoclonal mouse anti-TNR (#217 011, Synaptic Systems, Göttingen, Germany) for 24 h. The sections were then washed in PBS and incubated with 1:200 streptavidin Alexa Fluor® 405 (#S32351; Life Technologies, Thermofisher Scientific, USA) and 1:200 goat anti-mouse Alexa Fluor® 647 (#A21236; Life Technologies, Thermofisher Scientific, USA), on a shaker for 3 h at room temperature. Following the incubation, the sections were washed with PBS and then mounted on Superfrost glass slides (#J1800AMNZ, Thermofisher Scientific, USA) with Fluoromount medium (#F4680, Merck, Germany). Images were acquired with confocal laser-scanning microscopy (LSM 700, Zeiss) with the same acquisition parameters for the comparison of samples.

shRNA-mediated TNR knockdown
Generation of shRNA viral vectors. The shRNA plasmid to knockdown mouse TNR (GeneID:21960) was cloned by the insertion of the siRNA's sequence (siRNA ID: SASI_Mm01_00073137, Rosetta Predictions from Merck, Germany Aldrich, Merck) targeting the open reading frame of mouse Tenascin-R into adeno-associated viral (AAV) vector U6 GFP (Cell Biolabs Inc., San Diego, CA 92126, USA), using BamH1 and EcoR1 restriction sites[60]. A scrambled siRNA sequence was used as a non-targeting negative control. The sequences for TNR siRNA and control siRNA are 5′-gcgttcactctcctccctg, and 5′-cggctgaaacaagagttgg, respectively. Clones were verified by sequencing analysis and used for the production of adeno-associated particles as described previously[61]. Briefly, HEK 293 T cells (Thermo Scientificl #HCL4517) were transfected with the calcium phosphate method with an equimolar mixture of the expression plasmid, pHelper plasmid, and Rep/Cap plasmid pAAV2/DJ (for the production of the shRNA, pAAV2/1 and pAAV2/2 were combined to obtain a mixed capsid of AAV1/2). After 48 h of transfection, cells were lysed using freeze-thaw and treated with benzonase at a final concentration of 50 units/ml for 1 h at 37 °C. The lysate was centrifuged at 8000 g at 4 °C. The supernatant was collected and filtered with a 0.2-micron filter. Filtered supernatant was passed through pre-equilibrated Hitrap Heparin columns (#17-0406-01; Ge HealthCare Life science, USA), followed by a wash with Wash Buffer 1

(20 mM Tris, 100 mM NaCl, pH 8.0; filtered sterile). Columns were additionally washed with Wash Buffer 2 (20 mM Tris 250 mM NaCl, pH 8.0; filtered sterile). Viral particles were eluted with elution buffer (20 mM Tris 500 mM NaCl, pH 8.0; filtered sterile). Amicon ultra-4 centrifugal filters with a 100,000 molecular weight cutoff were used to exchange the elution buffer with sterile PBS. Finally, viral particles were filtered through 0.22 μm syringe filters (Nalgene®; # Z741696; Merck, Germany), aliquoted and stored at −80 °C until usage.

Culture preparation and infection with shRNA. Mouse hippocampal cultures were prepared from newborn C57BL/6 N mice as previously described[62] with minor modifications. For the glial feeder layer, the cortices were dissected in HBSS, and enzymatically digested for 15 min at 37 °C with 0.05% (w/v) trypsin/EDTA solution (Gibco, Thermo Fisher Scientific, USA). The dissected cortices were then triturated and the glia were cultured for 7 days in T-75 flasks in DMEM containing 10% FBS and penicillin/streptomycin (100 U/ml; 100 mg/ml) mixture and 0.1% MITO + serum extender (Biozym Scientific, Germany). After 7 days, the cells were seeded onto 18 mm coverslips at a density of (50,000/cm³), and 1 μM FUDR (Merck, Germany) was added to the medium 6 days later. For the neuronal culture, hippocampi were dissected in HBSS, and digested for 1 h at 37 °C in DMEM supplemented with 25 U/ml papain (Worthington Biomedical Corp., USA), 0.2 mg/ml cysteine (Merck, Germany), 1 mM CaCl₂, and 0.5 mM EDTA. The digestion was arrested by a 15-min incubation in DMEM supplemented with 2.5 mg/ml bovine serum albumin (Merck, Germany), 2.5 mg/ml trypsin inhibitor (Merck, Germany), and 10% (v/v) FBS. Neurons were triturated and seeded onto the astrocyte feeder layers at a density of ~ 75,000/cm³. Prior to the addition of the hippocampal neurons, the culture medium was switched to Neurobasal-A medium (Life Technologies, Carlsbad, CA, USA) containing B27 supplement (Gibco, Thermo Fisher Scientific, USA), 2 mM GlutaMax (Gibco, Thermo Fisher Scientific, USA) and penicillin/streptomycin (100 U/ml; 100 mg/ml) mixture (Biozym Scientific, Germany). At DIV7, the neurons were infected with AAV1/2-GFP-U6-shTNR (shRNA for TNR) or AAV1/2-GFP-U6-shScr (scramble shRNA) (1 μl/ml with a titer of 3.35×10^{10}). At DIV14, infected neurons were washed extensively in PBS and fixed by immersion in a solution of 4% PFA in 0.1 M PBS.

Immunostaining. The neurons were blocked with PBS containing 2.5% bovine serum albumin (BSA; #A1391-0250; Applichem, Germany) and 0.1% Triton X (#9005-64-5, Merck, Germany) for 1 h at room temperature. Then, the neurons were incubated with 1:500 Atto647N-conjugated mouse monoclonal anti-TNR (custom made, Synaptic Systems, Göttingen, Germany), overnight at 4 °C. The neurons were washed in PBS and then mounted in Mowiol.

Electrophysiology. Na^+, K^+ currents and mEPSCs were recorded by conventional whole-cell patch-clamping under a physiological temperature of 37 °C, with continuous perfusion of ACSF (pre-saturated with 95% O_2 and 5% CO_2). ACSF (artificial cerebrospinal fluid) contains (in mmol/L): 119 NaCl, 2.5 KCl, 2 CaCl₂, 2 MgSO₄, 1.25 NaH₂PO₄, 26.2 NaHCO₃, 11 Glucose, with pH ~7.4 and osmolarity 305-315 mOsm. Patch pipettes (2–4MΩ) were pulled from borosilicate glass (1.6 mm outside diameter) and filled with intracellular solution containing (in mmol/L): 130 HMeSO₄, 5 KCl, 1 EGTA, 10 HEPES, 4 MgCl₂, 2 ATP-Na₂, 0.4 GTP-Na, 7 Phosphocreatine-Na₂, with pH adjusted to 7.2–7.4 by KOH, and osmolarity adjusted to 290–295 mOsm. Final concentration (in mmol/L): K^+: 135; Na^+: 17.4; Cl^-: 9. Whole-cell configuration was first made under normal ACSF. Na^+ and K^+ currents were elicited by a series of depolarizing pulses between −60 mV and +50 mV, in 10 mV increments, from a holding potential of −70 mV. Miniature EPSCs were recorded at a holding potential of −70 mV under ACSF, with 1 μM TTX and 100 μM picrotoxin, after Na^+ currents have disappeared. An EPC-9 patch-clamp amplifier equipped with Patchmaster software (HEKA Electronics,

Germany) was used for data acquisition. No leak currents compensation was used, but fast and slow capacitances[63,64], and series resistances were corrected online. The data were sampled at 40 kHz and filtered at 10 kHz (four-pole Bessel) and 5.9 kHz (three-pole Bessel). Data were stored and exported to Matlab for further analysis, which was performed by thresholding the curves using an empirically derived threshold, to detect the mEPSCs. Control cultures were exposed to boiled TNR antibodies, while test cultures were incubated with normal TNR antibodies (#217 011; Synaptic Systems, Göttingen, Germany).

TNR 'blocking-labeling' experiment in rat dissociated hippocampal 'sandwich' cultures

Culture preparation. Dissociated primary hippocampal sandwich cultures, in which the neurons are physically separated from a glial feeding layer, were prepared from E18 Wistar rats as previously described[26], and maintained in N2 medium. The following modifications were made to the original protocol. For the feeding layer, the glia were seeded 3 days before the dissection of the E18 rats in 12-well plates, at a density of ~ 10,000 cells per well. The neurons were then seeded on circular glass coverslips (18 mm diameter) at a density of ~ 30,000 cells per coverslip. Paraffin dots were added to the coverslips as the spacers between the neurons and the glia. The blocking-labeling assay in sandwich cultures was performed as for the regular neuronal cultures (see 'Blocking-labeling assay and live treatments', above).

Application of recombinant His-tagged TNR to neuronal cultures/slices

Neuronal cultures. For the experiment shown in Fig. 5c–e, the neurons were incubated with 5 µg/mL recombinant TNR (# 3865-TR; Biotechne GmbH, Germany) diluted in their own cell media, for 1 h at 37 °C. The neurons were then washed in Tyrode's solution (124 mM NaCl, 30 mM glucose, 25 mM HEPES, 5 mM KCl, 2 mM $CaCl_2$, 1 mM $MgCl_2$, pH 7.4) and returned to their conditioned media. Immediately after, 1 or 3 days later the neurons were stripped with proteinase K (see 'Surface antibody stripping with proteinase K') and then fixed with 4% PFA in PBS (or immediately fixed, without stripping), as described in detail in the figure legend. The fixation and subsequent immunostaining were performed as in other experiments (see 'Fixation and post-fixation immunostaining'), using 1:250 rabbit monoclonal anti-His-Tag (#12698; Cell Signaling, Germany), followed by Cy3-conjugated goat anti-mouse IgG (#111-165-144; Dianova, Germany).

To assess the extent of rTNR degradation in neuronal cultures, they were incubated with the protein (5 µg/mL) for 2 h, 3 days and 6 days. Samples were then collected and lysed in SDS sample buffer, and were later boiled at 95 °C for 5 min, before SDS-PAGE procedures. To ensure even loading of material, we used as an internal control a monoclonal mouse anti-calmodulin (#MA3-917; Thermo Fisher Scientific, US) antibody that was also added to the cultures, and whose levels reflected the general protein concentrations in the cultures. The samples were loaded on 10% SDS polyacrylamide gels and were then transferred to nitrocellulose membranes. The membranes were blocked for 1 h at room temperature in blocking buffer consisting of PBS with 0.1% Tween-20 and 5% skimmed milk powder, and then incubated with 1:1000 rabbit monoclonal anti-His-Tag for 1 h at room temperature. After washing, the membranes were incubated with IRDye® 800CW donkey anti-mouse IgG and IRDye® 680RD donkey anti-rabbit IgG (#926-32212 and #926-68073; LI-COR Biotechnology, USA), for 1 h at room temperature. The primary and secondary incubations were performed in blocking solution. The membranes were then washed in PBS and scanned using Odyssey CLx (LI-COR).

Organotypic slices. The slices were incubated with 5 µg/mL recombinant TNR diluted in their own cell media, for 2 h at 37 °C. The slices were then washed in Tyrode's solution and returned to their original conditioned media. The slices were incubated a further 6 h to allow for internalization, and then stripped with proteinase K and fixed with 4% PFA, as described in detail in the figure legend. Stimulated and control slices were incubated with 40 µM bicuculline (#485-49-4; Merck, Germany) or 0.1% volume/volume DMSO (#67-68-5; Merck, Germany) added throughout the experiment. As additional controls, some of the slices were not incubated with the recombinant TNR (to measure background signal) or not stripped with proteinase K (to visualize the full population of molecules). The fixation and post-fixation immunostaining were performed as described above for the neuronal cultures.

Acute slices. The hippocampi of 3 week-old Wistar rats were extracted and cut into ~700 µm-thick transverse slices. The slices were placed in artificial cerebrospinal fluid at 37 °C (aCSF: 125 mM NaCl, 2.5 mM KCl, 1.25 mM NaHPO4, 25 mM NaHCO3, 25 mM D-Glucose, 2 mM $CaCl_2$ and 1 mM $MgCl_2$, bubbled with carbogen for 30 min). After a short period of recovery, 5 µg/mL recombinant was pipetted directly into the aCSF and the slices were incubated for 2 h. The slices were then incubated with proteinase K (see 'Surface antibody stripping with proteinase K') for a further 30 min, to remove any protein that remained at the surface. Stimulated and control slices were incubated with 40 µM bicuculline or 0.1% volume/volume DMSO added throughout the experiment. As additional controls, some of the slices were not incubated with the recombinant TNR (to measure background signal) or not stripped with proteinase K (to visualize the full population of molecules). After washing, the slices were fixed with 4% PFA in PBS for 1 h at room temperature, and the fixation reaction was quenched with 100 mM

NH_4Cl in PBS for 30 min. The slices were then blocked in 1 h with PBS containing 2.5% bovine serum albumin and 0.3% Triton X for 1 h at room temperature, and then incubated with 1:250 rabbit monoclonal anti-His-Tag and FluoTag-X2 anti-VGlut1 nanobodies directly conjugated to Atto 488 (#N1602; NanoTag, Göttingen, Germany), overnight at 4 °C. The slices were washed, and then incubated with 1:200 Cy3-conjugated goat anti-mouse IgG (#115-035-146; Dianova, Germany) for 2 h, at room temperature. All antibody incubation steps were performed in blocking solution. The slices were washed in PBS and embedded in Mowiol.

siRNA-mediated dynamin knockdown

siRNA transfection. The neurons were co-transfected with 50 nM dynamin 1, 2, and 3 siRNA constructs (previously described in[65]) or with non-targeting control siRNA (ON-TARGETplus Non-targeting Control Pool; # D-001810-10, Horizon Discovery) at DIV 7, using Lipofectamine RNAiMAX transfection reagent (#13778030; Thermo Fisher Scientific, USA). At DIV 14, labeling of newly-emerged TNR epitopes was performed as in the other experiments (see 'Blocking-labeling assay and live treatments'). Fixation and immunostaining were performed as in other experiments (see 'Fixation and post-fixation immunostaining'), using 1:100 rabbit anti-dynamin 1, 2, 3 (#115 002, Synaptic Systems, Göttingen, Germany), followed by 1:200 Cy3-conjugated goat anti-rabbit IgG (#111-165-144; Dianova, Germany).

Co-immunoprecipitation from rat synaptosomes and Western blotting.
Synaptosomes were prepared from 5- to 6-week-old rats as previously described[66]. In brief, brain homogenates were were centrifuged at 5000 rpm for 2 min. The resulting supernatants were then centrifuged at 11,000 rpm for 12 min. The pellets were resuspended and then loaded on Ficoll gradients (6, 9 and 13% w/v), and centrifuged at 22,500 rpm for 35 min. The synaptosomes (enriched between 9-13%) were collected. Precipitation of TNR was performed by incubating the synaptosomes with the same antibodies used in the rest of the study (#217 011; Synaptic Systems, Göttingen, Germany) for 1 h at 4 °C, rotating. The synaptosomes were then incubated with 4% CHAPS (1 h at 4 °C, rotating), to permeabilize the membranes (as previously described[67]). The supernatants were incubated with Dynabeads™ Protein G (#10003D; Thermofisher Scientific, USA) prewashed using PBS with 0.01% Tween-20 (#9005-64-5; Merck, Germany)), for 2 h at 4 °C, rotating. The beads were then washed 3 times again, and the samples were eluted using SDS-sample buffer and boiled at 95 °C for 5 min. Equal amounts (~15% of the starting synaptosome homogenate) were loaded on 10% SDS polyacrylamide gels, alongside 0.05% of synaptosome homogenate. The gels were transferred to nitrocellulose membranes, which were blocked for 1 h at room temperature, in blocking buffer consisting of PBS with 0.1% Tween-20 and 5% skimmed milk powder. The membranes were then incubated with 1:1000 mouse monoclonal anti-TNR antibodies or 1:1000 rabbit polyclonal anti-Dynamin 1,2,3 antibodies (#115 002, Synaptic Systems, Göttingen, Germany), overnight at 4 °C. After washing, the membranes were incubated with IRDye® 800CW donkey anti-mouse IgG or IRDye® 680RD donkey anti-rabbit IgG (#926-32212 or #926-68073; LI-COR Biotechnology, USA), for 1 h at room temperature. The primary and secondary incubations were performed in blocking solution. The membranes were then washed in PBS and scanned using Odyssey CLx (LI-COR). Full blots can be found in the Source Data file.

Metabolic labeling of newly synthesized proteins and glycans.
For visualization of newly-synthesized proteins on the cell surface, neurons were incubated in methionine-free media subsequent to TNR epitope blocking: DMEM (4.5 mg/ml glucose, lacking pyruvate, methionine, glutamine, and cysteine; Life Technologies, Carlsbad, CA, USA) supplemented with 50 µM L-azidohomoalanine (AHA; Life Technologies), 812 µM MgCl2, 6.5 mM HEPES, 260 µM cysteine, 1:50 B27 (Gibco, Life Technologies), and 1:100 GlutaMAX (Gibco, Life Technologies). For visualization of surface glycans, 50 µM Click-IT™ GalNAz and/or GlcNAz (#C33365, C33367, Thermo Fisher Scientific, USA) were diluted directly into the neurons' media subsequent to blocking, and remained throughout the experiment. Live, copper-free click labeling of surface AHA or glycans was performed after TNR labeling using strain-promoted azide-alkyne cycloaddition (SPAAC)[68]. Neurons were incubated with 1:1000 dibenzocyclooctyne (DBCO) conjugated to Alexa-Fluor647 (#CLK-1302, Jena Bioscience, Germany) diluted in Ca^{2+}/Mg^{2+}-free Tyrode's solution with 1 mM EGTA (#67-42-5; Merck, Germany).

Sequestration of TNR on the plasma membrane using large antibody aggregates.
Sequestration of TNR epitopes on the plasma membrane was done as previously described[41]. To perturb the newly-emerged TNR epitopes, cultured neurons or organotypic hippocampal slices cultures were blocked for 2 h with 1:100 unlabeled TNR antibodies (neurons) or 50 µg/mL unlabeled Fab fragments directed against TNR (organotypic slices), together with 1 mg/mL unlabeled FluoTag-X2 anti-mouse secondary nanobodies. The cultures were then labeled 12 h after blocking with 1:500 TNR antibodies (neurons) or 2 µg/mL Fab fragments directed against TNR (organotypic slices), together with 1 mg/mL biotinylated FluoTag-X2 secondary anti-mouse secondary nanobodies (custom-made; NanoTag, Göttingen, Germany). This ensures that only the newly-emerged epitopes, which surfaced during the 12 h after blocking, are tagged by biotin. Alternatively, to perturb

specifically the epitopes that do not recycle ("all other epitopes"), the blocking step was performed using unlabeled TNR antibodies/Fab fragments, but without unlabeled anti-mouse secondary nanobodies. The cultures were incubated for 12 h, to ensure that the recycling epitopes are endocytosed, and then the biotinylated secondary nanobodies alone were applied. These now cannot detect the endocytosed molecules, and cannot detect the newly-emerged TNR epitopes, since these molecules are not bound by the TNR antibodies. The biotinylated secondary nanobodies only detect the TNR antibodies on the surface molecules that were present at the time of labeling (12 h previously) and did not endocytose in the meanwhile – meaning the stable, non-recycling pool. Subsequently, the cultures were incubated with antibody aggregates diluted 1:20 in Tyrode (untreated cultures were incubated in plain Tyrode). The antibody aggregates consisted of goat anti-biotin (#B3640; Merck, Germany) and STAR635P-conjugated donkey anti-goat (#ST635P; Abberior GmbH, Göttingen, Germany). Donkey anti-goat and goat anti-biotin antibodies were diluted 1:10 in PBS, and the mixture was left to rotate overnight at 4 °C. For the analysis of stimulus-induced vesicle release in cultured neurons, the aggregates were added for 30 min, after which the neurons were incubated for 5 min with 1:100 polyclonal rabbit antibodies directed against the lumenal domain of Syt1 conjugated to the fluorescent dye Oyster488 (#105 103C2; Synaptic Systems, Göttingen, Germany) in either plain Tyrode (stimulated condition) or Ca^{2+}-free Tyrode containing 1 mM EGTA and 1 µM TTX (#1069; Tocris Bioscience, Germany) (unstimulated condition). To reveal the releasable vesicles, neurons were stimulated electrically with field pulses with a frequency of 20-Hz and an intensity of 100 mA, for 10 s. This stimulus causes the exo- and endocytosis of 50% of the active vesicle pool (the other ~50% are already present on the surface membrane, waiting for endocytosis[20,69]). The stimulations were performed with a 385 Stimulus Isolator and an A310 Accupulser Stimulator (World Precision Instruments, Sarasota, FL, USA), using a custom-made platinum plate field stimulator (8 mm-distanced plates). Following the stimulation, the neurons were incubated a further 5 min with the Syt1 antibodies and then briefly washed and fixed. For the analysis of structural changes to synapses in organotypic slices, the aggregates were added for 12 h, after which the cultures were washed and fixed (see 'Fixation and post-fixation immunostaining'), and then immunostained with FluoTag-X2 anti-VGlut1 nanobodies directly conjugated to STAR-580 (#N1602; NanoTag, Göttingen, Germany), to identify synapses. To visualize the synaptic membranes in neuronal cultures, the immunostained neurons were incubated with DiO (see 'Fixation and post-fixation immunostaining'). To visualize synaptic membranes in organotypic slices, the slices were infected with AAV9 Syn-eGFP (eGFP under the synapsin 1 (hSyn) promoter; Penn Vector Core, Pennsylvania, USA), at 1ul per well, with a titer of 1.32×10^{13}, at DIV 7, to ensure sufficient expression at DIV 14. Following the post-fixation labeling, the neuronal cultures/organotypic slices were mounted in Mowiol.

Live-cell incubations were performed at 37 °C, and live washing steps were performed in pre-warmed Tyrode.

Ca^{2+} imaging. For measuring Ca^{2+} responses, neurons were infected with Incu-Cyte® NeuroBurst Orange Reagent (#4736; Sartorius, Germany) at DIV7. After 7 days, the neurons were treated with antibody aggregates, (see 'Sequestration of TNR on the plasma membrane using large antibody aggregates') and then mounted in a live-imaging chamber in pre-warmed Tyrode. The neurons were imaged under constant temperature (37 °C) with an inverted Nikon Ti microscope with a Plan Apochromat 20× 0.75 NA air objective (Nikon Corporation, Chiyoda, Tokyo, Japan), equipped with a cage incubator system (OKOLab, Ottaviano, Italy). For recording spontaneous bursting activity, the neurons were imaged at a frequency of 1 frame per second (fps) for a total of 1 min. For imaging the Ca^{2+} response to stimulation, 1 µM TTX was added to inhibit the neurons' spontaneous activity, thus ensuring that the opening of presynaptic voltage-gated Ca^{2+} channels (VGCCs) is solely the result of the external electrical stimulations. The neurons were imaged with a Plan Apochromat 100×/1.4 NA oil objective at 1 fps for 10 s, after which a brief electrical stimulation was applied (20-Hz, 100 mA, 1 s) with an Accupulser Stimulator. Following the stimulation, the neurons were imaged for an additional 30 s.

Immunostaining of brain slices from kainic acid-treated mice and 5xFAD mice

Kainic acid treatment and preparation of sections. Kainic acid or vehicle injections were performed in 3 month-old C57BL6/J mice as previously described[47]. In brief, the animals were implanted with cannulas positioned above the right hippocampal CA1 region. Two weeks later, 120 nL of 10 mM kainic acid in vehicle (Millipore distilled sterile water) was delivered through the cannula. As a control, 120 nL of vehicle was delivered. Seven days later, the mice were sacrificed in a CO_2 chamber and perfused with PBS and 4% PFA in PBS. Brains were kept in 4% PFA in PBS for post-fixation overnight at 4 °C. Then the brains were put in a 1 M sucrose solution in PBS at 4 °C for cryoprotection. Two days later, brains were frozen in 2-methyl-butane at −80 °C and kept frozen until sectioning. The frozen tissues were sectioned into ~30 µm-thick slices using a cryostat.

Preparation of sections from 5xFAD mice. The sections were prepared as previously described[70]. In brief, 3 male 5xFAD (familiar Alzheimer's disease mouse model[71]) or wildtype littermates with the C57BL6/J background were decapitated at the age of 6–9 months and brain tissue was isolated in ice-cold PBS. The left hemispheres

were fixed in 4% PFA in PBS overnight, at 4 °C. The tissue was then cryoprotected overnight in 30% sucrose in PBS, and frozen in 2-methyl-butane at −80 °C until sectioning. The frozen tissues were sectioned into ~40 µm-thick slices using a cryostat.

Immunostaining. The slices were blocked with PBS containing 2.5%, with PBS containing 2.5% bovine serum albumin (BSA; #A1391-0250; Applichem, Germany) and 0.3% Triton X (#9005-64-5, Merck, Germany) for 1 h at room temperature. Then, the slices were incubated with 1:500 Atto647N-conjugated mouse monoclonal TNR antibodies (custom made, Synaptic Systems, Göttingen, Germany) and 1:100 rabbit polyclonal anti-calreticulin (#12238 S; Cell Signaling, Germany), overnight at 4 °C. The slices were washed, and then incubated with 1:200 Alexa488 donkey anti-rabbit IgG secondary antibodies (#711-545-152; Dianova, Germany) for 1 h at room temperature. All antibody incubations were performed in blocking solution. Following the staining, the slices were washed in PBS, and then mounted in Mowiol.

For both the KA-treated and 5xFAD mice, images were acquired of the CA1 and dentate gyrus regions.

Correlated fluorescence and nanoSIMS imaging of brain slices from ^{13}C-lysine-pulsed mice

Slice preparation. $^{13}C_6$-lysine pulsing of adult mice was performed as previously described[2]. The brains were snap-frozen immediately upon removal from the skull and stored at −80 °C. After thawing, a thick coronal slice was extracted from the center of each brain containing the hippocampal formation (~30-50 mm) and fixed in 4% PFA in PBS overnight, at 4 °C. The slices were then embedded in Tissue-Tek® O.C.T.™ Compound (Sakura, Finetek USA Inc., Torrance, CA, USA) and frozen at −80 °C. The frozen slices were sectioned into ~60 µm thick slices on a Leica CM1850 cryotome.

Immunostaining and mounting. The slices were blocked for 1 h with PBS containing 2.5% bovine serum albumin (BSA; #A1391-0250; Applichem, Germany) and 0.3% Triton X (#9005-64-5, Merck, Germany) for 1 h at room temperature. All sections were immunostained with 1:500 Atto647N-conjugated mouse monoclonal TNR antibodies (custom made, Synaptic Systems, Göttingen, Germany) and 1:100 rabbit polyclonal anti-calreticulin (#12238 S; Cell Signaling, Germany), overnight at 4 °C. The slices were washed, and then incubated with 1:100 Alexa546-conjugated goat anti-rabbit IgG (#A11035; Thermofisher Scientific, USA) for 1 h at room temperature. The incubations with the primary and secondary antibodies were performed in the same blocking solution. Following the immunostaining, the slices were embedded in medium grade LR white (London Resin Company, London, UK), as previously described[72]. In brief, the sections were dehydrated in increasing concentrations of ethanol, and then placed on glass coverslips and incubated for 1 h in a 1:1 mixture of LR white and 50% ethanol, and for a further hour with pure LR white (all at room temperature). The slices were then overlayed with Beem® capsules (BEEM Inc., West Chester, PA, USA), which were filled with a mixture of LR white and accelerator (1 drop of LR white accelerator was added to 10 mL LR white), and heated for 1.5 h at 60 °C to allow for polymerization. After cooling, the glass coverslips were broken off, and the samples were cut using an ultramicrotome (EM UC6, Leica Microsystems, Wetzlar, Germany) into thin sections of ~200 nm, and then placed on Silicon wafers (Siegert Wafer GmbH, Aachen, Germany).

Imaging. The samples were first imaged with epifluorescence microscopy, on an inverted Nikon Ti microscope (Nikon Corporation, Chiyoda, Tokyo, Japan) equipped with a Plan Apochromat 100×, 1.45 NA oil immersion objective, a a 1.5× optovar lens and an IXON X3897 Andor (Belfast, Northern Ireland, UK) camera. After fluorescence imaging, the same areas were imaged with a NanoSIMS 50 L instrument (Cameca, France) equipped with an 8 kV Cesium primary ion source. To reach the steady-state of the secondary ion yield, prior to each measurement, the area of interest was implanted with a current of 600 pA for 60 s (primary aperture D1:1). Subsequently, a primary ion current of ~2.5 pA (primary aperture D1:2) was applied during the imaging on areas of 55 × 55 µm, obtaining images of 512 × 512pixels and resulting in a pixel size of 107.4 nm. The dwell time was 5 ms per pixel. The detectors were set to simultaneously collect the following ions: $^{12}C^-$, $^{13}C^-$, $^{12}C^{14}N^-$ and $^{13}C^{14}N$ and the mass resolving power of the instrument was adjusted to ensure the discrimination between isobaric peaks such as $^{13}C^{14}N^-$ from $^{12}C^{15}N^-$, or $^{13}C^-$ from $^{12}C^1H^-$. A single plane was analyzed to avoid loss of lateral resolution caused by drift correction. The images were exported using the OpenMIMS plugin from Fiji (http://nano.bwh.harvard.edu).

Imaging of fluorescence recovery after photobleaching (FRAP)

Generation of viral vectors. In order to specifically investigate the recovery of hyaluronic acid-based matrix around synapses, AAV expression vector were designed, carrying mDlg4 (Gene ID: 13385) fused with EGFP with a linker sequence 3xGGGGS in between the ORF to label postsynaptic density, which was custom made as a service by VectorBuilder (Chicago, IL, USA). To label hyaluronic acid-based ECM an AAV expression vector was designed, carrying link protein hyaluronan and proteoglycan link protein 1 (HAPLN1, Gene ID: 12950) fused with mScarlet subcloned from the plasmid pCytERM_mScarlet_N1 (Addgene plasmid #

77

85066). Viral particles were produced as described above (see 'shRNA-mediated TNR knockdown')

Culture preparation and infection. For the FRAP live imaging experiments, rat cortical cultures (from E18-E19 and P0-P3) were prepared as previously described[73–75]. The neurons were seeded at a density of ~ 80,000/cm^3 on circular glass coverslips (18 mm diameter), and maintained in Neurobasal medium (Gibco, Thermofisher Scientific, USA), supplemented with B27 (Gibco, Thermofisher Scientific, USA), L-Glutamine (Gibco, Thermofisher Scientific, USA) and penicillin/streptomycin (PAA Laboratories, Pasching, Austria). At DIV7-9, the neurons were infected with the AAV-PSD95-eGFP (1 µl per well with a titer of 4.5×10^{12}) and AAV-HAPLN1-Scarlet (1 µl per well with a titer of 5×10^{12}).

FRAP imaging. All live imaging experiments were performed on neurons at DIV 21–23 after transferring infected cultures to a Quick Change Chamber 18 mm Low Profile RC-41LP (Warner Instruments), and keeping them in the original culture media at 37 °C in the constant presence of humidified carbogen for the duration of the imaging. The experiments were performed using a Leica SP5 confocal microscope (Leica-Microsystems, Mannheim, Germany; LAS AF software, version 2.0.2) equipped with Argon (458, 476, 488, 496, 514 nm laser lines), Diode Pumped Solid State (DPSS, 561 nm) and HeNe (633 nm) lasers and acousto-optic tunable filters (AOTF) for selection and intensity adaptation of laser lines. Confocal images with parameters of 512 × 512 pixels display resolution, 8-bit dynamic range, 63× objective, NA 1.40, 3× optical zoom, voxel size approximately $0.16 \times 0.16 \times 0.3$ µm³) were acquired. In all FRAP experiments, one baseline image was collected as a prebleach image before 15–16 circular ROIs of 12–15 µm² size around PSD-95 puncta were bleached by high-intensity 561-nm laser, resulting in bleaching of only HAPLN1-scarlet fluorescence. After bleaching, images were acquired at the rate of one image per 10 min up to 16–17 h to monitor the recovery of hyaluronic acid-based matrix. Images were acquired with the same settings for all samples before and after bleaching. Data were collected following bleaching at 7–16 bleaching spots in each experiment. 14 independent experiments (FRAP movies) were performed, using 14 coverslips from 3 independent culture preparations. The images were analyzed by manually selecting circular regions of interest (ROIs) centered on the bleached spots, and monitoring the signal in the ROIs. The signal was corrected for the loss of signal caused by the repeated imaging. This parameter was monitored in ROIs placed in regions from the same regions, which were not bleached initially. The fluorescence signals were normalized to the pre-bleaching intensity, and were then averaged, as shown in the respective figure. The synaptic enrichment values shown in Supplementary Fig. 20f represent the number of synapses identified, normalized to the total PSD95 fluorescence within the respective ROIs.

Fluorescence imaging. Fluorescence imaging was performed using the following setups, unless otherwise specified.

2-color STED microscopy. The imaging was performed on an Abberior easy3D STED microscope (Abberior GmbH, Göttingen, Germany) equipped with a UPlanSApo 100×/1.4 NA oil immersion objective (Olympus Corporation, Shinjuku, Tokyo, Japan). Pulsed 488 nm, 561 nm, and 640 nm lasers were used for excitation, and easy3D module 775 nm laser was used for depletion. For each channel, the pinhole was set to 1 Airy unit. Avalanche photodiodes (APDs) were used for detection.

Confocal microscopy. The imaging was performed either on an Abberior easy3D STED microscope (detailed above), or on a Leica TCS SP5 microscope (Leica, Wetzlar, Germany) equipped with HCX Plan Apochromat 100× and 63×/1.4 NA oil objectives. For the latter, the 488 nm line of an argon laser, the 561 nm and 633 nm lines of a Helium-Neon laser were utilized for excitation, using acousto-optic tunable filters to select appropriate emission wavelengths. The images were acquired with photomultiplier tubes or Hybrid detectors. For each channel the pinhole was set to 1 Airy unit.

Epifluorescence microscopy. The imaging was performed on either an inverted Nikon Ti microscope (Nikon Corporation, Chiyoda, Tokyo, Japan) equipped with 100×/1.45 NA (oil), 20×/0.8 NA (air) and 10×/0.5 NA (air) Plan Apochromat objectives, and an IXON X3897 Andor (Belfast, Northern Ireland, UK) camera, or with an inverted Olympus microscope (Olympus Corporation, Shinjuku, Tokyo, Japan), equipped with a UPlanFL 20×/0.5 NA air objective, a UPlanSApo 100×/1.4 NA objective and a charge-coupled device camera (F-View II; Olympus). The live imaging experiments described in Fig. 4a and Supplementary Fig. 6, were performed on the Nikon Ti microscope, fitted with a cage incubator system (OKOLab, Ottaviano, Italy). The temperature was maintained at 37 °C and CO_2 was maintained at 5%. The neurons were imaged in their own cell media at a rate of 1 frame every 2 h. For each frame, 5 z-slices were acquired resulting in a stitched mosaic image of 5 × 5 lateral fields of view. All other live imaging experiments were performed on the Olympus microscope. For the experiments described in Fig. 4c and Supplementary Figs. 13, 14e, and 15c, five images of different fields of view were acquired before and after treatment with Proteinase K. For the experiment

described in Supplementary Fig. 14c–d, an image was acquired in the same field of view before and after treatment with Proteinase K.

Image and data analysis. Data was acquired using Leica Application Suite Advanced Fluorescence 2.7.3.9723, Abberior Instruments Imspector v16.3, NIS Elements 5.02.03 and Olympus CellSens Dimension 2.3. Analyses were performed in Matlab (MathWorks, Natick, MA, USA) and Python (Python Software Foundation).

Calculation of mean fluorescence intensity in epifluorescent images. Background fluorescence was subtracted by selecting unlabeled regions in the images, or by using an empirically defined threshold. Regions of interest (ROIs) were selected manually and the mean fluorescence intensity was calculated within the ROIs. The ROIs were selected to include neurites (for the experiments described in Figs. 2b, c, f, 5a, b, 9d, e, and Supplementary Figs. 8, 9a, b, 10, 11, 12, 14a, b, 15b, d–g and 20a–c), both neurites and somas (Supplementary Figs. 5b and 18), or somas (Fig. 7c, d and Supplementary Fig. 15a). For analyzing the epifluorescent images from the experiments described in Supplementary Figs. 4a, b, c and 9c, d, the mean fluorescence intensity was calculated for entire images. For the live imaging experiment described in Fig. 4a and Supplementary Fig. 6, the mean intensity was calculated on the maximum intensity projection images acquired at each timepoint. ROIs were drawn around neuronal somas and the mean intensity for each individual neuron was normalized to the first timepoint. For the experiments described in Figs. 4c, 5d, e and Supplementary Figs. 13, 14e and 15c, ROIs containing neurites were selected within the images. For each experimental day, a ratio was calculated between the mean intensity before and after incubation with the proteinase. For the experiment described in Supplementary Fig. 14c, d, the images before and after proteinase incubation were aligned, and the mean fluorescence intensity was determined in selected ROIs in corresponding regions of the images.

Analysis of confocal images of immunolabeled beads. For analyzing the confocal images of immunolabeled beads (Fig. 1), the images were segmented based on an empirically defined threshold, to detect the individual beads, and the background signal was removed. The total fluorescence intensity was calculated for each bead, and a mean value was calculated per experiment.

Quantification of TNR at synapses by STED and confocal microscopy. The synapses in the images shown in Figs. 2d and 3 were identified by manual thresholding of the VGlut1 or Syt1 channels, and square regions of interest centered on the individual VGlut1 or Syt1 puncta were excised. For the visualization of synaptic enrichment of TNR, as depicted in Fig. 2d, the excised image segments were automatically rotated to maximally overlap in the DiO channel, and averaged to one single image illustrating TNR localization at an average synapse (following procedures previously described[22,76]). For the enrichment analysis at dendrites and axons, the mean TNR fluorescence intensity was calculated for all image segments in concentric circles of increasing radii. To quantify the amount of newly-emerged TNR epitopes after 12 h specifically at synapses, as shown in Fig. 2e, the mean fluorescence intensity of TNR was estimated in VGlut1-positive pixels. For the correlation of TNR fluorescence to the presynaptic recycling vesicle pool size, as depicted in Fig. 3, the image segments surrounding individual presynapses (determined by the Syt1 channel) were sorted by the mean Syt1 fluorescence intensity, and then binned in five ordinal groups, to include a similar number of synapses. For each experiment, the mean fluorescence was calculated in each bin, and was normalized to the median intensity of the respective experiment. A similar procedure was used to analyze the TNR fluorescence in relation to the postsynaptic spines: image segments were excised for synaptic regions based on the VGlut1 channel, and mushroom-shaped spines were identified manually in these segments through the DiO channel. The spine size (area) was determined by thresholding the DiO signal of each individual image segment and counting the pixels above the threshold. The image segments were sorted by the spine size, and then binned in five ordinal groups, to include a similar number of synapses. For each experiment, the mean fluorescence and size were calculated in each bin, and normalized to the median of the respective experiment. For colocalizing TNR with the excitatory and inhibitory synapse markers VGlut1 and VGAT, an image-wide pixel-by-pixel correlation was first calculated between the images. The pixels indicating a high correlation between the channels were selected, and the TNR amount corresponding to these pixels was calculated as % of the total TNR staining in the images (corrected for background). To analyse the percentage of VGlut1+ and VGAT + synapses that colocalize with TNR, ROIs were drawn around neurites within the images. The VGlut1/VGAT channels were thresholded to identify individual synapses, and the proportion of objects that overlapped with the signal in the TNR channel was quantified.

Characterization of cell types in dissociated neuronal cultures. To count the number of neurons, astrocytes, oligodendrocytes, and microglia, the images were manually thresholded in each channel to segment individual cells. The total number of cells was determined by counting the number of objects in the Hoechst channel. The fraction of each cell type was determined by calculating the percent of objects overlapping with the Hoechst signal, out of the total number of cells. To quantify

the proportion of PNN-associated neurons in dissociated hippocampal cultures at DIV14, the number of WFA + neurons per field of view was counted manually. The total number of neurons was determined automatically by counting the number of objects in the thresholded NeuN image.

Quantification of TNR uptake in astrocytes. ROIs were selected surrounding the GFAP + and NeuN+ cells, based on a manual thresholding procedure. The TNR signal overlapping with these ROIs was quantified, as a percentage of the total TNR signal in the images.

Quantification of TNR at neurites by confocal microscopy. For the comparison of TNR in axons and dendrites as depicted in Fig. 4b and Supplementary Fig. 7, ROIs were selected on the axons and dendrites separately, based on the DiO channel (and the AnkyrinG staining, for Fig. 4b). The mean TNR fluorescence was calculated within these ROIs, indicating the signal density.

Colocalization analysis. For colocalizing TNR and organelles or surface integrins in 2-color STED images, ROIs were drawn around cells to include TNR signal, and an image-wide pixel-by-pixel correlation was first calculated between the images. The pixels indicating a high correlation between each of the channels were selected, and the TNR amount corresponding to these pixels was calculated as % of the total TNR staining in the images. For colocalizing TNR with internalized integrins in confocal images, line scans were drawn through the images and Pearson's correlation was calculated between the two channels. ~400 lines were analyzed per experiment, and the mean correlation coefficient was calculated for each experiment. Afterward, the percentage of correlation coefficients equal to, or larger than 0.7 was calculated for each experiment and normalized to a positive control (two identical secondary antibodies conjugated to different fluorophores). A similar procedure was used for the colocalization of TNR-containing organelles to LysoTracker.

For colocalizing TNR with metabolically labeled glycans or proteins in 2-color STED images, a region of each image was sampled blindly, and the numbers of overlapping and separated spots were determined. The percentage of colocalizing spots was calculated, after which the colocalization percentage of a negative control (immunostaining with an unspecific antibody) was subtracted. To analyse the amount of recombinant TNR that is internalized into synaptic regions in acute rat brain slices, an image-wide pixel-by-pixel correlation was calculated between the VGlut1 and rTNR channels, and the mean correlation was determined.

Analysis of dendritic spine head size following treatment with TNR antibody aggregates. Individual synaptic images were cropped from full images and aligned based on the DiO and eGFP channel, as was described above (see 'Quantification of TNR at synapses by STED and confocal microscopy'). To quantify the average spine head area, the DiO channel was thresholded for each individual image segment, and the pixels above the threshold were counted.

Analysis of Ca^{2+} imaging experiments. ROIs were specified surrounding individual neurons. For the stimulation experiments, the fluorescent signal in each neuron was normalized to the baseline observed in the first few imaging frames, before stimulation. For analyzing the spontaneous activity, spontaneous events were identified as peaks in fluorescence above an empirically determined threshold.

Comparison of old /new TNR epitope localization with 2-color STED. To create the images of the average dendritic spine, image segments containing individual synaptic puncta were manually aligned based on the DiO channel (see 'Quantification of TNR at synapses by STED and confocal microscopy'). To calculate the percentage of newly-emerged epitopes that colocalize with old epitopes, the images were thresholded in the channel corresponding to the 'new epitopes', to find individual spots. The % colocalization was determined by the number of new epitope spots that also contained signal from the 'old epitopes' channel.

Comparison of extracellular and intracellular TNR in slices from 5xFAD mice and mice injected with kainic acid. For each slice, ROIs were selected in intracellular somatic (identified as an envelope of the calreticulin immunostaining, which labels the ER) and adjacent, presumably extracellular regions. The mean fluorescence intensity was calculated in the ROIs following subtraction of the background signal. The overall mean was determined for the extracellular and intracellular TNR signals, for each experimental condition. These were then normalized to the mean of extracellular TNR in the control mice.

Analysis of correlated fluorescence and nanoSIMS images. The analysis was done as previously described[72]. Briefly, the nanoSIMS images and the fluorescence images were overlayed, and circular ROIs (1.2 μm diameter) were selected in TNR or calreticulin-rich areas, or within cell nuclei, based on the fluorescence images. The average values were then calculated in the corresponding areas in the nanoSIMS images, and the respective isotope ratios were determined. This ratio was then expressed as fold over the baseline isotopic ratio of $^{13}C/^{12}C$ (or $^{13}C^{14}N/^{12}C^{14}N$), measured in regions of the embedded sample, outside the biological specimens.

Analysis of recombinant TNR (rTNR) Western blots. For each blot, the fluorescence intensity of the bands was determined by manually selecting a rectangular ROI surrounding the band and correcting for local background (see[77]).

Statistical analysis. Statistical significance was calculated with two-tailed t-tests, Mann-Whitney U-tests, Wilcoxon signed rank test, ANOVA, Kruskal-Wallis or Friedman tests, according to the type of data analyzed. Post-hoc analyses were calculated with the tests that were recommended and implemented in the software packages used for the respective tests (GraphPad Prism version 8, GraphPad Software, USA; Matlab version 2017b, the Mathworks Inc., Natick, MA, USA), as noted in the figure legends. For repeated-measures ANOVA, the Greenhouse-Geisser adjustment was applied to account for any departures from sphericity. Correlations were calculated with Pearson's R or Spearman's ρ. A *p*-value of < 0.05 was considered statistically significant.

Reporting summary. Further information on research design is available in the Nature Research Reporting Summary linked to this article.

Data availability
Image data are available from the corresponding author on reasonable request. Source data are provided with this paper.

Code availability
Code is available upon request from Tal M. Dankovich and Silvio O. Rizzoli.

References
1. Ferrer-Ferrer, M. & Dityatev, A. Shaping synapses by the neural extracellular matrix. *Front. Neuroanat.* **12**, 40 (2018).
2. Fornasiero, E. F. et al. Precisely measured protein lifetimes in the mouse brain reveal differences across tissues and subcellular fractions. *Nat. Commun.* **9**, 4230 (2018).
3. Dörrbaum, A. R., Kochen, L., Langer, J. D. & Schuman, E. M. Local and global influences on protein turnover in neurons and glia. *Elife* **7**, (2018).
4. Dansie, L. E. & Ethell, I. M. Casting a net on dendritic spines: the extracellular matrix and its receptors. *Dev. Neurobiol.* **71**, 956–981 (2011).
5. Wang, D. & Fawcett, J. The perineuronal net and the control of cns plasticity. *Cell Tissue Res.* **349**, 147–160 (2012).
6. Nägerl, U. V., Willig, K. I., Hein, B., Hell, S. W. & Bonhoeffer, T. Live-cell imaging of dendritic spines by STED microscopy. *Proc. Natl Acad. Sci. USA* **105**, 18982–18987 (2008).
7. Wegner, W., Mott, A. C., Grant, S. G. N., Steffens, H. & Willig, K. I. In vivo STED microscopy visualizes PSD95 sub-structures and morphological changes over several hours in the mouse visual cortex. *Sci. Rep.* **8**, 219 (2018).
8. Willig, K. I. et al. Nanoscopy of filamentous actin in cortical dendrites of a living mouse. *Biophys. J.* **106**, L01–L03 (2014).
9. Dityatev, A., Schachner, M. & Sonderegger, P. The dual role of the extracellular matrix in synaptic plasticity and homeostasis. *Nat. Rev. Neurosci.* **11**, 735–746 (2010).
10. Krishnaswamy, V. R., Benbenishty, A., Blinder, P. & Sagi, I. Demystifying the extracellular matrix and its proteolytic remodeling in the brain: structural and functional insights. *Cell. Mol. Life Sci.* **76**, 3229–3248 (2019).
11. Dityatev, A. et al. Activity-dependent formation and functions of chondroitin sulfate-rich extracellular matrix of perineuronal nets. *Dev. Neurobiol.* **67**, 570–588 (2007).
12. Korotchenko, S., Zanacchi, F. C., Diaspro, A. & Dityatev, A. Zooming in on the (Peri)synaptic Extracellular Matrix. in *Neuromethods* 187–203 https://doi.org/10.1007/978-1-4614-9179-8_10 (2014).
13. Rizzoli, S. O. Synaptic vesicle recycling: steps and principles. *EMBO J.* **33**, 788–822 (2014).
14. Rizzoli, S. O. & Betz, W. J. Synaptic vesicle pools. *Nat. Rev. Neurosci.* **6**, 57–69 (2005).
15. Ehlers, M. D. Reinsertion or degradation of AMPA receptors determined by activity-dependent endocytic sorting. *Neuron* **28**, 511–525 (2000).
16. Rissin, D. M. et al. Single-molecule enzyme-linked immunosorbent assay detects serum proteins at subfemtomolar concentrations. *Nat. Biotechnol.* **28**, 595–599 (2010).
17. Geissler, M. et al. Primary hippocampal neurons, which lack four crucial extracellular matrix molecules, display abnormalities of synaptic structure and function and severe deficits in perineuronal net formation. *J. Neurosci.* **33**, 7742–7755 (2013).

18. Wanner, I. B. et al. A new in vitro model of the glial scar inhibits axon growth. *Glia* **56**, 1691–1709 (2008).
19. Morganti, M. C., Taylor, J., Pesheva, P. & Schachner, M. Oligodendrocyte-derived J1-160/180 extracellular matrix glycoproteins are adhesive or repulsive depending on the partner cell type and time of interaction. *Exp. Neurol.* **109**, 98–110 (1990).
20. Truckenbrodt, S. et al. Newly produced synaptic vesicle proteins are preferentially used in synaptic transmission. *EMBO J.* **37**, 1–24 (2018).
21. Kraszewski, K., Daniell, L., Mundigl, O. & De Camilli, P. Mobility of synaptic vesicles in nerve endings monitored by recovery from photobleaching of synaptic vesicle-associated fluorescence. *J. Neurosci.* **16**, 5905–5913 (1996).
22. Wilhelm, B. G., Groemer, T. W. & Rizzoli, S. O. The same synaptic vesicles drive active and spontaneous release. *Nat. Neurosci.* **13**, 1454–1456 (2010).
23. Hua, Y. et al. A readily retrievable pool of synaptic vesicles. *Nat. Neurosci.* **14**, 833–839 (2011).
24. Humeau, Y. & Choquet, D. The next generation of approaches to investigate the link between synaptic plasticity and learning. *Nat. Neurosci.* **22**, 1536–1543 (2019).
25. Brückner, G., Grosche, J., Hartlage-Rübsamen, M., Schmidt, S. & Schachner, M. Region and lamina-specific distribution of extracellular matrix proteoglycans, hyaluronan and tenascin-R in the mouse hippocampal formation. *J. Chem. Neuroanat.* **26**, 37–50 (2003).
26. Kaech, S. & Banker, G. Culturing hippocampal neurons. *Nat. Protoc.* **1**, 2406–2415 (2006).
27. Morawski, M. et al. Tenascin-R promotes assembly of the extracellular matrix of perineuronal nets via clustering of aggrecan. *Philos. Trans. R. Soc. Lond. B. Biol. Sci.* **369**, 20140046 (2014).
28. Tischbirek, C. H. et al. Use-dependent inhibition of synaptic transmission by the secretion of intravesicularly accumulated antipsychotic drugs. *Neuron* **74**, 830–844 (2012).
29. Kerrisk, M. E., Cingolani, L. A. & Koleske, A. J. ECM receptors in neuronal structure, synaptic plasticity, and behavior. *Prog. Brain Res.* **214**, 101–131 (2014). in.
30. Liao, H. et al. β 1 Integrin-mediated Effects of Tenascin-R Domains EGFL and FN6-8 on neural stem/progenitor cell proliferation and differentiation in vitro. *J. Biol. Chem.* **283**, 27927–27936 (2008).
31. Huang, Z. et al. Distinct roles of the beta1-class integrins at the developing and the mature hippocampal excitatory synapse. *J. Neurosci.* **26**, 11208–11219 (2006).
32. Clegg, D. O. Integrins in the development function and dysfunction of the nervous system. *Front. Biosci.* **8**, 1020 (2003).
33. Shi, F. & Sottile, J. Caveolin-1-dependent β1 integrin endocytosis is a critical regulator of fibronectin turnover. *J. Cell Sci.* **121**, 2360–2371 (2008).
34. Südhof, T. C. The synaptic vesicle cycle. *Annu. Rev. Neurosci.* **27**, 509–547 (2004).
35. Wratil, P. R., Horstkorte, R. & Reutter, W. Metabolic glycoengineering with N-acyl side chain modified mannosamines. *Angew. Chem. Int. Ed.* **55**, 9482–9512 (2016).
36. Saka, S. K. et al. Multi-protein assemblies underlie the mesoscale organization of the plasma membrane. *Nat. Commun.* **5**, 4509 (2014).
37. Zamze, S. et al. Glycosylation of a CNS-specific extracellular matrix glycoprotein, tenascin-R, is dominated by O-linked sialylated glycans and 'brain-type' neutral N-glycans. *Glycobiology* **9**, 823–831 (1999).
38. Woodworth, A., Pesheva, P., Fiete, D. & Baenziger, J. U. Neuronal-specific synthesis and glycosylation of tenascin-R. *J. Biol. Chem.* **279**, 10413–10421 (2004).
39. Woodworth, A., Fiete, D. & Baenziger, J. U. Spatial and temporal regulation of tenascin-R glycosylation in the cerebellum. *J. Biol. Chem.* **277**, 50941–50947 (2002).
40. Dieterich, D. C. et al. In situ visualization and dynamics of newly synthesized proteins in rat hippocampal neurons. *Nat. Neurosci.* **13**, 897–905 (2010).
41. Richter, K. N., Patzelt, C., Phan, N. T. N. & Rizzoli, S. O. Antibody-driven capture of synaptic vesicle proteins on the plasma membrane enables the analysis of their interactions with other synaptic proteins. *Sci. Rep.* **9**, 9231 (2019).
42. Cohen, M. W., Hoffstrom, B. G. & DeSimone, D. W. Active zones on motor nerve terminals contain α3β1 integrin. *J. Neurosci.* **20**, 4912–4921 (2000).
43. Wang, Q., Han, T. H., Nguyen, P., Jarnik, M. & Serpe, M. Tenectin recruits integrin to stabilize bouton architecture and regulate vesicle release at the Drosophila neuromuscular junction. *Elife* **7**, (2018).
44. Son, Y.-J. et al. The synaptic vesicle protein SV2 is complexed with an α5-containing laminin on the nerve terminal surface. *J. Biol. Chem.* **275**, 451–460 (2000).
45. Chang, W.-P. & Sudhof, T. C. SV2 Renders Primed Synaptic Vesicles Competent for Ca2+-induced Exocytosis. *J. Neurosci.* **29**, 883–897 (2009).
46. Xiao, Z.-C. et al. Tenascin-R Is a Functional Modulator of Sodium Channel β Subunits. *J. Biol. Chem.* **274**, 26511–26517 (1999).
47. Broekaart, D. W. M. et al. The matrix metalloproteinase inhibitor IPR-179 has antiseizure and antiepileptogenic effects. *J. Clin. Invest.* **131**, (2021).
48. Saka, S. K. et al. Correlated optical and isotopic nanoscopy. *Nat. Commun.* https://doi.org/10.1038/ncomms4664 (2014).
49. Stawarski, M., Stefaniuk, M. & Wlodarczyk, J. Matrix metalloproteinase-9 involvement in the structural plasticity of dendritic spines. *Front. Neuroanat.* **8**, (2014).
50. Schanzenbächer, C. T. et al. Nascent proteome remodeling following homeostatic scaling at hippocampal synapses. *Neuron* **92**, 358–371 (2016).
51. Niekisch, H. et al. Learning induces transient upregulation of brevican in the auditory cortex during consolidation of long-term memories. *J. Neurosci.* **39**, 7049–7060 (2019).
52. Yasumatsu, N., Matsuzaki, M., Miyazaki, T., Noguchi, J. & Kasai, H. Principles of long-term dynamics of dendritic spines. *J. Neurosci.* **28**, 13592–13608 (2008).
53. Urban, N. T., Willig, K. I., Hell, S. W. & Nägerl, U. V. STED nanoscopy of actin dynamics in synapses deep inside living brain slices. *Biophys. J.* **101**, 1277–1284 (2011).
54. Wegner, W. et al. In vivo mouse and live cell STED microscopy of neuronal actin plasticity using far-red emitting fluorescent proteins. *Sci. Rep.* **7**, 11781 (2017).
55. Berning, S., Willig, K. I., Steffens, H., Dibaj, P. & Hell, S. W. Nanoscopy in a living mouse brain. *Science* **335**, 551 (2012).
56. Miyata, S. & Kitagawa, H. Formation and remodeling of the brain extracellular matrix in neural plasticity: roles of chondroitin sulfate and hyaluronan. *Biochim. Biophys. Acta - Gen. Subj.* **1861**, 2420–2434 (2017).
57. Banker, G. A. & Cowan, W. M. Rat hippocampal neurons in dispersed cell culture. *Brain Res.* **126**, 397–425 (1977).
58. Stoppini, L., Buchs, P.-A. & Muller, D. A simple method for organotypic cultures of nervous tissue. *J. Neurosci. Methods* **37**, 173–182 (1991).
59. Hartelt, N. et al. Imaging of respiratory network topology in living brainstem slices. *Mol. Cell. Neurosci.* **37**, 425–431 (2008).
60. Okuda, H. et al. Chondroitin sulfate proteoglycan tenascin-R regulates glutamate uptake by adult brain astrocytes. *J. Biol. Chem.* **289**, 2620–2631 (2014).
61. Mitlöhner, J. et al. Dopamine receptor activation modulates the integrity of the perisynaptic extracellular matrix at excitatory synapses. *Cells* **9**, 260 (2020).
62. López-Murcia, F. J., Reim, K., Jahn, O., Taschenberger, H. & Brose, N. Acute complexin knockout abates spontaneous and evoked transmitter release. *Cell Rep.* https://doi.org/10.1016/j.celrep.2019.02.030 (2019).
63. Sigworth, F. J. Design of the EPC-9, a computer-controlled patch-clamp amplifier. 1. Hardware. *J. Neurosci. Methods* **56**, 195–202 (1995).
64. Sigworth, F. J., Affolter, H. & Neher, E. Design of the EPC-9, a computer-controlled patch-clamp amplifier. 2. Software. *J. Neurosci. Methods* **56**, 203–215 (1995).
65. Kononenko, N. L. et al. Clathrin/AP-2 mediate synaptic vesicle reformation from endosome-like vacuoles but are not essential for membrane retrieval at central synapses. *Neuron* **82**, 981–988 (2014).
66. Rizzoli, S. O. et al. Evidence for early endosome-like fusion of recently endocytosed synaptic vesicles. *Traffic* https://doi.org/10.1111/j.1600-0854.2006.00466.x (2006).
67. Bennett, M. K., Calakos, N., Kreiner, T. & Scheller, R. H. Synaptic vesicle membrane proteins interact to form a multimeric complex. *J. Cell Biol.* **116**, 761–775 (1992).
68. Dommerholt, J., Rutjes, F. P. J. T. & van Delft, F. L. Strain-promoted 1,3-dipolar cycloaddition of cycloalkynes and organic azides. *Top. Curr. Chem.* **374**, 16 (2016).
69. Fernández-Alfonso, T. & Ryan, T. A. The kinetics of synaptic vesicle pool depletion at CNS synaptic terminals. *Neuron* **41**, 943–953 (2004).
70. Kaushik, R. et al. Traditional japanese herbal medicine yokukansan targets distinct but overlapping mechanisms in aged mice and in the 5xFAD mouse model of Alzheimer's Disease. *Front. Aging Neurosci.* https://doi.org/10.3389/fnagi.2018.00411 (2018).
71. Oakley, H. et al. Intraneuronal β-amyloid aggregates, neurodegeneration, and neuron loss in transgenic mice with five familial Alzheimer's disease mutations: Potential factors in amyloid plaque formation. *J. Neurosci.* https://doi.org/10.1523/JNEUROSCI.1202-06.2006 (2006).
72. Jähne, S. et al. Presynaptic activity and protein turnover are correlated at the single-synapse level. *Cell Rep.* **34**, 108841 (2021).
73. Bekkers, J. M. & Stevens, C. F. NMDA and non-NMDA receptors are co-localized at individual excitatory synapses in cultured rat hippocampus. *Nature* **341**, 230–233 (1989).
74. Dieterich, D. C. et al. Caldendrin–Jacob: a protein liaison that couples NMDA receptor signalling to the nucleus. *PLoS Biol.* **6**, e34 (2008).
75. Behnisch, T. et al. Nuclear translocation of Jacob in hippocampal neurons after stimuli inducing long-term potentiation but not long-term depression. *PLoS ONE* **6**, e17276 (2011).

80

76. Wilhelm, B. G. et al. Composition of isolated synaptic boutons reveals the amounts of vesicle trafficking proteins. *Sci. (80-.).* **344**, 1023–1028 (2014).
77. Bethani, I. et al. The specificity of SNARE pairing in biological membranes is mediated by both proof-reading and spatial segregation. *EMBO J.* **26**, 3981–3992 (2007).
78. Horton, A. C. & Ehlers, M. D. Dual modes of endoplasmic reticulum-to-golgi transport in dendrites revealed by live-cell imaging. *J. Neurosci.* **23**, 6188–6199 (2003).
79. Pierce, J. P., Mayer, T. & McCarthy, J. B. Evidence for a satellite secretory pathway in neuronal dendritic spines. *Curr. Biol.* **11**, 351–355 (2001).
80. Kabatas, S. et al. Fluorinated nanobodies for targeted molecular imaging of biological samples using nanoscale secondary ion mass spectrometry. *J. Anal. At. Spectrom.* https://doi.org/10.1039/c9ja00117d (2019).
81. Vreja, I. C. et al. Secondary-ion mass spectrometry of genetically encoded targets. *Angew. Chem. - Int. Ed.* **54**, 5784–5788 (2015).

Acknowledgements

Author contributions

S.O.R., T.M.D. and A.D. designed the experiments and statistical analysis. T.M.D. performed all fluorescence imaging experiments and the cell-surface biotinylation experiments, with the following exceptions: the fluorescence imaging of neurocan, hyaluronan and WFA was performed by G.C.P. and the imaging of metabolically labeled proteins and glycans was performed by P.E.G., T.M.D. and L.H.M.O. performed the co-immunoprecipitation experiments and the Western blotting. H.A.H. and S.K. assisted with cellular experiments. J.D. performed the fluorescence imaging of the brain sections from kainic acid-treated as well as the sections from 5xFAD mice. The AAV-based TNR shRNA vectors were designed, produced and provided by R.K., and the viral infections were performed by S.B. and B.C. The FRAP experiments were performed by R.K. The electrophysiology experiments were performed by G.B. T.M.D. and V.K. prepared the samples for nanoSIMS. NanoSIMS imaging was performed by P.A.G. and K.G. The data analysis was performed by T.M.D. and S.O.R. The manuscript was written by T.M.D. and S.O.R. and edited by A.D.

Competing interests

Additional information

Publisher's note Springer Nature remains neutral with regard to jurisdictional claims in published maps and institutional affiliations.

81

Extracellular matrix remodeling through endocytosis and resurfacing of Tenascin-R

Tal M. Dankovich[1,2*], Rahul Kaushik[3,4], Linda H.M. Olsthoorn[2,5], Gabriel Cassinelli Petersen[1], Philipp Emanuel Giro[1], Verena Kluever[1], Paola Agüi-Gonzalez[1], Katharina Grewe[1], Guobin Bao[1,6], Sabine Beuermann[7], Hannah Abdul Hadi[1], Jose Doeren[1], Simon Klöppner[1], Benjamin H. Cooper[7], Alexander Dityatev[3,4,8], Silvio O. Rizzoli[1,9*]

Affiliations
[1]University Medical Center Göttingen, Institute for Neuro- and Sensory Physiology, Excellence Cluster Multiscale Bioimaging, Göttingen, Germany.
[2]International Max Planck Research School for Neuroscience, Göttingen, Germany.
[3]Molecular Neuroplasticity, German Center for Neurodegenerative Diseases (DZNE), Magdeburg, Germany.
[4]Center for Behavioral Brain Sciences (CBBS), Magdeburg, Germany.
[5]Max Planck Institute for Biophysical Chemistry, Göttingen, Germany.
[6]University Medical Center Göttingen, Institute of Pharmacology and Toxicology, Göttingen, Germany.
[7]Max Planck Institute for Experimental Medicine, Göttingen, Germany.
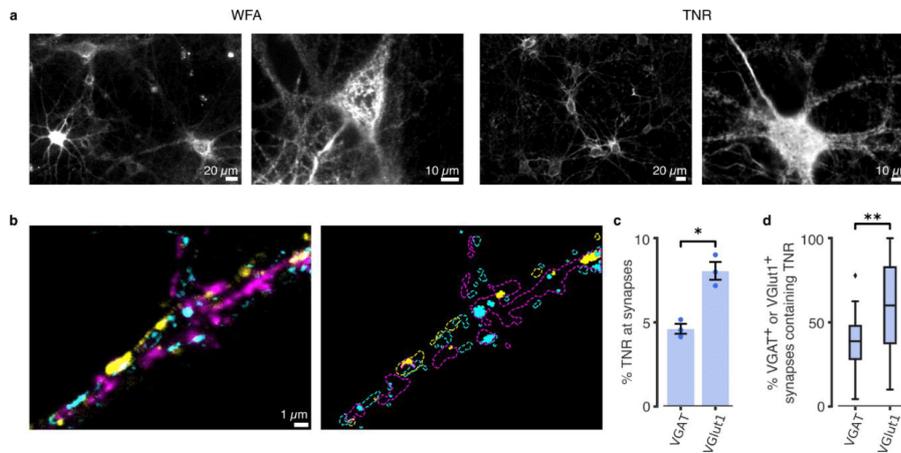[8]Medical Faculty, Otto von Guericke University, Magdeburg, Germany.
[9]Biostructural Imaging of Neurodegeneration (BIN) Center, Göttingen, Germany.
***Correspondence**: Tal M. Dankovich: tal.dankovich@med.uni-goettingen.de, Silvio O. Rizzoli: srizzol@gwdg.de

Included in this PDF:
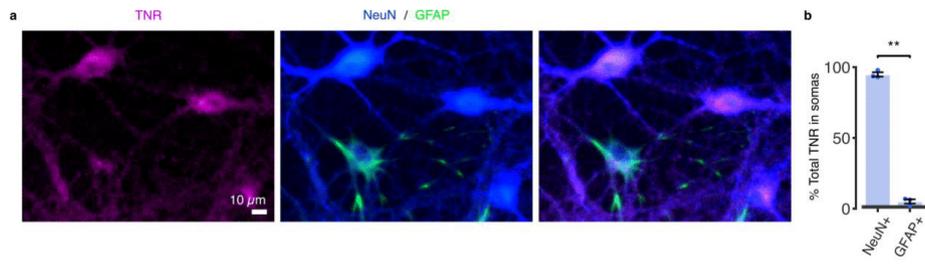Supplementary Figure 1-20
References for Supplementary Figures 1-20

Supplementary Figure 1 Antibody-labeled TNR molecules are present in the perineuronal net and at synapses, and are extremely stable. a, We fixed neuronal cultures at 14 days *in vitro* (DIV14), and we then labeled them with *Wisteria floribunda* agglutin (WFA), which binds chondroitin-sulfate (CS)-bearing proteoglycans [1] (left), or with TNR antibodies (right), and imaged them with epifluorescence microscopy. Both labels exhibited lattice-like structures that surrounded the somas and proximal dendrites of a subset of neurons (perineuronal nets; PNNs), which also suggests that the ECM has reached a sufficient level of maturity in these cultures. Scale bar = 20 µm (left panels), 10 µm (right panels). N = 3 independent experiments. **b**, To assess the amount of TNR at excitatory and inhibitory presynaptic boutons, we labeled all TNR epitopes by incubating live neurons with fluorophore-conjugated TNR antibodies (magenta). Glutamate-releasing (excitatory) and GABA-releasing (inhibitory) boutons were determined by immunostaining the synaptic vesicle markers VGlut1 (yellow) and VGAT (cyan), respectively. The right panel shows the boundaries of the boutons and of TNR domains. The regions where high intensities of TNR and synaptic signals overlap are indicated by full shading in yellow or cyan. TNR, VGlut1 and VGAT are imaged in confocal microscopy. Scale bar: 1 µm. **c-d**, We determined the colocalization of TNR with VGlut1- and VGAT-positive presynapses. We measured the amount of TNR in fully colocalizing pixels, as a percentage of the total TNR staining in the images (panel c). A higher proportion of all TNR epitopes can be found at excitatory synapses. Data represent the mean ± SEM, with dots indicating independent experiments. To determine the proportion of synapses that overlap with TNR signal, we thresholded the VGlut1/VGAT channels to identify individual synapses, and determined the percentage of these synapses that overlap with TNR signal (panel d). We found that the percentage of TNR+/VGlut1+ synapses (~60%) is significantly higher than the percentage of TNR+/VGAT+ synapses (~40%). Boxes show median (mid-line) and quartiles, and whiskers show minimum and maximum values. Outliers were omitted according to inter-quartile range (IQR) proximity (exceeding 1.5*IQR). N = 3 experiments, 15 neurons imaged per experiment.Statistical significance was evaluated using two-sided paired *t*-tests: t = 4.684, *p = 0.043 (panel c); t = 3.312, **p = 0.003 (panel d).

2
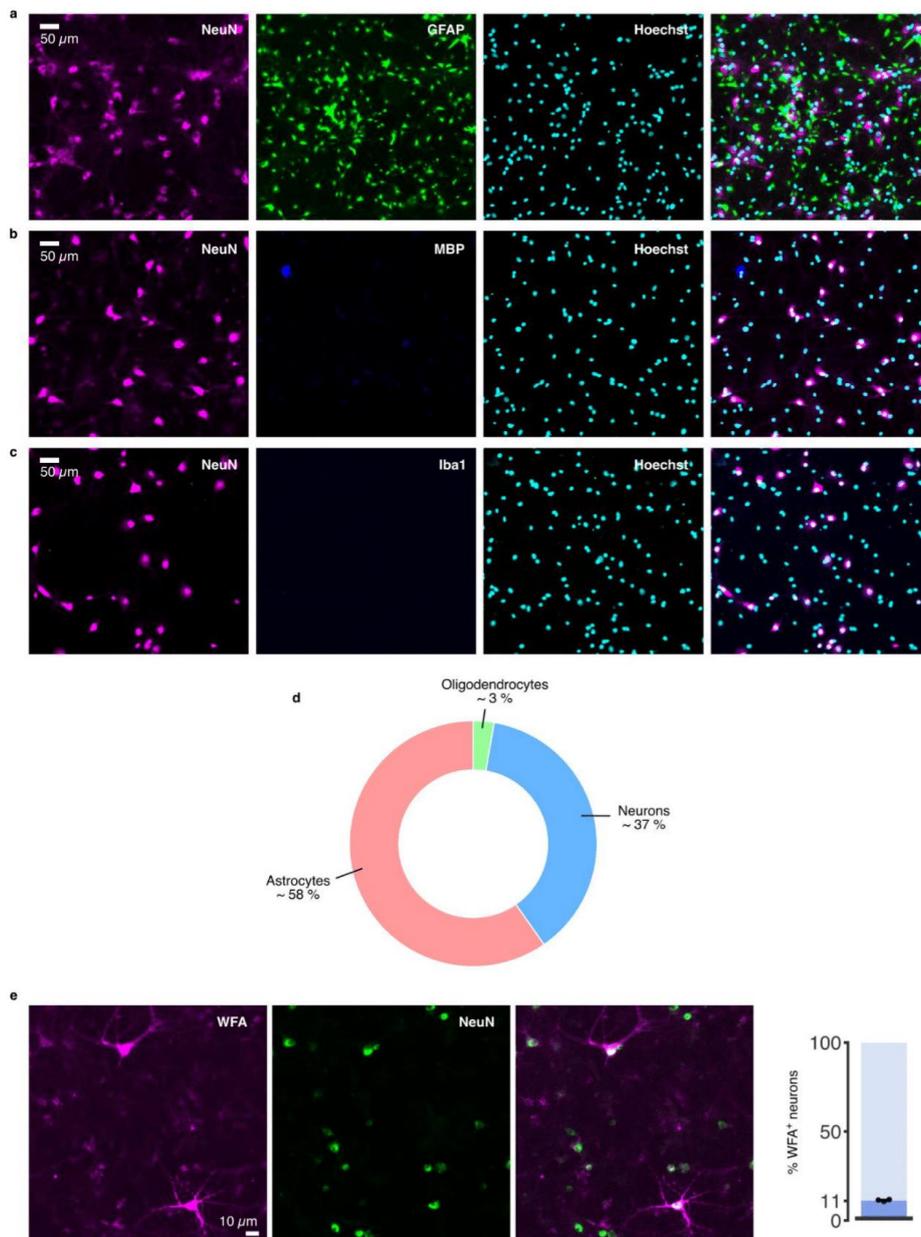
Supplementary Figure 2 Characterization of the dissociated neuronal cultures used in the study. a-d, To determine the fraction of different cell types in our cultures at 14 DIV, we performed a co-immunostaining with different cell-specific markers, and imaged large fields of view in epifluorescence microscopy. We counted cells overlapping with NeuN, GFAP (panel a), myelin basic protein (MBP) (panel b) or Iba1 (panel c) signals to quantify the number of neurons, astrocytes, oligodendrocytes and microglia, respectively. The cell nuclei were identified using a Hoechst staining. Scale bar = 50 μm. **d**, A quantification of the mean fraction of each cell type

3

in the culture. N = 3 independent experiments. **e**, To determine the proportion of PNN-associated neurons at 14 DIV, we fixed neurons and stained them with WFA (magenta), to detect PNNs, and with NeuN antibodies (green), to label all neurons. We then imaged large fields of view with epifluorescence microscopy and counted the number of WFA+ neurons. We determined the proportion of PNN-associated neurons in our cultures to be ~11%. N = 3 individual experiments, 10 images per datapoint. Data represent the mean ± SEM, with dots indicating independent experiments.

4

a TNR   NeuN / GFAP   **b**

10 μm

Supplementary Figure 3 A minimal amount of internalized TNR is found in astrocytes. We checked whether recycling TNR epitopes could be detected within astrocytes by co-immunostaining cultures with the astrocytic marker GFAP and the neuronal marker NeuN (using an antibody that recognizes multiple isoforms of the RNA-binding protein FOX-3, localizing to both the nuclei and the cytoplasm [2]). This staining reveals very strongly neuronal cell bodies and the main neurites of neurons, with only very low background in astrocytes. **a**, We labeled newly-emerged TNR epitopes 12 hours post-blocking, by applying fluorophore-conjugated antibodies for 1 hour. After a further incubation of 12 hours, to allow for internalization, we stripped the surface-bound epitopes using proteinase K. We then fixed the neurons and immunostained them with GFAP and NeuN to distinguish astrocytes and neurons, and imaged these with epifluorescence microscopy. The TNR signal was predominantly present in NeuN+/GFAP- cells, and was significantly weaker in GFAP+ cells. Scale bar = 10 μm. **b**, We quantified the TNR signal in NeuN+/GFAP- and GFAP+ regions of interest as a percentage of the total TNR staining in the images. We found that only ~5% of the internalized TNR could be detected in GFAP+ cells, confirming that this process occurs predominantly in neurons. N = 3 independent experiments, at least 10 images per datapoint. Statistical significance was evaluated using a two-sided paired *t*-test (t = 29.49, **p = 0.001). Data represent the mean ± SEM, with dots indicating individual experiments.

5

a

	24 h	48 h	72 h	96 h

All epitopes

New epitopes

10 μm

b

Fluorescence intensity (normalized)

Time (h)

Fluorescence intensity (normalized)

Time (h)

c

Day 0　　　Day 3

rTNR

20 μm

ns

Fluorescence intensity (normalized)

Day 0　Day 3

6
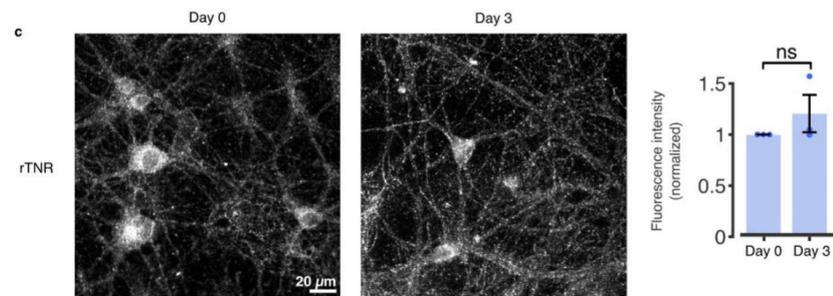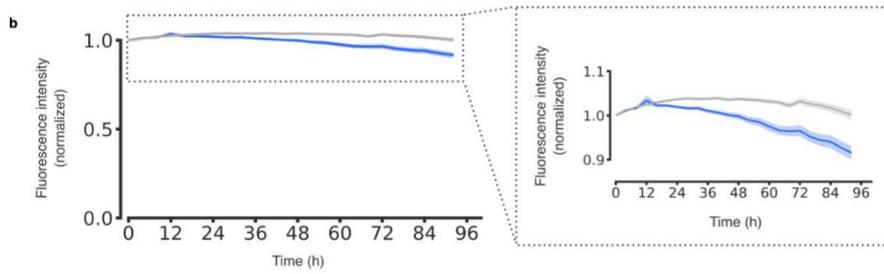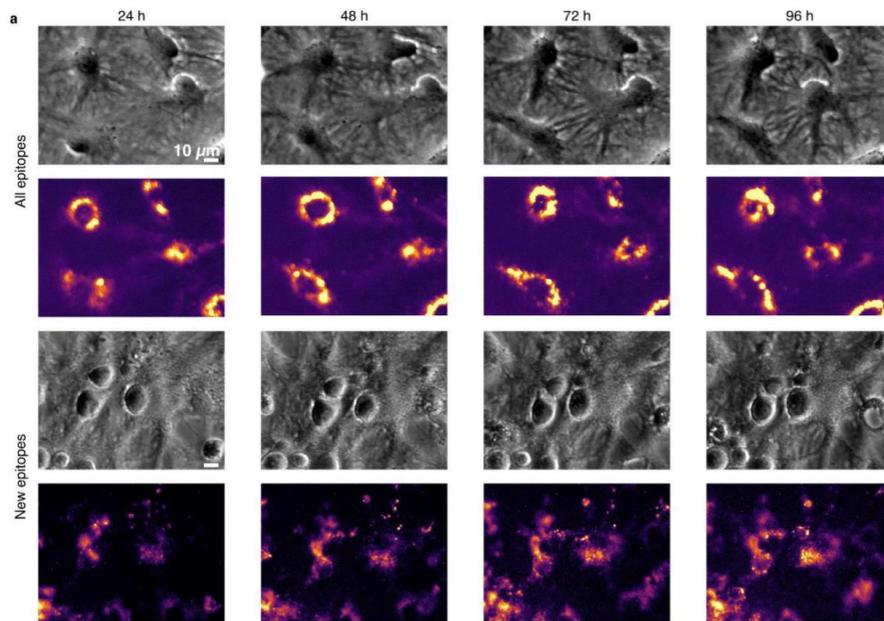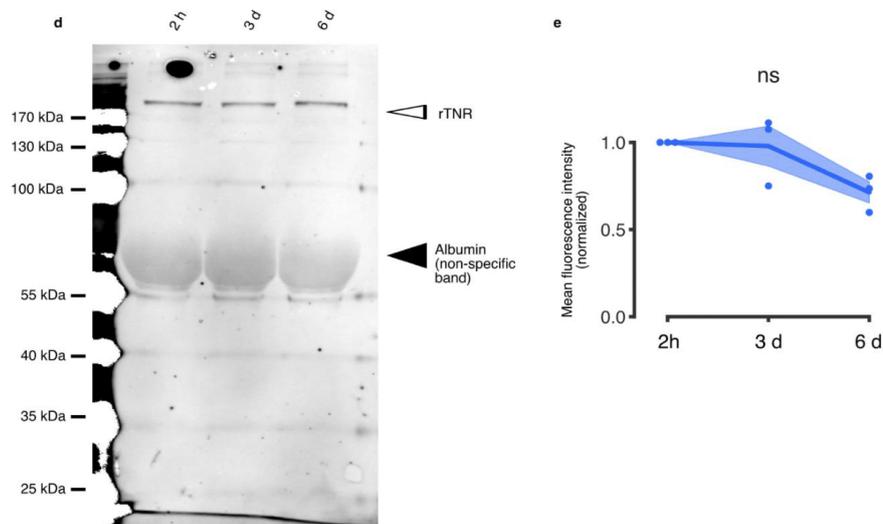
Supplementary Figure 4 TNR is degraded slowly in neuronal cultures. a-b, Either all TNR molecules or newly-emerged TNR molecules (4 hours post-blocking) were labeled by applying fluorophore-conjugated TNR antibodies for 1 hour. We then imaged the neurons for up to 96 hours using an automated cell incubator/microscope setup (BioSpa Live Cell Analysis System, BioTek, USA). **a**, Top panels: phase-contrast images of a single field of view after 1, 2, 3 and 4 days. Bottom panels: the corresponding images in the fluorescent channel. Scale bar = 10 µm. **b**, The graph shows the mean fluorescence intensity, analyzed over the entire images, normalized to the t_0 timepoint. A very small overall loss of signal is seen, confirming the slow degradation and turnover of TNR, as known from the literature. Blue and gray lines represent new and all epitopes, respectively. N = 3 independent experiments, >100 neurons imaged per experiment. Data represent the mean (line) ± SEM (shaded region). **c**, We pulsed the neuronal cultures with a His-tagged recombinant TNR (rTNR), and fixed the neurons immediately after or following a 3-day incubation. We then immunostained the neurons with antibodies against His tag and imaged these with epifluorescence microscopy. Neurons show similar amounts of rTNR at day 0 and day 3 following the pulse. Scale bar = 20 µm. A quantification of the mean fluorescence intensity expressed as fold over background, normalized to the 'day 0' condition, confirmed that there is no significant degradation of rTNR after 3 days. N = 3 independent experiments, 5 images per datapoint. Statistical significance was evaluated using a two-sided paired *t*-test (t = 1.126, *p* = 0.377). Data represent the mean ± SEM, with dots indicating independent experiments. **d**, We assessed the amounts of rTNR after 2 hours, 3 days and 6 days of incubation with neuronal cultures using Western blotting. A typical example is shown here. **e**, A quantification of the rTNR band intensities (normalized), demonstrates only a minor reduction of rTNR. This is in line with the long lifetime of TNR in cultures (half-life of ~7 days [3]). N = 3 independent experiments. Statistical significance was assessed using repeated-measures one-way ANOVA ($F_{1.045, 2.09}$ = 7.565, *p* = 0.106). Data represent the mean (lines) ± SEM (shaded regions); dots indicate the individual experiments. The black arrowhead indicates the large non-specific band induced by the presence of albumin, which is extremely abundant in the cultures (similar to the situation in serum, which has been well described in the literature [4–6].

7
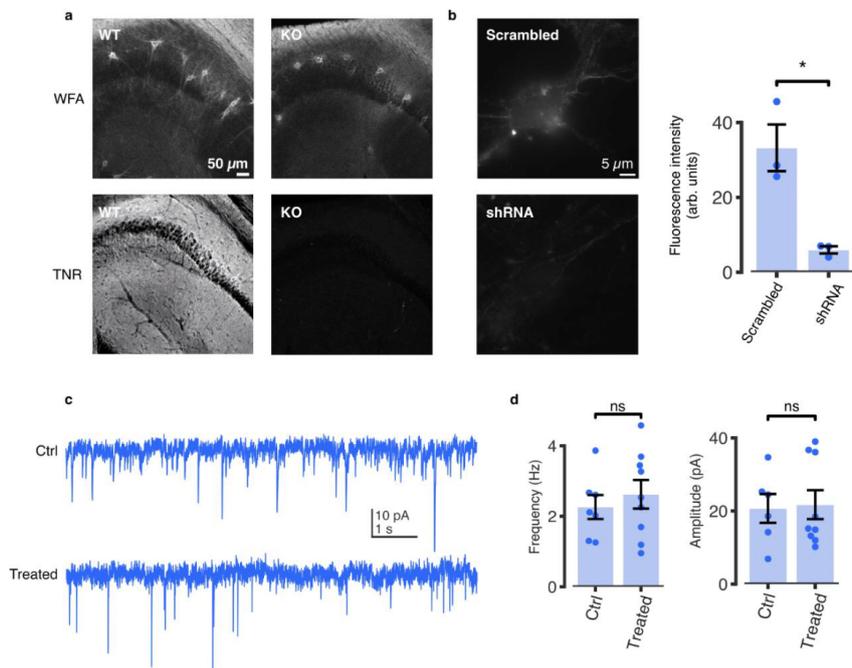
Supplementary Figure 5 Validation of TNR antibodies. a-b, The TNR antibodies used throughout this study were validated in both knock-out and knockdown neurons. **a**, Hippocampal slices of Brevican/TNR KO mice, which were generated by cross-breading of TNR and brevican KO mice [13,14] imaged in epifluorescence microscopy. Top panels: *Wisteria floribunda* agglutin (WFA) staining. Bottom panels: TNR staining. The TNR signal is entirely lost in the KO (right) as compared to wildtype (WT) slices (left). Hippocampal CA2 regions are shown. Scale bar = 50 µm. N = 9 sections from 3 different mice **b**, Neuronal cultures were infected at DIV7 with AAV vectors co-expressing eGFP together with shRNA against TNR, or a scrambled control. Sample images of neurons fixed at DIV21 from scrambled- (top panel) or shRNA-treated (KD) cultures (bottom panel). Scale bar = 5 µm. An analysis of the mean fluorescence intensity (from epifluorescence microscopy experiments) indicates that TNR is significantly reduced in KD cultures, to ~ 20% of the amount in untreated cultures. N = 3 independent experiments, at least 10 neurons imaged per datapoint. Statistical significance was evaluated using a two-sided Student's *t*-test (t = 4.562, *p = 0.045). The slow turnover of TNR, with a half-life of ~7 days in rat neuronal cultures [3] suggests that ~25% of the TNR should still be present after a knockdown treatment of two weeks. At the same time, this experiment was performed in mouse cultures, for which the AAV vectors were optimized, while other measurements from this work, and from the literature, refer to rat cultures. This implies that turnover values may be somewhat different in this experiment, which was performed solely to verify the antibodies used here. **c-d**, Treatment with TNR antibodies does not affect synaptic transmission. **c**, We measured miniature EPSCs in control rat hippocampal cultures (top) and in cultures treated with TNR antibodies (bottom). Scale bar = 10 pA (vertical axis) and 1 s (horizontal axis). **d**, We analyzed the mEPSC frequency and amplitude in the cultures, and found no significant differences. N = 7 independent experiments for control and 9 for cultures treated with TNR antibodies. Statistical significance was evaluated using two-sided Mann-Whitney U tests (U = 28, p = 0.758; U = 27, p > 0.999 for the comparison of frequency and amplitude, respectively). Data represent the mean ± SEM, with dots indicating independent experiments.

8

89
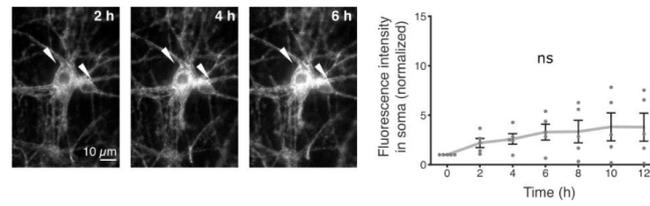
Supplementary Figure 6 TNR molecules endocytose over several hours. All TNR molecules were labeled by applying fluorophore-conjugated TNR antibodies for 1 hour, and were monitored by live epifluorescence imaging over 12 hours. TNR molecules accumulate in the soma over time, but many do not appear to change their location, and neurites remain fully visible over time. Arrowheads indicate cell somas. Scale bar = 10 µm. The plot shows the mean fluorescence intensity in the cell somas, normalized to the t_0 timepoint. A significant increase in the signal over time confirms the suggestion that some proportion of the TNR molecules are endocytosed. N = 5 independent experiments. Statistical significance was evaluated using a two-sided Mann-Whitney U test between the t_0 timepoint and the all sequential timepoints (U = 25, *p = 0.016). Data represent the mean ± SEM.

9
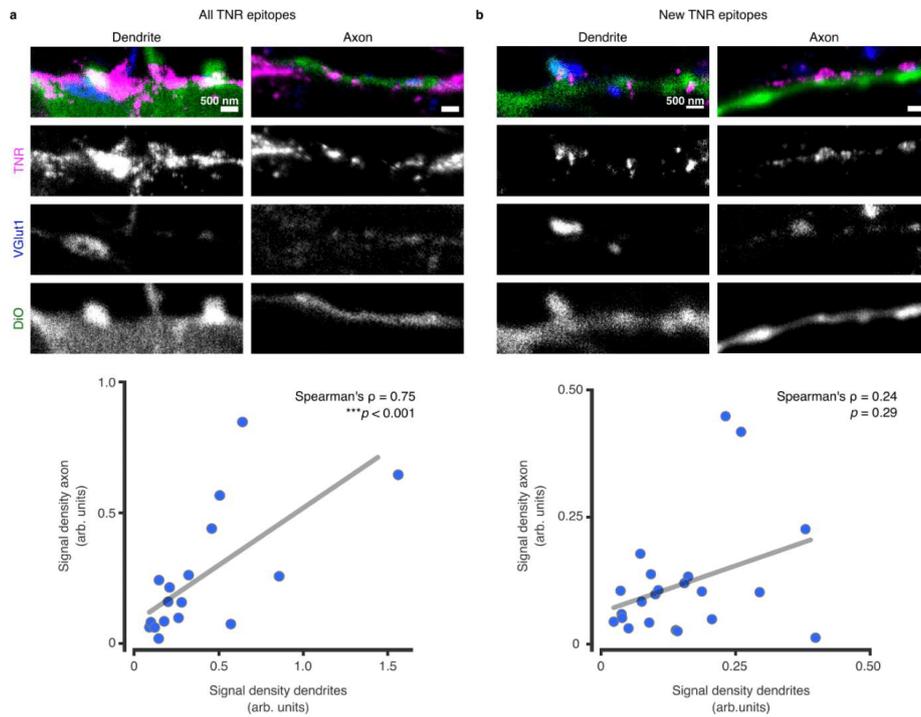
Supplementary Figure 7 The total TNR load of individual neurons is similar for their axons and dendrites, but the load of newly-emerged epitopes is not. We stained individual neurons by incubating the cultures with low levels of DiO crystals (green), which label the plasma membranes of only a few neurons on each coverslip. We then labeled the TNR epitopes (magenta) and the VGlut1-positive boutons (blue) as in Figure 2, and we analyzed the average TNR intensity in the dendrites and the axons of individual neurons. Highly branching neurites with clear spine-shaped protrusions were classified as dendrites, whereas thin, continuous neurites with a substantial number of overlapping VGlut1 puncta were classified as axons. **a**, All TNR molecules in the ECM were labeled. A significant correlation is found between the axonal and dendritic TNR loads. N= 3 independent experiments, with 17 individual neurons imaged; Spearman's $\rho = 0.745$, ***$p = 0.0006$ (two-sided). **b**, Only the newly-emerged TNR epitopes were labeled. No significant correlation could be determined . N = 3 independent experiments, with 22 individual neurons imaged; Spearman's $\rho = 0.237$, $p = 0.289$ (two-sided).

10
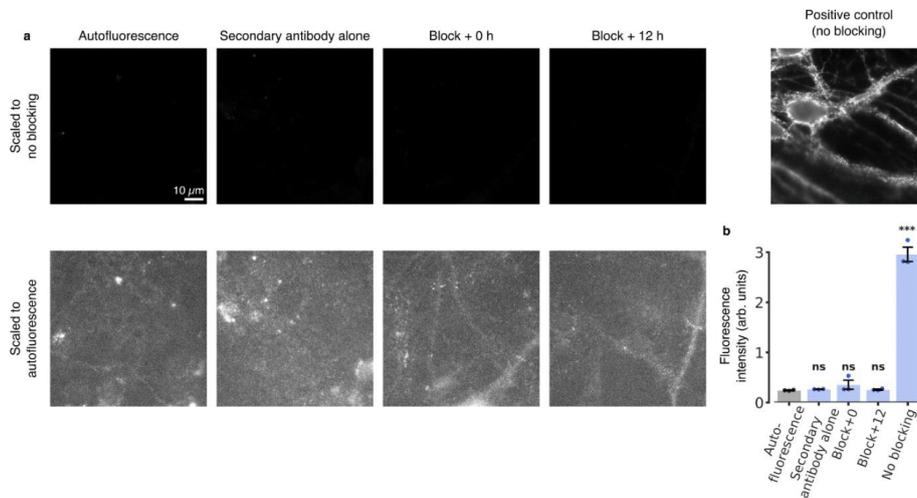
Supplementary Figure 8 The TNR antibodies do not separate from their epitopes in fixed cells at 37 °C. a, We fixed neuronal cultures, and we then blocked their surface TNR epitopes with non-fluorescent antibodies. Immediately afterwards, or after 12 hours, we incubated the neurons with Atto647N-conjugated TNR antibodies. As a control, all TNR epitopes were labeled, by omitting the blocking step. The blocked cultures showed virtually no detectable fluorescence when imaged in epifluorescence microscopy (top panels). In the bottom panels, we enhanced the image contrast, to reveal the outlines of the cells. These are as bright in these images as in negative controls exposed only to Atto647N-conjugated secondary anti-mouse antibodies (leftmost panel). Scale bar = 10 µm. **b**, The analysis of the mean fluorescence intensity confirms that no new TNR epitopes emerge after 12 hours of incubation in fixed neurons, indicating that the blocking antibodies persist on their epitopes, and do not allow the Atto647N-conjugated TNR antibodies to bind. N = 3 independent experiments, at least 10 neurons imaged per datapoint. Statistical significance was evaluated using one-way ANOVA ($F_{4, 10}$ = 120.3, ***p = 2.06 x 10^{-8}), followed by the Holm-Sidak multiple comparisons test (***p = 8.20 x 10^{-9}, ***p = 8.24 x 10^{-9}, ***p = 1.02 x 10^{-8} and ***p = 8.11 x 10^{-9}, for the comparison of the 'autofluorescence', 'secondary antibody alone', 'block+0' and 'block+12' to the 'no blocking' condition, respectively). None of the other conditions were significantly different from the autofluorescence negative control (p = 0.993, p = 0.716 and p = 0.981, for 'secondary antibody alone', 'block+0' and 'block+12', respectively). All data represent the mean ± SEM, with dots indicating individual experiments.

11
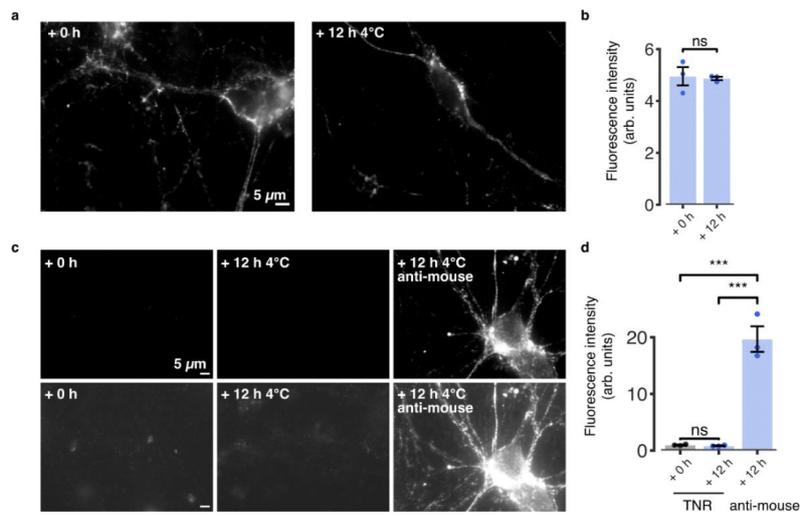
**Supplementary Figure 9 The TNR antibodies do not separate from their epitopes in live cells at 4 °C. a,** We labeled live neuronal cultures with Atto647N-conjugated TNR antibodies, and imaged them either immediately or following a 12 hour-long incubation at 4°C, in epifluorescence microscopy. Scale bar = 5 µm. **b,** An analysis of the mean fluorescence intensity shows that no significant change in staining is apparent after 12 hours at 4°C, indicating that the antibodies persist on their epitopes. N = 3 independent experiments, at least 10 neurons imaged per datapoint. Statistical significance was evaluated using a two-sided paired *t*-test (t = 0.286, *p* = 0.802). **c,** We blocked surface epitopes with unlabeled TNR antibodies, and fixed them either immediately or following a 12 hour-long incubation at 4°C. We then labeled the neurons with Atto647N-conjugated TNR antibodies, to reveal the available TNR epitopes, made available by the putative un-binding of blocking TNR antibodies, or with Atto647N-conjugated mouse secondary antibodies, to reveal the unlabeled blocking TNR antibodies. We then imaged the neurons in epifluorescence microscopy. The lower row of panels shows the same images as the top one, with enhanced imaging gain. Scale bar = 5 µm. **d,** An analysis of the fluorescence intensity shows that the staining with TNR antibodies is similar, and extremely low, both immediately and 12 hours after the blocking step. N = 3 independent experiments, at least 10 neurons imaged per datapoint. Statistical significance was evaluated using one-way ANOVA ($F_{2, 6}$ = 69.32, p^{***} = 7.14 x 10^{-5}) followed by the Holm-Sidak multiple comparisons test (*p* = 0.945 for the comparison between 'TNR 0 h' and 'TNR 12 h', and p^{***} = 0.0002 for both comparisons to the 'anti-mouse' condition). All data represent the mean ± SEM, with dots indicating individual experiments.

12
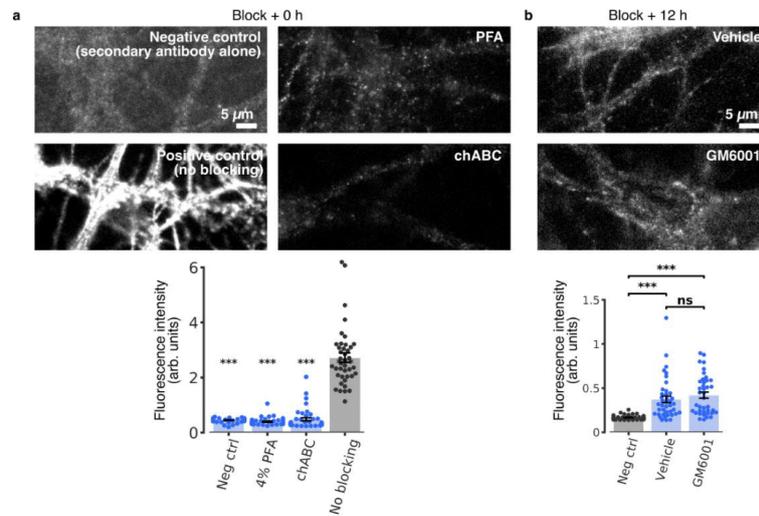
Supplementary Figure 10 The labeled TNRs are not pre-existing extracellular epitopes or the result of cleavage of existing ECM structures. **a**, To test whether the newly-emerged epitopes observed after TNR blocking could represent pre-existing epitopes that simply become available to antibody binding, we blocked surface epitopes with unlabeled antibodies, and then subjected them to several treatments that severely modify the cell surface. The treatments were fixation with 4% PFA or digestion of the surface glycosaminoglycans with chondroitinase ABC. We then added fluorophore-conjugated TNR antibodies to assess the number of epitopes that become available through these procedures. As positive and negative controls we used neurons incubated with TNR antibodies where we omitted the blocking step, or neurons incubated with anti-mouse secondary antibodies, respectively. We then imaged the neurons in epifluorescence microscopy. Scale bar = 5 µm. The graph (bottom panel) indicates that all conditions show substantially less fluorescence than the positive control, and are not distinguishable from the negative control. N = 2 independent experiments for the 'chABC' and 'No blocking' conditions, and 3 independent experiments for the 'neg ctrl' and 'PFA-fixed' conditions. 40 neurons were imaged in total per condition. Statistical significance was evaluated using the Kruskal-Wallis test (H_3 = 89.06, ***p < 0.001), followed by a two-sided Dunn multiple comparisons test for comparing each mean to the 'no blocking' condition (***p < 0.001). **b**, To test whether the newly-emerged TNRs could represent new epitopes that are exposed through the cleavage of existing ECM structures by secreted proteases, we blocked surface epitopes with unlabeled antibodies, and then treated the cultures with GM6001 to block the activity of matrix metalloproteinases (or with DMSO, as a control). We then added fluorophore-conjugated TNR antibodies to assess the amount of epitopes that become available, and imaged the neurons with epifluorescence microscopy. Scale bar = 5 µm. The graph (bottom panel) indicates that drug-treated cultures do not differ significantly from a negative control where neurons were incubated with anti-mouse secondary antibodies. N = 3 independent experiments, 40 neurons imaged in total per condition. Statistical significance was evaluated using the Kruskal-Wallis test (H_2 = 53.34, ***p < 0.001), followed by a two-sided Dunn multiple comparisons test for comparing the 'neg ctrl' condition to 'vehicle' or 'GM6001' (***p < 0.001), and 'vehicle' to 'GM6001' *(p = 0.95)*. All data represent the mean ± SEM.

13
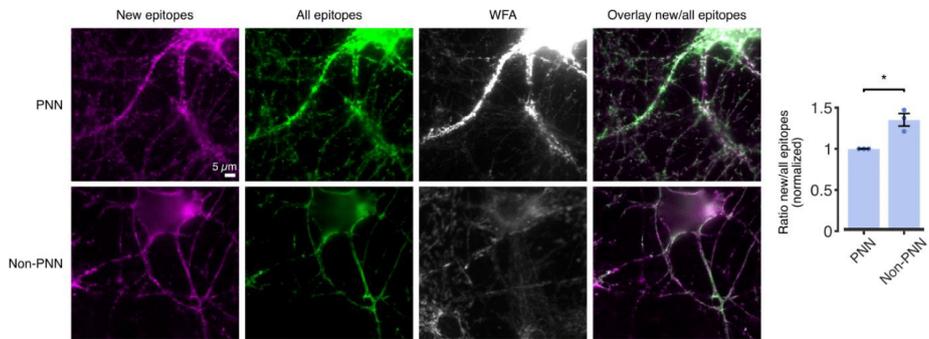
Supplementary Figure 11 TNR uptake and recycling occurs in both PNN and non-PNN-associated neurons. To assess whether the TNR dynamics we observed also hold true for PNN-associated neurons, we checked whether newly-emerged TNR epitopes could be observed in PNN-associated neurons (identified by a co-staining with WFA). We blocked surface epitopes with unlabeled antibodies against TNR, and then labeled newly-emerged TNR epitopes with fluorophore-conjugated TNR antibodies. We then fixed the neurons and incubated them with secondary anti-mouse antibodies, to label all TNR epitopes, and with WFA to label PNNs, before imaging them in epifluorescence microscopy. Newly-emerged TNR epitopes are visible in both PNN-associated (WFA+, top row) and non-PNN-associated (WFA-, bottom row) neurons. Scale bar = 5 μm. An analysis of the fluorescence ratio between new and all TNR epitopes shows that the proportion of newly-emerged epitopes is ~30% smaller for PNN-associated neurons. Nevertheless, this experiment demonstrates that PNN- and non-PNN-associated neurons behave similarly. N = 3 independent experiments, at least 10 neurons imaged per datapoint. Statistical significance was assessed using a two-sided paired *t*-test (t = 4.663, *p* = 0.043). Data represent the mean ± SEM, with dots indicating individual experiments.
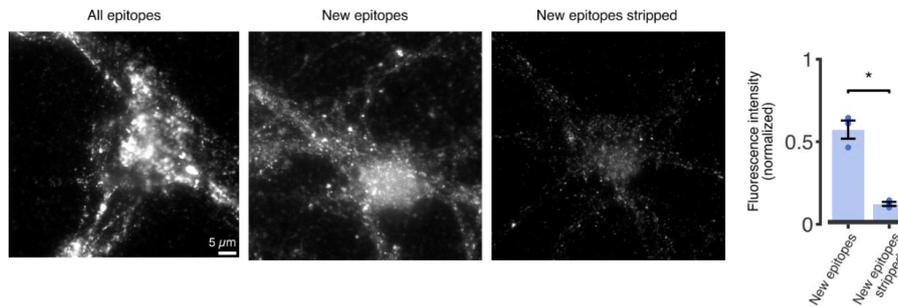
Supplementary Figure 12 TNR dynamics are observed in dissociated hippocampal 'sandwich' cultures.
We repeated our 'blocking-labeling' assay in dissociated hippocampal sandwich cultures, in which the neurons are grown at a physical distance above an astrocyte feeder layer. We labeled newly-emerged TNR epitopes 12 hours post-blocking, by applying fluorophore-conjugated antibodies for 1 hour. We then incubated the neurons for an additional 6 hours, to allow for TNR internalization. We stripped the surface-bound epitopes by incubation with proteinase K, and then fixed the neurons and imaged them in epifluorescence microscopy. As controls, we labeled newly-emerged TNR epitopes without stripping the surface-bound molecules, and we also labeled all TNR epitopes by omitting the blocking steps. TNR could be detected in the stripped cultures, suggesting that these molecules are readily endocytosed by the neurons. Scale bar = 5 μm. An analysis of the mean fluorescence intensity (normalized to the 'all epitopes' condition) shows that a fraction of the newly-emerged TNR epitopes is internalized within 6 hours. To confirm that the internalization we observe is not due to unspecific uptake in these cultures, we incubated neurons with Atto647N-conjugated mouse secondary antibodies. This value was subtracted from the mean intensities shown in the plot. N = 3 independent experiments, at least 10 neurons imaged per datapoint. Statistical significance was evaluated using a two-sided paired *t*-test (t = 8.258, *p* = 0.014). Data represent the mean ± SEM, with dots indicating individual experiments.

15
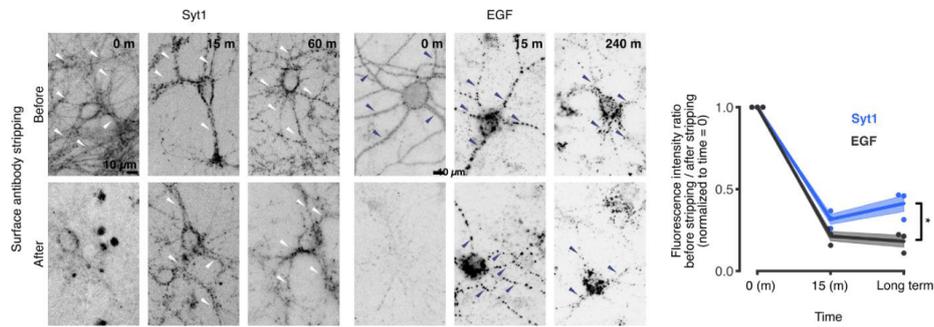
Supplementary Figure 13 Measurement of Syt1 and EGF using the surface antibody stripping assay. As additional controls for the experiment shown in original Fig. 3c, we applied the same surface-stripping assay to two proteins: synaptotagmin 1 (Syt1), which is well known to undergo recycling, and the epidermal growth factor (EGF) receptor, which is endocytosed but does not recycle readily. We incubated the neurons with fluorophore-conjugated antibodies directed against the lumenal domain of Syt1, or with fluorophore-conjugated EGF, and then imaged the neurons in epifluorescence before and after stripping the surface molecules with proteinase K. Immediately after the labeling, the staining was strongly reduced by the stripping, causing neurites to become virtually invisible for both proteins. After 15 minutes, the staining is similar before and after stripping, for both proteins, indicating that they have been endocytosed. Following a longer time period (60 minutes for Syt1; 4 hours for EGF, to account for any long-term recycling of this molecule), a loss of Syt1 from the neurites was observed after stripping, indicating that a portion of Syt1 had resurfaced. This was not the case in EGF-labeled cultures, indicating that they remained inside the cells. We quantified this by reporting the fluorescence ratio between the images taken before and after stripping (normalized to the first timepoint), as in the assay we devised initially for TNR. Scale bar = 10 μm. The graph demonstrates the diverging trends for the two proteins at the latest timepoint. N = 3 independent experiments, 5 images for each condition per datapoint. Statistical significance was evaluated using a two-sided Student's *t*-test (t = 3.782, *p = 0.019). Data represent the mean (lines) ± SEM (shaded regions); dots indicate the individual experiments.

16
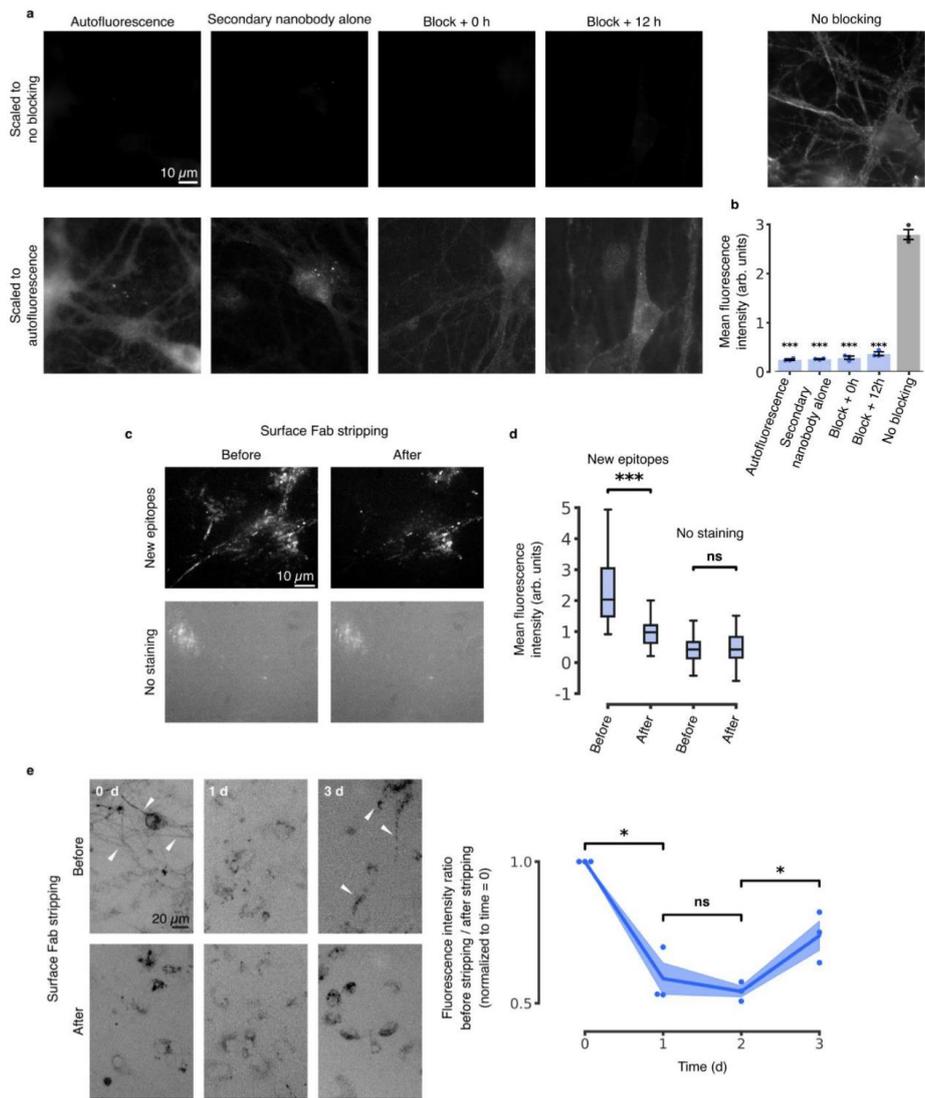
Supplementary Figure 14 The experiments with antibodies are validated with Fab fragments directed against TNR. a, We fixed neuronal cultures, and we then blocked their surface TNR epitopes with Fab fragments directed against TNR, applied together with non-fluorescent anti-mouse nanobodies. Immediately afterwards, or after 12 hours, we incubated the neurons with Fab fragments directed against TNR, applied together with STAR580-conjugated anti-mouse nanobodies. As a control, all TNR epitopes were labeled, by omitting the blocking step. The blocked neurons showed virtually no detectable fluorescence when imaged in epifluorescence microscopy (top panels). In the bottom panels, we enhanced the image contrast, to reveal the outlines of the cells. These are as bright in these images as in negative controls exposed only to STAR580-conjugated secondary anti-mouse nanobodies (leftmost panel). Scale bar = 10 µm. **b**, The application of Fab fragments and STAR580-conjugated anti-mouse nanobodies after 12 hours of incubation in fixed neurons results in no discernible fluorescence signal, indicating that the blocking Fab fragments (coupled to non-fluorescent anti-mouse nanobodies) persist on their epitopes. N = 3 independent experiments, at least 10 neurons imaged per

98

17

datapoint. Statistical significance was evaluated using one-way ANOVA ($F_{4,10}$ = 515.909, ***p = 1.56 x 10^{-11}), followed by the Holm-Sidak multiple comparisons test (***p = 5.90 x 10^{-12}, ***p = 6.18 x 10^{-12}, ***p = 5.90 x 10^{-12} and ***p = 9.58 x 10^{-12}, for the comparison of 'autofluorescence', 'secondary nanobody only, 'block+0' and 'block+12' to the 'no blocking' condition, respectively). None of the other conditions was significantly different from the autofluorescence negative control. All data represent the mean ± SEM, with dots indicating independent experiments. **c**, We blocked surface TNR epitopes with Fab fragments directed against TNR, applied together with non-fluorescent anti-mouse nanobodies. Newly-emerged TNR epitopes were labeled 12 hours later with new Fab fragments directed against TNR, applied together with STAR635P-conjugated anti-mouse nanobodies. The Fab fragments bound to surface TNR molecules were then stripped by incubation with proteinase K after a further incubation period of 4 hours. The samples were imaged in epifluorescence microscopy before and after the antibody stripping, and were compared to unstained neurons. Scale bar = 10 µm. **d**, A quantification of the mean fluorescence intensity indicates that a significant amount of surface TNR molecules were stripped at 4 hours after staining, whereas no such reduction was observed for unstained neurons. The amount of intracellular molecules that persisted after stripping was higher than background levels of fluorescence, indicating that a portion of the TNR molecules has endocytosed. n = 28 and 42 regions of interest analyzed from 2 sets of images for the 'new epitopes' and 'no staining' conditions respectively. Statistical significance was evaluated using two-way mixed ANOVA ($F_{1, 136}$ = 36.58, ***p < 0.001 for the interaction staining x time) followed by the Sidak multiple comparisons test (***p < 0.001 and p = 0.727 for 'before' vs. 'after', for stained and unstained neurons, respectively). Boxes show median (mid-line) and quartiles, and whiskers show minimum and maximum values. Outliers were omitted according to inter-quartile range (IQR) proximity (exceeding 1.5*IQR). **e**, TNR epitopes labeled with Fab fragments recycled back to the plasma membrane. This experiment reproduced the assay presented in Fig. 4c, but using Fab fragments instead of antibodies. We blocked surface TNR epitopes with Fab fragments directed against TNR, applied together with non-fluorescent anti-mouse nanobodies, and labeled the newly-emerged TNR epitopes 4 hours later with new Fab fragments directed against TNR, applied together with fluorophore-conjugated anti-mouse nanobodies. We then measured the fraction present on the surface after different time intervals. To determine this, we imaged the neurons (in epifluorescence) before and after stripping the surface molecules using proteinase K. At day 0 (immediately after labeling), the stripping procedure strongly reduced the staining. The effect was less visible at 1 day after staining, but became again evident at 3 days after staining, indicating that a high proportion of TNR molecules returned to the surface at 3 days after labeling. Scale bar = 20 µm. We quantified this by reporting the fluorescence ratio between the images taken before and after stripping (normalized to the day 0 timepoint). The amount stripped at day 3 is significantly higher than at days 1 and 2. N = 3 independent experiments, 5 images for each condition per datapoint. Statistical significance was evaluated using repeated-measures one-way ANOVA ($F_{1.519, 3.037}$ = 40.91, **p = 0.007), followed by Fisher's LSD test ('day 0' vs. 'day 1': *p = 0.018; 'day 1' vs. 'day 2': p = 0.522; 'day 2' vs. 'day 3': *p = 0.044). Data show mean (lines) ± SEM (shaded regions), with dots indicating independent experiments. All measurements in this figure refer to neurites, to avoid the bias caused by the higher autofluorescence of the cell bodies, which is evident in such epifluorescence images.

18
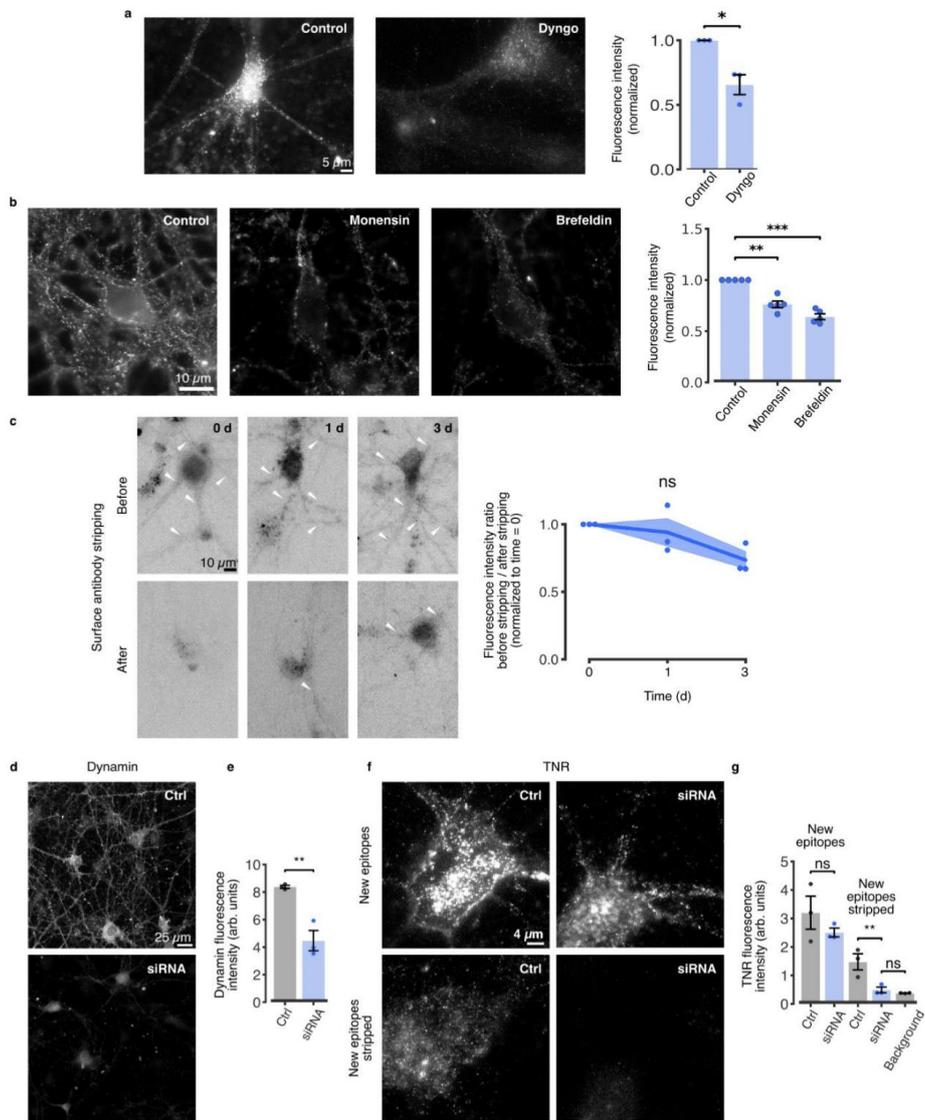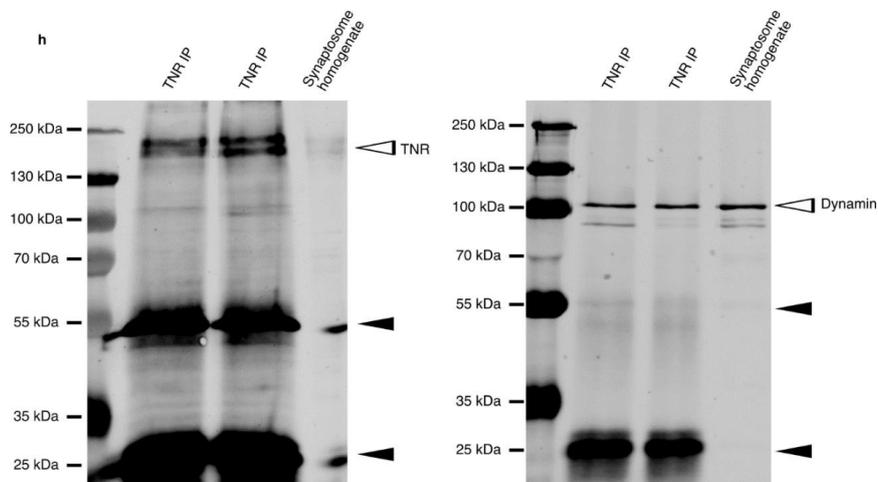
Supplementary Figure 15 Perturbing endocytosis and cellular trafficking reduces TNR recycling. a, Newly-emerged TNR epitopes were labeled 12 hours post-blocking, by the application of fluorophore-conjugated antibodies for 1 hour. Immediately after labeling, dynamin-mediated endocytosis was blocked by incubating the neurons with 30 μM Dyngo® 4a for 2 hours, after which the neurons were stripped by incubation with proteinase K, to reveal only the intracellular epitopes, and imaged with epifluorescence microscopy. The images were compared to control neurons treated with DMSO. Scale bar = 5 μm. The graph shows the mean fluorescence intensity normalized to the control condition in the respective experiment. The drug treatment significantly reduced the amount the internalized TNR epitopes. This treatment cannot be expected to inhibit endocytosis completely in this assay, as the antibodies need to be applied for one hour before the drug, which enables a significant level of endocytosis before the drug can take effect, and because Dyngo at this concentration is not expected to completely remove dynamin function. N = 3 independent experiments, at least 10 neurons imaged per datapoint. Statistical significance was evaluated using a two-sided paired t-test (t = 4.076, *p= 0.015). Data represent the mean ± SEM, with dots indicating individual experiments. **b**, The emergence of new TNR molecules was inhibited by drugs perturbing ER/Golgi traffic. We imaged newly-emerged TNR epitopes (in epifluorescence microscopy) after treatments of 7 hours with DMSO (as a control), with the Golgi-stressing ionophore monensin [7,8], or with the COPI-disturbing inhibitor brefeldin [9]. Scale bar = 10 μm. The graph shows the mean fluorescence intensity normalized to the control condition in the respective experiment. Both drugs reduced substantially the amount of newly-emerged TNR epitopes. N = 4 independent experiments for each condition, at least 10 neurons imaged per datapoint. Statistical significance was evaluated using two-sided paired t-tests with Bonferroni correction for multiple comparisons (t = 7.359, **p = 0.004 and t = 12.61,***p < 0.001 for the 'monensin' and 'brefeldin' conditions respectively). Data represent the mean ± SEM, with dots indicating individual experiments. **c**, We repeated the experiment shown in Fig. 4c in the presence of 30 μM Dyngo® 4a, to inhibit dynamin-dependent endocytosis. As expected, stripping significantly decreased the TNR staining immediately after labeling, indicating that the majority of the epitopes are present at the surface. However, this was also apparent at 1 and 3 days after labeling. Scale bar = 10 μm. The graph shows the fluorescence ratio between the images taken before and after stripping (normalized to the first timepoint). A similar ratio across all days suggests that TNR endocytosis is significantly slowed as a result of the drug treatment. N = 3 independent experiments, 5 images for each condition per datapoint. Statistical significance was evaluated using the Kruskal-Wallis test (H_2 = 4.782, p = 0.104). Data represent the mean (lines) ± SEM (shaded regions); dots indicate the individual experiments. **d-f**, The endocytosis of recycling TNR epitopes is slowed down by knockdown of dynamin. We performed a triple knockdown of dynamin 1, 2 and 3 using previously described siRNA constructs [10], and assessed the effects on TNR dynamics. **d**, We immunostained control and siRNA-treated neurons with antibodies against dynamin and imaged the cultures with epifluorescence microscopy. The fluorescence signal was visibly reduced in siRNA-treated neurons, demonstrating the effectiveness of the knockdown. Scale bar = 25 μm. **e**, A quantification of the mean fluorescence intensity shows

20

that the knockdowns reduced the amount of dynamin by ~ 50%. N = 3 independent experiments, 10 images per datapoint. Statistical significance was assessed using a two-sided Student's t-test (t = 5.259, $**p = 0.006$). Data represent the mean ± SEM, with dots indicating individual experiments. **f**, We labeled newly-emerged TNR epitopes by applying fluorophore-conjugated antibodies 12 hours post-blocking, and then incubated the neurons a further 6 hours to allow for endocytosis. One group of neurons was fixed immediately after, and the other was subjected to a treatment with proteinase K to remove surface-bound TNR epitopes before stripping. The fluorescence signal was not visibly different when labeling the newly-emerged TNR epitopes in control vs. siRNA-treated cultures (top row). However, the signal when labeling internalized TNR epitopes (following stripping) is significantly reduced in siRNA-treated neurons. Scale bar = 4 μm. **g**, An analysis of the fluorescence intensity confirms that siRNA knockdown of dynamin significantly reduces the internalization of recycling TNR epitopes after 6 hours. The internalized amount in siRNA-treated neurons is not significantly different from the fluorescence background, determined by measuring internalized secondary antibodies in these neurons. N = 3 independent experiments, 10 images per datapoint. Statistical significance was evaluated using one-way ANOVA on log-transformed data ($F_{4, 10} = 38.22$, $***p < 0.001$), followed by Tukey's multiple comparisons test (New epitopes 'ctrl' vs. 'siRNA': $p = 0.86$; New epitopes stripped 'ctrl' vs. 'siRNA': $**p = 0.004$; New epitopes stripped 'siRNA' vs. 'autofluorescence': $p = 0.832$). Data represent the mean ± SEM, with dots indicating individual experiments. **h**, Dynamin co-immunoprecipitates with TNR. We prepared synaptosomes from the cortices of 5 to 6-week-old rats, using a previously established protocol [11]. The synaptosomes were then subjected to a conventional immunoprecipitation procedure, using TNR antibodies. The left panel shows the immunoprecipitation of TNR, while the right panel shows a similar blot, revealing dynamin (using a pan-dynamin antibody). N = 4 independent experiments. The complete lanes are shown in the blots. The IP lanes correspond to 15% of the IP material. For the synaptosome lane, used as a positive control, only 0.05% of the material was run. Filled arrowheads show the bands of the antibodies using for the IP.

21
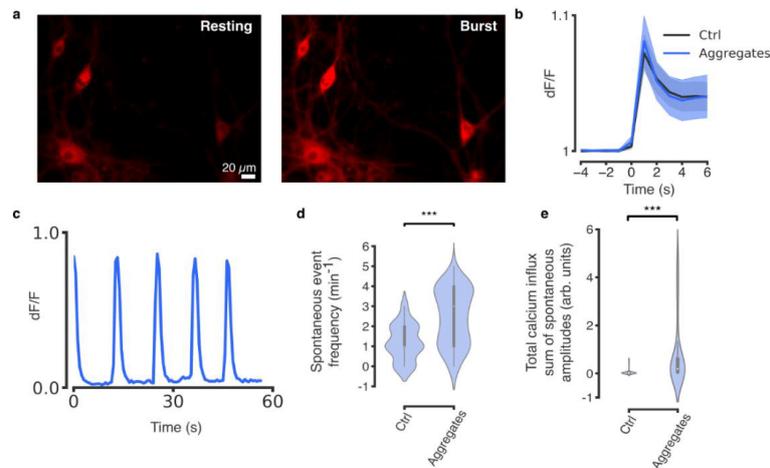
Supplementary Figure 16 Perturbing the recycling pool of TNR molecules affects spontaneous, but not evoked Ca²⁺ activity. To assess the effects the perturbation of the TNR recycling pool on Ca^{2+} dynamics, we incubated dissociated hippocampal cultures with antibody aggregates that bound specifically to newly-emerged TNR. To test whether the TNR pool has an influence on Ca^{2+} dynamics, we measured the Ca^{2+} influx using a neuron-specific fluorescent indicator (red) in live neurons under basal conditions, or following a brief stimulation. **a**, The images show neurons under basal conditions, either at rest (left), or during bursting activity (right). Scale bar = 20 µm. **b**, The Ca^{2+} influx in response to a 1-second, 20-Hz stimulus is not affected by perturbing the TNR pool. N = 4 independent experiments, with 30 and 29 neurons imaged for the 'Ctrl' and 'Aggregates' conditions, respectively. Data show mean (lines) ± SEM (shaded regions). **c-e**, Typical traces from control and aggregate-treated neurons indicate that under basal conditions, perturbing the TNR pool increases the spontaneous firing rate and the total Ca^{2+} influx over time. N = 4 independent experiments, with 74 and 75 neurons imaged for the 'Ctrl' and 'Aggregates' conditions, respectively. Statistical significance was evaluated using two-sided Mann-Whitney U-tests (spontaneous firing rate: $U_{145} = 717.5$, ***$p = 2.32$ x 10^{-14}; total Ca^{2+} influx: $U_{56} = 147.5$, ***$p = 1.05$ x 10^{-5}). Violin plots show the median (white dot), quartiles (box boundaries) and the range of the kernel density estimation (filled area).

22
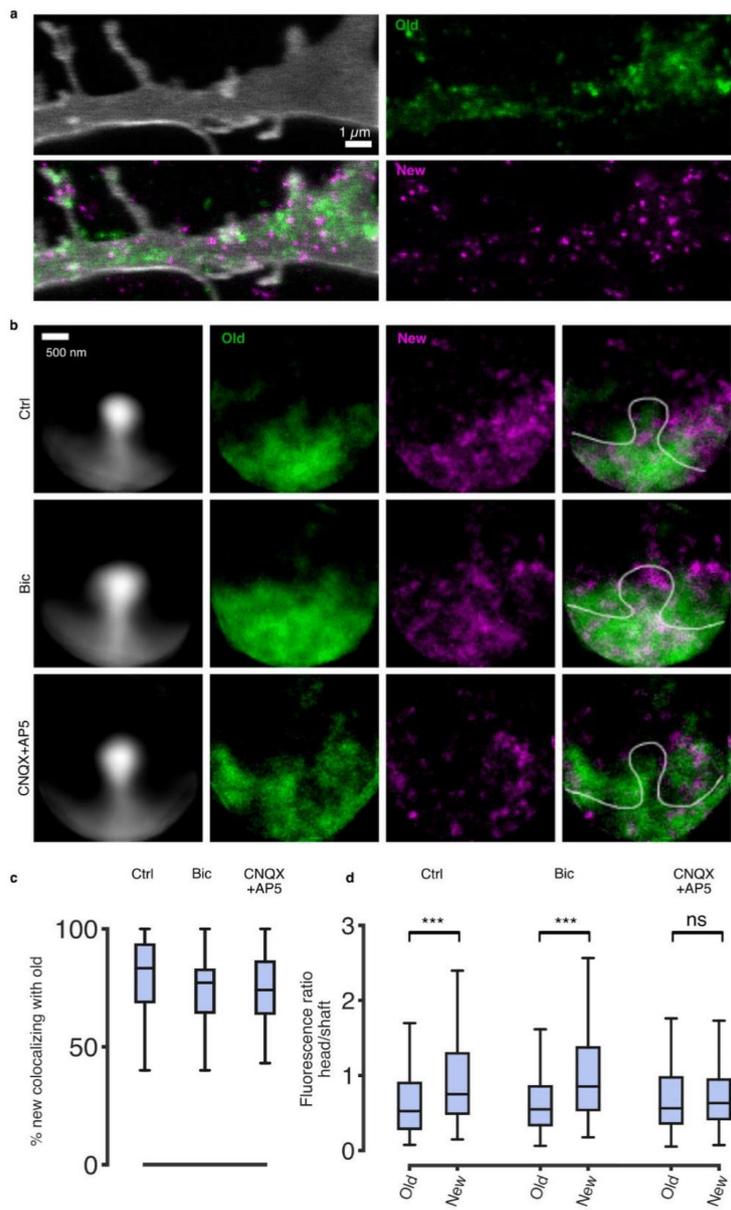
Supplementary Figure 17 New TNR epitopes integrate into the perisynaptic ECM, preferentially near the spine head. To test whether the recycling TNR molecules integrate into the perisynaptic ECM, we performed 2-color-STED super-resolution imaging, to compare the stable and newly-emerged TNR epitopes at the same synapses. In addition, we checked whether the organization of the newly-emerged epitopes is dependent on synaptic activity, by comparing control cultures with cultures treated with bicuculline (40 µM) or with a combination of CNQX (10 µM) and AP5 (50 µM). **a**, An exemplary image of a dendrite. The plasma membrane was visualized by incubating the neurons with DiO. We performed the same 'blocking-labeling' assay as in the

23

rest of the study, but used fluorophore-conjugated (rather than unlabeled) antibodies against TNR for the blocking step. "Old" and newly-emerged epitopes are typically in the vicinity of each other, albeit they do not correlate strongly, as already suggested in Fig. 2. Scale bar = 1 μm. N = 3 independent experiments. **b**, We imaged many dendrites for each treatment condition and extracted segments containing individual spines. We then aligned these to the same orientation, in order to visualize the average spine under each treatment condition. This visualization showed that the newly-emerged epitopes embed in the ECM, and are especially visible in the vicinity of the spine head. This tendency to localize to the spine head was increased when activity was enhanced with bicuculline, and abolished when activity was reduced with CNQX+AP5. Scale bar = 500 nm. **c**, A quantification of percentage of new TNR epitopes colocalizing with old epitopes showed that the majority of the newly-emerged molecules colocalize with existing molecules, confirming they integrate into the perisynaptic ECM. The remaining epitopes presumably represent endocytosed TNR, found within the dendrites. N = 3 independent experiments, with 88, 114 and 137 synapses analyzed for the 'Ctrl', 'Bic' and 'CNQX+AP5' conditions, respectively. **d**, To test our observation that the new TNR epitopes preferentially localize to the spine head (panel b), we calculated the fluorescence ratio between the spine head and the dendritic shaft at its base, for both the old and the new epitopes. This analysis confirmed that the newly-emerged TNR epitopes preferentially appear in the spine head, whereas the old epitopes are distributed in both the head and the shaft. As we observed in the average images (b), this bias was slightly increased in bicuculline-treated cultures, and was lost in CNQX+AP5-treated cultures. N = 3 independent experiments, with 88, 114 and 137 synapses analyzed for the 'Ctrl', 'Bic' and 'CNQX+AP5' conditions, respectively. Statistical significance was evaluated using two-sided Wilcoxon signed rank tests ('Ctrl': W = -1782, ***$p < 0.001$; 'Bic': W = -3633, ***$p < 0.001$; 'CNQX+AP5': W = -1313, $p = 0.159$). Boxes in panels c-d show median (mid-line) and quartiles, and whiskers show minimum and maximum values. Outliers were omitted according to inter-quartile range (IQR) proximity (exceeding 1.5*IQR).

24

a

Blocked + 0 h Blocked + 12 h Blocked + 12 h + CNQX + AP5

b

Blocked + 12 h + Bic No blocking

c

- rTNR Untreated - stripped

Bic - stripped No stripping
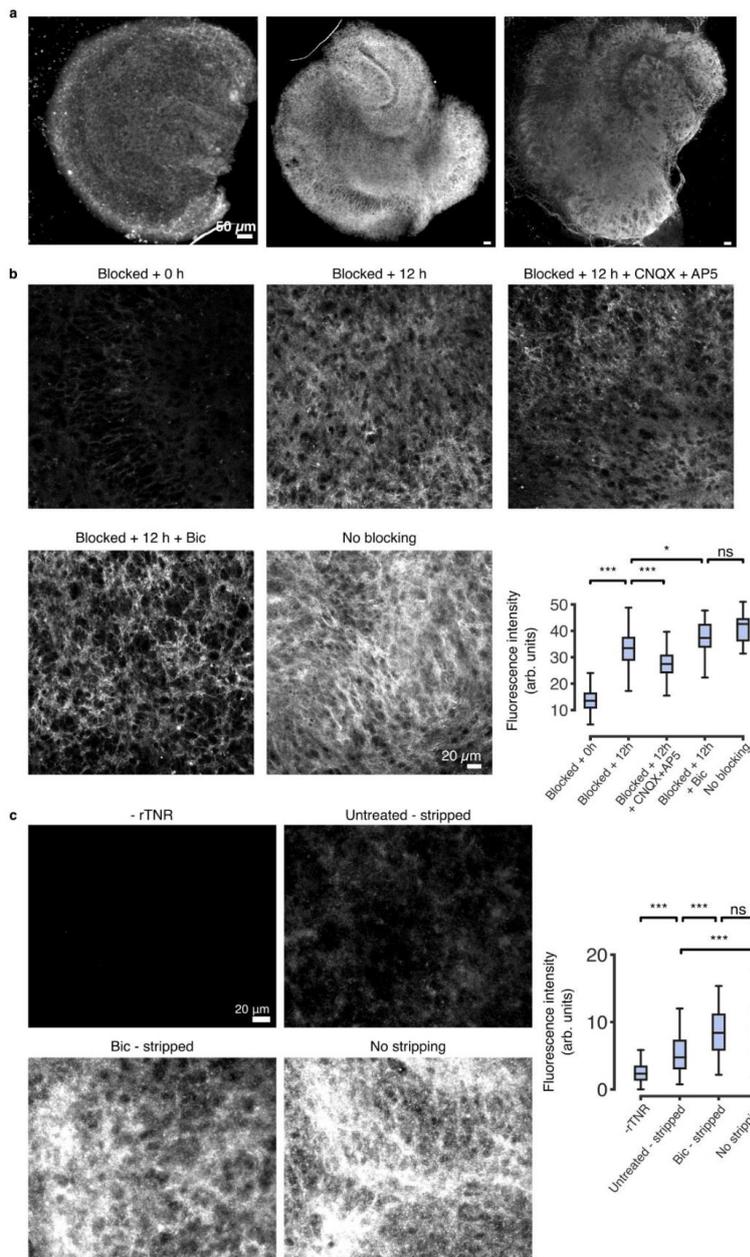
Supplementary Figure 18 TNR dynamics can also be observed in cultured slices. a, Exemplary large field-of-view images of organotypic hippocampal cultured slices, fixed and immunostained for TNR. Scale bar = 50 µm. N = 3 independent experiments. **b**, To test whether Fab fragments can be used to block TNR surface epitopes in a model that is closer to the *in vivo* morphology of neuronal tissue, we applied our 'blocking-labeling' assay to organotypic hippocampal slice cultures. We first blocked TNR surface epitopes by incubating live slices with Fab fragments directed against TNR, applied together with non-fluorescent anti-mouse

25

106

nanobodies, for 2 hours. Newly-emerged TNR epitopes were labeled with new Fab fragments directed against TNR, applied together with fluorophore-conjugated anti-mouse nanobodies, 12 hours post-blocking. We compared control cultures with cultures treated with bicuculline (40 µM) or with a combination of CNQX (10 µM) and AP5 (50 µM). To test the efficacy of the blocking procedure, we also labeled the newly-emerged TNR epitopes immediately after the blocking step. The blocked slices ('block + 0 h') showed little fluorescence when imaged in confocal microscopy, when compared with a full surface labeling ('no blocking'). Newly-emerged epitopes can be detected 12 hours post-blocking, and their amounts are visibly higher in the presence of bicuculline, and lower in the presence of CNQX + AP5. Scale bar = 20 µm. An analysis of the mean fluorescence intensity confirms that the amount of newly-emerged TNR epitopes is significantly lower following CNQX + AP5 treatment, and significantly higher following bicuculline treatment. N = 3 independent experiments, 10 images for each condition per experiment. Statistical significance was evaluated using one-way ANOVA ($F_{4, 266} = 115.8$, ***$p = 4.76 \times 10^{-57}$), followed by Tukey's multiple comparisons test ('block+0' vs. 'block+12': ***$p = 9.92 \times 10^{-5}$; 'block+12' vs. 'block+12+ CNQX+AP5': ***$p = 0.0002$; 'block+12' vs. 'block+12+bic': *$p = 0.04$; 'block+12+bic' vs. 'no blocking': $p = 0.492$). Boxes show median (mid-line) and quartiles, and whiskers show minimum and maximum values. Outliers were omitted according to inter-quartile range (IQR) proximity (exceeding 1.5*IQR). **c**, We pulsed organotypic hippocampal slices with His-tagged recombinant TNR (rTNR) for 2 hours, and then incubated them a further 6 hours to allow for internalization. Afterwards, the rTNR that remained at the surface of the slices was stripped by incubation with proteinase K. The slices were then fixed and immunostained with anti-His-tag antibodies (to reveal internalized rTNR), and imaged with epifluorescence microscopy. We compared control slices to slices treated with bicuculline (40 µM). To assess the total amount of rTNR and the background fluorescence, we omitted the incubation with proteinase K (no stripping) or the incubation with rTNR (- rTNR), respectively. Scale bar = 20 µm. An analysis of the fluorescence intensity revealed that the amount of rTNR in stripped organotypic slices is significantly higher than the background fluorescence, suggesting that rTNR is internalized in these slices, and that this amount is increased in the presence of bicuculline. In the absence of proteinase K, the amount of rTNR is higher still, showing that a population of the molecules remains at the surface. N = 3 independent experiments, 15 images per condition. Statistical significance was evaluated using the Kruskal-Wallis test ($H_3 = 184.1$, ***$p = 1.13 \times 10^{-39}$), followed by a two-sided Dunn multiple comparisons test ('-rTNR' vs. 'untreated – stripped': ***$p = 2.47 \times 10^{-11}$; 'untreated – stripped' vs. 'bic – stripped': ***$p = 1.28 \times 10^{-5}$; 'untreated – stripped' vs. 'no stripping': ***$p = 3.25 \times 10^{-7}$; 'bic - stripped' vs. 'no stripping': $p = 0.519$;). Boxes show median (mid-line) and quartiles, and whiskers show minimum and maximum values. Outliers were omitted according to inter-quartile range (IQR) proximity (exceeding 1.5*IQR).

26
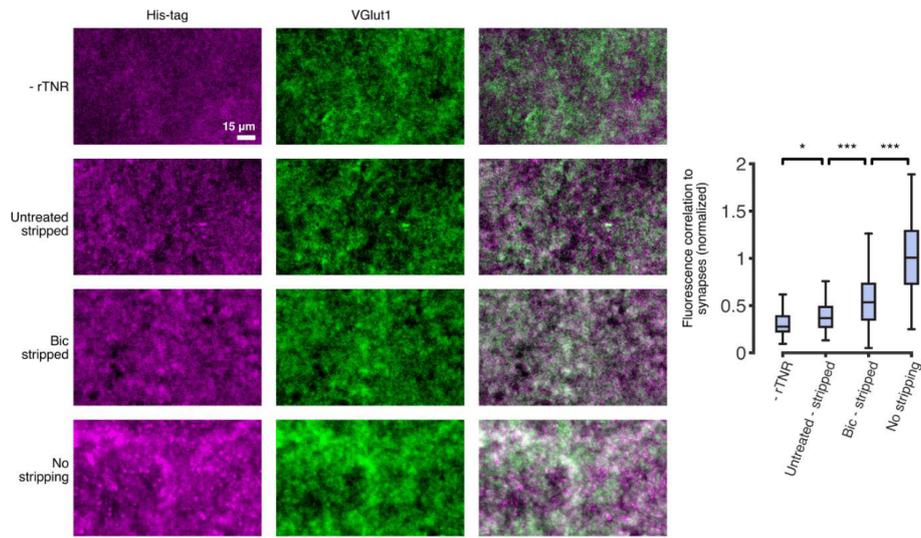
**Supplementary Figure 19 His-tagged recombinant TNR is internalized in acute hippocampal slices from rats**. To assess whether acute hippocampal slices are capable of internalizing TNR, we incubated slices from 3 week-old rats with His-tagged recombinant TNR (rTNR). Afterwards, the rTNR that remained at the surface of the slices was stripped by incubation with proteinase K. The slices were then fixed and immunostained with anti-His-tag antibodies (to reveal internalized rTNR) and anti-VGlut1 nanobodies (to reveal synapses), and were imaged with epifluorescence microscopy. We compared control slices to slices treated with bicuculline (40 µM). To assess the total amount of rTNR and the background fluorescence, respectively, we omitted the incubation with proteinase K (top row) or the incubation with rTNR (bottom row). Scale bar = 15 µm. We analyzed the pixel-by-pixel correlation between the rTNR and VGlut1 images as a measure for the presence of rTNR in synaptic regions. Unsurprisingly, high amounts of rTNR are found before stripping (as expected from the literature [12]). rTNR was also found in synaptic regions after stripping, and this was enhanced by bicuculline stimulation. N = 3 sections for each condition from 3 different mice, with 20 images acquired per condition. Statistical significance was evaluated using the Kruskal-Wallis test ($H_3 = 179$, ***$p = 1.44$ x 10^{-38}), followed by a two-sided Dunn multiple comparisons test ('-rTNR' vs. 'untreated – stripped': *$p = 0.035$; 'untreated – stripped' vs. 'bic – stripped': ***$p = 0.0006$; 'bic – stripped' vs. 'no stripping': ***$p = 4.15$ x 10^{-10}). Boxes show median (mid-line) and quartiles, and whiskers show minimum and maximum values. Outliers were omitted according to inter-quartile range (IQR) proximity (exceeding 1.5*IQR).

27
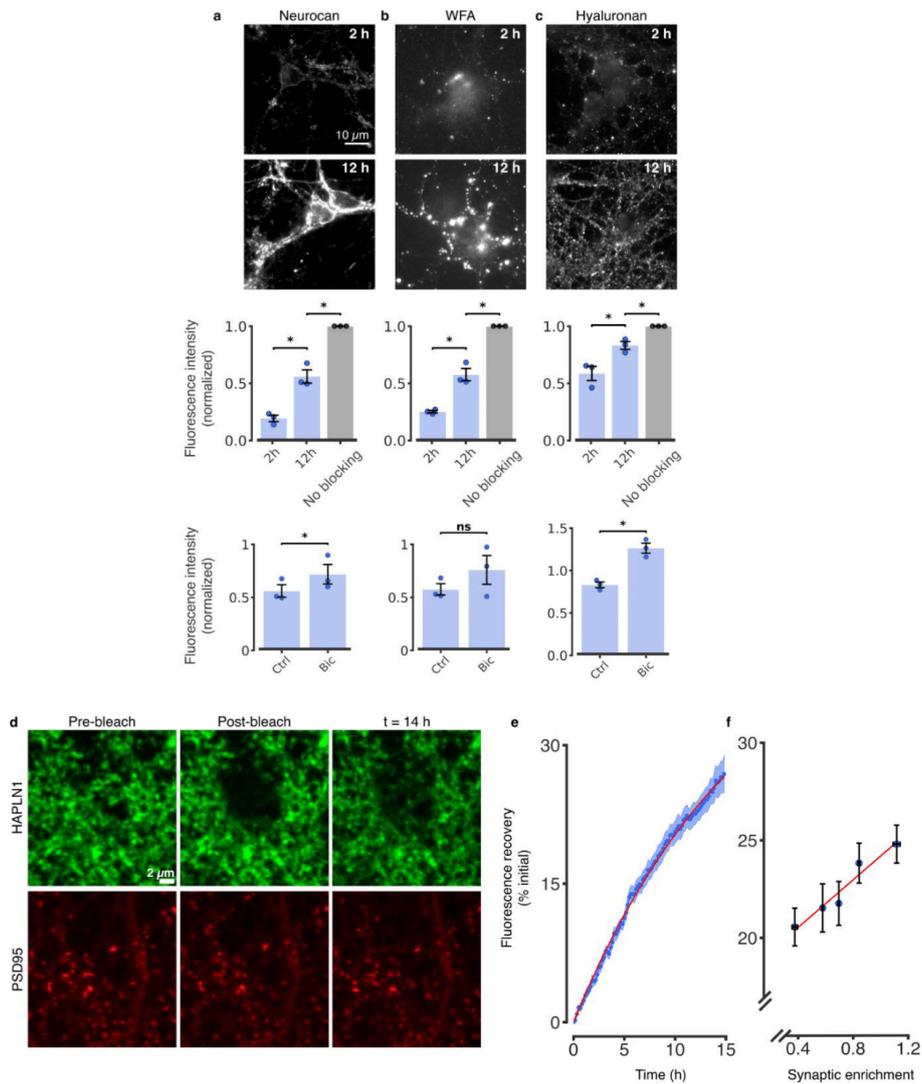
Supplementary Figure 20 Additional ECM molecules are more dynamic than previously presumed, and surface in neurons in an activity-dependent fashion. a-c, Top row: experiments were performed as in Fig. 2b using antibodies for neurocan (panel a) and hyaluronan-binding protein (panel c), or with *Wisteria floribunda* agglutin (WFA), which labels chondroitin-sulfate-bearing proteoglycans (panel b). The cultures were then imaged in epifluorescence microscopy. Scale bar = 10 μm. Middle row: The graphs show the mean fluorescence intensity normalized to a control condition in which the blocking step was omitted. A gradual increase in newly-emerged epitopes was measured, similarly to the dynamics observed for TNR. N = 3 independent experiments for each condition, at least 10 neurons imaged per experiment. Statistical significance was evaluated using repeated-measures one-way ANOVA ($F_{1.005, 2.011} = 85.74$, *p = 0.011; $F_{1.013, 2.026} = 119.8$, **p = 0.008; $F_{1.095, 2.190} = 42.81$, *p = 0.018) for neurocan, WFA and hyaluronan respectively, followed by Fisher's LSD test (*p = 0.050 and *p = 0.017*; *p = 0.036 and *p = 0.016*; *p = 0.034 and *p = 0.038) for the comparisons between '2 h', and '12 h' and '12 h and 'no blocking' conditions for neurocan, WFA and

28

109

hyaluronan respectively. Bottom row: we compared control cultures with cultures in which network activity was enhanced by inhibiting GABA$_A$ receptors using bicuculline (40 µM). The graphs show the mean fluorescence intensity normalized to the mean of the bicuculline-treated condition. The bicuculline treatment had a significant effect for 3 molecules. N = 3 independent experiments, at least 10 neurons imaged per datapoint. Statistical significance was evaluated using two-sided paired t-tests (neurocan: t = 4.57, *p = 0.045; WFA: t = 1.925, p = 0.194; hyaluronan: t = 4.661, *p = 0.043). Data represent the mean ± SEM, with dots indicating independent experiments. **d-f**, A FRAP-based assay also demonstrates fast ECM dynamics at synapses. **d**, We used FRAP to observe the local turnover dynamics of the hyaluronan-binding protein HAPLN1. The postsynaptic marker PSD95 (red) and HAPLN1 (green) were expressed in neurons, as fluorescent protein chimeras (see Methods). At time 0, regions of ~5 µm radius were bleached in the HAPLN1 channel, using a strong laser pulse. The cells were then imaged once every 10 minutes, for 14 hours, in confocal microscopy. Scale bar = 2 µm. **e-f**, The fluorescence recovery in the bleached regions was analyzed from 14 independent experiments. **e**, A single exponential process was fitted to the fluorescence recovery (red curve), which provided a half-life of approximately 12 hours for the recovery process. The curve shows mean (lines) ± SEM (shaded regions). **f**, To determine whether turnover dynamics differ in synaptic regions, the density of synapses was calculated for the analyzed regions. A strong correlation was found between the percent of fluorescence recovery and synaptic enrichment, indicating that turnover is significantly higher in synaptic regions (R^2 = 0.941, **p = 0.006). Data represent the mean ± SEM.

29

References

1. Härtig, W., Brauer, K. & Brückner, G. Wisteria floribunda agglutinin-labelled nets surround parvalbumin-containing neurons. *Neuroreport* **3**, 869–872 (1992).
2. Lind, D., Franken, S., Kappler, J., Jankowski, J. & Schilling, K. Characterization of the neuronal marker NeuN as a multiply phosphorylated antigen with discrete subcellular localization. *J. Neurosci. Res.* **79**, 295–302 (2004).
3. Dörrbaum, A. R., Kochen, L., Langer, J. D. & Schuman, E. M. Local and global influences on protein turnover in neurons and glia. *Elife* **7**, (2018).
4. Aroca-Aguilar, J.-D., Fernández-Navarro, A., Ontañón, J., Coca-Prados, M. & Escribano, J. Identification of myocilin as a blood plasma protein and analysis of its role in leukocyte adhesion to endothelial cell monolayers. *PLoS One* **13**, e0209364 (2018).
5. Bottenus, D. *et al.* Preconcentration and detection of the phosphorylated forms of cardiac troponin I in a cascade microchip by cationic isotachophoresis. *Lab Chip* **11**, 3793 (2011).
6. Chart, H., Evans, J., Chalmers, R. M. & Salmon, R. L. Escherichia coli O157 serology: false-positive ELISA results caused by human antibodies binding to bovine serum albumin. *Lett. Appl. Microbiol.* **27**, 76–78 (1998).
7. Dinter, A. & Berger, E. G. Golgi-disturbing agents. *Histochem. Cell Biol.* **109**, 571–590 (1998).
8. Sbodio, J. I., Snyder, S. H. & Paul, B. D. Golgi stress response reprograms cysteine metabolism to confer cytoprotection in Huntington's disease. *Proc. Natl. Acad. Sci. U. S. A.* **115**, 780–785 (2018).
9. Nebenfuhr, A. Brefeldin A: Deciphering an Enigmatic Inhibitor of Secretion. *PLANT Physiol.* **130**, 1102–1108 (2002).
10. Kononenko, N. L. *et al.* Clathrin/AP-2 Mediate Synaptic Vesicle Reformation from Endosome-like Vacuoles but Are Not Essential for Membrane Retrieval at Central Synapses. *Neuron* **82**, 981–988 (2014).
11. Rizzoli, S. O. *et al.* Evidence for early endosome-like fusion of recently endocytosed synaptic vesicles. *Traffic* (2006). doi:10.1111/j.1600-0854.2006.00466.x
12. Morawski, M. *et al.* Tenascin-R promotes assembly of the extracellular matrix of perineuronal nets via clustering of aggrecan. *Philos. Trans. R. Soc. Lond. B. Biol. Sci.* **369**, 20140046 (2014).
13. Brakebusch, C. *et al.* Brevican-deficient mice display impaired hippocampal CA1 long-term potentiation but show no obvious deficits in learning and memory. *Mol. Cell. Biol.* **22**, 7417-7427 (2002).
14. Rauch, U., Zhou, X.H. & Roos, G. Extracellular matrix alterations in brains lacking four of its components. *Biochem. Biophys. Res. Commun.* **328**, 608-617 (2005).

30

4: Discussion and outlook

The ideas that motivated this thesis can be summarized as follows:
- When synapses undergo structural changes, the ECM in which they are embedded is remodeled.
- The existing paradigm for ECM remodeling is through the proteolytic cleavage of the molecules, followed by the secretion of newly synthesized molecules.
- ECM molecules are among the most long-lived in the body.
- This last point implies that the rate at which synapses undergo structural changes (minutes to hours) is too fast to be accounted for by the destruction and synthesis of its local ECM.
- Thus, an additional mechanism must exist for the remodeling of synaptic ECM, which does not require the destruction of ECM molecules and *de novo* synthesis.

To determine whether ECM recycling at synapses is plausible, we first needed to assess two prerequisites to this mechanism: (1) synapses should be capable of secreting ECM molecules locally, and (2) synapses should be capable of endocytosing ECM molecules into the trafficking route. In addition, both processes are expected to correlate to synaptic activity, which is known to strongly influence synaptic structural fluctuations (Hazan and Ziv, 2020). A review of the existing literature (Chapter 1.4.2) suggested that the first prerequisite can be met in both the pre- and postsynaptic compartments: the presynapse can package secreted molecules into synaptic or dense-core vesicles, and the postsynapse can rapidly exocytose molecules from local endosomes. Importantly, all of these processes are known to be modulated by synaptic activity. As for the second prerequisite, a review of the existing literature did not provide a comprehensive answer (Chapter 1.4.3). It was apparent that the postsynapse is a more likely locus for the endocytosis and retrograde trafficking of ECM (since presynaptic trafficking appears to be mostly limited to synaptic vesicles), but its correlation to synaptic activity had not yet been explored. Thus, the assessment of the link between synaptic activity and the postsynaptic trafficking machinery constituted the first portion of this thesis.

4.1. Establishing a link between synaptic activity and the postsynaptic trafficking machinery

The postsynapse is known to contain extensive trafficking machinery, which includes extensions of the ER, ERGIC, and Golgi outposts (Tang, 2008). Nevertheless, the abundance of this machinery and its organization at postsynaptic regions had never previously been correlated to local synaptic activity, and hence, the goal of this investigation was to establish such a link. An important point to keep in mind is that the results represent two roles of the postsynaptic trafficking machinery: the retrograde trafficking of endocytosed proteins and the local synthesis and secretion of new proteins (anterograde trafficking), and thus the latter role may be a confounding factor to our measurements. Nevertheless, our findings (summarized below) demonstrate that the postsynapse has the potential to be the locus of activity-dependent retrograde trafficking.

(1) Trafficking machinery is recruited to spines in more active synapses

Predictably, we observed that more active synapses have a higher abundance of trafficking machinery. In addition, this machinery was more abundant in the perisynaptic region (versus the PSD), which suggests that these proteins are recruited to the vicinity of the synapse. This could reflect the fact that highly active synapses require a local synthesis of new proteins to support plasticity and/or are trafficking proteins more vigorously. With regard to ECM trafficking, our observations that TNR recycling is increased at more active synapses, and that these molecules colocalize with Golgi outposts at dendrites (Chapter 3), makes it tempting to assume that these outposts are recruited to the vicinity of more active synapses, but this remains to be tested directly. An additional observation that we made is that the ER protein calreticulin was only moderately more abundant at active synapses as compared with the other trafficking proteins. This might indicate that local ER is only necessary for *in situ* production of protein but not for retrograde trafficking (as the literature suggests; Johannes and Popoff, 2008), and hence, local ER activity would not be required to the same extent. In the future, this could be verified by assessing the colocalization between recycling TNR molecules and calreticulin in the vicinity of synapses (though we did report a colocalization between the two, our analysis was restricted to somatic ER).

(2) Trafficking machinery is abundant in stronger synapses (with larger PSDs and bigger synaptic vesicle pools)

Our observation that stronger synapses have a greater abundance of trafficking machinery is likely to reflect the fact that more protein turnover is required to maintain them. While this is expected, it nevertheless reveals that this process can, to a large extent, occur locally. Besides the replenishment of synaptic proteins, the abundant trafficking machinery could also support more extensive recycling of local ECM. Indeed, we found that larger spines (size being a known determinant of synaptic strength; Humeau and Choquet, 2019) have a greater amount of recycling TNR in their ECM, and would therefore require more extensive local recycling.

A major caveat of this study is that all of these measurements are purely correlative. Our observation that more active synapses have a greater abundance of trafficking machinery in their periphery does not guarantee that synaptic activity is the cause of protein recruitment. Thus, it is necessary to determine whether manipulating synaptic activity could lead to similar observations. For example, it would be expected that an acute global blockade of GABAergic inhibition with bicuculline would lead to an increased abundance of trafficking machinery in the synaptic periphery. In contrast, longer treatments (~24 hours or more) might be expected to globally *decrease* local trafficking machinery through mechanisms of homeostatic plasticity [18]. An even more convincing approach would be the manipulation of individual synapses and

---

[18] Homeostatic plasticity refers to the ability of neurons to maintain their excitability about a set point, in order to balance the destabilizing effects of faster plasticity processes such as LTP (Turrigiano, 2012). For example, while a strong, short-term enhancement of neuronal activity with bicuculline would lead to an increase in synaptic strength through LTP-associated mechanisms (Grover and Yan, 1999), a milder, long-term enhancement would lead to synaptic weakening (Hou et al., 2008). Similarly, a long-term silencing of neuronal activity with low concentrations of

subsequent imaging of the trafficking machinery in their vicinity, *e.g.,* by electrically stimulating individual neurons while simultaneously loading them with a fluorescent dye, to facilitate the subsequent identification of their synapses (Horikawa and Armstrong, 1988).

In the future, it may be worth extending these measurements to additional organelle markers such as Rabs, in order to visualize endosomes at various trafficking stages, and paint a more comprehensive picture of the machinery recruited for local recycling. To gain insight into TNR recycling, this knowledge could be combined with an assessment of the colocalization between recycling TNR and synaptic trafficking machinery (in our existing investigations, we focused mostly on somatic organelles). Such an investigation could reveal, for example, whether a separate pool of TNR undergoes local short-loop recycling in the vicinity of synapses (as is known, for example, for AMPARs; Parkinson and Hanley, 2018). Such a pool may have gone undetected in our measurements, and its existence would lend further support to the rapid remodeling at synapses.

4.2.   Proof of local ECM recycling at synapses

The second portion of this thesis was dedicated to directly assessing whether ECM molecules can be recycled at synapses, focusing specifically on TNR. The major findings, along with a short discussion of several caveats, are summarized below. In the next section, I will highlight additional outstanding questions and discuss possible directions for future research.

(1) *A pool of recycling TNR molecules is continually secreted at synapses*

We discovered that two separate pools of TNR molecules are found in neurons: one fixed in the neuronal ECM, and one that continually cycles in and out of the cell. While the stable pool covers the neuronal surface uniformly, the recycling pool is mostly located at synapses. Our results also suggest that this holds true for adult animals *in vivo*, and that the proportions of these pools may be modified in disease.

Caveat: While we thoroughly characterized this mechanism in hippocampal neuronal culture *in vitro*, the experiments in models that are more physiological, such as organotypic slice cultures and brain slices, are much less substantial.

(2) *The recycling is dependent on local synaptic activity*

We observed that the activity of a synapse is strongly correlated to the amount of recycling TNRs in its ECM. In addition, the amount of TNR molecules that emerge at the surface of the neuron can be increased by pharmacological enhancement of neuronal activity.

Caveat: For the latter finding, it should be noted that enhanced neuronal activity is also expected to lead to the *de novo* synthesis of ECM that would surface alongside the recycling molecules and confound our measurements. Hence, the extent to which activity controls the rate of TNR recycling should be established more definitively. This could be assessed, for example, by

tetrodotoxin (TTX), a voltage-gated sodium channel blocker, would result in synaptic strengthening. These homeostatic counterbalancing actions are thought to be achieved through the global removal or addition of synaptic AMPARs, also known as 'synaptic scaling' (Turrigiano, 2012).

measuring the amount of surfacing TNR molecules following pharmacological activity enhancement in the presence of protein synthesis blockers, thus ensuring that the molecules appearing at the surface are not newly-synthesized. Alternatively, this measurement could be repeated with a concurrent metabolic labeling of newly-synthesized proteins using AHA (as described in Chapter 3), to assess the proportion of surfacing TNRs that are newly-synthesized.

(3) Unexpected: the recycling loop is very long (~3 days): the molecules traffic to the cell soma (reaching the Golgi apparatus and the ER) before resurfacing

Compared with other recycling proteins, the length of the TNR cycle was found to be exceptionally long (*e.g.,* integrin recycling lasts minutes to hours; Bridgewater et al., 2012; Lobert et al., 2010). The reason, we discovered, is that the molecules do not simply traffic to and from local recycling endosomes, but are retrograde-trafficked to the soma, ultimately reaching the Golgi apparatus and the ER. There, they are presumably re-glycosylated and then delivered once again to synapses.

Caveat: We have yet to determine the function of TNR re-glycosylation. Such mechanisms have received little attention in studies of cellular trafficking and, to my knowledge, there are no accounts of such processes occurring in the brain. However, there are several reports of post-translational modifications of glycan residues in other cell types, such as liver cells (Kreisel et al., 1988; Porwoll et al., 1998; Volz et al., 1995). A relatively high prevalence of glycan modifications was found in a liver cancer cell line, which presumably reflects transformations that allow these to migrate freely or that offer protection from immune surveillance. However, the biological significance of re-glycosylation remains to be established for healthy cells. One straightforward possibility is that prolonged exposure of glycans to the extracellular space leads them to be damaged and that re-glycosylation allows them to be replaced without the need for a renewal of the protein core. In this case, the re-glycosylation of TNR in neurons might simply serve to repair the wear and tear of these frequently recycling molecules. A more elaborate possibility is that the identity of the glycan residues itself plays a functional role in TNR recycling by determining its sorting mechanism, as has been proposed for other cell types (Scheiffele et al., 1995). Along these lines, one might speculate that the re-glycosylation of recycling TNR molecules can direct their trafficking to synapses or to other cellular locations.

(4) Unexpected: the ongoing recycling of TNR molecules is necessary for normal synaptic function

It was foreseeable that interference with TNR recycling would lead to a modification of synaptic structure and, indeed, sequestering recycling TNR molecules at the surface for 12 hours resulted in smaller dendritic spines. We did not expect, however, the extent to which this interference would affect synaptic vesicle release, nor that a 30-minute-long perturbance would be sufficient to produce this. Indications that TNR may modulate presynaptic vesicle release can be drawn from mice deficient in TNR, which have a smaller fraction of vesicles in proximity to the active zone, indicating a smaller readily-releasable pool (Nikonenko et al., 2003). However, this study only assessed perisomatic inhibitory synapses, and so it remains to be determined whether this also holds true for excitatory synapses. In any case, it is disproportionate to compare a full knockout of TNR to a 30-minute-long perturbance of its recycling.

Caveat: As discussed above, it is unclear how synaptic vesicle release can be influenced by recycling TNR molecules at the synapse. Since calcium influx into these synapses appeared unaffected, it is likely that TNR exerts its influence through an interaction with presynaptic membrane proteins that are involved in vesicle priming and/or release. One possibility is that, by proxy of their interaction with presynaptic integrins, recycling TNR molecules can modulate the activity of laminins, which are known to be important for the organization of the presynaptic active zone (Chapter 1.2.2). This modulation could, in turn, lead to a reduction in the number of docked vesicles (available for release) or the coupling between synaptic vesicle pools and calcium channels, which is necessary for their stimulus-evoked release. It is also curious that the recycling TNR pool, but not the stable pool, influences presynaptic vesicle release. While it is true that recycling TNR molecules are particularly enriched at synapses, the non-recycling TNRs are nonetheless abundant at synapses as well. One possible explanation is that the two pools are differentially distributed *within* the perisynaptic space. If the recycling molecules are closer to the synaptic membrane, they would be more likely to interact with presynaptic receptors. Another possibility is that the molecules belonging to either pool have different glycosylation patterns, which might lend them different affinities for their presynaptic binding partners.

4.3.   Outstanding questions

Arguably, the most pertinent question to be answered is whether this mechanism holds true for additional ECM molecules. We were successful in repeating our main surface-blocking assay with three additional ECM labels (antibodies against neurocan, hyaluronan binding proteins, and the lectin WFA, which binds GalNAc-terminated glycans). However, these findings should be verified with the same diversity of experiments (and controls) as those that were performed for TNR. In this regard, it is also interesting to speculate about the nature of a recycling pathway for hyaluronan. Unlike other ECM molecules, which have a protein core, and whose synthesis takes place in the ER and Golgi apparatus, hyaluronan is synthesized by enzymes in the plasma membrane (Fowke et al., 2017). As I described earlier (Chapter 1.4.1), it is well-established that hyaluronan can be internalized into endosomes, but it has subsequently only been shown to reach lysosomes to be degraded. However, an electron microscopy study (using the hyaluronan-cleaving enzyme hyaluronidase conjugated to gold as a probe) found that hyaluronan was present in the ER of pancreatic cells and intestinal tissues (Londoño and Bendayan, 1988). It is, therefore, possible that internalized hyaluronan may not necessarily be degraded but continues to be trafficked.

With regard to TNR, there are still numerous open questions that remain to be addressed, as already alluded to when discussing the caveats of our existing results. These can largely be separated into two categories: the specific details of this mechanism (where and how TNR recycling takes place, and with whom it interacts) and the bona fide function of TNR recycling. In the former category, one of the most pressing questions concerns the location of TNR exo- and endocytosis. Although the literature suggests that both of these processes are feasible in both synaptic compartments (with endocytosis being likelier at the postsynapse), this question remains to be addressed experimentally. It is tempting to imagine that the recycling of TNR at synapses is analogous to canonical synaptic transmission, *i.e.,* the molecules are released at the presynapse and received at the postsynapse. Such a mechanism has been suggested, for example, for

the microtubule-associated protein Tau (known to contribute to the pathology of Alzheimer's disease), which was shown to be transported trans-synaptically via exosomes (Wang et al., 2017).

Another question pertains to the interaction of TNR with the integrin receptors that mediate its internalization: it remains to be determined at what point throughout the TNR trafficking route these molecules dissociate. Our current data show that TNR can still be found in intracellular compartments alongside integrins for up to 12 hours following its initial internalization (Chapter 3). These same experiments could be repeated in the future, but continue to follow these molecules for longer periods of time. With that being said, it is reasonable to assume that the molecules dissociate shortly following the 12-hour timepoint, since integrin dynamics are known to be significantly faster than those of TNR (Bridgewater et al., 2012).

A mechanistic question that was already alluded to in the previous section, is whether and how the separate TNR pools differ to each other (and how they are granted different functional capacities). Two possibilities that come to mind are that the pools represent different isoforms and/or have different glycosylation patterns, both of which could be assessed in the future through biochemical analyses. Alternatively (or additionally), the molecules belonging to the two pools may be distributed differently within the perisynaptic space. Our data already suggest that this is the case (recycling TNRs are more enriched in the spine head region; Chapter 3, Extended Data Fig. 17), but resolution on the order of single nanometers will be needed to answer this question more fully (*e.g.*, with an advanced super-resolution approach such as MINFLUX; Balzarotti et al., 2017).

Regarding the function of the recycling mechanism, the claims in this thesis would be further strengthened by drawing a direct link between TNR recycling and spine fluctuations, for example, by imaging these processes in tandem in live neurons. According to our current assumptions, we would expect that a greater extent of TNR recycling would be accompanied by increased spine volatility. By the same assumptions, it might also be expected that the magnitude of TNR recycling (determined by the size of the recycling pool and/or the speed of recycling) could influence the capacity of a neuron to undergo plastic changes. In view of this, an outstanding question is whether juvenile neurons, which are known to be more plastic, have larger TNR recycling pools or faster recycling dynamics.

An additional outstanding question concerns the function of TNR recycling and its dysregulation in disease. Our previous finding that intracellular TNR is increased in a mouse model of epilepsy (Chapter 3, Figure 10) invites the interpretation that a larger TNR recycling pool is linked to higher neuronal excitability (though the cause and effect remains to be determined). This idea could be corroborated by assessing additional models of brain disease, which could also serve to shed further light on the functions of TNR recycling in the healthy brain. Potential models of interest would be schizophrenia, autism, fragile X syndrome, Rett syndrome and bipolar disorder, all of which have been linked to disturbances in the brain ECM (Pantazopoulos and Berretta, 2016).

In addition to the questions raised above, which could be easily addressed *in vitro* and *ex vivo*, many more experiments are required to assess TNR, as well as other ECM molecule recycling, *in vivo*. Here, our main assay will no longer be applicable, and new, more creative tools will need to be developed to tackle these

questions. Some inspiration can be drawn from recent studies which tracked fluorescently-tagged AMPARs in the synapses of behaving mice (Roth et al., 2020; Zhang et al., 2015). Similar experiments using fluorescently-tagged ECM molecules in combination with *in vivo* manipulations of ECM (*e.g.,* enzymatically) or manipulations of synaptic activity (*e.g.,* using optogenetics) could provide a significant amount of insight. Needless to say, once feasible, such experiments are expected to be the focus of future research.

4.4.   Outlook

In 2013, the Nobel laureate Roger Tsien likened the perineuronal net to "a punched card, fantastically convoluted in 3D, in which the position and size of holes preserve the long-term location and strength of synapses" (Tsien, 2013). Indeed, the ECM both in dense PNNs and in looser configurations appears to act as a barrier to the synapse, and prevent it from undergoing structural changes. It is interesting, then, to reconcile this idea with the discovery that the components of the ECM can be highly mobile and in continual transit in and out of the perisynaptic extracellular space. How, then, can it preserve synaptic structure long-term? The gradual understanding that synapses continually fluctuate in size already suggests that this barrier is not as rigid as previously presumed. However, despite their volatility, spines are still able to retain a stable shape over longer timeframes, which suggests that their fluctuations occur about a predetermined mean (Bonilla-quintana and Florentin, 2019; Fischer et al., 1998; Steffens et al., 2021). In a similar manner, the perisynaptic ECM could also retain its mean dimensions while still undergoing continual remodeling. If this is indeed the case, then where would the information about these dimensions be located? In keeping with Tsien's original hypothesis, it is still possible that this information can be stored in the ECM itself. One could imagine, for example, that the ECM directly adjacent to the synapse retains a degree of flexibility through the increased mobility of its components, while the ECM in the periphery is sturdier and less mobile. In this case, the peripheral ECM would represent the bona fide physical barrier to synaptic growth, presumably requiring extensive remodeling (*e.g.,* through proteolytic cleavage) in order to yield. This peripheral ECM, then, would represent the memory storage unit that was originally predicted to exist. In the following years, this premise (or similar ideas) may be confirmed or, perhaps, a paradigm shift will be required to understand the long-term stability of memory.

5. References

Abraham, W.C., and Bear, M.F. (1996). Metaplasticity: the plasticity of synaptic plasticity. Trends Neurosci. *19*, 126–130.

Aerts, J., Nys, J., Moons, L., Hu, T.-T., and Arckens, L. (2015). Altered neuronal architecture and plasticity in the visual cortex of adult MMP-3-deficient mice. Brain Struct. Funct. *220*, 2675–2689.

Aguiar, D.J., Knudson, W., and Knudson, C.B. (1999). Internalization of the Hyaluronan Receptor CD44 by Chondrocytes. Exp. Cell Res. *252*, 292–302.

Annies, M., Bittcher, G., Ramseger, R., Löschinger, J., Wöll, S., Porten, E., Abraham, C., Rüegg, M.A., and Kröger, S. (2006). Clustering transmembrane-agrin induces filopodia-like processes on axons and dendrites. Mol. Cell. Neurosci. *31*, 515–524.

Apóstolo, N., Smukowski, S.N., Vanderlinden, J., Condomitti, G., Rybakin, V., ten Bos, J., Trobiani, L., Portegies, S., Vennekens, K.M., Gounko, N. V., et al. (2020). Synapse type-specific proteomic dissection identifies IgSF8 as a hippocampal CA3 microcircuit organizer. Nat. Commun. *11*, 5171.

Apte, S.S. (2004). A disintegrin-like and metalloprotease (reprolysin type) with thrombospondin type 1 motifs: the ADAMTS family. Int. J. Biochem. Cell Biol. *36*, 981–985.

Araque, A., Parpura, V., Sanzgiri, R.P., and Haydon, P.G. (1999). Tripartite synapses: Glia, the unacknowledged partner. Trends Neurosci. *22*, 208–215.

Arpino, V., Brock, M., and Gill, S.E. (2015). The role of TIMPs in regulation of extracellular matrix proteolysis. Matrix Biol. *44–46*, 247–254.

Aspberg, A., Miura, R., Bourdoulous, S., Shimonaka, M., Heinegârd, D., Schachner, M., Ruoslahti, E., and Yamaguchi, Y. (1997). The C-type lectin domains of lecticans, a family of aggregating chondroitin sulfate proteoglycans, bind tenascin-R by protein-protein interactions independent of carbohydrate moiety. Proc. Natl. Acad. Sci. U. S. A. *94*, 10116–10121.

Aumailley, M., Gerl, M., Sonnenberg, A., Deutzmann, R., and Timpl, R. (1990). Identification of the Arg-Gly-Asp sequence in laminin A chain as a latent cell-binding site being exposed in fragment P1. FEBS Lett. *262*, 82–86.

Baeten, K.M., and Akassoglou, K. (2011). Extracellular matrix and matrix receptors in blood-brain barrier formation and stroke. Dev. Neurobiol. *71*, 1018–1039.

Bal, M., Leitz, J., Reese, A.L., Ramirez, D.M.O., Durakoglugil, M., Herz, J., Monteggia, L.M., and Kavalali, E.T. (2013). Reelin Mobilizes a VAMP7-Dependent Synaptic Vesicle Pool and Selectively Augments Spontaneous Neurotransmission. Neuron *80*, 934–946.

Balzarotti, F., Eilers, Y., Gwosch, K.C., Gynnå, A.H., Westphal, V., Stefani, F.D., Elf, J., and Hell, S.W. (2017). Nanometer resolution imaging and tracking of fluorescent molecules with minimal photon fluxes. Science (80-.). *355*, 606–612.

Banerjee, S.B., Gutzeit, V.A., Baman, J., Aoued, H.S., Doshi, N.K., Liu, R.C., and Ressler, K.J. (2017). Perineuronal Nets in the Adult Sensory Cortex Are Necessary for Fear Learning. Neuron *95*, 169-179.e3.

Bartsch, U. (1996). The extracellular matrix molecule tenascin-C: Expression in vivo and functional characterization in vitro. Prog. Neurobiol. *49*, 145–161.

Bartsch, U., Pesheva, P., Raff, M., and Schachner, M. (1993). Expression of janusin (J1–160/180) in the retina and optic nerve of the developing and adult mouse. Glia *9*, 57–69.

Becker, T., Anliker, B., Becker, C.G., Taylor, J., Schachner, M., Meyer, R.L., and Bartsch, U. (2000). Tenascin-R inhibits regrowth of optic fibers in vitro and persists in the optic nerve of mice after injury. Glia *29*, 330–346.

Beffert, U., Weeber, E.J., Durudas, A., Qiu, S., Masiulis, I., Sweatt, J.D., Li, W.P., Adelmann, G., Frotscher, M., Hammer, R.E., et al. (2005). Modulation of synaptic plasticity and memory by Reelin involves

differential splicing of the lipoprotein receptor Apoer2. Neuron *47*, 567–579.

Benarroch, E.E. (2015). Extracellular matrix in the CNS. Neurology *85*, 1417–1427.

Bernard-Trifilo, J.A., Kramár, E.A., Torp, R., Lin, C.Y., Pineda, E.A., Lynch, G., and Gall, C.M. (2005). Integrin signaling cascades are operational in adult hippocampal synapses and modulate NMDA receptor physiology. J. Neurochem. *93*, 834–849.

Berning, S., Willig, K.I., Steffens, H., Dibaj, P., and Hell, S.W. (2012). Nanoscopy in a living mouse brain. Science *335*, 551.

Bharat, V., Siebrecht, M., Burk, K., Ahmed, S., Reissner, C., Kohansal-Nodehi, M., Steubler, V., Zweckstetter, M., Ting, J.T., and Dean, C. (2017). Capture of Dense Core Vesicles at Synapses by JNK-Dependent Phosphorylation of Synaptotagmin-4. Cell Rep. *21*, 2118–2133.

Bijata, M., Labus, J., Guseva, D., Stawarski, M., Butzlaff, M., Dzwonek, J., Schneeberg, J., Böhm, K., Michaluk, P., Rusakov, D.A., et al. (2017). Synaptic Remodeling Depends on Signaling between Serotonin Receptors and the Extracellular Matrix. Cell Rep. *19*, 1767–1782.

Bilousova, T. V., Rusakov, D.A., Ethell, D.W., and Ethell, I.M. (2006). Matrix metalloproteinase-7 disrupts dendritic spines in hippocampal neurons through NMDA receptor activation. J. Neurochem. *97*, 44.

Blosa, M., Sonntag, M., Jäger, C., Weigel, S., Seeger, J., Frischknecht, R., Seidenbecher, C.I., Matthews, R.T., Arendt, T., Rübsamen, R., et al. (2015). The extracellular matrix molecule brevican is an integral component of the machinery mediating fast synaptic transmission at the calyx of Held. J. Physiol. *593*, 4341–4360.

Bodrikov, V., Pauschert, A., Kochlamazashvili, G., and Stuermer, C.A.O. (2017). Reggie-1 and reggie-2 (flotillins) participate in Rab11a-dependent cargo trafficking, spine synapse formation and LTP-related AMPA receptor (GluA1) surface exposure in mouse hippocampal neurons. Exp. Neurol. *289*, 31–45.

Bonilla-quintana, M., and Florentin, W. (2019). Modeling the Shape of Synaptic Spines by their Actin Dynamics Author summary.

Borgdorff, A.J., and Choquet, D. (2002). Regulation of AMPA receptor lateral movements. Nature *417*, 649–653.

Bourdon, M.A., and Ruoslahti, E. (1989). Tenascin mediates cell attachment through an RGD-dependent receptor. J. Cell Biol. *108*, 1149–1155.

Bozdagi, O., Nagy, V., Kwei, K.T., and Huntley, G.W. (2007). In Vivo Roles for Matrix Metalloproteinase-9 in Mature Hippocampal Synaptic Physiology and Plasticity. J. Neurophysiol. *98*, 334–344.

Bretscher, M.S. (1989). Endocytosis and recycling of the fibronectin receptor in CHO cells. EMBO J. *8*, 1341–1348.

Briatore, F., Pregno, G., Di Angelantonio, S., Frola, E., De Stefano, M.E., Vaillend, C., Sassoè-Pognetto, M., and Patrizi, A. (2020). Dystroglycan Mediates Clustering of Essential GABAergic Components in Cerebellar Purkinje Cells. Front. Mol. Neurosci. *13*, 164.

Bridgewater, R.E., Norman, J.C., and Caswell, P.T. (2012). Integrin trafficking at a glance. J. Cell Sci. *125*, 3695–3701.

Brückner, G., Grosche, J., Schmidt, S., Härtig, W., Margolis, R.U., Delpech, B., Seidenbecher, C.I., Czaniera, R., and Schachner, M. (2000). Postnatal development of perineuronal nets in wild-type mice and in a mutant deficient in tenascin-R. J. Comp. Neurol. *428*, 616–629.

Brzdąk, P., Wlodarczyk, J., Mozrzymas, J.W., and Wójtowicz, T. (2017). Matrix Metalloprotease 3 Activity Supports Hippocampal EPSP-to-Spike Plasticity Following Patterned Neuronal Activity via the Regulation of NMDAR Function and Calcium Flux. Mol. Neurobiol. *54*, 804–816.

Budnik, V., Ruiz-Cañada, C., and Wendler, F. (2016). Extracellular vesicles round off communication in the nervous system. Nat. Rev. Neurosci. *17*, 160–172.

Bukalo, O., Schachner, M., and Dityatev, A. (2007). Hippocampal Metaplasticity Induced by Deficiency in the Extracellular Matrix Glycoprotein Tenascin-R. J. Neurosci. *27*, 6019–6028.

De Camilli, P., and Jahn, R. (1990). Pathways to regulated exocytosis in neurons. Annu. Rev. Physiol. *52*, 625–645.

Carlson, S.S., Valdez, G., and Sanes, J.R. (2010). Presynaptic calcium channels and α3-integrins are complexed with synaptic cleft laminins, cytoskeletal elements and active zone components. J. Neurochem. *115*, 654–666.

Carnemolla, B., Leprini, A., Borsi, L., Querzé, G., Urbini, S., and Zardi, L. (1996). Human Tenascin-R. J. Biol. Chem. *271*, 8157–8160.

Chan, C.S., Weeber, E.J., Zong, L., Fuchs, E., Sweatt, J.D., and Davis, R.L. (2006). β1-integrins are required for hippocampal AMPA receptor-dependent synaptic transmission, synaptic plasticity, and working memory. J. Neurosci. *26*, 223–232.

Chang, W.-P., and Sudhof, T.C. (2009). SV2 Renders Primed Synaptic Vesicles Competent for Ca2+-Induced Exocytosis. J. Neurosci. *29*, 883–897.

Chua, C.E.L., and Tang, B.L. (2008). Syntaxin 16 is enriched in neuronal dendrites and may have a role in neurite outgrowth. Mol. Membr. Biol. *25*, 35–45.

Collin, T., Marty, A., and Llano, I. (2005). Presynaptic calcium stores and synaptic transmission. Curr. Opin. Neurobiol. *15*, 275–281.

Colombo, M., Raposo, G., and Théry, C. (2014). Biogenesis, Secretion, and Intercellular Interactions of Exosomes and Other Extracellular Vesicles. Annu. Rev. Cell Dev. Biol. *30*, 255–289.

Conant, K., Lonskaya, I., Szklarczyk, A., Krall, C., Steiner, J., Maguire-Zeiss, K., and Lim, S.T. (2011). Methamphetamine-associated cleavage of the synaptic adhesion molecule intercellular adhesion molecule-5. J. Neurochem. *118*, 521–532.

Coopman, P.J., Thomas, D.M., Gehlsen, K.R., and Mueller, S.C. (1996). Integrin alpha 3 beta 1 participates in the phagocytosis of extracellular matrix molecules by human breast cancer cells. Mol. Biol. Cell *7*, 1789–1804.

D'Arcangelo, G. (2014). Reelin in the Years: Controlling Neuronal Migration and Maturation in the Mammalian Brain. Adv. Neurosci. *2014*, 1–19.

Dalva, M.B., McClelland, A.C., and Kayser, M.S. (2007). Cell adhesion molecules: Signalling functions at the synapse. Nat. Rev. Neurosci. *8*, 206–220.

Dankovich, T.M., Kaushik, R., Olsthoorn, L.H.M., Petersen, G.C., Giro, P.E., Kluever, V., Agüi-Gonzalez, P., Grewe, K., Bao, G., Beuermann, S., et al. (2021). Extracellular matrix remodeling through endocytosis and resurfacing of Tenascin-R. Nat. Commun. 2021 121 *12*, 1–23.

David, L.S., Schachner, M., and Saghatelyan, A. (2013). The Extracellular Matrix Glycoprotein Tenascin-R Affects Adult But Not Developmental Neurogenesis in the Olfactory Bulb. J. Neurosci. *33*, 10324–10339.

Deepa, S.S., Carulli, D., Galtrey, C., Rhodes, K., Fukuda, J., Mikami, T., Sugahara, K., and Fawcett, J.W. (2006). Composition of perineuronal net extracellular matrix in rat brain: a different disaccharide composition for the net-associated proteoglycans. J. Biol. Chem. *281*, 17789–17800.

Denker, A., Kröhnert, K., Bückers, J., Neher, E., and Rizzoli, S.O. (2011). The reserve pool of synaptic vesicles acts as a buffer for proteins involved in synaptic vesicle recycling. Proc. Natl. Acad. Sci. U. S. A. *108*, 17183–17188.

Dityatev, A., and Schachner, M. (2003). Extracellular matrix molecules and synaptic plasticity. Nat. Rev. Neurosci. *4*, 456–468.

Dityatev, A., Frischknecht, R., and Seidenbecher, C.I. (2006). Extracellular Matrix and Synaptic Functions. In Cell Communication in Nervous and Immune System, (Springer Berlin Heidelberg), pp. 69–97.

Dityatev, A., Schachner, M., and Sonderegger, P. (2010). The dual role of the extracellular matrix in synaptic plasticity and homeostasis. Nat. Rev. Neurosci. *11*, 735–746.

Djerbal, L., Lortat-Jacob, H., and Kwok, J. (2017). Chondroitin sulfates and their binding molecules in the central nervous system. Glycoconj. J. *34*, 363–376.

Dörrbaum, A.R., Kochen, L., Langer, J.D., and Schuman, E.M. (2018). Local and global influences on protein turnover in neurons and glia. Elife *7*.

Dulabon, L., Olson, E.C., Taglienti, M.G., Eisenhuth, S., McGrath, B., Walsh, C.A., Kreidberg, J.A., and Anton, E.. (2000). Reelin Binds α3β1 Integrin and Inhibits Neuronal Migration. Neuron *27*, 33–44.

Dziembowska, M., Milek, J., Janusz, A., Rejmak, E., Romanowska, E., Gorkiewicz, T., Tiron, A., Bramham, C.R., and Kaczmarek, L. (2012). Activity-Dependent Local Translation of Matrix Metalloproteinase-9. J. Neurosci. *32*, 14538.

Dzyubenko, E., Gottschling, C., and Faissner, A. (2016). Neuron-Glia Interactions in Neural Plasticity: Contributions of Neural Extracellular Matrix and Perineuronal Nets (Hindawi Publishing Corporation).

Ehlers, M.D. (2000). Reinsertion or Degradation of AMPA Receptors Determined by Activity-Dependent Endocytic Sorting. Neuron *28*, 511–525.

Embry, J.J., and Knudson, W. (2003). G1 domain of aggrecan cointernalizes with hyaluronan via a CD44-mediated mechanism in bovine articular chondrocytes. Arthritis Rheum. *48*, 3431–3441.

Evers, M.R., Salmen, B., Bukalo, O., Rollenhagen, A., Bösl, M.R., Morellini, F., Bartsch, U., Dityatev, A., and Schachner, M. (2002). Impairment of L-type Ca2+ channel-dependent forms of hippocampal synaptic plasticity in mice deficient in the extracellular matrix glycoprotein tenascin-C. J. Neurosci. *22*, 7177–7194.

Faissner, A. (1997). The tenascin gene family in axon growth and guidance. Cell Tissue Res. *290*, 331–341.

Faissner, A., Pyka, M., Geissler, M., Sobik, T., Frischknecht, R., Gundelfinger, E.D., and Seidenbecher, C. (2010). Contributions of astrocytes to synapse formation and maturation - Potential functions of the perisynaptic extracellular matrix. Brain Res. Rev. *63*, 26–38.

Fauré, J., Lachenal, G., Court, M., Hirrlinger, J., Chatellard-Causse, C., Blot, B., Grange, J., Schoehn, G., Goldberg, Y., Boyer, V., et al. (2006). Exosomes are released by cultured cortical neurones. Mol. Cell. Neurosci. *31*, 642–648.

Fawcett, J.W., Oohashi, T., and Pizzorusso, T. (2019). The roles of perineuronal nets and the perinodal extracellular matrix in neuronal function. Nat. Rev. Neurosci. *20*, 451–465.

Fell, B., Eckrich, S., Blum, K., Eckrich, T., Hecker, D., Obermair, G.J., Münkner, S., Flockerzi, V., Schick, B., and Engel, J. (2016). α2δ2 controls the function and trans-synaptic coupling of cav1.3 channels in mouse inner hair cells and is essential for normal hearing. J. Neurosci. *36*, 11024–11036.

Ferhat, L., Chevassus Au Louis, N., Jorquera, I., Niquet, J., Khrestchatisky, M., Ben-Ari, Y., and Represa, A. (1996). Transient increase of tenascin-C in immature hippocampus: Astroglial and neuronal expression. J. Neurocytol. *25*, 53–66.

ffrench-Constant, C., and Raff, M.C. (1986). The oligodendrocyte-type-2 astrocyte cell lineage is specialized for myelination. Nature *323*, 335–338.

Fischer, M., Kaech, S., Knutti, D., and Matus, A. (1998). Rapid Actin-Based Plasticity in Dendritic Spines. Neuron *20*, 847–854.

Fletcher, T.L., De Camilli, P., and Banker, G. (1994). Synaptogenesis in hippocampal cultures: Evidence indicating that axons and dendrites become competent to form synapses at different stages of neuronal development. J. Neurosci. *14*, 6695–6706.

Fornasiero, E.F., Mandad, S., Wildhagen, H., Alevra, M., Rammner, B., Keihani, S., Opazo, F., Urban, I., Ischebeck, T., Sakib, M.S., et al. (2018). Precisely measured protein lifetimes in the mouse brain reveal differences across tissues and subcellular fractions. Nat. Commun. *9*, 4230.

Fowke, T.M., Karunasinghe, R.N., Bai, J.-Z., Jordan, S., Gunn, A.J., and Dean, J.M. (2017). Hyaluronan synthesis by developing cortical neurons in vitro. Sci. Rep. *7*, 44135.

Fraser, J.R.E., Laurent, T.C., and Laurent, U.B.G. (1997). Hyaluronan: its nature, distribution, functions and turnover. J. Intern. Med. *242*, 27–33.

Frischknecht, R., Fejtova, A., Viesti, M., Stephan, A., and Sonderegger, P. (2008). Activity-Induced Synaptic Capture and Exocytosis of the Neuronal Serine Protease Neurotrypsin. J. Neurosci. *28*, 1568–1579.

Frischknecht, R., Heine, M., Perrais, D., Seidenbecher, C.I., Choquet, D., and Gundelfinger, E.D. (2009). Brain extracellular matrix affects AMPA receptor lateral mobility and short-term synaptic plasticity (Reprinted from Erschienen in Nature Neuroscience, vol 12, pg 897-804, 2009). Neuroforum *15*, 94–95.

Fujimoto, T., Kawashima, H., Tanaka, T., Hirose, M., Toyama-Sorimachi, N., Matsuzawa, Y., and Miyasaka, M. (2001). CD44 binds a chondroitin sulfate proteoglycan, aggrecan. Int. Immunol. *13*, 359–366.

Fuss, B., Wintergerst, E.S., Bartsch, U., and Schachner, M. (1993). Molecular characterization and in situ mRNA localization of the neural recognition molecule J1-160/180: a modular structure similar to tenascin. J. Cell Biol. *120*, 1237–1249.

Gautam, M., Noakes, P.G., Moscoso, L., Rupp, F., Scheller, R.H., Merlie, J.P., and Sanes, J.R. (1996). Defective Neuromuscular Synaptogenesis in Agrin-Deficient Mutant Mice. Cell *85*, 525–535.

Gesemann, M., Brancaccio, A., Schumacher, B., and Ruegg, M.A. (1998). Agrin Is a High-affinity Binding Protein of Dystroglycan in Non-muscle Tissue. J. Biol. Chem. *273*, 600–605.

Giagtzoglou, N., Ly, C. V., and Bellen, H.J. (2009). Cell adhesion, the backbone of the synapse: "vertebrate" and "invertebrate" perspectives. Cold Spring Harb. Perspect. Biol. *1*.

Giannelli, G. (1997). Induction of Cell Migration by Matrix Metalloprotease-2 Cleavage of Laminin-5. Science (80-.). *277*, 225–228.

Glass, D.J., Bowen, D.C., Stitt, T.N., Radziejewski, C., Bruno, J., Ryan, T.E., Gies, D.R., Shah, S., Mattsson, K., Burden, S.J., et al. (1996). Agrin Acts via a MuSK Receptor Complex. Cell *85*, 513–523.

Glebov, O.O., Tigaret, C.M., Mellor, J.R., and Henley, J.M. (2015). Clathrin-Independent Trafficking of AMPA Receptors. J. Neurosci. *35*, 4830–4836.

Gogolla, N., Caroni, P., Luthi, A., and Herry, C. (2009). Perineuronal Nets Protect Fear Memories from Erasure. Science (80-.). *325*, 1258–1261.

Golgi, C. (1898). Intorno alla struttura delle cellule nervose. Boll. Della Soc. Med. Chir. Di Pavia *13*, 3–16.

Gottschall, P.E., and Howell, M.D. (2015). ADAMTS expression and function in central nervous system injury and disorders. Matrix Biol. *44–46*, 70.

Gray, E.G. (1959). Electron Microscopy of Synaptic Contacts on Dendrite Spines of the Cerebral Cortex. Nature *183*, 1592–1593.

Grover, L.M., and Yan, C. (1999). Blockade of GABA A Receptors Facilitates Induction of NMDA Receptor-Independent Long-Term Potentiation. J. Neurophysiol. *81*, 2814–2822.

Gruenberg, J., and Stenmark, H. (2004). The biogenesis of multivesicular endosomes. Nat. Rev. Mol. Cell Biol. *5*, 317–323.

Gschwend, T.P., Krueger, S.R., Kozlov, S. V., Wolfer, D.P., and Sonderegger, P. (1997). Neurotrypsin, a Novel Multidomain Serine Protease Expressed in the Nervous System. Mol. Cell. Neurosci. *9*, 207–219.

Gupton, S.L., and Gertler, F.B. (2010). Integrin signaling switches the cytoskeletal and exocytic machinery that drives neuritogenesis. Dev. Cell *18*, 725–736.

Gürth, C.M., Dankovich, T.M., Rizzoli, S.O., and D'Este, E. (2020). Synaptic activity and strength are reflected by changes in the post-synaptic secretory pathway. Sci. Reports 2020 101 *10*, 1–13.

Hagihara, K., Miura, R., Kosaki, R., Berglund, E., Ranscht, B., and Yamaguchi, Y. (1999).

Immunohistochemical evidence for the brevican-tenascin-R interaction: Colocalization in perineuronal nets suggests a physiological role for the interaction in the adult rat brain. J. Comp. Neurol. *410*, 256–264.

Hamel, M.G., Ajmo, J.M., Leonardo, C.C., Zuo, F., Sandy, J.D., and Gottschall, P.E. (2008). Multimodal signaling by the ADAMTSs (a disintegrin and metalloproteinase with thrombospondin motifs) promotes neurite extension. Exp. Neurol. *210*, 428–440.

Härtig, W., Brauer, K., and Brückner, G. (1992). Wisteria floribunda agglutinin-labelled nets surround parvalbumin-containing neurons. Neuroreport *3*, 869–872.

Haunsoø, A., Ibrahim, M., Bartsch, U., Letiembre, M., Celio, M.R., and Menoud, P.A. (2000). Morphology of perineuronal nets in tenascin-R and parvalbumin single and double knockout mice. Brain Res. *864*, 142–145.

Hazan, L., and Ziv, N.E. (2020). Activity Dependent and Independent Determinants of Synaptic Size Diversity. J. Neurosci. *40*, 2828–2848.

Heck, N., Garwood, J., Loeffler, J.-P., Larmet, Y., and Faissner, A. (2004). Differential upregulation of extracellular matrix molecules associated with the appearance of granule cell dispersion and mossy fiber sprouting during epileptogenesis in a murine model of temporal lobe epilepsy. Neuroscience *129*, 309–324.

Helm, M.S., Dankovich, T.M., Mandad, S., Rammner, B., Jähne, S., Salimi, V., Koerbs, C., Leibrandt, R., Urlaub, H., Schikorski, T., et al. (2021). A large-scale nanoscopy and biochemistry analysis of postsynaptic dendritic spines. Nat. Neurosci.

Heo, S., Diering, G.H., Na, C.H., Nirujogi, R.S., Bachman, J.L., Pandey, A., and Huganir, R.L. (2018). Identification of long-lived synaptic proteins by proteomic analysis of synaptosome protein turnover. Proc. Natl. Acad. Sci. *115*, E3827–E3836.

Herndon, M.E., and Lander, A.D. (1990). A diverse set of developmentally regulated proteoglycans is expressed in the rat central nervous system. Neuron *4*, 949–961.

Herring, B.E., and Nicoll, R.A. (2016). Long-Term Potentiation: From CaMKII to AMPA Receptor Trafficking. Annu. Rev. Physiol. *78*, 351–365.

Hisanaga, A., Morishita, S., Suzuki, K., Sasaki, K., Koie, M., Kohno, T., and Hattori, M. (2012). A disintegrin and metalloproteinase with thrombospondin motifs 4 (ADAMTS-4) cleaves Reelin in an isoform-dependent manner. FEBS Lett. *586*, 3349–3353.

Holt, C.E., Martin, K.C., and Schuman, E.M. (2019). Local translation in neurons: visualization and function. Nat. Struct. Mol. Biol. *26*, 557–566.

Horikawa, K., and Armstrong, W.E. (1988). A versatile means of intracellular labeling: injection of biocytin and its detection with avidin conjugates. J. Neurosci. Methods *25*, 1–11.

Hou, Q., Zhang, D., Jarzylo, L., Huganir, R.L., and Man, H.-Y. (2008). Homeostatic regulation of AMPA receptor expression at single hippocampal synapses. Proc. Natl. Acad. Sci. U. S. A. *105*, 775–780.

Hsia, H.C., and Schwarzbauer, J.E. (2005). Meet the tenascins: Multifunctional and mysterious. J. Biol. Chem. *280*, 26641–26644.

Huang, Z., Shimazu, K., Woo, N.H., Zang, K., Muller, U., Lu, B., and Reichardt, L.F. (2006). Distinct Roles of the beta1-Class Integrins at the Developing and the Mature Hippocampal Excitatory Synapse. J. Neurosci. *26*, 11208–11219.

Humeau, Y., and Choquet, D. (2019). The next generation of approaches to investigate the link between synaptic plasticity and learning. Nat. Neurosci. *22*, 1536–1543.

Hunter, D.D., Manglapus, M.K., Bachay, G., Claudepierre, T., Dolan, M.W., Gesuelli, K.A., and Brunken, W.J. (2019). CNS synapses are stabilized trans-synaptically by laminins and laminin-interacting proteins. J. Comp. Neurol. *527*, 67–86.

Huntley, G.W. (2012). Synaptic circuit remodelling by matrix metalloproteinases in health and disease. Nat. Rev. Neurosci. *13*, 743.

Izumi, Y., Wakita, S., Kanbara, C., Nakai, T., Akaike, A., and Kume, T. (2017). Integrin α5β1 expression

on dopaminergic neurons is involved in dopaminergic neurite outgrowth on striatal neurons. Sci. Rep. *7*, 42111.

Jähne, S., Rizzoli, S.O., and Helm, M.S. (2015). The structure and function of presynaptic endosomes. Exp. Cell Res. *335*, 172–179.

Jenkins, H.G., and Bachelard, H.S. (1988). Developmental and Age-Related Changes in Rat Brain Glycosaminoglycans. J. Neurochem. *51*, 1634–1640.

Johannes, L., and Popoff, V. (2008). Tracing the Retrograde Route in Protein Trafficking. Cell *135*, 1175–1187.

John, N., Krügel, H., Frischknecht, R., Smalla, K.H., Schultz, C., Kreutz, M.R., Gundelfinger, E.D., Seidenbecher, C.I., Krugel, H., Frischknecht, R., et al. (2006). Brevican-containing perineuronal nets of extracellular matrix in dissociated hippocampal primary cultures. Mol. Cell. Neurosci. *31*, 774–784.

Jones, F.S., and Jones, P.L. (2000). The tenascin family of ECM glycoproteins: Structure, function, and regulation during embryonic development and tissue remodeling. Dev. Dyn. *218*, 235–259.

Jung, N., and Haucke, V. (2007). Clathrin-Mediated Endocytosis at Synapses. Traffic *8*, 1129–1136.

Jurado, S. (2014). The dendritic SNARE fusion machinery involved in AMPARs insertion during long-term potentiation. Front. Cell. Neurosci. *8*.

Kawaguchi, S., and Hirano, T. (2006). Integrin α3β1 suppresses long-term potentiation at inhibitory synapses on the cerebellar Purkinje neuron. Mol. Cell. Neurosci. *31*, 416–426.

Kawashima, H., Atarashi, K., Hirose, M., Hirose, J., Yamada, S., Sugahara, K., and Miyasaka, M. (2002). Oversulfated Chondroitin/Dermatan Sulfates Containing GlcAβ1/IdoAα1–3GalNAc(4,6-O-disulfate) Interact with L- and P-selectin and Chemokines. J. Biol. Chem. *277*, 12921–12930.

Kerrisk, M.E., Cingolani, L.A., and Koleske, A.J. (2014). ECM receptors in neuronal structure, synaptic plasticity, and behavior. In Progress in Brain Research, pp. 101–131.

Kim, S.H., Turnbull, J., and Guimond, S. (2011). Extracellular matrix and cell signalling: The dynamic cooperation of integrin, proteoglycan and growth factor receptor. J. Endocrinol. *209*, 139–151.

Kim, T., Gondré-Lewis, M.C., Arnaoutova, I., and Loh, Y.P. (2006). Dense-Core Secretory Granule Biogenesis. Physiology *21*, 124–133.

Knudson, W., Chow, G., and Knudson, C.B. (2002). CD44-mediated uptake and degradation of hyaluronan. Matrix Biol.

Kochlamazashvili, G., Henneberger, C., Bukalo, O., Dvoretskova, E., Senkov, O., Lievens, P.M.J., Westenbroek, R., Engel, A.K., Catterall, W.A., Rusakov, D.A., et al. (2010). The extracellular matrix molecule hyaluronic acid regulates hippocampal synaptic plasticity by modulating postsynaptic L-type Ca2+ channels. Neuron *67*, 116–128.

Koenig, J.A., and Edwardson, J.M. (1997). Endocytosis and recycling of G protein-coupled receptors. Trends Pharmacol. Sci. *18*, 276–287.

Koh, S., Lee, W., Park, S.M., and Kim, S.H. (2021). Caveolin-1 deficiency impairs synaptic transmission in hippocampal neurons. Mol. Brain 2021 141 *14*, 1–10.

Konopacki, F.A., Rylski, M., Wilczek, E., Amborska, R., Detka, D., Kaczmarek, L., and Wilczynski, G.M. (2007). Synaptic localization of seizure-induced matrix metalloproteinase-9 mRNA. Neuroscience *150*, 31–39.

Kramar, E.A., Lin, B., Rex, C.S., Gall, C.M., and Lynch, G. (2006). Integrin-driven actin polymerization consolidates long-term potentiation. Proc. Natl. Acad. Sci. *103*, 5579–5584.

Kramár, E.., Bernard, J.., Gall, C.., and Lynch, G. (2002). Alpha3 integrin receptors contribute to the consolidation of long-term potentiation. Neuroscience *110*, 29–39.

Kreisel, W., Hanski, C., Tran-Thi, T.A., Katz, N., Decker, K., Reutter, W., and Gerok, W. (1988). Remodeling of a rat hepatocyte plasma membrane glycoprotein. De- and reglycosylation of dipeptidyl

peptidase IV. J. Biol. Chem. *263*, 11736–11742.

Kruse, J., Keilhauer, G., Faissner, A., Timpl, R., and Schachner, M. (1985). The J1 glycoprotein—a novel nervous system cell adhesion molecule of the L2/HNK-1 family. Nature *316*, 146–148.

Kumari, S., MG, S., and Mayor, S. (2010). Endocytosis unplugged: multiple ways to enter the cell. Cell Res. *20*, 256–275.

Laabs, T., Carulli, D., Geller, H.M., and Fawcett, J.W. (2005). Chondroitin sulfate proteoglycans in neural development and regeneration. Curr. Opin. Neurobiol. *15*, 116–120.

Lachenal, G., Pernet-Gallay, K., Chivet, M., Hemming, F.J., Belly, A., Bodon, G., Blot, B., Haase, G., Goldberg, Y., and Sadoul, R. (2011). Release of exosomes from differentiated neurons and its regulation by synaptic glutamatergic activity. Mol. Cell. Neurosci. *46*, 409–418.

Lemarchant, S., Pruvost, M., Montaner, J., Emery, E., Vivien, D., Kanninen, K., and Koistinaho, J. (2013). ADAMTS proteoglycanases in the physiological and pathological central nervous system. J. Neuroinflammation *10*, 133.

Leonoudakis, D., Huang, G., Akhavan, A., Fata, J.E., Singh, M., Gray, J.W., and Muschler, J.L. (2014). Endocytic trafficking of laminin is controlled by dystroglycan and disrupted in cancers. J. Cell Sci. *127*, 4894.

Lévi, S., Grady, R.M., Henry, M.D., Campbell, K.P., Sanes, J.R., and Craig, A.M. (2002). Dystroglycan Is Selectively Associated with Inhibitory GABAergic Synapses But Is Dispensable for Their Differentiation. J. Neurosci. *22*, 4274–4285.

Li, Z., and Sheng, M. (2003). Some assembly required: The development of neuronal synapses. Nat. Rev. Mol. Cell Biol. *4*, 833–841.

Liao, H., Huang, W., Schachner, M., Guan, Y., Guo, J., Yan, J., Qin, J., Bai, X., and Zhang, L. (2008). β 1 Integrin-mediated Effects of Tenascin-R Domains EGFL and FN6-8 on Neural Stem/Progenitor Cell Proliferation and Differentiation in Vitro. J. Biol. Chem. *283*, 27927–27936.

Lobert, V.H., Brech, A., Pedersen, N.M., Wesche, J., Oppelt, A., Malerød, L., and Stenmark, H. (2010). Ubiquitination of α5β1 Integrin Controls Fibroblast Migration through Lysosomal Degradation of Fibronectin-Integrin Complexes. Dev. Cell *19*, 148–159.

Löffek, S., Schilling, O., and Franzke, C.-W. (2011). Biological role of matrix metalloproteinases: a critical balance. Eur. Respir. J. *38*, 191–208.

Londoño, I., and Bendayan, M. (1988). High-resolution cytochemistry of neuraminic and hexuronic acid-containing macromolecules applying the enzyme-gold approach. J. Histochem. Cytochem. *36*, 1005–1014.

Lundell, A., Olin, A.I., Mörgelin, M., Al-Karadaghi, S., Aspberg, A., and Logan, D.T. (2004). Structural basis for interactions between tenascins and lectican C-type lectin domains: Evidence for a crosslinking role for tenascins. Structure *12*, 1495–1506.

Magnowska, M., Gorkiewicz, T., Suska, A., Wawrzyniak, M., Rutkowska-Wlodarczyk, I., Kaczmarek, L., and Wlodarczyk, J. (2016). Transient ECM protease activity promotes synaptic plasticity. Sci. Rep. *6*, 27757.

Man, H.-Y., Lin, J.W., Ju, W.H., Ahmadian, G., Liu, L., Becker, L.E., Sheng, M., and Wang, Y.T. (2000). Regulation of AMPA Receptor–Mediated Synaptic Transmission by Clathrin-Dependent Receptor Internalization. Neuron *25*, 649–662.

Marchetti, G., Escuin, S., van der Flier, A., De Arcangelis, A., Hynes, R.O., and Georges-Labouesse, E. (2010). Integrin α5β1 is necessary for regulation of radial migration of cortical neurons during mouse brain development. Eur. J. Neurosci. *31*, 399–409.

Margolis, R.U., Margolis, R.K., Chang, L.B., and Preti, C. (1975). Glycosaminoglycans of Brain during Development. Biochemistry *14*, 85–88.

Matsumoto-Miyai, K., Sokolowska, E., Zurlinden, A., Gee, C.E., Lüscher, D., Hettwer, S., Wölfel, J.,

Ladner, A.P., Ster, J., Gerber, U., et al. (2009). Coincident Pre- and Postsynaptic Activation Induces Dendritic Filopodia via Neurotrypsin-Dependent Agrin Cleavage. Cell *136*, 1161–1171.

Matsumoto, K., Saga, Y., Ikemura, T., Sakakura, T., and Chiquet-Ehrismann, R. (1994). The distribution of tenascin-X is distinct and often reciprocal to that of tenascin-C. J. Cell Biol. *125*, 483–493.

McCarty, J.H., Lacy-Hulbert, A., Charest, A., Bronson, R.T., Crowley, D., Housman, D., Savill, J., Roes, J., and Hynes, R.O. (2005). Selective ablation of αv integrins in the central nervous system leads to cerebral hemorrhage, seizures, axonal degeneration and premature death. Development *132*, 165–176.

McCroskery, S., Chaudhry, A., Lin, L., and Daniels, M.P. (2006). Transmembrane agrin regulates filopodia in rat hippocampal neurons in culture. Mol. Cell. Neurosci. *33*, 15–28.

McGraw, C.F., Somlyo, A. V, and Blaustein, M.P. (1980). Localization of calcium in presynaptic nerve terminals. An ultrastructural and electron microprobe analysis. J. Cell Biol. *85*, 228–241.

Mercuri, F.A., Maciewicz, R.A., Tart, J., Last, K., and Fosang, A.J. (2000). Mutations in the Interglobular Domain of Aggrecan Alter Matrix Metalloproteinase and Aggrecanase Cleavage Patterns. J. Biol. Chem. *275*, 33038–33045.

Merighi, A. (2018). Costorage of High Molecular Weight Neurotransmitters in Large Dense Core Vesicles of Mammalian Neurons. Front. Cell. Neurosci. *12*, 272.

Michaluk, P., Wawrzyniak, M., Alot, P., Szczot, M., Wyrembek, P., Mercik, K., Medvedev, N., Wilczek, E., De Roo, M., Zuschratter, W., et al. (2011). Influence of matrix metalloproteinase MMP-9 on dendritic spine morphology. J. Cell Sci. *124*, 3369–3380.

Midwood, K.S., Chiquet, M., Tucker, R.P., and Orend, G. (2016). Tenascin-C at a glance. J. Cell Sci. *129*, 4321–4327.

Migaud, M., Charlesworth, P., Dempster, M., Webster, L.C., Watabe, A.M., Makhinson, M., He, Y., Ramsay, M.F., Morris, R.G.M., Morrison, J.H., et al. (1998). Enhanced long-term potentiation and impaired learning in mice with mutant postsynaptic density-95 protein. Nat. 1998 3966710 *396*, 433–439.

Miyata, S., Nishimura, Y., Hayashi, N., and Oohira, A. (2005). Construction of perineuronal net-like structure by cortical neurons in culture. Neuroscience *136*, 95–104.

Morawski, M., Dityatev, A., Hartlage-Rübsamen, M., Blosa, M., Holzer, M., Flach, K., Pavlica, S., Dityateva, G., Grosche, J., Brückner, G., et al. (2014). Tenascin-R promotes assembly of the extracellular matrix of perineuronal nets via clustering of aggrecan. Philos. Trans. R. Soc. Lond. B. Biol. Sci. *369*, 20140046.

Morellini, F., Sivukhina, E., Stoenica, L., Oulianova, E., Bukalo, O., Jakovcevski, I., Dityatev, A., Irintchev, A., and Schachner, M. (2010). Improved reversal learning and working memory and enhanced reactivity to novelty in mice with enhanced GABAergic innervation in the dentate gyrus. Cereb. Cortex *20*, 2712–2727.

Morganti, M.C., Taylor, J., Pesheva, P., and Schachner, M. (1990). Oligodendrocyte-derived J1-160/180 extracellular matrix glycoproteins are adhesive or repulsive depending on the partner cell type and time of interaction. Exp. Neurol. *109*, 98–110.

Mortillo, S., Elste, A., Ge, Y., Patil, S.B., Hsiao, K., Huntley, G.W., Davis, R.L., and Benson, D.L. (2012). Compensatory redistribution of neuroligins and N-cadherin following deletion of synaptic β1-integrin. J. Comp. Neurol. *520*, 2041–2052.

Murphy, G. (2011). Tissue inhibitors of metalloproteinases. Genome Biol. *12*, 233.

Nagy, V., Bozdagi, O., Matynia, A., Balcerzyk, M., Okulski, P., Dzwonek, J., Costa, R.M., Silva, A.J., Kaczmarek, L., and Huntley, G.W. (2006). Matrix Metalloproteinase-9 Is Required for Hippocampal Late-Phase Long-Term Potentiation and Memory. J. Neurosci. *26*, 1923.

Nakic, M., Manahan-Vaughan, D., Reymann, K.G., and Schachner, M. (1998). Long-term potentiationin vivo increases rat hippocampal tenascin-C expression. J. Neurobiol. *37*, 393–404.

Neidhardt, J., Fehr, S., Kutsche, M., Löhler, J., and Schachner, M. (2003). Tenascin-N: characterization

of a novel member of the tenascin family that mediates neurite repulsion from hippocampal explants. Mol. Cell. Neurosci. *23*, 193–209.

Niekisch, H., Steinhardt, J., Berghäuser, J., Bertazzoni, S., Kaschinski, E., Kasper, J., Kisse, M., Mitlöhner, J., Singh, J.B., Weber, J., et al. (2019). Learning Induces Transient Upregulation of Brevican in the Auditory Cortex during Consolidation of Long-Term Memories. J. Neurosci. *39*, 7049–7060.

Nikonenko, A., Schmidt, S., Skibo, G., Brückner, G., and Schachner, M. (2003). Tenascin-R-deficient mice show structural alterations of symmetric perisomatic synapses in the CA1 region of the hippocampus. J. Comp. Neurol.

Nirwane, A., and Yao, Y. (2019). Laminins and their receptors in the CNS. Biol. Rev. *94*, 283–306.

Nishimune, H., Sanes, J.R., and Carlson, S.S. (2004). A synaptic laminin–calcium channel interaction organizes active zones in motor nerve terminals. Nature *432*, 580–587.

Okada, T., and Suzuki, H. (2021). The Role of Tenascin-C in Tissue Injury and Repair After Stroke. Front. Immunol. *11*, 3553.

Okulski, P., Jay, T.M., Jaworski, J., Duniec, K., Dzwonek, J., Konopacki, F.A., Wilczynski, G.M., Sánchez-Capelo, A., Mallet, J., and Kaczmarek, L. (2007). TIMP-1 Abolishes MMP-9-Dependent Long-lasting Long-term Potentiation in the Prefrontal Cortex. Biol. Psychiatry *62*, 359–362.

Oliet, S.H., Malenka, R.C., and Nicoll, R.A. (1997). Two distinct forms of long-term depression coexist in CA1 hippocampal pyramidal cells. Neuron *18*, 969–982.

Omar, M.H., Campbell, M.K., Xiao, X., Zhong, Q., Brunken, W.J., Miner, J.H., Greer, C.A., and Koleske, A.J. (2017). CNS Neurons Deposit Laminin α5 to Stabilize Synapses. Cell Rep. *21*, 1281–1292.

Oohashi, T., Edamatsu, M., Bekku, Y., and Carulli, D. (2015). The hyaluronan and proteoglycan link proteins: Organizers of the brain extracellular matrix and key molecules for neuronal function and plasticity. Exp. Neurol. *274*, 134–144.

Orlando, C., Ster, J., Gerber, U., Fawcett, J.W., and Raineteau, O. (2012). Perisynaptic Chondroitin Sulfate Proteoglycans Restrict Structural Plasticity in an Integrin-Dependent Manner. J. Neurosci. *32*, 18009–18017.

Pantazopoulos, H., and Berretta, S. (2016). In Sickness and in Health: Perineuronal Nets and Synaptic Plasticity in Psychiatric Disorders. Neural Plast. *2016*, 1–23.

Park, Y.K., and Goda, Y. (2016). Integrins in synapse regulation. Nat. Rev. Neurosci. *17*, 745–756.

Parkinson, G.T., and Hanley, J.G. (2018). Mechanisms of AMPA Receptor Endosomal Sorting. Front. Mol. Neurosci. *11*.

Pastuzyn, E.D., Day, C.E., Kearns, R.B., Kyrke-Smith, M., Taibi, A. V., McCormick, J., Yoder, N., Belnap, D.M., Erlendsson, S., Morado, D.R., et al. (2018). The Neuronal Gene Arc Encodes a Repurposed Retrotransposon Gag Protein that Mediates Intercellular RNA Transfer. Cell *172*, 275-288.e18.

Pesheva, P., Spiess, E., and Schachner, M. (1989). J1-160 and J1-180 are oligodendrocyte-secreted nonpermissive substrates for cell adhesion. J. Cell Biol. *109*, 1765–1778.

Pesheva, P., Gennarini, G., Goridis, C., and Schachner, M. (1993). The F3/11 cell adhesion molecule mediates the repulsion of neurons by the extracellular matrix glycoprotein J1-160/180. Neuron *10*, 69–82.

Pesheva, P., Gloor, S., Schachner, M., and Probstmeier, R. (1997). Tenascin-R is an intrinsic autocrine factor for oligodendrocyte differentiation and promotes cell adhesion by a sulfatide-mediated mechanism. J. Neurosci. *17*, 4642–4651.

Pierce, J.P., Mayer, T., and McCarthy, J.B. (2001). Evidence for a satellite secretory pathway in neuronal dendritic spines. Curr. Biol. *11*, 351–355.

Pizzorusso, T. (2002). Reactivation of Ocular Dominance Plasticity in the Adult Visual Cortex. Science (80-.). *298*, 1248–1251.

Porwoll, S., Loch, N., Kannicht, C., Nuck, R., Grunow, D., Reutter, W., and Tauber, R. (1998). Cell

Surface Glycoproteins Undergo Postbiosynthetic Modification of Their N -Glycans by Stepwise Demannosylation. J. Biol. Chem. *273*, 1075–1085.

Probstmeier, R., and Pesheva, P. (1999). Tenascin-C inhibits 1 integrin-dependent cell adhesion and neurite outgrowth on fibronectin by a disialoganglioside-mediated signaling mechanism. Glycobiology *9*, 101–114.

Pujadas, L., Gruart, A., Bosch, C., Delgado, L., Teixeira, C.M., Rossi, D., De Lecea, L., Martínez, A., Delgado-García, J.M., and Soriano, E. (2010). Reelin regulates postnatal neurogenesis and enhances spine hypertrophy and long-term potentiation. J. Neurosci. *30*, 4636–4649.

Qiu, S., Korwek, K.M., Pratt-Davis, A.R., Peters, M., Bergman, M.Y., and Weeber, E.J. (2006). Cognitive disruption and altered hippocampus synaptic function in Reelin haploinsufficient mice. Neurobiol. Learn. Mem. *85*, 228–242.

Qu, L., Akbergenova, Y., Hu, Y., and Schikorski, T. (2009). Synapse-to-synapse variation in mean synaptic vesicle size and its relationship with synaptic morphology and function. J. Comp. Neurol. *514*, 343–352.

Rainero, E. (2016). Extracellular matrix endocytosis in controlling matrix turnover and beyond: emerging roles in cancer. Biochem. Soc. Trans. *44*, 1347–1354.

Ramón y Cajal, S. (1909). Histologie du système nerveux de l'homme & des vertébrés. (Paris : Maloine,).

Rao-Ruiz, P., Couey, J.J., Marcelo, I.M., Bouwkamp, C.G., Slump, D.E., Matos, M.R., Loo, R.J. van der, Martins, G.J., Hout, M. van den, IJcken, W.F. van, et al. (2019). Engram-specific transcriptome profiling of contextual memory consolidation. Nat. Commun. 2019 101 *10*, 1–14.

Rehberg, K., Kliche, S., Madencioglu, D.A., Thiere, M., Müller, B., Manuel Meineke, B., Freund, C., Budinger, E., and Stork, O. (2014). The serine/threonine kinase Ndr2 controls integrin trafficking and integrin-dependent neurite growth. J. Neurosci. *34*, 5342–5354.

Rex, C.S., Chen, L.Y., Sharma, A., Liu, J., Babayan, A.H., Gall, C.M., and Lynch, G. (2009). Different Rho GTPase-dependent signaling pathways initiate sequential steps in the consolidation of long-term potentiation. J. Cell Biol. *186*, 85–97.

Rizzoli, S.O. (2014). Synaptic vesicle recycling: steps and principles. EMBO J. *33*, 788–822.

Rogers, J.T., Rusiana, I., Trotter, J., Zhao, L., Donaldson, E., Pak, D.T.S., Babus, L.W., Peters, M., Banko, J.L., Chavis, P., et al. (2011). Reelin supplementation enhances cognitive ability, synaptic plasticity, and dendritic spine density. Learn. Mem. *18*, 558–564.

Rosenmund, C., and Stevens, C.F. (1996). Definition of the readily releasable pool of vesicles at hippocampal synapses. Neuron *16*, 1197–1207.

Roszkowska, M., Skupien, A., Wójtowicz, T., Konopka, A., Gorlewicz, A., Kisiel, M., Bekisz, M., Ruszczycki, B., Dolezyczek, H., Rejmak, E., et al. (2016). CD44: A novel synaptic cell adhesion molecule regulating structural and functional plasticity of dendritic spines. Mol. Biol. Cell *27*, 4055–4066.

Roth, R.H., Cudmore, R.H., Tan, H.L., Hong, I., Zhang, Y., and Huganir, R.L. (2020). Cortical Synaptic AMPA Receptor Plasticity during Motor Learning. Neuron *105*, 895-908.e5.

Ruoslahti, E. (1996). Brain extracellular matrix. Glycobiology *6*, 489–492.

Saghatelyan, A.K., Dityatev, A., Schmidt, S., Schuster, T., Bartsch, U., and Schachner, M. (2001). Reduced perisomatic inhibition, increased excitatory transmission, and impaired long-term potentiation in mice deficient for the extracellular matrix glycoprotein tenascin-R. Mol. Cell. Neurosci.

Saghatelyan, A.K., Snapyan, M., Gorissen, S., Meigel, I., Mosbacher, J., Kaupmann, K., Bettler, B., Kornilov, A. V., Nifantiev, N.E., Sakanyan, V., et al. (2003). Recognition molecule associated carbohydrate inhibits postsynaptic GABAB receptors: A mechanism for homeostatic regulation of GABA release in perisomatic synapses. Mol. Cell. Neurosci. *24*, 271–282.

Scheiffele, P., Peränen, J., and Simons, K. (1995). N-glycans as apical sorting signals in epithelial cells.

Nature *378*, 96–98.

Scherberich, A., Tucker, R.P., Samandari, E., Brown-Luedi, M., Martin, D., and Chiquet-Ehrismann, R. (2004). Murine tenascin-W: a novel mammalian tenascin expressed in kidney and at sites of bone and smooth muscle development. J. Cell Sci. *117*, 571–581.

Schnell, E., Sizemore, M., Karimzadegan, S., Chen, L., Bredt, D.S., and Nicoll, R.A. (2002). Direct interactions between PSD-95 and stargazin control synaptic AMPA receptor number. Proc. Natl. Acad. Sci. *99*, 13902–13907.

Sheng, M., and Kim, E. (2011). The postsynaptic organization of synapses. Cold Spring Harb. Perspect. Biol. *3*, a005678.

Shi, F., and Sottile, J. (2008). Caveolin-1-dependent β1 integrin endocytosis is a critical regulator of fibronectin turnover. J. Cell Sci. *121*, 2360–2371.

Shi, Y., and Ethell, I.M. (2006). Integrins Control Dendritic Spine Plasticity in Hippocampal Neurons through NMDA Receptor and Ca2+/Calmodulin-Dependent Protein Kinase II-Mediated Actin Reorganization. J. Neurosci. *26*, 1813–1822.

Sloan Warren, M., Bradley, W.D., Gourley, S.L., Lin, Y.C., Simpson, M.A., Reichardt, L.F., Greer, C.A., Taylor, J.R., and Koleske, A.J. (2012). Integrin β1 signals through Arg to regulate postnatal dendritic arborization, synapse density, and behavior. J. Neurosci. *32*, 2824–2834.

Son, Y.-J., Scranton, T.W., Sunderland, W.J., Baek, S.J., Miner, J.H., Sanes, J.R., and Carlson, S.S. (2000). The Synaptic Vesicle Protein SV2 Is Complexed with an α5-Containing Laminin on the Nerve Terminal Surface. J. Biol. Chem. *275*, 451–460.

Sonntag, M., Blosa, M., Schmidt, S., Reimann, K., Blum, K., Eckrich, T., Seeger, G., Hecker, D., Schick, B., Arendt, T., et al. (2018). Synaptic coupling of inner ear sensory cells is controlled by brevican-based extracellular matrix baskets resembling perineuronal nets. BMC Biol. *16*, 1–18.

Sorg, B.A., Berretta, S., Blacktop, J.M., Fawcett, J.W., Kitagawa, H., Kwok, J.C.F., and Miquel, M. (2016). Casting a Wide Net: Role of Perineuronal Nets in Neural Plasticity. J. Neurosci. *36*, 11459–11468.

Spicer, A.P., Joo, A., and Bowling, R.A. (2003). A hyaluronan binding link protein gene family whose members are physically linked adjacent to chrondroitin sulfate proteoglycan core protein genes. The missing links. J. Biol. Chem. *278*, 21083–21091.

Srinivasan, Y., Elmer, L., Davis, J., Bennett, V., and Angelides, K. (1988). Ankyrin and spectrin associate with voltage-dependent sodium channels in brain. Nature *333*, 177–180.

Stamenkovic, V., Stamenkovic, S., Jaworski, T., Gawlak, M., Jovanovic, M., Jakovcevski, I., Wilczynski, G.M., Kaczmarek, L., Schachner, M., Radenovic, L., et al. (2017). The extracellular matrix glycoprotein tenascin-C and matrix metalloproteinases modify cerebellar structural plasticity by exposure to an enriched environment. Brain Struct. Funct. *222*, 393–415.

Stanton, H., Melrose, J., Little, C.B., and Fosang, A.J. (2011). Proteoglycan degradation by the ADAMTS family of proteinases. Biochim. Biophys. Acta - Mol. Basis Dis. *1812*, 1616–1629.

Stefaniuk, M., Beroun, A., Lebitko, T., Markina, O., Leski, S., Meyza, K., Grzywacz, A., Samochowiec, J., Samochowiec, A., Radwanska, K., et al. (2017). Matrix Metalloproteinase-9 and Synaptic Plasticity in the Central Amygdala in Control of Alcohol-Seeking Behavior. Biol. Psychiatry *81*, 907–917.

Steffens, H., Mott, A.C., Li, S., Wegner, W., Švehla, P., Kan, V.W.Y., Wolf, F., Liebscher, S., and Willig, K.I. (2021). Stable but not rigid: Chronic in vivo STED nanoscopy reveals extensive remodeling of spines, indicating multiple drivers of plasticity. Sci. Adv. *7*, eabf2806.

Stephan, A., Mateos, J.M., Kozlov, S. V., Cinelli, P., Kistler, A.D., Hettwer, S., Rülicke, T., Streit, P., Kunz, B., and Sonderegger, P. (2008). Neurotrypsin cleaves agrin locally at the synapse. FASEB J. *22*, 1861–1873.

Südhof, T.C. (2012). The Presynaptic Active Zone. Neuron *75*, 11.

Syková, E., and Nicholson, C. (2008). Diffusion in brain extracellular space. Physiol. Rev. *88*, 1277–

1340.

Takada, Y., Ye, X., and Simon, S. (2007). The integrins. Genome Biol. *8*, 215.

Tammi, R., Rilla, K., Pienimäki, J.-P., MacCallum, D.K., Hogg, M., Luukkonen, M., Hascall, V.C., and Tammi, M. (2001). Hyaluronan Enters Keratinocytes by a Novel Endocytic Route for Catabolism. J. Biol. Chem. *276*, 35111–35122.

Tan, C.L., Kwok, J.C.F., Patani, R., Ffrench-Constant, C., Chandran, S., and Fawcett, J.W. (2011). Integrin activation promotes axon growth on inhibitory chondroitin sulfate proteoglycans by enhancing integrin signaling. J. Neurosci. *31*, 6289–6295.

Tang, B.L. (2008). Emerging aspects of membrane traffic in neuronal dendrite growth. Biochim. Biophys. Acta - Mol. Cell Res. *1783*, 169–176.

Taoufiq, Z., Ninov, M., Villar-Briones, A., Wang, H.-Y., Sasaki, T., Roy, M.C., Beauchain, F., Mori, Y., Yoshida, T., Takamori, S., et al. (2020). Hidden proteome of synaptic vesicles in the mammalian brain. Proc. Natl. Acad. Sci. *117*, 33586–33596.

Testa, I., Urban, N.T., Jakobs, S., Eggeling, C., Willig, K.I., and Hell, S.W. (2012). Nanoscopy of Living Brain Slices with Low Light Levels. Neuron *75*, 992–1000.

Tian, L., Stefanidakis, M., Ning, L., Lint, P. Van, Nyman-Huttunen, H., Libert, C., Itohara, S., Mishina, M., Rauvala, H., and Gahmberg, C.G. (2007). Activation of NMDA receptors promotes dendritic spine development through MMP-mediated ICAM-5 cleavage. J. Cell Biol. *178*, 687.

Timpl, R. (1996). Macromolecular organization of basement membranes. Curr. Opin. Cell Biol. *8*, 618–624.

Tissir, F., and Goffinet, A.M. (2003). Reelin and brain development. Nat. Rev. Neurosci. *4*, 496–505.

Tkach, M., and Théry, C. (2016). Communication by Extracellular Vesicles: Where We Are and Where We Need to Go. Cell *164*, 1226–1232.

Toole, B.P. (2004). Hyaluronan: From extracellular glue to pericellular cue. Nat. Rev. Cancer *4*, 528–539.

Toyama, B.H., Savas, J.N., Park, S.K., Harris, M.S., Ingolia, N.T., Yates, J.R., Hetzer, M.W., Ingolia, T., Yates, J.R., and Hetzer, M.W. (2014). Identification of long-lived proteins reveals exceptional stability of essential cellular structures. Cell *154*, 971–982.

Triller, A., and Choquet, D. (2008). New Concepts in Synaptic Biology Derived from Single-Molecule Imaging. Neuron *59*, 359–374.

Truscott, R.J.W., Schey, K.L., and Friedrich, M.G. (2016). Old Proteins in Man: A Field in its Infancy. Trends Biochem. Sci. *41*, 654–664.

Tsien, R.Y. (2013). Very long-term memories may be stored in the pattern of holes in the perineuronal net. Proc. Natl. Acad. Sci. U. S. A. *110*, 12456–12461.

Turrigiano, G. (2012). Homeostatic synaptic plasticity: local and global mechanisms for stabilizing neuronal function. Cold Spring Harb. Perspect. Biol. *4*, a005736–a005736.

Vilcaes, A.A., Chanaday, N.L., and Kavalali, E.T. (2021). Interneuronal exchange and functional integration of synaptobrevin via extracellular vesicles. Neuron *109*, 971-983.e5.

Visse, R., and Nagase, H. (2003). Matrix Metalloproteinases and Tissue Inhibitors of Metalloproteinases. Circ. Res. *92*, 827–839.

Vitellaro-Zuccarello, L., De Biasi, S., and Spreafico, R. (1998). One hundred years of Golgi's "perineuronal net": history of a denied structure. Ital. J. Neurol. Sci. *19*, 249–253.

de Vivo, L., Landi, S., Panniello, M., Baroncelli, L., Chierzi, S., Mariotti, L., Spolidoro, M., Pizzorusso, T., Maffei, L., and Ratto, G.M. (2013). Extracellular matrix inhibits structural and functional plasticity of dendritic spines in the adult visual cortex. Nat. Commun. *4*, 1484.

Volz, B., Orberger, G., Porwoll, S., Hauri, H.P., and Tauber, R. (1995). Selective reentry of recycling

cell surface glycoproteins to the biosynthetic pathway in human hepatocarcinoma HepG2 cells. J. Cell Biol. *130*, 537–551.

Wang, X., Bozdagi, O., Nikitczuk, J.S., Zhai, Z.W., Zhou, Q., and Huntley, G.W. (2008). Extracellular proteolysis by matrix metalloproteinase-9 drives dendritic spine enlargement and long-term potentiation coordinately. Proc. Natl. Acad. Sci. U. S. A. *105*, 19520.

Wang, Y., Balaji, V., Kaniyappan, S., Krüger, L., Irsen, S., Tepper, K., Chandupatla, R., Maetzler, W., Schneider, A., Mandelkow, E., et al. (2017). The release and trans-synaptic transmission of Tau via exosomes. Mol. Neurodegener. *12*, 5.

Webb, D.J., Zhang, H., Majumdar, D., and Horwitz, A.F. (2007). α5 Integrin Signaling Regulates the Formation of Spines and Synapses in Hippocampal Neurons. J. Biol. Chem. *282*, 6929–6935.

Weber, P., Bartsch, U., Rasband, M.N., Czaniera, R., Lang, Y., Bluethmann, H., Margolis, R.U., Levinson, S.R., Shrager, P., Montag, D., et al. (1999). Mice deficient for tenascin-R display alterations of the extracellular matrix and decreased axonal conduction velocities in the CNS. J. Neurosci. *19*, 4245–4262.

Weeber, E.J., Beffert, U., Jones, C., Christian, J.M., Förster, E., David Sweatt, J., and Herz, J. (2002). Reelin and apoE receptors cooperate to enhance hippocampal synaptic plasticity and learning. J. Biol. Chem. *277*, 39944–39952.

Wegner, W., Mott, A.C., Grant, S.G.N., Steffens, H., and Willig, K.I. (2018). In vivo STED microscopy visualizes PSD95 sub-structures and morphological changes over several hours in the mouse visual cortex. Sci. Rep. *8*, 219.

Wegrzyn, J.L., Bark, S.J., Funkelstein, L., Mosier, C., Yap, A., Kazemi-Esfarjani, P., La Spada, A.R., Sigurdson, C., O'Connor, D.T., and Hook, V. (2010). Proteomics of Dense Core Secretory Vesicles Reveal Distinct Protein Categories for Secretion of Neuroeffectors for Cell−Cell Communication. J. Proteome Res. *9*, 5002–5024.

Willig, K.I., Steffens, H., Gregor, C., Herholt, A., Rossner, M.J., and Hell, S.W. (2014). Nanoscopy of Filamentous Actin in Cortical Dendrites of a Living Mouse. Biophys. J. *106*, L01–L03.

Wintergerst, E.S., Fuss, B., and Bartsch, U. (1993). Localization of Janusin mRNA in the Central Nervous System of the Developing and Adult Mouse. Eur. J. Neurosci. *5*, 299–310.

Wintergerst, E.S., Rathjen, F.G., Schwaller, B., Eggli, P., and Celio, M.R. (2001). Tenascin-R associates extracellularly with parvalbumin immunoreactive neurones but is synthesised by another neuronal population in the adult rat cerebral cortex. J. Neurocytol. *30*, 293–301.

Wójtowicz, T., and Mozrzymas, J.W. (2014). Matrix metalloprotease activity shapes the magnitude of EPSPs and spike plasticity within the hippocampal CA3 network. Hippocampus *24*, 135–153.

Wong, M.Y., Zhou, C., Shakiryanova, D., Lloyd, T.E., Deitcher, D.L., and Levitan, E.S. (2012). Neuropeptide Delivery to Synapses by Long-Range Vesicle Circulation and Sporadic Capture. Cell *148*, 1029–1038.

Wratil, P.R., Horstkorte, R., and Reutter, W. (2016). Metabolic Glycoengineering with N -Acyl Side Chain Modified Mannosamines. Angew. Chemie Int. Ed. *55*, 9482–9512.

Xiao, Z.-C., Ragsdale, D.S., Malhotra, J.D., Mattei, L.N., Braun, P.E., Schachner, M., and Isom, L.L. (1999). Tenascin-R Is a Functional Modulator of Sodium Channel β Subunits. J. Biol. Chem. *274*, 26511–26517.

Xiao, Z.C., Taylor, J., Montag, D., Rougon, G., Schachner, M., Rougon', G., and Schachner, M. (1996). Distinct Effects of Recombinant Tenascin-R Domains in Neuronal Cell Functions and Identification of the Domain Interacting with the Neuronal Recognition Molecule F3/11. Eur. J. Neurosci. *8*, 766–782.

Xu, W., Schlüter, O.M., Steiner, P., Czervionke, B.L., Sabatini, B., and Malenka, R.C. (2008). Molecular dissociation of the role of PSD-95 in regulating synaptic strength and LTD. Neuron *57*, 248–262.

Xue, Y.-X., Xue, L.-F., Liu, J.-F., He, J., Deng, J.-H., Sun, S.-C., Han, H.-B., Luo, Y.-X., Xu, L.-Z., Wu, P., et al. (2014). Depletion of Perineuronal Nets in the Amygdala to Enhance the Erasure of Drug Memories. J. Neurosci. *34*, 6647–6658.

Yamada, J., and Jinno, S. (2013). Spatio-temporal differences in perineuronal net expression in the mouse hippocampus, with reference to parvalbumin. Neuroscience *253*, 368–379.

Yamaguchi, Y. (2000). Lecticans: Organizers of the brain extracellular matrix. Cell. Mol. Life Sci. *57*, 276–289.

Yuan, W., Matthews, R.., Sandy, J.., and Gottschall, P.. (2002). Association between protease-specific proteolytic cleavage of brevican and synaptic loss in the dentate gyrus of kainate-treated rats. Neuroscience *114*, 1091–1101.

Zaccaria, M.L., Di Tommaso, F., Brancaccio, A., Paggi, P., and Petrucci, T.C. (2001). Dystroglycan distribution in adult mouse brain: a light and electron microscopy study. Neuroscience *104*, 311–324.

Zagulska-Szymczak, S., Filipkowski, R.K., and Kaczmarek, L. (2001). Kainate-induced genes in the hippocampus: lessons from expression patterns. Neurochem. Int. *38*, 485–501.

Zhai, R.G., Vardinon-Friedman, H., Cases-Langhoff, C., Becker, B., Gundelfinger, E.D., Ziv, N.E., and Garner, C.C. (2001). Assembling the Presynaptic Active Zone. Neuron *29*, 131–143.

Zhang, Y., Cudmore, R.H., Lin, D.-T., Linden, D.J., and Huganir, R.L. (2015). Visualization of NMDA receptor–dependent AMPA receptor synaptic plasticity in vivo. Nat. Neurosci. *18*, 402.

Zimmermann, D.R., and Dours-Zimmermann, M.T. (2008). Extracellular matrix of the central nervous system: from neglect to challenge. Histochem. Cell Biol. *130*, 635–653.

List of abbreviations

AAV	Adeno-associated virus
ACSF	Artificial cerebrospinal fluid
ADAMTS	A Disintegrin and Metalloproteinase with Thrombospondin motifs
AHA	L-azidohomoalaine
AMPA(R)	α-amino-3-hydroxy-5-methyl-4-isoxazolepropionic acid (receptor)
AP5	(2R)-amino-5-phosphonovaleric acid
BSA	Bovine Serum Albumin
CNQX	Cyanquixaline
COIN	Correlated optical and isotopic nanoscopy
CSPG	Chondroitin sulfate proteoglycan
DiO	Dioctadecyl-oxacarbocyanin
DIV	Days in vitro
DMEM	Dulbecco's Modified Eagle Medium
DMSO	Dimethyl sulfoxide
ECM	Extracellular matrix
EGF	Epidermal growth factor
eGFP	Enhanced green fluorescent protein
EGTA	Egtazic acid
ER	Endoplasmic reticulum
ERGIC	Endoplasmic-reticulum–Golgi intermediate compartment
FITC	Fluorescein isothiocyanate
FRAP	Fluorescence recovery after photobleaching
GABA	Gamma-Aminobutyric acid
GalNAc	N-Acetylgalactosamine
GalNAz	N-azidoacetylgalactosamine
GFAP	Glial fibrillary acidic protein
GlcNAc	N-Acetylglucosamine
GlcNAz	N-Azidoacetylglucosamine
HA	Hyaluronic acid
HABP	Hyaluronan binding protein
HAPLN	Hyaluronan and proteoglycan binding link protein
HNK1	Human natural killer-1
KA	Kainic acid
LAMP1	Lysosomal-associated membrane protein 1
LTP	Long-term potentiation
MBP	Myelin basic protein
mEPSC	Miniature excitatory synaptic current
MMP	Matrix metalloproteinase
nanoSIMS	Nanoscale secondary ion mass spectrometry
NMDA(R)	N-Methyl-D-aspartate (receptor)
PBS	Phosphate-buffered saline
PFA	Paraformaldehyde
PNN	Perineuronal net
POI	Protein of interest
PSD	Postsynaptic density
RFP	Red fluorescent protein
ROI	Region of interest
SA	Spine apparatus
SEM	Standard error of the mean
shRNA	Small hairpin RNA
siRNA	Small interfering RNA

STED	Stimulated emission depletion microscopy
Syt1	Synaptotagmin 1
TBST	Tris-buffered saline with Tween 20
TGN	Trans-Golgi network
TIMP	Tissue inhibitor of metalloproteinase
TNC	Tenascin C
TNR	Tenascin R
TTX	Tetrodotoxin
VGAT	Vesicular GABA transporter
VGCC	Voltage-gated calcium channel
VGlut1	Vesicular glutamate transporter 1
WFA	Wisteria floribunda agglutinin